

Durability of Multi Layered Plasma and HVOF Coatings

By

Sultan A. Al-Mutairi B.Sc M.Sc

A thesis submitted in fulfillment of the requirement for the
degree of

Doctor of Philosophy

Supervisors

Dr. Joseph Stokes
Prof. M. S. J. Hashmi, Prof. B. S. Yilbas

Dublin City University
School of Mechanical and Manufacturing Engineering

January 2013

Declaration

I hereby certify that this material, which I now submit for assessment on the program of study leading to the award of Doctor of Philosophy is entirely my own work, that I have exercised reasonable care to ensure that the work is original, and does not to the best of my knowledge breach any law of copyright, and has not been taken from the work of others save and to the extent that such work has been cited and acknowledged within the text of my work.

Signed:

I.D. Number: 58102752

Date:

Acknowledgements

First of all I thank Allah who gave me the life, the health, the power, and the success to finish this work.

Foremost, I would like to express my sincere gratitude to my supervisors Dr. Joseph T. Stokes, Prof. M. S. J. Hashmi (Co-supervisor), and Prof. B. S. Yilbas (External Supervisor) for the continuous support of my Ph.D study and research, for their patience, motivation, enthusiasm, and immense knowledge. Their guidance helped me in all the time of research and writing of this thesis.

Besides my supervisors, I would like to thank all lab technicians in Saudi Aramco, King Fahd University of Petroleum and Minerals, and Dublin City University (DCU) for their help during lab tests.

My sincere thanks also go to Ms. Suzanne Dockery (DCU) and Ms. Nancy Kennedy (Aramco Overseas Company U.K. Limited) for all logistic support they provided during the course of my assignment.

Thank you for my PhD sponsor “Saudi Aramco” for sponsoring all costs of my research and tracking of my progress.

My special thank goes to my close friends in Saudi Aramco R&DC, Mr. Helal M. Al-Mutairi and Abdullatif I. Al-Abdulhadi (my mentor) for their encouragement, insightful comments, and best wishes.

I am deeply and forever indebted to my parents for their love, support and encouragement throughout my entire life. I pray to Allah to improve their health and help them to overcome their sickness. I also thank my uncle “Abu Nawaf” for asking about me while I am away from home.

I am very grateful to my wife “Sara” and to my daughters (Danah, Demah, Ghade, and Kenaz) who joined me every moment of my PhD assignment and made life easy and happy for me. I will not forget my son “Omar” who born at end of my PhD program to have the five star children. I thank my wonderful and beautiful family for instilling in me confidence and a drive for pursuing my PhD.

Finally, I thank everyone who wished me a good luck in my PhD or/and attended my graduation ceremony, or he/she think that I have forgotten his/her name in this acknowledgment.

TABLE OF CONTENTS

	Page
Declaration	ii
Acknowledgements	iii
Table of Contents	v
List of Figures	ix
List of Tables	xviii
Abstract	xx

CHAPTER 1	INTRODUCTION	1
------------------	---------------------	----------

CHAPTER 2	LITERATURE SURVEY	10
------------------	--------------------------	-----------

2.1	Introduction	10
2.2	Wear	11
2.3	Corrosion	19
2.4	Thermal Spray Technology	21
2.4.1	High Velocity Oxygen Fuel	21
2.4.2	Plasma Spray Process	23
2.5	Thermal Spray Coatings for Wear Protection	24
2.6	Thermal Spray Coatings for Corrosion Protection	26

2.7	Coating Materials	28
2.7.1	Nanostructured Materials	29
2.7.2	Bond Coat	32
2.7.3	Multi-Layer Coatings	32

CHAPTER 3	EQUIPMENT, MATERIALS, AND PROCEDURES	35
------------------	---	-----------

3.1	Introduction	35
3.2	HVOF Thermal Spraying System	35
3.3	Plasma Thermal Spraying System	38
3.4	Workpiece /Substrates	39
3.5	Coating Materials	42
3.6	Coating Procedures	45
3.6.1	Coating Matrix	46
3.6.2	Coating Systems Parameters	51
3.6.3	Thermal Spraying Processes	52
3.7	Powder Characterization	56
3.7.1	EDXRF Analysis of Mixed Metallic Powders	56
3.7.2	XRD Analysis	57
3.7.3	Particles Size Distribution	58
3.7.4	Powder- ESEM/EDS Analysis	60
3.8	Powder Reactions	61
3.9	Coating Characterization	65
3.9.1	Methods of Coatings Characterization	65
3.9.2	Metallographic Preparation	65
3.9.3	Coatings ESEM/EDS Analysis	67
3.9.4	Surface Roughness Measurement of the Coating	67
3.9.5	Porosity Measurements	70
3.9.6	Coating Hardness Assessment	71

3.10	Static Corrosion Test	71
3.11	Erosion-Corrosion Behaviour of Thermally Sprayed Coatings	78
3.12	Mechanical Behaviour of Thermally Sprayed Coatings	81
3.12.1	Three Points Bending Test	81
3.12.2	Tensile Test	84
3.12.3	Fatigue Test	85
<hr/>		
CHAPTER 4	RESULTS AND DISCUSSION- POWDERS CHARACTERIZATION AND REACTION	87
<hr/>		
4.1	Powder Characterization	87
4.2	Possible Powder Reactions During the HVOF and Plasma Spray	111
4.4.1	Formation of an Amorphous Co Binder Phase	113
4.2.2	Dissolution of W and C in the Co	115
4.2.3	Phase Transformation	117
<hr/>		
CHAPTER 5	RESULTS AND DISCUSSION- COATINGS CHARACTERIZATION	129
<hr/>		
5.1	Coating Structure	129
5.1.1	Coating Formation and Build Up	129
5.1.2	Coating Roughness Measurements	131
5.1.3	Analysis of HVOF Produced Coatings	138
5.1.4	Analysis of Plasma Produced Coatings	142
5.1.5	Effect of Addition of AMDRY Powder to the Original WC-Co Powder	146
5.1.6	Evaluation of Coating Porosity	148
5.1.7	Evaluation of Coating Adhesion	153
5.1.8	Coating Hardness Assessment	155
5.2	Corrosion Behaviour of Applied Coatings	159
5.2.1	Dissolution of the Binder Phase In the NaCl Solution	172

5.2.2	Corrosion Mechanism	175
5.2.3	WC-Co Powder Size Effect	176
5.2.4	AMDRY Powder Effect	177
5.3	Erosion-Corrosion Behaviour of Thermally Sprayed Coatings	177
5.4	Mechanical Behaviour of Thermally Sprayed Coatings	182
5.4.1	Three Points Bending Test	182
5.4.2	Tensile Test	191
5.4.3	Fatigue Test	200
5.5	Results Summary	203
5.6	Cost of Coating Manufacturing	205
<hr/>		
CHAPTER 6	CONCLUSION AND RECOMMENDATIONS	208
<hr/>		
6.1	Conclusions	208
6.2	Recommendations for Future Work	210
<hr/>		
PUBLICATIONS ARISING FROM THIS WORK		211
<hr/>		
REFERENCES		212
<hr/>		
APPENDIX		A1
<hr/>		

LIST OF FIGURES

Figure No.	Description	Page No.
1.1	Sour gas well production pipe failure due to localized corrosion.....	2
1.2	Corrosion on the internal walls of sour crude pipeline.....	2
1.3	Hydrogen Induced Cracking (HIC) occurs when carbon steel is exposed to hydrogen sulphide (H ₂ S).....	4
1.4	Research Process Chart.....	8
2.1	(a) Adhesive wear mechanism, (b) Metal subjected to adhesive wear	12
2.2	(a) Abrasive wear mechanism, (b) Metal Affected by abrasive wear..	13
2.3	(a) Surface fatigue mechanism, (b) Fatigue of a metal surface.....	15
2.4	Example of fretting wear.....	16
2.5	(a) Erosive wear mechanism, (b) Erosive wear associated with the movement of slurries through piping.....	17
2.6	Schematic diagram of the HVOF spray system.....	22
2.7	Schematic diagram of the plasma spray system.....	24
3.1	Schematic of High velocity oxygen fuel system.....	36
3.2	(a) Model 5520 gun used in this research and (b) Model 1264 Powder Feeder used in this research.....	37
3.3	(a) Model 3710 Praxair used to produce the coating and (b) SG-100 Plasma Spray Gun.....	38
3.4	Shape of substrates used for the three point bending test, corrosion test, and for microstructural characterizations.....	40

Figure No.	Description	Page No.
3.5	Shape of substrates used for fatigue and tensile tests.....	40
3.6	Shape of substrates used for jet impingement test.....	41
3.7	Photograph of the substrate types used in this research.....	41
3.8	Photograph of the substrates holder used for spraying.....	42
3.9	SEM micrograph of WC-12Co micron sized powder.....	43
3.10	SEM micrograph of Infralloy S7412 nano sized feedstock powder showing spherical geometry.....	44
3.11	SEM micrographs of AMDRY powders (a) AMDRY 9954 and (b) AMDRY 995M.....	45
3.12	Application of the multi-layer coating for Batch 4.....	48
3.13	Powders mixed by weight percentage.....	48
3.14	Substrates loaded onto sample holder.....	49
3.15	Aluminum Oxide used for grit blasting.....	49
3.16	Grit blasting cabinet.....	50
3.17	Loading sample holder to the lathe machine.....	50
3.18	Thermal spray mass flux distribution.....	51
3.19	HVOF thermal spraying coating process used in this research.....	53
3.20	Plasma thermal spraying coating process used in this research.....	54
3.21	Test specimens produced from this research.....	55
3.22	Test Specimens: (A) Base metal, (B) After grit blasting, and (C) After multi-layer coating applied.....	55
3.23	SPECTRO X-LAB 2000 used to perform the EDXRF Spectrometry.	57
3.24	PANalytical instrument, used to perform the XRD analysis.....	58
3.25	Mastersizer 2000 used for particle size analysis.....	60
3.26	High resolution ESEM XL30 and EDS used for powder/coating analysis.....	61

Figure No.	Description	Page No.
3.27	Metallographic Preparation of the coated samples.....	67
3.28	Surface profiler used for Coating roughness measurements.....	69
3.29	Example of 3D roughness measurements.....	69
3.30	Three phase colour contrast method used to detect voids/porosity.....	70
3.31	The LEICA VMHTMOT machine.....	71
3.32	Salt Spray Testing Chamber.....	74
3.33	Arrangement of Fog Collectors.....	75
3.34	Salt used, (b) 5 parts by mass of salt , (c) NaCl solution preparation and pH measurement.....	76
3.35	Salt Spray Test conducted in the laboratory.....	77
3.36	Schematic representation of the erosion-corrosion testing rig.....	80
3.37	The erosion-corrosion testing rig.....	80
3.38	Instron testing instruments used for three point bending test.....	82
3.39	Markings on fixed specimen supports.....	83
3.40	Geometry of the three point bending test.....	83
3.41	Photograph of the Instron tensile testing machine with sample attached.....	85
3.42	Photograph of fatigue testing machine.....	86
4.1	EDXRF results of powder MIX-1 in wt. %	88
4.2	XRD Diffractogram of Identified Compounds- Powder MIX-1.....	89
4.3	Particles Size Distribution of MIX-1.....	89
4.4	MIX- 1: ESEM backscattered electron and BSE image.....	90

Figure No.	Description	Page No.
4.5	EDXRF results of powder MIX-2 in wt. %.....	91
4.6	XRD Diffractogram with Identified Compounds- Powder MIX-2.....	92
4.7	Particles Size Distribution of MIX-2.....	92
4.8	Mix No. 2: ESEM images of (A) BS image.....	94
4.9	Energy dispersive X-ray fluorescence Spectrometry of Powder MIX-3 in wt. %.....	95
4.10	XRD Diffractogram with Identified Compounds- Powder MIX-3.....	96
4.11	Particles Size Distribution of MIX-3.....	97
4.12	Mix No. 3: (A) ESEM backscattered electron (BSE) image.....	98
4.13	Energy dispersive X-ray fluorescence Spectrometry of Powder MIX-4 in wt. %.....	99
4.14	XRD Diffractogram with Identified Compounds- Powder MIX-4.....	100
4.15	Particles Size Distribution of MIX-4.....	100
4.16	Mix No. 4: (A) ESEM backscattered electron (BSE) image.....	102
4.17	Energy dispersive X-ray fluorescence Spectrometry of Powder MIX-13 in wt.%.....	103
4.18	XRD Diffractogram with Identified Compounds- Powder MIX-13...	104
4.19	Particles Size Distribution of MIX-13.....	104
4.20	Mix No. 13: (A) ESEM backscattered electron (BSE) image.....	106
4.21	Energy dispersive X-ray fluorescence Spectrometry of Powder MIX-14 in wt.%.....	107
4.22	XRD Diffractogram with Identified Compounds- Powder MIX-14...	108
4.23	Particles Size Distribution of MIX-14.....	108
4.24	Mix No. 14: (A) ESEM backscattered electron (BSE) image.....	110
4.25	Sequence of events of WC-Co responses to high temperatures.....	111

Figure No.	Description	Page No.
4.26	Thermal spray work space and WC-Co response.....	111
4.27	ESEM analysis of the applied coatings confirms the formation the Co binder phase.....	113
4.28	Presentation of cobalt both the starting powders and in the top coat layer.....	114
4.29	Dissolution of W and C in the Co phase post thermal spray.....	116
4.30	Phase transformation diagram of WC-Co at 1425 °C.....	118
4.31	XRD Diffractogram with Identified Compounds of Coating of Batch 1.....	122
4.32	XRD Diffractogram with Identified Compounds of Coating of Batch 2.....	122
4.33	XRD Diffractogram with Identified Compounds of Coating of Batch 3.....	123
4.34	XRD Diffractogram with Identified Compounds of Coating of Batch 4.....	123
4.35	XRD Diffractogram with Identified Compounds of Coating of Batch 11.....	124
4.36	XRD Diffractogram with Identified Compounds of Coating of Batch 12.....	124
4.37	XRD Diffractogram with Identified Compounds of Coating of Batch 13.....	125
4.38	XRD Diffractogram with Identified Compounds of Coating of Batch 14.....	125
5.1	Batch 4 coating showing a pancake morphology.....	130
5.2	Batch 14 coating shows layers of different lamellas.....	131
5.3	Coating roughness measurements for Batch 1 sprayed by the HVOF process.....	132
5.4	Topographical features of the coatings results from spraying different metallic powders sizes show peaks and valleys.....	134
5.5	Example of waviness of the thermal spray coatings produced by HVOF, Batch 3.....	135
5.6	Example of waviness of the thermal spray coatings produced by Plasma system, Batch 14.....	135

Figure No.	Description	Page No.
5.7	Coating waviness produced by HVOF and Plasma thermal spray using different powder sizes.....	136
5.8	Comparison of peaks and valleys of HVOF and Plasma coating conducted in this research.....	137
5.9	Example of HVOF coatings produced, Batch 1; (a) Sharp edges; (b) Coating thickness.....	139
5.10	HVOF coatings produced by different powder size: A) Batch 1, B) Batch 2.....	140
5.11	EDS Analysis of HVOF coatings produced by different powder size: (a) Batch 1, (b) Batch 2.....	141
5.12	Plasma coatings produced in this research; (a) Voids and rounded edges; (b) Coating thickness.....	143
5.13	Plasma sprayed coatings at different powder size: (a) Batch 11- Micro, (b) Batch 12- Nano.....	144
5.14	EDS Analysis of Plasma spray coatings produced by different powder size; (a) Micro-sized; (b) Nano-sized.....	146
5.15	Multilayers structures showing the effect of AMDRY powders on the top layer.....	147
5.16	Effect of addition of AMDRY powders on overall layers porosity....	150
5.17	The addition of the AMDRY powder to the original WC-Co powders at different ratios	150
5.18	Example of pores features of HVOF produced coatings, Batch 2.....	151
5.19	Example of pores features of Plasma produced coatings, Batch 12....	152
5.20	Multilayer coating interface and adhesion, Batch 3.....	154
5.21	Coating adhesion in the base metal, Batch 3 at 2200X.....	154
5.22	Bottom-Middle layer interface and adhesion, Batch 3 at 2200X.....	155
5.23	Hardness of coatings produced by different systems (HVOF/Plasma) using different powder particle size (micro/nano).....	157

Figure No.	Description	Page No.
5.24	Effect of AMDRY powder on coating hardness for HVOF and Plasma sprayed samples.....	159
5.25	Corrosion products growth on selected samples representing the coating response to the corrosive medium.....	160
5.26	Solution pH during the course of the test.....	160
5.27	Collected corrosion products.....	161
5.28	Corrosion Products of CP-Batch 1.....	163
5.29	CP-Batch 2 BSE images and corresponding EDS spectrum.....	164
5.30	CP-Batch 3: BSE images and corresponding EDS spectrum.....	165
5.31	CP-Batch 4: BSE images and corresponding EDS spectrum.....	166
5.32	CP-Batch 11 BSE images and corresponding EDS spectrum.....	167
5.33	CP-Batch 12 BSE images and corresponding EDS spectrum.....	168
5.34	CP-Batch 13 BSE images and corresponding EDS spectrum.....	169
5.35	CP-Batch 14 BSE images and corresponding EDS spectrum.....	170
5.36	Visual Examination and corresponding rating of the coating batch...	171
5.37	Potential/pH diagram for tungsten.....	174
5.38	Eh-pH Diagram of dissolved cobalt in the presence of dissolved chloride, nitrate, sulfate, and carbonate.....	174
5.39	Coating materials losses due to erosion–corrosion combined effect...	178
5.40	Plasma coatings (Batch 13), pre and post test erosion corrosion.....	179
5.41	HVOF coatings (Batch 4), pre and post test erosion corrosion.....	180
5.42	Scale sample analysis by XRD, collected after jet impingement test..	181
5.43	Test specimens after the three points bending test, inside bend (U-shape).....	183

Figure No.	Description	Page No.
5.44	Test specimens after the three points bending test, the outside bend...	184
5.45	Flexural propriety resulted from applying the three points bending test on substrate base metal.....	185
5.46	Process effect on coating flexural propriety resulted from applying the three points bending test using different powder size.....	186
5.47	AMDRY powder effect on HVOF coating flexural propriety resulted from applying the three points bending test.....	188
5.48	AMDRY powder effect on plasma coating flexural propriety resulted from applying the three points bending test.....	189
5.49	Maximum load required to undergo the bending test.....	190
5.50	Stress-Strain curve resulted from tensile test applied on uncoated substrate.....	191
5.51	Stress-Strain curve resulted from tensile test showing powder size effect on HVOF coating.....	192
5.52	Stress-Strain curve resulted from tensile test showing powder size effect on plasma coating.....	193
5.53	Stress-Strain curve resulted from tensile test showing AMDRY effect on HVOF coatings.....	194
5.54	Stress-Strain curve resulted from tensile test showing AMDRY effect on plasma coatings.....	195
5.55	Coatings crack shapes post tensile test.....	196
5.56	Elastic modulus of coatings.....	198
5.57	Ultimate stress of the coatings before and after the corrosion test.....	199
5.58	Example of the cyclic loading applied on to a coated specimen.....	200
5.59	Powder size effect on fatigue propriety of the coating for HVOF and plasma coatings.....	201
5.60	Number of cycles to coating failure.....	202
5.61	Corrosion effect on number of cycles to coating failure.....	203

Figure No.	Description	Page No.
5.62	Coating manufacturing main steps.....	205
5.63	Costs distribution in the production of a cylindrical component.....	207

LIST OF TABLES

Table No.	Description	Page No.
2.1	Wear test methods, adapted from ASTM Book of Standards.....	18
2.2	Mechanical properties comparison (n WC-Co vs. m WC-Co)...	31
3.1	HVOF System Features.....	37
3.2	Plasma System Features.....	39
3.3	Physical and chemical properties of the selected substrates.....	39
3.4	Powders contribution to the expected aggressive environment...	45
3.5	Coating Systems Matrix.....	47
3.6	Process parameters of HVOF and Plasma thermal spray.....	52
3.7	Characteristic of thermal spray processes and coatings.....	54
3.8	Grinding work parameters for metallographic preparation.....	66
3.9	Polishing work parameters for metallographic preparation.....	66
3.10	Scale for grading result using salt spray test.....	73
4.1	Percentage of W, C, and Co before and after reactions.....	112
4.2	Phase transformations during reactions	119
4.3	Powders particle size distribution measurements.....	127
5.1	Coating roughness measurements.....	133
5.2	Average overall porosity percentages of the produced coatings.	149
5.3	Hardness test measurements.....	155
5.4	Powders surface area effect on coating hardness.....	156
5.5	Elements of corrosion products detected by EDS.....	161

5.6	Coating groups rating according to ASTM B 117.....	170
5.7	Post test solution analysis.....	173
5.8	Analytical report of the jet fluid after test termination.....	181
5.9	Summary of tests results.....	204
6.1	Recommended coating applications.....	209

Durability of Multi Layered Plasma and HVOF Coatings

By

Sultan A. Al-Mutairi B.Sc M.Sc

The aim of this research is to investigate the effect of variable compositional coating layers on their mechanical and chemical behaviour under certain environments typically experienced in the Oil and Gas Industry. The research centers on using thermal spray coating techniques such as the HVOF and plasma spray equipment. The coating was applied onto selected carbon steel substrates (API-5L, Schedule-40, Grade-B) to simulate the material application used in oil and gas components that subject to corrosion and corrosion-erosion phenomena. The coating was deposited using three layers of coatings with various combinations of sprayed powders to create graded multi-layered coating. WC-12Co powders with two different powder structures (micro-sized powders and nano-sized agglomerated into micro-sized powders – nano-structured) were mixed at different ratios with AMDRY (9954 and 995M) powders to enhance the mechanical behaviour, wear, and corrosion protection (Hardness, corrosion, erosion-corrosion) of the coatings. The surface morphology and the elemental composition of the coatings were examined using SEM and EDS techniques. The results indicated that coating deposited by the HVOF (60% Micro WC-12Co and 40% Micro AMDRY 9954) was the most effective coating system in preventing corrosion. If the erosion is the dominant concern, then replacing the Microsized WC-12Co powder with the Nanosized WC-12Co powder is effective for protecting materials from wear caused by erosion-corrosion. The addition of the AMDRY powder to the original WC-Co powders helped to lower the overall coating porosity, enhanced the corrosion protection, and improved the overall erosion–corrosion performance, which addresses issues currently faced in the Oil/Gas industry. A Design of Experiment (DOE) technique may be used to optimize the powders blending ratios to give better results in future work.

INTRODUCTION

Chemical, petroleum and petrochemical industries demand increased productivity in the presence of an aggressive environment. However production equipment components are subjected to thermal cycling, abrasion, erosion and corrosion.

Oil and Gas industries encounter many problems caused by materials degradation. These problems are mainly attributed to corrosion and/or erosion phenomena. Problems related to the erosion of drilling tools, erosion caused by sand in three phase separation plants, severe corrosion caused by H₂S and elemental sulphur, and corrosion-erosion of transport pipelines, were encountered in gas and oil separation plants and refineries [1, 2]. Figures 1.1 and 1.2 are example of material degradation in oil and gas industries.

Unscheduled shutdowns due to material failures, result in process disturbance and production loss. Process disturbance can occur when an inspection reveals that one of pipeline segments is heavily attacked by corrosion. The plants operators then have to divert the high pressure gasses to another pipeline network. This diversion requires tremendous coordination and communications with other plants that use the same network, which often disturb other processes. The amount of overhead gasses has to be recalculated to avoid producing excess gas volumes. Pressures, temperatures, flow rates and other operating variables must be readjusted and manipulated to accommodate the diverted gases to the network. If plant operators did not control the situation properly, then the safety of personnel and facilities would be at risk. In some cases, plant operators cut off the production immediately

if the situation was seen to be getting worst or running out of control. If inspections revealed that there was an initiation of a pin hole in any of the operating vessels then production shut down would be safer. The shutdown of production can affect profit and disturb the total budget. Managements then have to find solutions to recap this shortage in budget.



Figure 1.1, Sour gas well production pipe failure due to localized corrosion [3].



Figure 1.2, Corrosion on the internal walls of sour crude pipeline [4].

Material degradation in the oil and gas plants is not only disruptive to plants personnel, but also costly to avoid. The cost of inspecting the plant pipelines and vessels are very high. High advanced corrosion and erosion monitoring systems must be installed in the critical areas of the plant. Maintaining degradation in materials is also very costly. Internal and external parts of the equipment and pipelines must be well inspected and maintained. Thousands of miles of pipelines have to be scheduled for T&I (Testing and Inspection) every 3-5 years. Saudi Aramco Oil Company have reported that the cost of corrosion is 60% to 70% of the plant maintenance budget and in the region of 25% of the plant operating budget [1].

Hydrogen Sulfide (H₂S) in Oil and Gas Industry

Hydrogen sulfide “H₂S” is a gas that is contained in the crude oil as it comes from the wells. It not only has a vile odour (rotten eggs odour), it is also poisonous. It can kill a human if inhaled. It is also very corrosive to metals. If the crude is wet, and contains water, then the H₂S and the H₂O will react to form H₂SO₄ (sulfuric acid), a heavy oily liquid that can corrode its way through a steel pipeline or a storage tank [2]. The dissolved H₂S in water promotes corrosion and a free hydrogen environment. Free Hydrogen penetrates the metal, reduces the ductility of metal and potentially leads to stress failure below its yield stress, resulting in Sulphide Stress Corrosion Cracking (SSCC) [5]. H₂S also causes other cracking, including stress corrosion cracking, hydrogen-induced cracking (Figure 1.3) and stepwise cracking, stress-oriented hydrogen induced cracking, soft zone cracking and galvanically induced hydrogen stress cracking.

Hydrogen gas can lead to Hydrogen embrittlement and it can occur in dry environments. H₂ embrittlement is the embrittlement of metal or an alloy involving hydrogen ingress into a metal or alloys matrix and significantly decrease its ductility, cause the metal or alloys to crack and catastrophic fail at stresses below normal yield stress levels of the attacked material. Hydrogen can react with carbon

to form methane in a high temperature environment. The methane forms and stays in the grain boundaries and voids, however it does not diffuse out of the metal. Once it accumulated in the grains and voids, it expands and forms blisters, weakening the metal strength and initiating cracks in the steel [5].

Crude oil stabilization processes sweeten the crude (removes the hydrogen sulfide) by which it is basically a form of partial distillation. But not all hydrogen sulfide can be removed by this process. By the time the stabilizer has finished its job, the hydrogen sulfide that was in the oil has been reduced but not entirely removed. Thus the crude oil is deemed “sour”. All of the crude produced in Saudi Arabia, except for that in the offshore Safaniya Field in the Arabian Gulf, is "sour". The sour crude is shipped via pipelines in stages, to a series of drums, columns, and vessels which can cause severe corrosion and degradation to these materials, if un-protected [2].



Figure 1.3, Hydrogen Induced Cracking (HIC) occurs when carbon steel is exposed to hydrogen sulphide (H₂S) [6].

For these reasons, many efforts and projects have commenced to look for new advanced materials that can be used in the oil and gas industries (e.g. non-metallic). Some research aims to address a long term solution to material degradation. It requires creating new materials with new physical and chemical specifications. It may require modification of current materials in terms of casting and fabrication. On the other hand, some research have been proposed, to find a protective tool for the existing materials, such as applying new types of coatings. Such proposals are more economical and viable to plants personnel than some long term proposed research.

Producing superior high temperature corrosion/wear resistant coating materials would help in decreasing the number of unplanned shutdowns. At the same time, it would help to increase the planned scheduled inspection (T&I) to occur on larger periods of 5 years or greater. Hence, time and money would be saved; therefore a superior coating providing this protection is the ultimate short term solution.

The use of protective coatings produced by common surface coating processes such as, Thermal Spray, Physical Vapour Deposition, Chemical Vapour Deposition and Electrolytic hard-chromium processes, among others is highly recommended to avoid materials degradation. In this work, thermal-spray processes were preferred due to the following [8]:

- Ease of coating for large and complex parts
- Relative low cost
- High rates of material deposition
- Possibility of coating components and parts with little equipment disassembly of the components
- Can be used to deposit various materials with low process-heating requirements.

Thermal spray is a generic term used for a coating process in which the coating material is heated or melted quickly by means of combustion, electric arc or plasma, and simultaneously projected by gases under high pressure and high speed onto a prepared substrate [5]. The particles striking against the surface flatten and adhere to the material base (known as a substrate) or onto previously deposited particles to form a surface layer. These layers are composed of small particles flattened in a parallel direction relative to the substrate and typically exhibit a lamellar structure with oxides, inclusions and porosity.

During the last 20 years, many carbide compositions have been successfully deposited using the coating process of HVOF (High Velocity Oxy Fuel) thermal spray. Materials such as WC-10Ni and WC-10Co-4Cr were developed to deliver an excellent combination of wear and corrosion resistance [9,10]. These materials are now being specified for critical applications for aircraft components such as landing gears.

Metallic coatings used in high temperature mixed gas environment fail primarily due to sulfidation and/or chloridation of the structural materials. After the development of high temperature sulfidation resistant materials such as FeCrAlY, NiCrAl and CoCrAlY alloys and some other ceramic materials, premature failure of these components still occurs. Failures are mainly attributed to one or more of the following mechanisms [11]:

- Coating texture (porosity) which is primarily induced by coating techniques used in applying the coating
- Improper selection of application technique
- Poor or improper surface preparation prior to applying the coating materials
- Mechanical properties of coating materials
- Differential thermal expansion coefficient between coating material and alloy substrate.

Porosity has been overcome, to some extent, by the use of both the High Velocity Oxy-Fuel (HVOF) and Plasma Spray techniques. These techniques are capable of producing dense coatings which significantly reduce inward gas penetration/diffusion through the coating material. In regard to surface preparation and coating procedures, methodologies had been developed for specific coating materials and associated procedures. Mechanical properties of coatings and the difference in the thermal expansion coefficient between the coating and the substrate are still considered to be the limiting factors in maintaining service coating integrity.

Thesis Objectives:

This study aims to produce coating materials that will provide superior corrosion and corrosion-erosion resistance to prevent material degradation in the oil and gas industry. The scope of work is to identify a single thermal spray method capable of producing a multi-layer coating by blending metallic ceramic powders that approved by literature to have high elasticity, high tensile strength, and low porosity coatings, such as tungsten carbide cobalt and Nickel based coatings [12]. Powders were blended into different weight percentages based on the total weight of the powder blend. The main objective was to replace currently used high alloy substrate with lower cost carbon steel with this layer of high corrosion and corrosion-erosion resistant coating material applied to it, Figure 1.4. The successful selection of such materials would significantly extend the service life of the material in the oil and gas industry and reduces the number of scheduled and unscheduled shutdown.

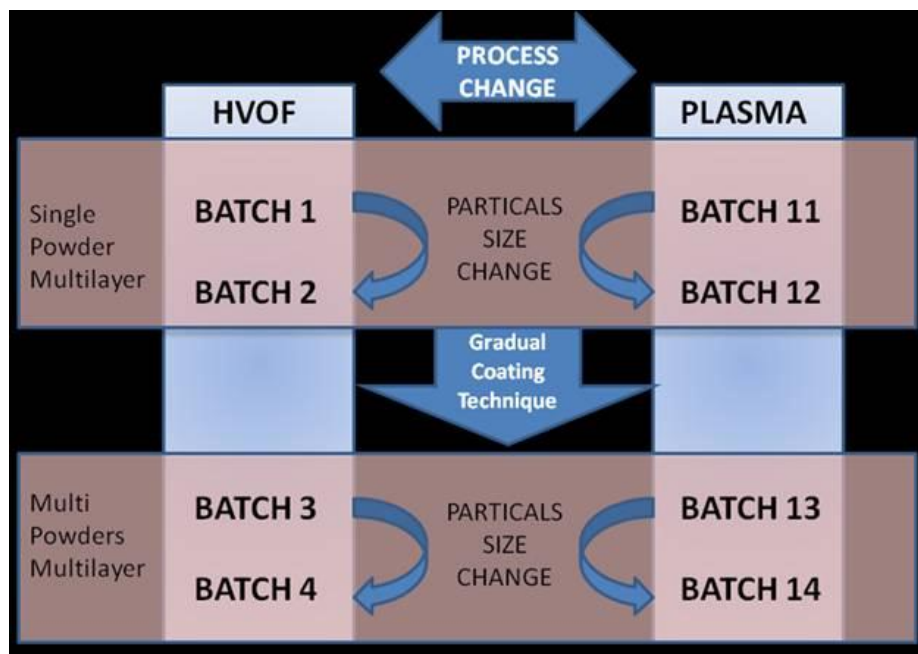


Figure 1.4, Research Process Chart

Structure of the Thesis:

This thesis was structured over a number of chapters as follows:

Chapter 2 presents a literature review of material degradation processes that are encountered in oil and gas industry. It presents the effect of corrosion and wear on materials and explain degradation mechanisms. Thermal spray technology to deposit metallic coatings is also presented in this chapter. It focused on the HVOF (High Velocity Oxygen Fuel) and Plasma thermal spraying technique due to its high flexibility and cost effectiveness techniques. Cermet coatings (tungsten carbide/cobalt “WC–Co”) are presented as selective coatings which used for producing wear/corrosion resisting surfaces. The nanostructured coatings are compared to conventional microstructured coatings. Multi-layer coatings are also explained in this chapter.

Chapter 3 presents the materials used to perform the experimental and laboratory work. It shows the coating matrix and explains the experimental procedures and the coatings processes parameters. It discusses the testing equipment, examination tools, analysis techniques, and engineering standards. It presents corrosion and mechanical tested as well as some of surface and microstructural analysis used in this research.

Chapters 4 and 5 discuss the results of the corrosion, erosion, and mechanical tests. they also explain results of laboratory analysis and compares the data. Chapter 4 investigates the powders reactions and characterization during the spraying process. Chapter 5 studies the produced coatings in terms of porosity, hardness, and surface roughness and morphology, and investigates the effect of process, powder size, and graded coating techniques on the produced coatings.

Finally, the conclusion drawn from this work and the recommendations for future research are presented in chapter 6.

LITERATURE SURVEY

2.1 INTRODUCTION

Wear, corrosion, and high temperature failure of a component are important issues in industries, especially from a safety and economical point of view. Material degradation processes due to the combined effect of corrosion and wear are named Tribocorrosion [13]. Tribocorrosion covers the science of surface transformations resulting from the interaction of mechanical loading and chemical reactions that occur between elements of a tribosystem exposed to corrosive environments [14].

Wear is a mechanical material degradation process occurring during the rubbing or impacting of surfaces, while corrosion involves chemical or electrochemical reactions of the material. Corrosion may accelerate wear and, wear can accelerate corrosion. Both of these phenomena fall into the broader category of tribocorrosion. Erosion-corrosion is another tribocorrosion phenomenon involving mechanical and chemical effects: impacting particles or fluids eroding a solid surface by abrasion, chipping or fatigue while simultaneously corroding the surface [15].

Tribocorrosion is an irreversible transformation of a metal. This phenomenon is encountered in many technological areas where they cause damage to installations, machines and devices.

Tribocorrosion affects the friction, wear and the lubrication behaviour within a tribological system. Examples of tribocorrosion systems are pumps for corrosive liquids, orthopedic implants and food processing equipment. [16]

Good corrosion resistant metals are widely used in tribocorrosion system, however, under rubbing conditions depassivation is likely to occur because of local abrasion of the passive film. The passive film forms again when the depassivated metal undergoes dissolution. This cyclic depassivation-passivation mechanism then leads to wear accelerated corrosion [17].

Researchers have used wear tests operating under controlled electrochemical conditions to investigate the tribocorrosion of metals [18]. The combination of mechanical and electrochemical techniques offers the possibility to impose different corrosion conditions by varying the applied potential and to determine the corrosion rate by measuring the current flowing from the metal into a corrosive solution [19].

2.2 WEAR

Wear is defined as the loss of material from a surface by means of some mechanical action [20]. The study of the process of wear is part of the discipline known as tribology, that is the science and technology of interacting surfaces in relative motion [21].

The complex nature of wear has delayed its investigations and resulted in isolated studies towards specific wear mechanisms or processes [22]. Wear can be classified into the following modes: Abrasive Wear, Adhesive Wear, Erosive wear, Surface Fatigue wear, and Fretting Wear [23].

A number of different wear phenomena are also commonly encountered and represented in the literature [23-26]. Impact wear, diffusive wear, cavitation, and corrosive wear are all such examples.

These wear mechanisms however, do not necessarily act independently in many applications and are not mutually exclusive [27]. "Industrial Wear" is the term used

to describe the incidence of multiple wear mechanisms occurring in unison. Wear mechanisms and/or sub-mechanisms frequently overlap and occur in a synergistic manner, producing a greater rate of wear than the sum of the individual wear mechanisms [28].

Wear Mechanisms:

The mechanism of wear is very complex. The material intrinsic surface properties such as hardness, strength, ductility, work hardening are very important factors linked to wear resistance, but other factors like surface finish, lubrication, load, speed, corrosion, temperature and properties of the opposing surface are equally important [29, 30].

Adhesive wear:

Adhesive wear occurs when two bodies slide over each other, or pressed into one another and fragments are pulled off one surface and adhere to the other, due to the strong adhesive forces between atoms [31], (Figure 2.1).

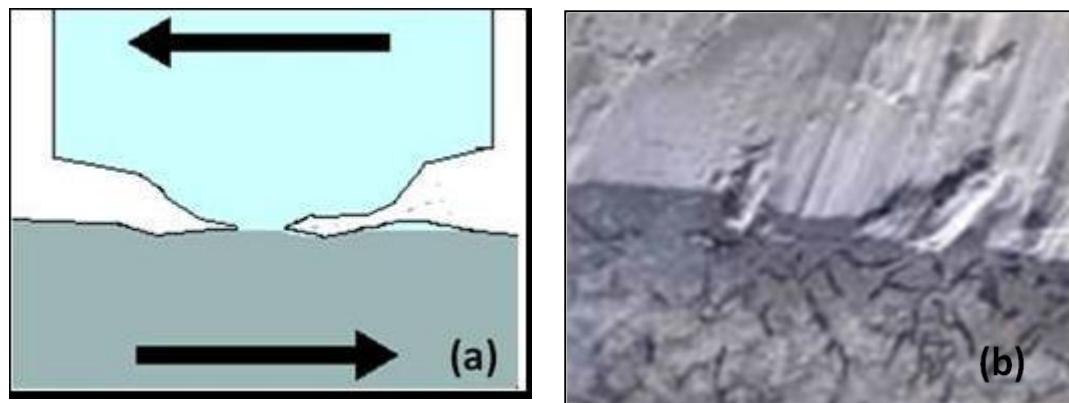


Figure 2.1, (a) Adhesive wear mechanism [32], (b) Metal subjected to adhesive wear [33]

It is the most common form of wear and is commonly encountered in conjunction with lubricant failures. The tendency of contacting surfaces to adhere arises from

the attractive forces that exist between the surface atoms of the two materials. The type and mechanism of attraction varies between different materials. Most solids will adhere on contact to some extent [34].

Surfaces also generally have low energy states due to reacted and absorbed species. The mechanism of adhesive wear occurs due to contact possibly producing surface plastic flow, scraping off soft surface films or breaking up and the removal of oxide layers. This brings clean regions into contact and introduces the possibility of strong adhesion [35]. The removal of material, or wear, takes the form of small particles. These small particles are usually transferred to the other surface but may loosen and fall off afterwards.

Abrasive wear:

Abrasive wear occurs when a hard rough surface slides across a softer surface [36]. Hard particles or hard protuberances are forced against and moving along a solid surface [37], (Figure 2.2).

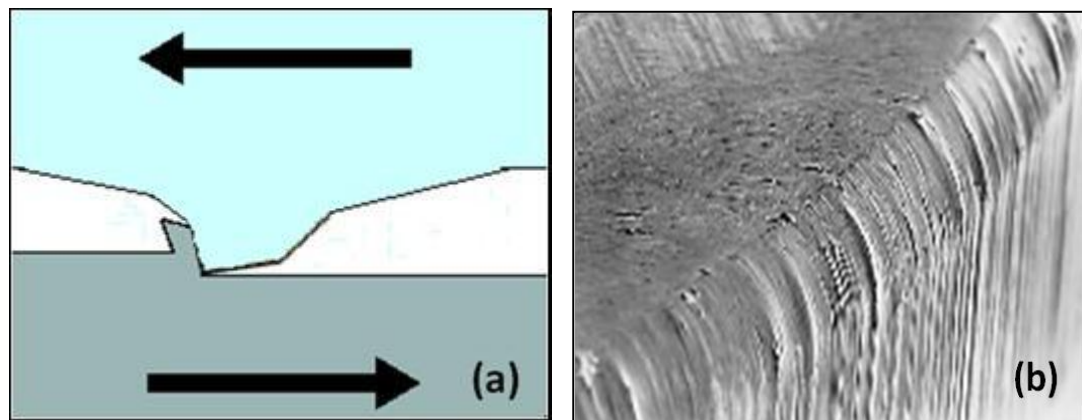


Figure 2.2, (a) Abrasive wear mechanism [33], (b) Metal Affected by abrasive wear [38].

Abrasive wear is commonly classified according to the type of contact and the contact environment. The type of contact determines the mode of abrasive wear.

The two modes of abrasive wear are known as two-body and three-body abrasive wear. Two-body wear occurs when grit, or hard particles, are rigidly mounted or adhere to a surface, and then remove the material from the other surface [39]. The common analogy is that of material being removed by sand paper. Three-body wear occurs when the particles are not constrained, and are free to roll and slide with a surface.

There are a number of factors which influence abrasive wear and hence the manner of material removal. Several different mechanisms have been proposed to describe the manner in which the material is removed. Three commonly identified mechanisms of abrasive wear are [40]:

- Ploughing
- Cutting
- Fragmentation

At low particle attack angles ploughing wear can result. This wear is similar to the sliding wear of two metal surfaces in contact. Ploughing occurs when a material is displaced to the side, away from the wear particles, resulting in the formation of grooves that do not involve direct material removal. The displaced material forms ridges adjacent to the grooves, which may be removed by the subsequent passage of abrasive particles. Cutting tends to occur at higher attack angles, and occurs when the material is separated from the surface in the form of primary debris, or microchips, with little or no material displaced to the sides of the grooves. This mechanism closely resembles conventional machining [41].

Fragmentation occurs when material is separated from a surface by a cutting process and the indenting abrasive causes localized fracture of the wear material. These cracks then freely propagate locally around the wear groove, resulting in additional material removal by spalling. Adhesion between particle and metal results in large sub-surface shear strains which leads to the fragmentation of the wear surface after the passage of several particles. The transition from one mode to

another and the relative efficiency of each mode may depend on the material properties, the load and the state of lubrication [37, 42]. Abrasive wear can be measured as loss of mass, typically measured by the Taber Abrasion Test according to ISO 9352 or ASTM D 1044.

Surface fatigue wear:

Surface fatigue is a process by which the surface of a material is weakened by cyclic loading, which is one type of general material fatigue. It can also be defined as the wear of a solid surface caused by fracture arising from material fatigue [43], (Figure 2.3).

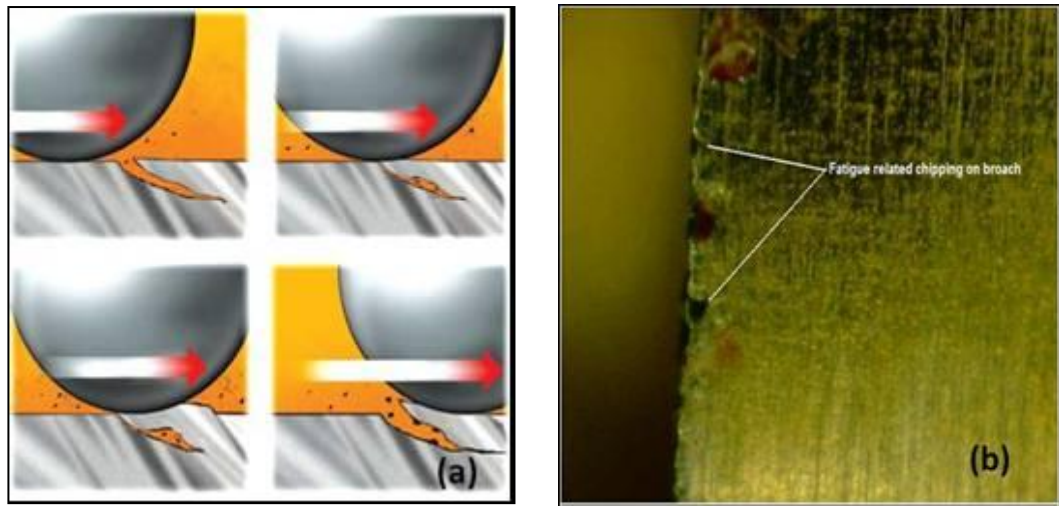


Figure 2.3, (a) Surface fatigue mechanism [44], (b) Fatigue of a metal surface [45].

Contact fatigue is a particular mode of wear that occurs in components subjected to cyclic pressures such as gears. This mode of wear is the main cause of failure. A mechanical system is usually composed of elements that are in contact and under loading. Wear can take place as a result of this contact after a certain period of time. [46]

Fretting wear:

This type of wear arises as a result of fretting due to the repeated cyclical rubbing between two surfaces. Material will be removed from one or both surfaces in contact. It occurs typically in bearings, although most bearings have their surfaces hardened to resist the problem. Another problem occurs when cracks in either surface are created, known as fretting fatigue [47]. This is the more serious of the two phenomena because it can lead to catastrophic failure of the bearing. An associated problem occurs when the small particles removed by wear are oxidized in air. The oxides are usually harder than the underlying metal, so wear accelerates as the harder particles abrade the metal surfaces further, (Figure 2.4).

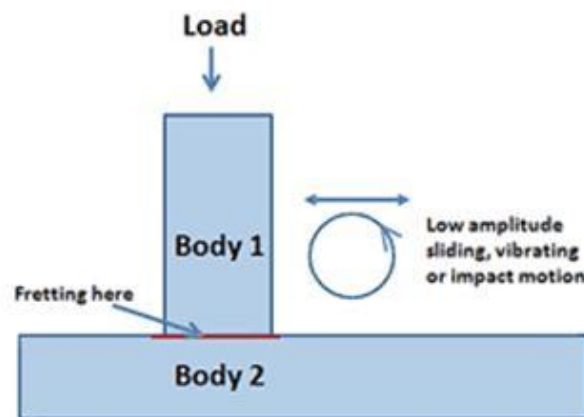


Figure 2.4, Example of fretting wear [48].

Erosive wear:

This type of wear caused by the impact of particles of solid or liquid against the surface of an object [34]. It occurs due to mechanical interaction between that surface and a fluid, a multi-component fluid, or impinging liquid or solid particles, (Figure 2.5).

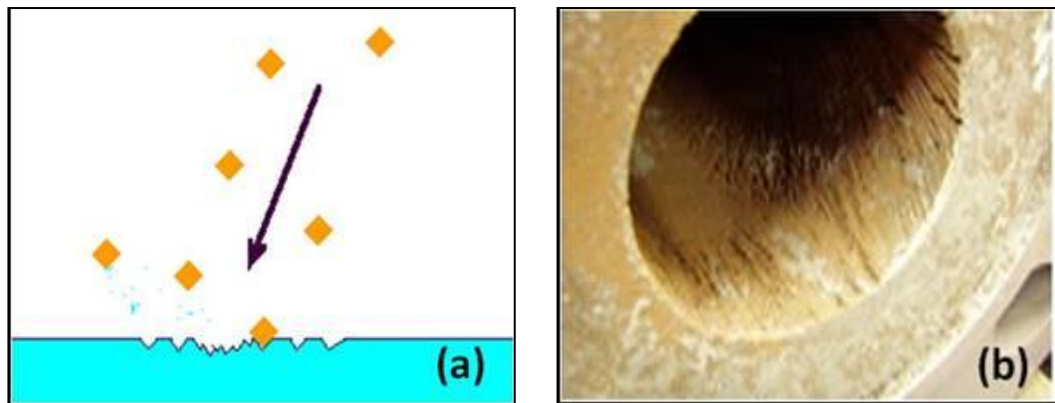


Figure 2.5, (a) Erosive wear mechanism , (b) Erosive wear associated with the movement of slurries through piping. [33]

The impacting particles gradually remove material from the surface through repeated deformations and cutting actions [49]. It is a widely encountered mechanism in the oil industry. A common example is the erosive wear associated with the movement of slurries through piping and pumping equipment (Figure 2.5 (b)).

The rate of erosive wear is dependent upon a number of factors. The material characteristics of the particles, such as their shape, hardness, impact velocity, and impingement angle are primary factors along with the properties of the surface being eroded. The impingement angle is one of the most important factors and is widely recognized in the literature. [50]

Al-Bukhaiti et al. [51] investigated the influence of impingement angle on erosion mechanisms of 1017 steel and high-Cr white cast iron using a slurry whirling-arm test rig. This research concluded that the effect of impingement angle on slurry erosion mechanisms of 1017 steel can be divided into three regions. The three regions are related to the normal and tangential components of the impacting force. First region of small impingement angles: $\theta \leq 15^\circ$ where shallow ploughing and particle rolling were the dominant erosion mechanisms. The region of intermediate impingement angles: $15^\circ < \theta < 70^\circ$, dominated by microcutting and deep

ploughing. While in the third region, region of high impingement angles: $75^\circ \leq \theta \leq 90$, indentations and material extrusion prevailed.

For ductile materials the maximum wear rate was found when the impingement angle was approximately 30° , whilst for brittle materials the maximum wear rate occurred when the impingement angle was normal to the surface [51]. Table 2.1 shows some of ASTM test methods sorted according to the wear mechanism. [52]

Table 2.1, Wear test methods, adapted from ASTM Book of Standards [52].

<i>Form of wear</i>	<i>Designation</i>	<i>Title</i>	<i>Means of wear measurement</i>
Abrasive wear, 2-body	G 56	Test Method for Abrasiveness of Ink-Impregnated Fabric Printer Ribbon	Surface profiling or other method
	G 132	Test Method for Pin Abrasion Testing	
	G 119	Guide for Determining Synergism between Wear and Corrosion	Mass loss and corrosion-related measurements
Erosive wear, cavitation fluid	G 32	Test Method for Cavitation Erosion Using Vibratory Apparatus	Mass loss
Erosive wear, liquid droplets	G 73	Practice for Liquid Impingement Erosion Testing	Mass loss
Erosive wear, slurry	G 75	Test Method for Determination of Slurry Abrasivity (Miller Number) and Slurry Abrasion Resistance Response of Materials (SAR Number)	Mass loss
Erosive wear, solid particles	G 76	Test Method for Conducting Erosion Tests by Solid Particle Impingement Using Gas Jets	Mass loss
Fretting wear	D 4170	Test Method for Fretting Wear Protection of Lubricating Greases	Mass loss ratio
Sliding wear	D 2266	Test Method for Wear Preventative Characteristics of Lubricating Grease (Four-Ball Method)	Wear scar diameter
Surface damage, galling	G 98	Test Method for Galling Resistance of Materials	Visual inspection, critical load for galling
Surface damage, scoring	D 2782	Test Method for Extreme-Pressure Properties of Lubricating Fluids	"OK" value of maximum mass (weight) for load just below critical scoring condition

2.3 CORROSION

Corrosion is an electrochemical process in which a metal reacts with its environment to form an oxide or other compound. The cell which causes this corrosion process has three essential constituents: an anode, a cathode and an electrolyte (electrically conducting solution). The anode is the site at which the metal is corroded; the electrolyte is the corrosive medium; and the cathode (part of the same metal surface or of another metal surface in contact with it) forms the other electrode in the cell and is not consumed in the corrosion process. [53]

The effects of corrosion can be accelerated or induced when operating in conjunction with stress and various other wear mechanisms. Usually the mechanisms works by disallowing the corroded metal from becoming passive by continually removing protective films and setting up active/passive corrosion cells where the mechanism is not uniform applied. The corrosion products formed may introduce abrasive debris as a consequence. [54]

There are many types of corrosion that destroy the surface of the metal such as; corrosion fatigue, cavitation corrosion, erosion corrosion, fretting corrosion, and stress corrosion cracking. [55]

According to NACE International (The Corrosion Society) the total direct cost of corrosion in the USA was determined to be \$276 billion per year, which is 3.1 percent of the U.S. gross domestic product (GDP). The report recommended metallic coating of the component as a protection tool that can protect the surface of the metal, to extend its life and hence lower the cost [56].

Proper selection of the coating technique, system, and materials are essential to enhance the required properties of the component when applying the such protective layers.

H₂S Corrosion in Oil and Gas Industry

In the presence of hydrogen sulfide (H₂S), internal corrosion of carbon steel in oil and gas industry represents significant problem to plants materials. This type of corrosion is called sour corrosion which is different than sweet corrosion resulting from CO₂ corrosion. In this type of corrosion, protective film (oxides, ferrous sulfides) formation is one of the important factors governing the corrosion rate [57].

The overall reaction between H₂S and carbon steel results in the formation of iron sulfide film and can be represented by the following reaction [58]:



The acidity (pH) of the stream solution determines the mechanism of H₂S corrosion. At lower values of pH (< 2), iron sulfide phases become very soluble which results in the dissolution of iron sulfides. Hence, sulfide is not precipitated on the surface of the metal. The acceleration effect of H₂S accelerates the dissolution reaction. At pH values of 2 < pH < 5, an inhibitive effects of H₂S results in the formation of ferrous sulfide (FeS) protective film on the metal surface [59]. As the concentration of H₂S increases, the protective film is rather loose even at 2 < pH < 5 and does not prevent the corrosion of the process piping and vessels [60].

This has prompted the industry to conduct numerous inspections of all vessels and piping to prevent operation during wet H₂S service. Wet H₂S corrosion may result in hydrogen blistering, sulfide stress cracking (SSC), hydrogen induced cracking (HIC), and stress oriented hydrogen induced cracking (SOHIC). Excessive corrosion products can plug boiler tubes and damage the rotating equipment in the plant [61]. It may also work as an erodent to cause an erosion-corrosion effect on the metals.

In the oil wells, H₂S dissolves in water and then causes severe corrosion to metals and drilling tools. H₂S dissolution creates a corrosion cell (the metal– electrolyte – hydrogen sulfide). Depending on the pH of the electrolyte, elemental sulfur can be present in the system [59]. Elemental sulfur may transfer to downstream facilities which can corrode every component in the presence of water susceptible to corrosion if it is not removed quickly from the system.

2.4 THERMAL SPRAY TECHNOLOGY

The thermal spray technology has developed rapidly over the past twenty years. New materials and new surfacing contact have led to the development of engineering coatings that provide protection from wear, corrosion, and elevated temperatures. [62]

2.4.1 High Velocity Oxygen Fuel

The HVOF (High Velocity Oxygen Fuel) thermal spraying technique has been widely adapted in many industries due to its high flexibility and cost effectiveness [63]. The HVOF Process has been developed to produce extremely high spray velocity. There are a number of HVOF guns/techniques which use different methods to achieve high velocity spraying. One method is basically a high pressure water cooled HVOF combustion chamber and long nozzle. Fuel (kerosene, acetylene, propylene or hydrogen) and oxygen are fed into the chamber, combustion produces a hot high pressurized flame which is forced down a nozzle and increases its velocity (approximately 1350 m/s). Powder may be fed axially into the HVOF combustion chamber under high pressure or fed through a nozzle where the pressure is lower. Another method uses a simpler system of a high pressure combustion nozzle and an air cap. Fuel gas (propane, propylene or hydrogen) and oxygen are supplied at high pressure. Thus combustion occurs outside the nozzle but within an air cap supplied with compressed air. The

compressed air pinches and accelerates the flame and acts as a coolant for the HVOF gun. Powder is fed at high pressure axially through the centre of the nozzle [64], (Figure 2.6).

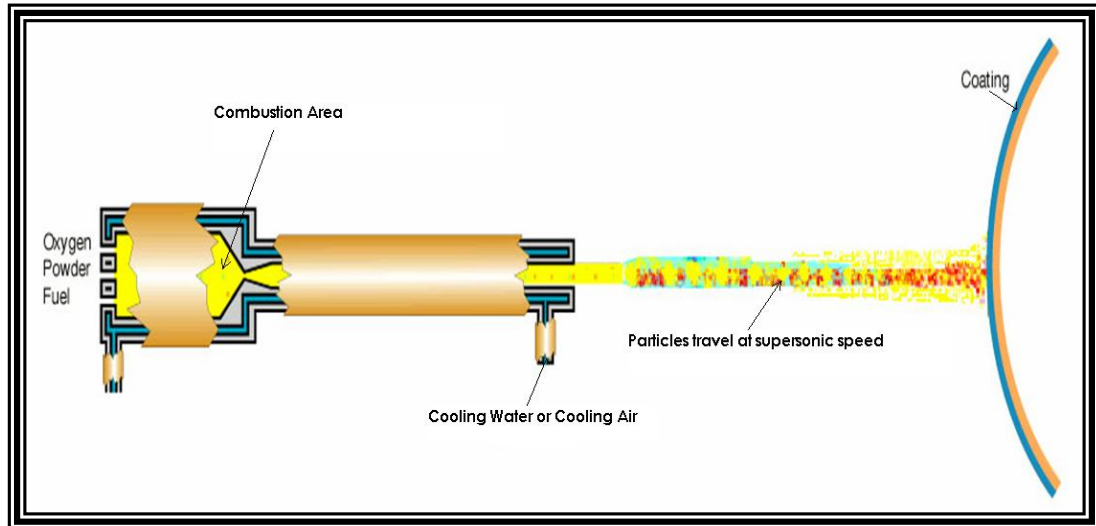


Figure 2.6, Schematic diagram of the HVOF spray system [65].

The coatings produced by HVOF are very dense, strong and show low residual tensile stress which enable very much thicker coatings to be applied than that previously possible with the other processes [66].

The very high kinetic energy of particles striking the substrate surface do not require the particles to be fully molten to form high quality HVOF coatings. This is certainly an advantage for the carbide cermet type coatings and is where this process really excels. HVOF coatings are used in applications requiring the highest density and strength, which are not found in most other thermal spray processes. New applications previously were not suitable for thermal spray coatings are now becoming available; such as landing gears and HVOF coatings have become the accepted and proven alternative to electroplated hard chrome coatings [67].

2.4.2 Plasma Spray Process:

The Plasma Spray Process has also been adapted in industry. It is basically the spraying of molten or heat softened material onto a surface to provide a coating. Material in the form of powder is injected into a very high temperature plasma flame/plume, where it is rapidly heated and accelerated to a relatively high velocity (approximately 600 m/s). The hot material impacts on the substrate surface and rapidly cools forming a coating. This plasma spray process when carried out correctly is called a "cold process" (relative to the substrate material being coated) as the substrate temperature can be kept low during processing that avoiding damage, metallurgical changes and distortion to the substrate material [68].

The plasma spray gun comprises a copper anode and tungsten cathode, both of which are chilled with cooled water. Plasma gas (argon, nitrogen, hydrogen, or helium) flows around the cathode and through the anode which is shaped as a constricting nozzle. The plasma is initiated by a high voltage discharge which causes localized ionization and a conductive path for a DC arc to form between the cathode and anode. The resistance heating from the arc causes the gas to reach extreme temperatures, dissociating and ionizing to form a plasma. The plasma exits the anode nozzle as a free or neutral plasma flame (plasma which does not carry electric current) which is quite different to the Plasma Transferred Arc coating process where the arc extends to the surface to be coated. When the plasma is stabilized ready for spraying, the electric arc extends down the nozzle, instead of shorting out to the nearest edge of the anode nozzle. This stretching of the arc is due to a thermal pinch effect. Cold gas around the surface of the water cooled anode nozzle being electrically non-conductive constricts the plasma arc, raising its temperature and velocity. Powder is fed into the plasma flame most commonly via an external powder port mounted near the anode nozzle exit. The powder is so rapidly heated and accelerated that spray distances can be in the order of 25 to 150 mm, (Figure 2.7).

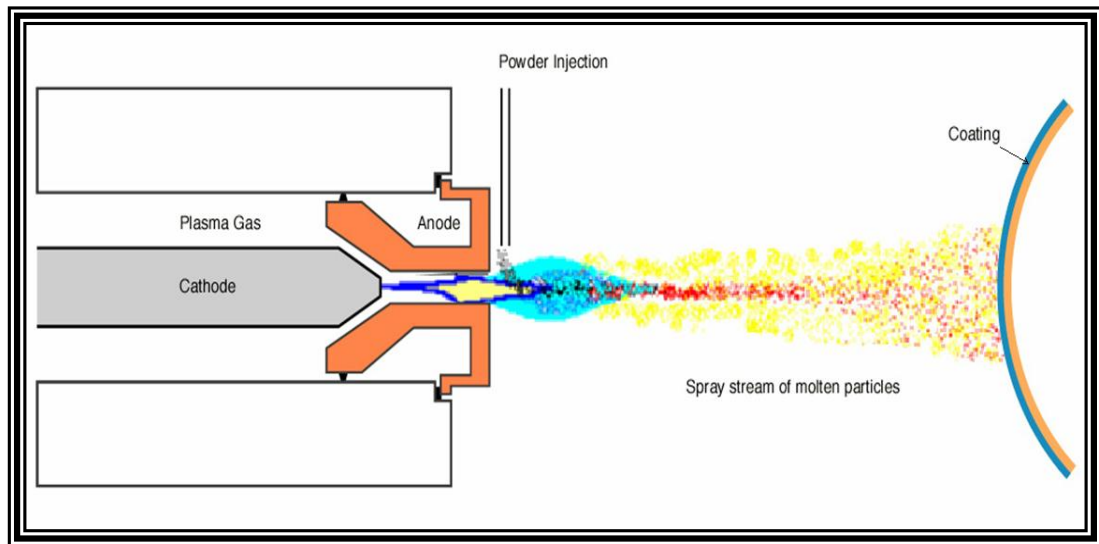


Figure 2.7, Schematic diagram of the plasma spray system, [65].

The plasma spray process is most commonly used in normal atmospheric conditions and referred to as APS. Some plasma spraying is conducted in protective environments using vacuum chambers normally back filled with a protective gas at low pressure and referred to as VPS or LPPS. [69]

Plasma spraying has the advantage that it can spray very high melting point materials such as tungsten unlike HVOF combustion process. Plasma sprayed coatings are generally much denser, stronger and cleaner than the other thermal spray processes with the exception of HVOF and detonation processes. Plasma spray coatings probably account for the widest range of thermal spray coatings and applications [70]. Disadvantages of the plasma spray process are relative high cost and complexity of process [71].

2.5 THERMAL SPRAY COATINGS FOR WEAR PROTECTION

Thermal spray coatings are used for producing wear resisting surfaces and also for the repair of worn surfaces. Thermal spray coatings can improve the surface properties and the component substrate material and can be chosen from the bulk

requirements without the need to consider its wear resistance or other surface properties if you have the proper coating materials that enhance these properties.

The selection of the best coating for an application is not often straightforward. Selection based on hardness or from standard wear testing would indicate coatings like HVOF tungsten carbide/cobalt, or plasma sprayed chromium oxide ceramic coatings as giving the ultimate performance. Indeed, these coatings do provide the best solution to many applications, but they are certainly not universally suited to all applications. Other factors which must be considered are; cost, life expectancy, temperature, porosity, loads, lubrication, and corrosion [72].

An example of these factors is coating of a soft bearing material which allow the embedding of abrasive particles and permit deformation to accommodate some misalignment of the bearing surfaces. These surfaces require adequate lubrication and should be low in cost as they wear in preference to the mating surface. Some of these coatings are quite porous with the advantage that they act as reservoirs for lubricants. The coatings that are commonly used in this applications are: Aluminium bronze [73] and Phosphor bronze [74].

On the other hand, hard bearing materials which have high wear resistance, lubrication may be marginal because the embedding of abrasive particles and self-alignment are not required. Thermal spray coatings provide additional benefits over comparable wrought or cast materials due to porosity acting as a lubricating reservoir. Some coatings show relatively low macrohardness compared to their relative wrought or cast materials, but very often show improved wear resistance. Coatings commonly used in these applications are cermet coatings like tungsten carbide/cobalt and chromium carbide/nickel chromium, oxide ceramics like chromium oxide and alumina, molybdenum, and various hard alloys of iron, nickel, chromium or cobalt [75].

Cermet coatings like tungsten carbide/cobalt are also used to protect metals/alloys from the abrasive wear because the cermet coatings have the hardness that are in

excess of that of the abrasive particles [76]. Cermet coatings are also used as coating resistant to wear caused by the repeated sliding, rolling, impacting or vibration. These types of coatings have good toughness and low residual tensile properties [77].

The selection of a coating for erosive wear is dependent on the severity and type of erosion. For solid impingement erosion at a shallow angle of attack where the wear is similar to that of abrasion, it is desirable to have high hardness coatings. For solid impingement angles near 90° coating toughness becomes more important. For cavitation and liquid impingement generally, a coating with good surface fatigue resistance is needed. The following coatings are commonly used [78]: Cermet coatings like tungsten carbide/cobalt, chromium carbide/nickel chromium, non ferrous alloys, aluminium bronze, monel, in addition to various alloys of iron, nickel, chromium or cobalt.

It has been claimed that thermal sprayed WC–Co coatings are inferior in wear resistance due to a decomposition of WC and a reaction with the binder cobalt metal resulting in carbides phases like W_2C , and Co_3W_3C . These carbides reduce wear resistance due to their brittle nature. Wettability of hard carbides by the binder matrix influences the structure and mechanical properties of WC–Co coatings [79].

2.6 THERMAL SPRAY COATINGS FOR CORROSION PROTECTION

Thermal spray coatings are widely used in the prevention of corrosion of many materials, with very often, additional benefits of properties such as wear resistance, due to the very wide selection of coatings that can be sprayed. Broadly, thermal spray coatings fall into three main groups: Anodic, Cathodic, and Neutral Coatings.

Anodic coatings for the protection of iron and steel substrates are almost entirely limited to zinc and aluminium coatings or their alloys. Where anodic type coatings are applied to a substrate, the corrosion protection is referred to as cathodic protection or sacrificial protection [80].

An ordinary sprayed coating of zinc or aluminium, although somewhat porous, can to a large extent exclude the environment and provide cathodic protection. Where desired the porosity can be sealed with organic sealers, or the coating painted, which can in some cases prolong the life of the protective system by increasing the barrier effect [81].

Cathodic coatings are those which comprise of a coating metal which is cathodic with respect to the substrate. A stainless steel or nickel alloy coating is cathodic to a steel base substrate [82]. Cathodic coatings can provide excellent corrosion protection. There can be a wide choice to choose from particularly for steel base materials ranging from stainless steel to more exotic materials like tantalum to cater for the more extreme corrosive environments. However, one limitation of such coatings is that they must provide a complete barrier between the substrate and the environment [83]. If the substrate is exposed to a corrosive environment, the substrate will become the anode and corrosion will be dramatically accelerated resulting in spalling of the coating. Generally, sealing of these coatings is always recommended. Processes which provide the densest coatings are preferred (HVOF, plasma and fused coatings). Additionally, thick coatings will provide better protection than thin coatings [84].

Neutral materials such as alumina or chromium oxide ceramics provide excellent corrosion resistance across corrosive environments by the exclusion of the environment from the substrate [84, 85]. Generally a neutral material will not accelerate the corrosion of the substrate even if the coating is somewhat permeable. However any corrosion at the substrate-coating interface should be avoided to prevent coating separation. An exception to this is with stainless steel type materials where the exclusion of oxygen can cause crevice corrosion. Nickel

chromium bond coats are required to prevent this [86]. Hence, sealing of the coatings is recommended, and the densest and thickest plasma sprayed coatings are also recommended [83, 88], to isolate the base metal and prevent the forming of the corrosion cell.

Cermet coatings (tungsten carbide/cobalt “WC–Co”) were investigated by Godoy et al. [87]. Five coating systems were thermally sprayed by HVOF and deposited onto an AISI 1020 steel substrate. These coating combinations were: a WC–Co, a duplex WC–Co/NiCrAl, NiCrAl, and as sprayed and post-melted 50% (WC–Co) + 50% (NiCr). The coated substrates were then evaluated by immersion tests in 1N HCl and potentiodynamic tests in 1N H₂SO₄. The results obtained from both tests indicated that the duplex WC–Co/NiCrAl coating was the best system in protecting the AISI 1020 steel substrate from chloride acid corrosion. The corrosion response of this coating was even superior to that of a non-duplex corrosion-resistant NiCrAl system.

2.7 COATING MATERIALS

WC thermal spray coating is used for wear/corrosion resistant applications due to its low friction coefficient and exceptional hardness. The addition of a Co binder phase in WC matrix can present high hardness together with sufficient ductility [89].

It is common practice to deposit WC–Co surface coatings by thermal spraying; typically air plasma spraying (APS) and high velocity oxy-fuel (HVOF) spraying. HVOF spraying has emerged as a superior process to APS in achieving coatings which are well bonded to the substrate with minimal porosity and a reduced quantity of undesirable reaction products [90, 92]. This is attributed to the higher particle impact velocities and lower peak particle temperatures in HVOF compared to APS. However, within the HVOF process, there are wide varieties of conditions

available depending on the design of the gun and the fuel type employed. Systems which employ a gaseous fuel such as hydrogen often yield comparatively higher particle temperatures and lower velocities than systems which employ a liquid fuel such as kerosene [90].

It has been well established that thermally sprayed WC–Co coatings exhibit complex, multi-phase microstructures, with a significantly lower volume fraction of primary carbide than that of their starting powders [93].

The degree of decomposition of the powders during spraying, resulting from these complex microstructures, depends primarily upon two factors, the time–temperature history of the particle and the particle characteristics such as size, porosity and WC grain size within the particle. Decomposition occurs due to high temperatures and low velocities (leading to a long residence time in the flame) and the use of small carbide grain sizes within the powder particles, all of which promote carbide dissolution in the molten matrix and subsequent decarburization [94]. However, whilst decomposition has been reported to be deleterious to wear behaviour, low temperature spraying has, in some cases, shown to result in coatings with poorer adhesion between the splats, again resulting in high rates of wear [96]. Steel allows the weldability of cemented carbides so it is recommended to join cemented carbide towards steel. Therefore, studies have been made to reveal the thermal stability and the reaction products of tungsten carbide and steel [95].

2.7.1 Nanostructured Materials

A great interest has been taken in nanostructured materials because of their excellent properties, which differ from conventional bulk materials [95]. Some fundamental aspects pertinent to their physical and chemical properties have also been studied and various processes have been developed for the preparation of nanostructured materials [96, 97].

Coating as a surface modification technique is an effective and economical method to improve the wear-resistant properties of materials. Thus, thermal spraying as a conventional surface modification technology to deposit coatings is preferentially utilized to prepare nanostructured coatings. It has been reported that thermal spraying is a convenient method to prepare a nanostructured coating. [98, 99]

Nanostructured WC–Co is one of the wear-resistant materials with wide applications in machinery industries, due to the advantageous combination of hardness and toughness, and its wear properties have been extensively investigated [100, 101]. However, it is difficult to spray nano-sized powders since they are too light [102].

The tribological properties of sintered nanostructured WC–Co cermet were investigated in comparison with the sintered conventional WC–Co cermet by Jia et al. [103, 104]. It was reported that the nanostructured cermets showed higher wear resistance than the conventional one. Thus, it is supposed that nanostructured WC–Co coatings should also have a better wear resistance than conventional coatings. However, it was found that a thermally sprayed nanostructured WC–Co coating had a wear resistance inferior to that of a conventional WC–Co coating, despite their higher hardness [105]. WC-Co powder size plays an important role in decarburization rate. It is difficult to deposit a dense nanostructured WC–Co with a limited decarburization by thermal spraying due to severe decarburization of nano-sized powder [106]. Generally, nanostructured WC–Co coatings demonstrated good adhesion, adhesive strengths exceeded 60 MPa [107].

Table 2.2 discusses and compares some of the mechanical properties of WC-Co nanostructured coating (n WC-Co) and WC-Co microstructured coating (m WC-Co) drawn from the literature [8, 108-110].

Table 2.2, Mechanical properties comparison (n WC-Co versus m WC-Co) adapted from references [8, 108-110].

Property	Comparison (n WC-Co vs. m WC-Co)	Remarks
Hardness	Hardness of sintered WC-Co decreases with increasing cobalt content and carbide size. The hardness of n WC-Co depends more on the degree of WC decomposition. At high temperatures, WC decompose to less hard W_2C , W and graphite.	Hardness of coating is strongly dependent on powder size and spray parameters (SP) because of their strong influence on in-flight parameters.
Porosity	Porosity of n WC-Co coating is larger than that of m WC-Co because of larger evolution of carbon oxide gasses through n WC-Co coating.	Coating is porous since the decomposed graphite, which is resulted from the WC decomposition reaction, forms carbon oxide gasses by reaction with excess oxygen, and the gas evolution from coating makes porous coating.
Friction coefficient (FC)	FC of n WC-Co is lower than that of m WC-Co at low and high temperatures because of the more decomposition of n WC-Co.	Friction coefficient (FC) is strongly dependent on the coating process (CP) since hardness and porosity of coating are dependent on the CP. FC increases with increasing coating temperature (at low and high T) both at m and n WC-Co because of the increase of adhesion by increasing surface T.
Sticking friction		Sticking friction on WC-Co coating surface occurs easily at higher temperature due to the higher FC at the higher temperature. Low temperature operation of WC-Co coated system is recommended for protection from sticking friction.
Reduction of carbide size to the nanometer	Sintered nanostructured WC-Co materials exhibit enhanced performance in both sliding and abrasive wear and substantially higher hardness than their conventional counterparts.	The nanostructured WC-Co coatings showed higher hardness but lower wear resistance than conventional coatings. This lack of performance of HVOF sprayed nanostructured coatings has been attributed to their higher tendency of decarburization, as the surface-to-volume ratio of the nano-sized WC is higher than that of their conventional counterparts. It has been suggested that optimization of spray parameter is necessary to improve properties. There has been no specific answer.
Abrasive wear resistance	The effect of Co content of nanostructured coatings on wear properties, was that the abrasive wear resistance increased with decreasing Co content while the hardness was almost the same. The fracture toughness slightly increased with increasing Co content.	

2.7.2 Bond Coat

A bond coat is a coating applied as an intermediary between the main or top coating and the substrate in order to improve the bond strength and/or to provide a corrosion or an oxidation barrier [111].

The bonding mechanisms at the thermal spray coating/substrate interface and between the particles making up the thermal spray coating is an area which in many cases is still subject to speculation. It is generally adequate to state that both mechanical interlocking and diffusion bonding occur. Thermal spray coating bonding mechanisms include: interlocking, diffusion bonding or by other adhesive bonding mechanisms [111-114]. Cleanliness, surface area, surface profile, temperature, time, and velocity are factors effecting bonding and the subsequent build up of a coating.

Cleaning and grit blasting are important for substrate preparation. This provides a more chemically and physically active surface needed for good bonding. Increased surface area increases the coating bond strength. A rough surface profile promotes mechanical keying. Some metals have very high melting points thus the interaction between substrate and coating particles increases due to the higher temperatures involved and longer cooling cycles. Higher preheat temperatures for the substrate increases diffusion bonding activities, however this can increase the oxidation of the substrate which can defeat the objective of achieving higher bond strengths. [113, 115]

2.7.3 Multi-Layer Coatings

Multi-layer coatings are used as protective coatings for metal alloy components, such as the working components of drilling tools or gas turbine engines that are exposed to high temperature gas environments and severe operating conditions. By necessity, the surfaces of the metal substrates used to form these components must exhibit greater than average mechanical strength, durability, oxidation resistance,

and erosion resistance in aggressive, high temperature environments. These types of coatings can be applied to a metal substrate using high velocity oxy-fuel (HVOF) and plasma thermal spraying systems [116,117].

Multi-layer coatings usually consist of a dense layer (inner layer) that provides oxidation protection to the metal substrate. This layer can be iron, nickel or cobalt-based alloys. The outer layer controls porosity will tend to promote roughness, mechanical compliance, and promotes adherence of the thermal coating. Preferably, the outer, less dense layer, is formed from a mixture of metallic powder and bond coat to adjust and control the porosity but without sacrificing mechanical compliance. Together, the layers enhance adherence to the substrate and improve the overall life of the coating system [118-120]. Lee et al. [121] had concluded that coatings produced by spraying mixed powders have mechanical properties better than those of the coating layers sprayed with the single powders. This was due to the increase in the hardness caused by the decrease in porosity attributed to the densification of the coating layers sprayed using small molten particles. The mechanical properties of sprayed coating layers therefore depend on the mixing ratio of the different sized powders as well as the size of the powder.

The objectives of an effective bond coat on metal substrates, are that the coating must form a dense, protective and adherent layer will protects the underlying base material against oxidation, corrosion, and degradation. Secondly, the coating should serve to promote adherence of the other layers. For thermal spray coatings, a high degree of surface roughness is required to provide mechanical interlocking. Bond layers are typically made of alloys such as MCrAlY, where M represents a metal such as Ni, Co, or Fe. The structure and physical properties of bond coats are dependent on the process and equipment by which they are deposited [122-126].

The prime methods used to apply multi-layer coats fall into three general categories: (1) fully dense coats produced by APS, VPS, or HVOF processes; (2) fully porous coating formed by APS processing; or (3) a bi-layers of dense coating

followed by one or more porous layers. The bi-layer coatings are often produced by two different processes (typically HVOF or VPS for the dense layer and APS for the porous layer). The bi-layer structure can also be formed by modification of particle size and/or spray parameters to create a rougher or more porous outer layer. Literature indicates that HVOF has not been used to form both the dense and porous layers [122-126].

The use of two different thermal spray processes to form the multi-layer coating creates an undesirable complication in the manufacturing process. Typically, the known HVOF/APS multi-layer coatings require an intermediate vacuum heat treatment after the HVOF layer is applied. Such coating system consisting of HVOF layers utilizing different powder sizes to provide increased roughness at the surface. However, the outer layer is close to maximum density and lacks the mechanical advantages of a more porous coating layer. It is now recognized that the use of a single HVOF system to apply both the dense and porous layers of the multi-layer coating could greatly simplify the manufacturing process and lead to cost reductions due to reduced cycle time. A reduction in cycle time could also be achieved by eliminating the intermediate vacuum heat treatment of the HVOF. It was found that the outer layer having controlled porosity can be formed by spraying a mixture of metallic powders.

Using both HVOF and APS to form a multi-layer coat having such attributes would not be considered "manufacturing friendly" due to the need to switch process methods during the course of manufacture, and the need for an intermediate heat treatment after the application of the HVOF layer. Thus, fabricating the dense layer and porous layer by a single thermal spray method and performing the heat treatment after both layers, greatly simplifies the manufacturing process, reduces cost and improves the mechanical properties of the end product [122-126].

EQUIPMENT, MATERIALS, AND PROCEDURES

3.1 INTRODUCTION

In this work, the HVOF/Plasma thermal spray facilities were used to spray the metallic powders onto carbon steel specimens. This section will describe the procedures and the equipment used as well as the substrate and coating materials.

3.2 HVOF THERMAL SPRAYING SYSTEM

A Praxair JP-8000 HVOF Thermal Spray System (using kerosene liquid as fuel) was used to produce the coatings used in this research (Figure 3.1). This system is a high-pressure, high velocity oxy-fuel (HP/HVOF) thermal spray system that builds on the proven performance of the popular JP-5000 system. The system combines advanced closed-loop control features with ease of operation for coating deposition [127].

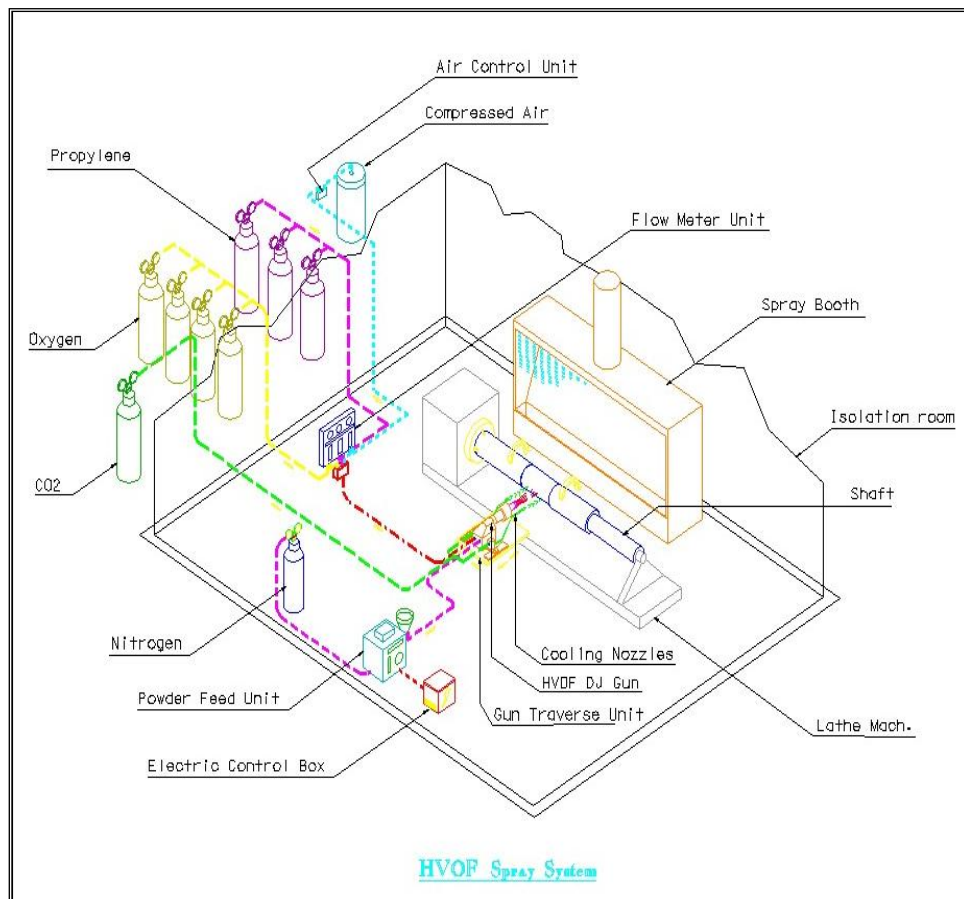


Figure 3.1, Schematic of High velocity oxygen fuel system [128].

JP-8000 system features the Model 8100 CORONA console that is designed around the concepts of real-time process monitoring. The control system operates using a mass flow, closed-loop, PLC-based control.

The JP-8000 operates using the traditional Model 5520 gun and the Model 1264 Powder Feeder, (Figure 3.2). The powder feeder has a reputation for consistent, pulse-free feeding of powders of all types, delivering unparalleled accuracy. It has an open-loop pressurized feeder specifically designed for thermal spray applications, operating on proven volumetric-feed technology. It has powder wheel speed control, and other useful functions including canister clean mode, local/remote selector, and a set-temperature heater blanket protects the powder from absorbing moisture.

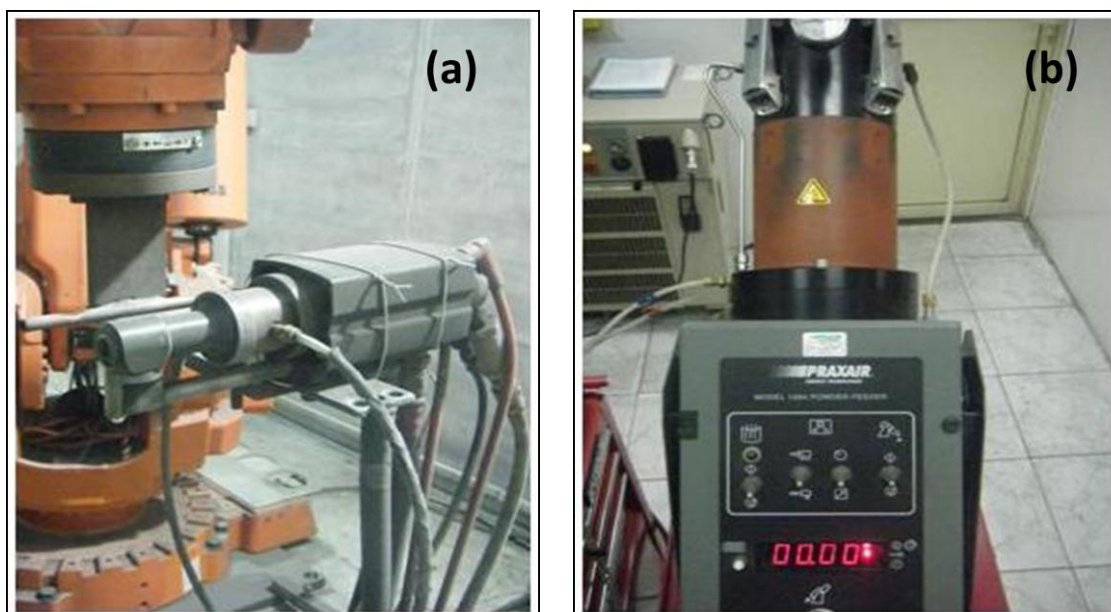


Figure 3.2, (a) Model 5520 gun used in this research and (b) Model 1264 Powder Feeder used in this research.

As claimed by the manufacturer that JP-8000 systems delivers spray rates up to four times higher than other HVOF systems [127]. This increased spray rate allows for higher productivity resulting in greater throughput. It can produce coatings over 12 mm in thickness with microhardness levels higher than other HVOF processes. Table 3.1 shows the features of the HVOF system used in this work.

Table 3.1, HVOF System Features [127].

<i>JP-8000 system features:</i>	<i>Gun features of the Model 5220:</i>	<i>1264 powder feeder features:</i>
<ul style="list-style-type: none"> » CE compliant » Constant process monitoring » Easy maintenance drawer design » Engineered for safety » Graphic User Interface » Liquid fuel » Mass flow gas metering » PLC based, closed loop controls » Recipe storage 	<ul style="list-style-type: none"> » Efficient combustion and particle heating » Efficient gun cooling » Liquid fuel (kerosene) » Multiple gun configurations » Radial, low pressure powder injection » Simple, robust design » Thick coating capability 	<ul style="list-style-type: none"> » Digital display and toggle-switch controls » Variable powder wheel speed » High-capacity powder canister » Plasma/HVOF operation selector » Heater blanket with on/off control » Multiple powder wheel options available

3.3 PLASMA THERMAL SPRAYING SYSTEM

Plasma System Model 3710 Praxair was also used to produce coatings, (Figure 3.3 (a)). This model can control two powder feeders (or one at a time) and has an auxiliary power circuit that can be used. It operates using SG-100 Plasma Spray Gun (80 kW), Figure 3.3 (b). The gun is a multi-mode plasma spray gun that is suitable for a wide range of thermal spray applications.

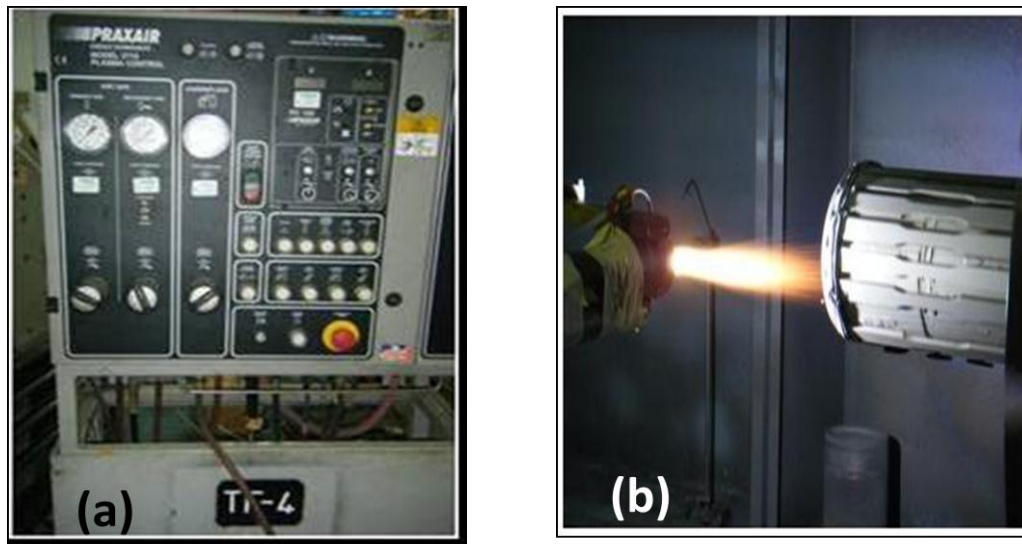


Figure 3.3, (a) Model 3710 Praxair used to produce the coating and (b) SG-100 Plasma Spray Gun.

The same Model 1264 Powder Feeder that was used for the HVOF system was also used for the plasma system. Table 3.2 shows the features of the Plasma system used in this research [127].

Table 3.2, Plasma System Features [127].

<i>3710 Praxair system features:</i>	<i>Gun features of the Model SG-100:</i>	<i>1264 powder feeder features:</i>
<ul style="list-style-type: none"> » Economical, manual control » Critical orifice gas flow control » Built-in power supply controller with digital displays » Two powder feeder capability (one at a time) » CE compliant » Compact, wall-mountable design » NFPA Type "Z" purging with audio/visual alarm 	<ul style="list-style-type: none"> ➤ 3 modes of operation for tailored coatings ➤ Internal or external powder injection (or both) ➤ Self-aligning components ➤ Long-life anodes and cathodes ➤ High spray rates ➤ CE Compliant ➤ Up to 80 kW 	<ul style="list-style-type: none"> » Digital display and toggle-switch controls » Variable powder wheel speed » High-capacity powder canister » Plasma/HVOF operation selector » Heater blanket with on/off control » Multiple powder wheel options available

3.4 WORKPIECE/SUBSTRATES

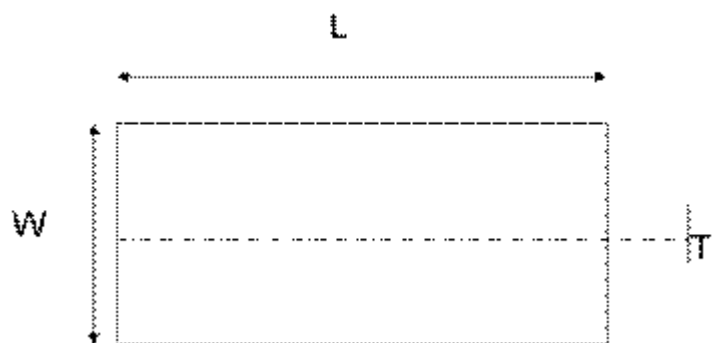
Carbon steel workpieces were selected for the coating substrate. The selection was based on those used most by Saudi Aramco oil company for oil and gas plant materials (API-5L, Schedule-40, Grade-B). Most vessels, drums, tank farms, and pipelines in oil separation plants and refineries are made of this type of carbon steel. Table 3.3 summarizes the physical and chemical properties of the selected substrates as approved by Saudi Aramco Material system.

Table 3.3, Physical and chemical properties of the selected substrates [129].

Thickness mm	Physical Properties			Chemical Properties (%)									
	Y.S (MPa)	T.S (MPa)	E.L (%)	C	Si	Mn	P	S	Cr	Ni	Cu	Al	Mo
3.8	340	395	35.5	0.07	0.01	0.37	0.011	0.008	0.018	0.012	0.018	0.042	0.002
5.8	295	405	34.0	0.05	0.03	0.36	0.010	0.010	0.022	0.014	0.021	0.043	0.002

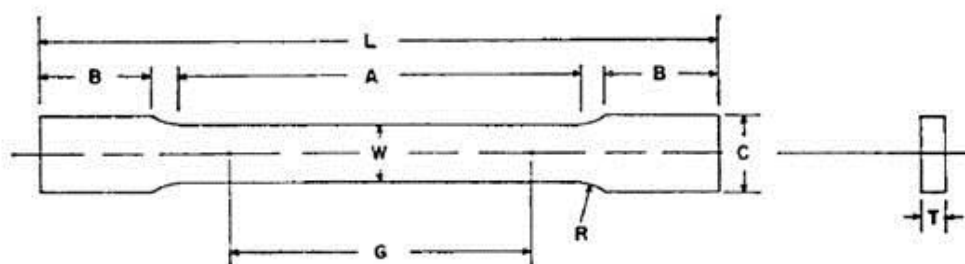
The substrates were fabricated as three different shapes (Figures 3.4-3.7) based on the laboratory testing need and as per the ASTM A 370 standard [130]. Substrates that have the shape as described in Figure 3.4 were used for the three bending test, corrosion test, and for microstructural characterizations. Substrates that have the

shape as described in Figure 3.5 were used for fatigue and tensile tests. Substrates that have the shape as described in Figure 3.6 were used for jet impingement test, surface roughness profile, and microscopic analysis.



W—Width = 25 mm
 T—Thickness = thickness of material (4mm thick)
 L—Overall length, min = 150 mm

Figure 3.4, Shape of substrates used for the three point bending test, corrosion test, and for microstructural characterizations.

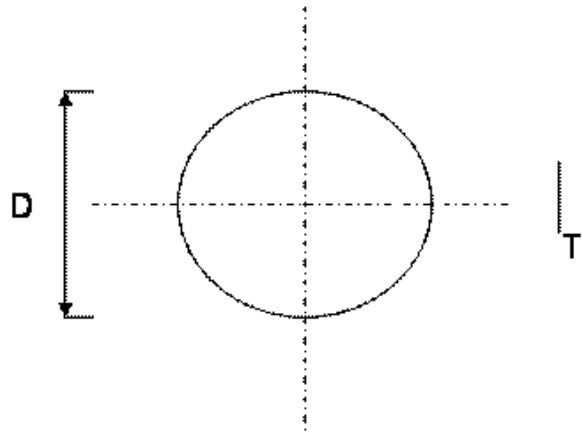


DIMENSIONS

Standard Specimens: Sheet-Type, 1/2 in. (12.5-mm) Wide

G—Gauge length = 50.0 mm ± 0.10	L—Overall length, min= 305.0 mm
W—Width = 12.5 mm ± 0.25	A—Length of reduced section, min= 60.0 mm
T—Thickness = 6 mm	B—Length of grip section, min = 102.0 mm
R—Radius of fillet, min = 13 mm	C—Width of grip section, approximate = 20.0 mm

Figure 3.5, Shape of substrates used for fatigue and tensile tests.



D— Diameter = 35 mm (coin)
T—Thickness = thickness of material (3 mm)

Figure 3.6, Shape of substrates used for jet impingement test.

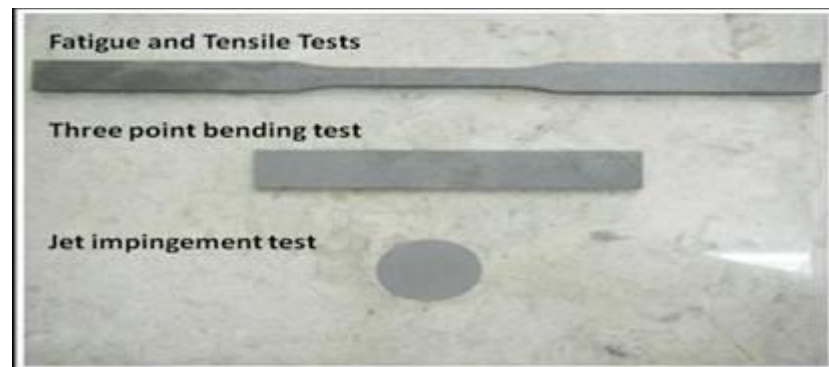


Figure 3.7, Photograph of the substrate types used in this research.

Substrate Holder

A rig was designed in order to hold flat samples during coating spray. A rotating lathe machine (Figure 3.8) was used to perform uniform coatings and allow time for the coating to solidify in order to avoid superheating the substrate. The spray distance for HVOF and Plasma were equal to 381 mm and 127 mm respectively, while the gun speeds were 10.16 mm/s and 9.11 mm/s respectively.

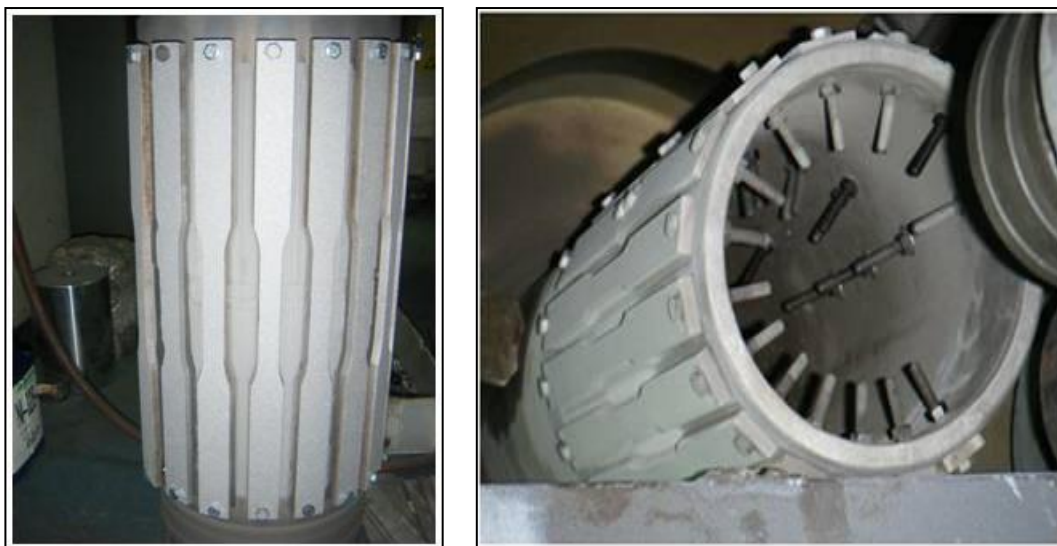


Figure 3.8, Photograph of the substrates holder used for spraying.

3.5 COATING MATERIALS

Four types of powders were used to perform the coatings used in this research. The powders were selected based on powder manufacturers claims to cover the main four areas that industry are concerned about when selecting the proper coating materials for aggressive environments, Wear resistance, Corrosion resistance, Oxidation /Sulfidation Resistance, and High Temperature Service use. Table 3.4 describes the contribution of each powder to these concerns. These powders were:

1. Tungsten Carbide-Cobalt (WC-12%Co) Microsize (Sulzer Metco 5812 deposited by both Plasma and HVOF equipment). This powder (Figure 3.9) is ideal for high abrasion, erosion and sliding wear resistance. It produces compressive coating; smooth as-sprayed surface for applications where grinding cannot be conducted. It uses include pump housings, exhaust fans and machine parts applications [131]:

Chemistry: WC-12Co

Particle Size: -53 +11 μm (-270 mesh +11 μm)

Morphology: Agglomerated and Sintered

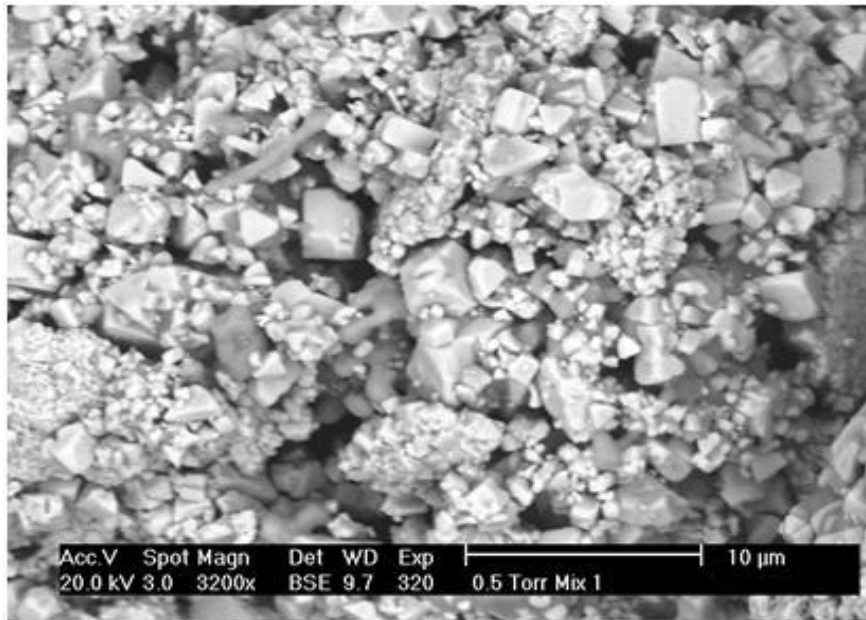


Figure 3.9, SEM micrograph of WC-12Co micron sized powder.

2. Tungsten Carbide-Cobalt (WC-12%Co) Nano size (Infralloy S7412 Powders deposited by both Plasma and HVOF equipment). This powder is a superior coating material providing wear-, erosion-, and corrosion-resistance. It is used for surfaces where excellent fracture toughness is required. Figure 3.10 shows the SEM micrograph of this powder and its physical geometry [132]:

Alloy content:	< 1 %	Particle size:	0.1 - 0.5 μm
Powder grain size (avg.):	50 - 500 nm		
Agglomerated powder size:	$5 < \Phi < 45 \mu\text{m}$		
Coating hardness (typical):	1100 VHN		

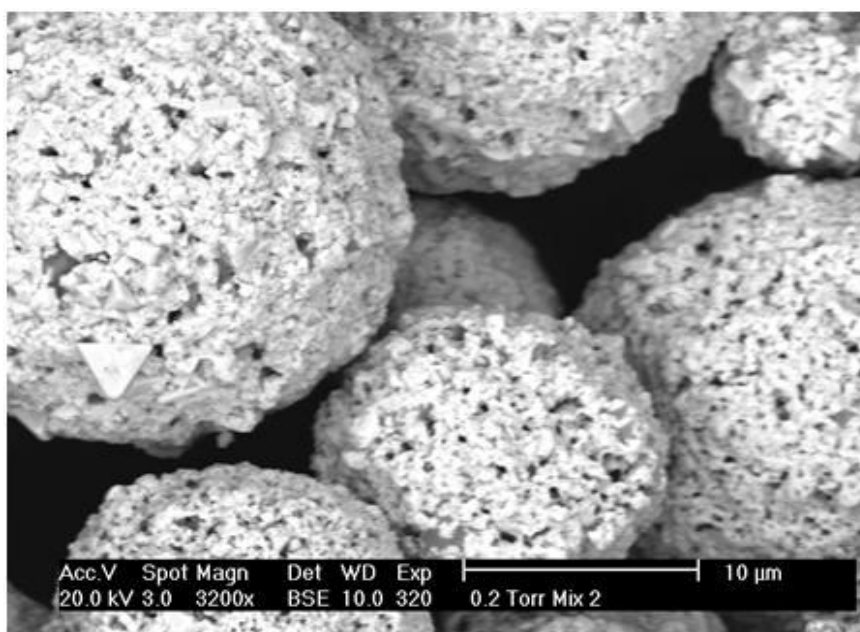


Figure 3.10, SEM micrograph of Infralloy S7412 nano sized feedstock powder showing spherical geometry.

3. AMDRY 995M (Microsize, manufactured for Plasma equipment deposition) this powder (Figure 3.11 (a)) is used in demanding aerospace applications that can be sprayed using atmosphere plasma (APS). It is used for protection in hot corrosive or oxidizing environments up to approximately 850°C (1560°F) for APS coatings. [131]

Chemistry: Co 32Ni 21Cr 8Al 0.5Y
 Particle Size: -63 +45 μm (-230 +325 mesh)
 Morphology: Spheroidal, Gas Atomized

4. AMDRY 9954 (Microsize, almost identical to AMDRY 995M but manufactured for HVOF equipment deposition). It is used for protection in hot corrosive or oxidizing environments up to approximately 1050°C (1920°F) for heat treated chambered coatings [131], (Figure 3.11 (b)).

Chemistry: Co 32Ni 21Cr 8Al 0.5Y
 Particle Size: -62 + 11 μm
 Morphology: Spheroidal, Gas Atomized

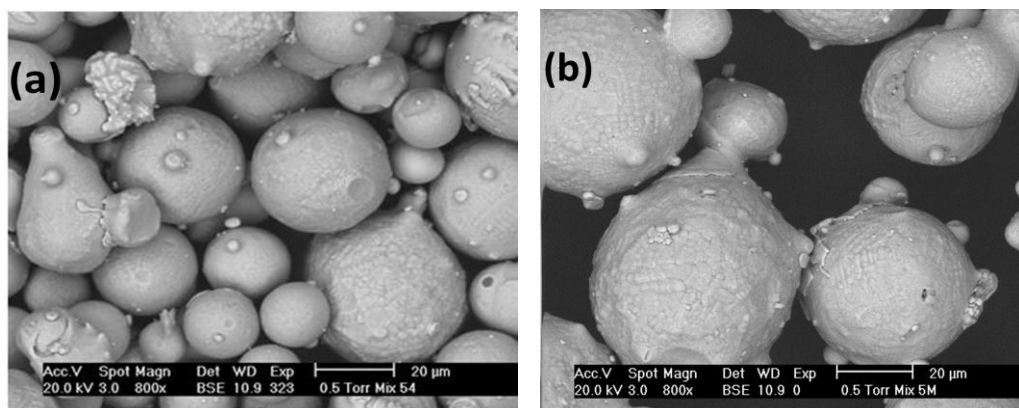


Figure 3.11, SEM micrographs of AMDRY powders (a) AMDRY 9954 and (b) AMDRY 995M.

Table 3.4, Powders contribution to the expected aggressive environment [131].

	Wear Resistance	Corrosion Resistance	Oxidation /Sulfidation Resistance	High Temperature Service
WC – 12% Co (S7412/SM5812)	●			
CoNiCrAlY (AMDRY 9954/995M)		●	●	●

3.6 COATING PROCEDURES

Two coating systems (HVOF/APS) were used to spray combinations of powders onto carbon steel substrates. There were eight combinations of powders (Table 3.5) in order to fabricate different coating layers and produced eight different groups (batches) of coatings. Every specimen was assigned a batch number.

3.6.1 Coating Matrix

The overall coating was made up having three coating layers onto the base metal using either HVOF or Plasma spray at various coating combinations. Bottom layer is hard and the top layer has enhanced corrosion resistance as a result of mixing the WC-Co powder with AMDRY powders. Each layer thickness was approximately 160 microns as described in Figure 3.12 (for batch# 4 as an example). The powders mixing ratio was made up to characterize the graded multilayered coatings as the following:

Bond layer: 100% WC-Co, to protect the base metal from erodent during operation. Mainly, it is erosion/corrosion protection layer.

Intermediate layer: Give the gradual property of the coating; enhance the uniform adhesion, more protection.

Top layer (MIX): Mainly for corrosion/erosion protection, corrosive environment interface. This layer is investigated more in this research because it determines coating degradation step (failure initiation) due to tribocorrosion.

Table 3.5, Coating Systems Matrix .

Batch No.	Substrate	Coating System	1 st Layer (Bond Layer)		2 nd Layer (Intermediate Layer)		3 rd Layer (Top Layer)	
			Coating Medium (Base)	Thickness (micron)	Coating Medium (Gradual)	Thickness (micron)	Coating Medium (MIX-interface)	Thickness (micron)
1	CS*	HVOF	WC-12Co (Micro Size)	160	WC-12Co (Micro Size)	160	MIX-1= (Micro WC-12Co)	160
2	CS	HVOF	WC-12Co (Nano Size)	160	WC-12Co (Nano Size)	160	MIX-2= (Nano WC-12Co)	160
3	CS	HVOF	WC-12Co (Micro Size)	160	80% WC-12Co (Micro Size) 20% Micro AMDRY 9954	160	MIX-3**= (60% Micro WC-12Co + 40% Micro AMDRY 9954)	160
4	CS	HVOF	WC-12Co (Nano Size)	160	80% WC-12Co (Nano Size) 20% Micro AMDRY 9954	160	MIX-4**= (60% Nano WC-12Co + 40% Micro AMDRY 9954)	160
11	CS	Plasma Spray	WC-12Co (Micro Size)	160	WC-12Co (Micro Size)	160	MIX-1= (Micro WC-12Co)	160
12	CS	Plasma Spray	WC-12Co (Nano Size)	160	WC-12Co (Nano Size)	160	MIX-2= (Nano WC-12Co)	160
13	CS	Plasma Spray	WC-12Co (Micro Size)	160	80% WC-12Co (Micro Size) 20% Micro AMDRY 995M	160	MIX-13**= (60% Micro WC-12Co + 40% Micro AMDRY 995M)	160
14	CS	Plasma Spray	WC-12Co (Nano Size)	160	80% WC-12Co (Nano Size) 20% Micro AMDRY 995M	160	MIX-14**= (60% Nano WC-12Co + 40% Micro AMDRY 995M)	160

(*) CS = Carbon steel

(**) MIX-3 & MIX-13 are almost identical, same for MIX-4 & MIX-14, except AMDRY 995M used instead of AMDRY 9954.

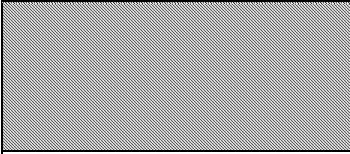
Batch No. 4		Coating System: HVOF	
		}	Substrate- CS
Pass # 1	}	}	Bond Layer (160 micron) 100% Tungsten Carbide-Cobalt (WC-12%Co)
Pass # 2			
Pass # 3			
Pass #			
Pass # 1	}	}	Intermediate Layer (160 micron) 80% Tungsten Carbide-Cobalt (WC-12%Co) 20% AMDRY 9954
Pass # 2			
Pass # 3			
Pass #			
Pass # 1	}	}	Top Layer (160 micron) 60% Tungsten Carbide-Cobalt (WC-12%Co) 40% AMDRY 9954
Pass # 2			
Pass # 3			
Pass #			

Figure 3.12, Application of the multi-layer coating for Batch 4.

The coating work preparation was considered as follows:

1. Powders Mixing: Powders were mixed based on weight percentage as per the coating matrix shown in Table 3.5 (Figure 3.13).



Figure 3.13, Powders mixed by weight percentage.

2. The substrates were loaded onto the sample holder (Figure 3.14) and cleaned using a cleaning solution to remove any traces of oil or contamination (degreased).

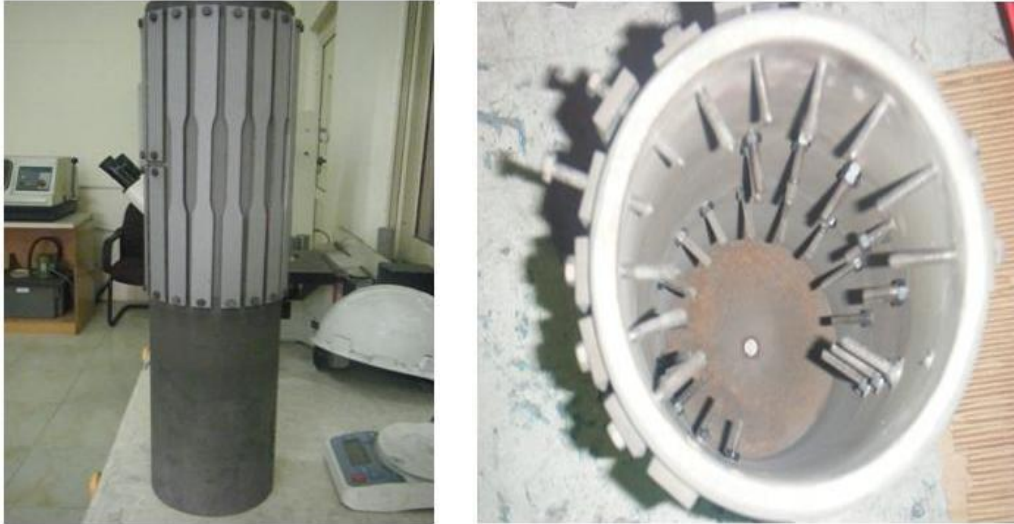


Figure 3.14, Substrates loaded onto sample holder.

3. Pre-deposition, all substrates were grit blasted using Aluminium Oxide, 36 grit (zero contamination) Figure 3.15 and 3.16. The Aluminium Oxide chemical analysis was as follows: Al_2O_3 : 99.00% Min., TiO_2 : 0.05% Max., Fe_2O_3 : 0.05% Max., SiO_2 : 0.05% Max., Na_2O : 0.50% Max [130].

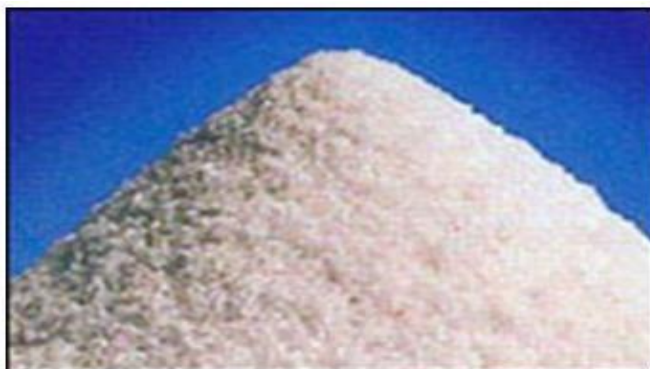


Figure 3.15, Aluminium Oxide used for grit blasting [133].

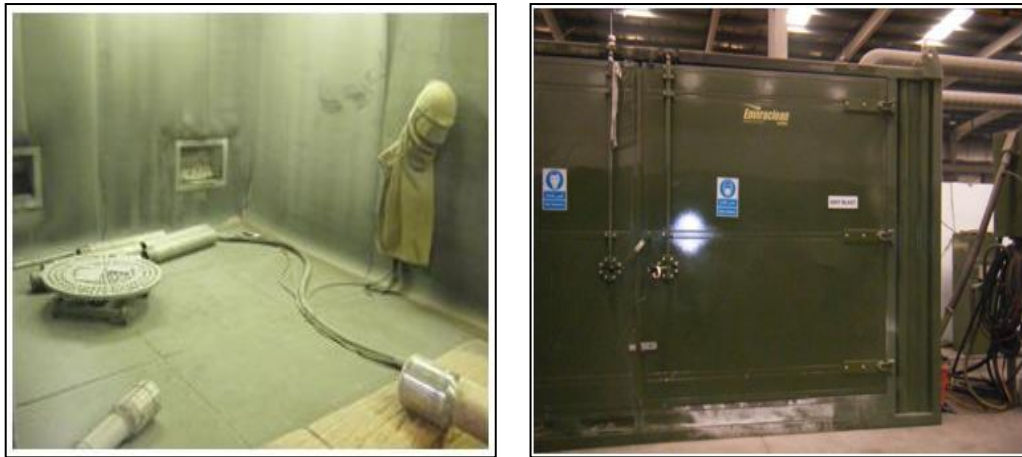


Figure 3.16, Grit blasting cabinet.

Immediately, after grit blasting, specimens were covered with paper and moved quickly to the coating system cabinet to reduce the possibility of oxidation. Preheating was performed before conducting deposition to reduce oxidation, at approximately 75°- 85° C.

4. Finally the samples were loaded onto a lathe machine (Figure 3.17), for deposition.

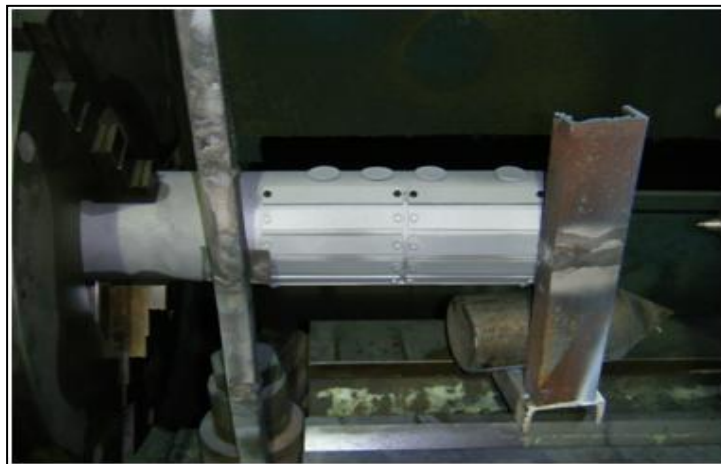


Figure 3.17, Loading sample holder to the lathe machine.

The coating spray angle was perpendicular to that of the substrate, Figure 3.18. The spray distance for both HVOF and plasma processes was 381 mm and 127 mm respectively. The powders flow rates were varied to assure proper powder melting in the hot zone. This variation was due to the fact that this research included different powder particles sizes and used two different coating systems.

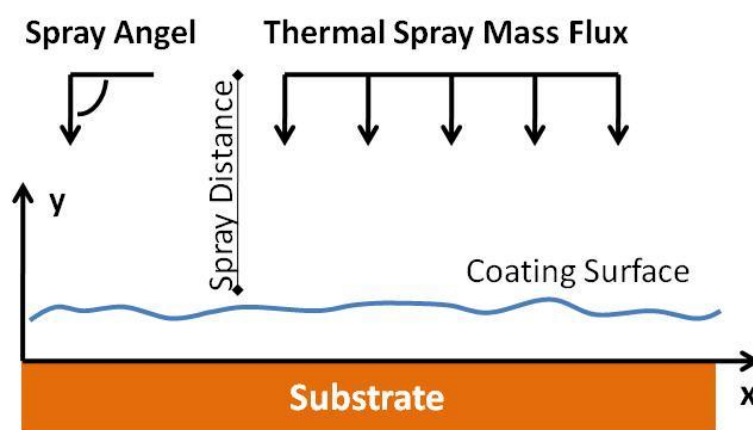


Figure 3.18, Thermal spray mass flux distribution.

3.6.2 Coating Systems Parameters:

The parameters of both HVOF and Plasma spray equipment were set first based on the powders manufacturers recommended coating parameters and then fine tuned. From these trials the efficiency of the sprayed equipment was calculated. When the maximum efficiency was achieved, the final spray parameters for both HVOF and Plasma spray equipment were chosen (Table 3.6).

The powder flow rates were calculated by measuring the flow of powders for one minute and manipulating the feeder speed RPM. The spray temperature was maintained below the specified target by passes of cool air to maintain the substrate temperature below 65°C to avoid superheating. The current was varied by

changing the system voltage. Coating process parameters are listed in the Appendix section of this thesis.

Table 3.6, Process parameters of HVOF and Plasma thermal spray.

HVOF Spray Parameters		Plasma System Spray Parameters	
Spray Distance (mm)	381	Spray Distance (mm)	127
Radial Speed (RPM)	90	Radial Speed (RPM)	76
Oxygen Flow (L/S)	15.34	Powder Feed Rate (g/min)	32 +/- 2
Fuel Rate (L/S)	0.0063	Prim. Ar (bar)	3.45
Micro Powder Feed Rate (g/min)	77	Aux. He (bar)	6.895
Nano Powder Feed Rate- (g/min)	90	Carrier Gas (bar)	3.792
Avg. Substrate Temp.	168 °C	Avg. Substrate Temp.	105 °C (micro), 95 °C (nano)
Avg. Cooling Temp.	67 °C	Avg. Cooling Temp.	65 °C (micro), 48 °C (nano)
Feeder Speed RPM (Micro)	8.8	Voltage (volt)	46 +/- 2
Feeder Speed RPM (Nano)	7.2	Current (A)	744 +/-2
Pass length (mm)	200, 305	Pass length (mm)	200, 305

3.6.3 Thermal Spraying Processes:

The coatings sprayed by the HVOF gun system, used kerosene and oxygen in its combustion chamber. The hot gas passes through a converging–diverging throat nozzle and along a final nozzle before emerging as a free jet. Powder was injected downstream of the throat. The hot gas jet and powder were propelled along the nozzle to impact the substrate at high speeds (600-1200 m/sec, Table 3.7 [128]). All coatings were deposited onto the carbon steel base metal. The substrates were

degreased and grit-blasted prior to spraying. All specimens were cooled during and after spraying with compressed air jets (Figure 3.19).

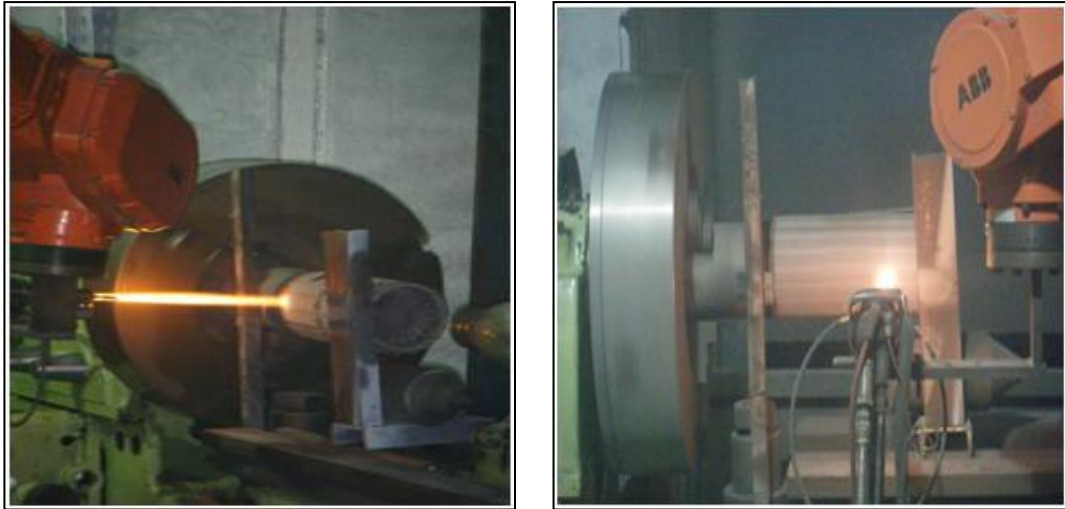


Figure 3.19, HVOF thermal spraying coating process used in this research.

The plasma spraying was carried out using a mixture of two gases: the primary gas, argon (Ar), and the secondary gas helium (He). The plasma was initiated by a high voltage discharge which caused localized ionization and a conductive path for a DC arc to form between the cathode and anode nozzle arrangement. The resistance heating from the arc caused the gas to reach extreme temperatures, dissociate, and ionize to form a plasma. When the plasma jet reaches extremely high temperatures in its core, it melts the powder. The melted powder left the system to impact the substrate at speed of 150-600 m/sec [128], Table 3.7, (Figure 3.20).



Figure 3.20, Plasma thermal spraying coating process used in this research.

The composition of the plasma forming gas influences the formation of the plasma jet and the arc behaviour inside the anode nozzle. Also, it influences accelerations and heating of the particles injected in the flow [115].

Argon ensures arc stabilization inside the nozzle and controls the transport rate of mass and the momentum of the flow. Helium increases the energy capacity of the gun. It also enhances the heat transfer to the particles, which occurs mainly by conduction through the boundary layer surrounding particles, as it has a high thermal conductivity. Test specimens produced from this work are shown in Figures 3.21 and 3.22. The characteristics of the thermal spray processes and coatings are shown in Table 3.7.

Table 3.7, Characteristics of thermal spray processes and coatings, [128].

Spray Process	Combustion Temperature (°C)	Gas Velocity (m/sec)	Bond Strength (MPa)	Porosity (%)
High Velocity Oxygen Fuel (HVOF)	2750	600-1200	>70	1-2
Plasma Spraying	15000	150-600	20-70	1-8



Figure 3.21, Test specimens produced from this research.



Figure 3.22, Test Specimens: (A) Base metal, (B) After grit blasting, and (C) After multi-layer coating applied.

The thermally sprayed specimens were used to conduct tribocorrosion tests in order to investigate coating degradation process due to the effects of chemical (corrosion) and mechanical factors on the performed multilayered coating. The mechanical factors can be performed by investigating the bending, fatigue, and tensile characteristics of HVOF/Plasma thermally sprayed coating. Also in this step, the coating characterization was investigated by the determination of

elemental chemical composition using the Energy Dispersive Spectroscopy (EDS) in conjunction to Scanning Electron Microscope (SEM), as will be detailed later.

3.7 POWDER CHARACTERIZATION

The properties of the powder such as particle shape, size distribution and surface chemistry have great impact on the performance of the coatings. It is essential to characterize the powders prior to applying thermal spray coating, hence this will help to study the behaviour of the powder particles within the spray process and during the reaction. Accordingly, the quality of the coating will be affected. In this research, the following methods of powder characterization and techniques were used:

- Energy dispersive X-ray fluorescence Spectrometry (EDXRF)
- X-ray powder diffraction (XRD)
- Particles Size Distribution (PSD)
- Environmental scanning electron microscope (ESEM)
- Energy Dispersive Spectrometry (EDS)

All bond layer sprayed powders (metal-interface) and all top layer sprayed powders (medium-interface) were characterized using the above methods.

3.7.1 EDXRF Analysis of Mixed Metallic Powders

Energy dispersive X-ray fluorescence EDXRF Spectrometry was used to determine the chemical composition of the mixed metallic powders which used top layer deposition. These powders were labelled Mix-1, Mix-2, Mix-3, Mix4, Mix-13, and Mix-14, Table 3.7. The analysis was performed using the SPECTRO X-LAB 2000 instrument which uses crystals to polarize the X-rays, Figure 3.23. This enables

high quality scanning and detection limits at the ppm level to be achieved for critical elements

Four grams of each sample were combined with 0.9 gram of Hoechstwax material and mixed thoroughly using a mixer/mill. The homogenized mixtures were prepared as a briquette and analyzed for elemental composition by EDXRF spectrometry. The semiquantitative results of the EDXRF elemental analysis are listed in Chapter 4.



Figure 3.23, SPECTRO X-LAB 2000 used to perform the EDXRF Spectrometry.

3.7.2 XRD Analysis

The X-ray powder diffraction (XRD) method was used to determine the chemical composition and crystallographic structure of the mixed metallic powders. PANalytical instrument was used to perform the XRD analysis (Figure 3.24). The metallic powders samples were grounded by an agate mortar and pestle. Then, the fine powder was mounted in an XRD sample holder. The identification of the

crystalline phases was achieved using X-Pert HighScore Plus program. The relative approximate values of the crystalline phases and the diffractograms with identified compounds are illustrated and discussed in Chapter 4.



Figure 3.24, PANalytical instrument, used to perform the XRD analysis.

3.7.3 Particles Size Distribution

The particle size distribution (PSD) of a powder is a list of values that defines the relative amounts of particles present, sorted according to size. PSD is also known as grain size distribution. The PSD can be important in understanding the physical and chemical properties of the sprayed powder. Particle size of a sprayed powder can be used to predict the flow behaviour of the particles within the spray gun and the melting in the torch. For instance, using small sized particles in a high melting temperature system such as the plasma spray process results in powder evaporation which reduces the decomposition efficiency of the coating. Conversely, using large sized particle in a moderate flame temperature system such as HVOF results in having non-melted particles in the coating. PSD results can also affect the

reactivity of the powder in chemical reactions which should be tightly controlled during the spray by selecting the proper spray parameters. Specific surface area of the powder is a property that measures the total surface area per unit of mass. It can be used to determine the type and properties of the powder. It has a particular importance in cases of reactions on surfaces. The value obtained for specific surface area depends critically upon the method of measurement.

In thermal spray process, as Volume/Surface Weighted Mean can be used as an indicator of dissolution rate. Larger surface to volume ratio of the sprayed powder may lead to more decarburization and formation of the W_2C [134].

The particle size distribution measurements were conducted using the Mastersizer 2000 particle size analyzer. This modular instrument was designed for the measurement of the particle size distribution of wet and dry samples. It has a wide range of sample dispersion units. It delivers results based on standardized procedures designed to eliminate user-to-user variability (Figure 3.25). The mass median diameter (D) was obtained for powders particles distribution. The mass median diameter considered to be the average particle diameter by mass. D 50% is the particle diameter that divides the frequency distribution in half, 50% of aerosol mass has particles with a larger diameter, and 50% of aerosol mass has particles with a smaller diameter.



Figure 3.25, Mastersizer 2000 used for particle size analysis.

3.7.4 Powder- ESEM/EDS Analysis

Environmental Scanning Electron Microscopy (ESEM) is a method for high-resolution imaging of surfaces. The ESEM uses electrons to form an image, much as a light microscope uses visible light to reflect an image. Imaging with backscattered electrons gives contrasts based on atomic number to resolve microscopic composition variations as well as topographical information. Qualitative and quantitative chemical analysis information can be obtained using an Energy Dispersive X-Ray Spectroscopy (EDS).

EDS is defined as an analytical method used in the determination of elemental chemical composition. The technique utilizes x-rays that are emitted from the sample during the bombardment by the electron beam to characterize the elemental composition of the analyzed material.

All powders were examined in the XL30 ESEM-FEG (Figure 3.26). The ESEM was operated at 15-20 kV acceleration potential, 0.2-0.6 torr water vapour pressure and working distance of 11 mm. Backscattered electron images together with EDS

spectra were acquired from different parts of the samples in order to analyze and evaluate the metallic powder composition, and microstructure. The particle size and coating thickness measurements were performed during the course of analysis.



Figure 3.26, High resolution ESEM XL30 and EDS used for powder/coating analysis.

3.8 POWDER REACTIONS

AMDRY powder is roughly a spherical dark grey particles. It consists mainly from Cobalt, Nickel, Aluminium, and Yttrium. While, tungsten carbide cobalt physically is a fine grey powder. It consists of an inorganic chemical compound containing equal parts of tungsten and carbon atoms (WC) that is simply called “carbide”. Cobalt is the most commonly used as a binder because it has excellent carbide wetting and adhesion properties [135].

Tungsten carbide is approximately three times stiffer than steel, with a Young's modulus of approximately 550 GPa [136] and is much denser than steel or titanium. It is comparable with corundum in hardness and can only be polished and finished with abrasives of superior hardness such as silicon carbide and diamond amongst others, in the form of powder, wheels and compounds.

There are two well characterized compounds of tungsten and carbon, WC and tungsten semicarbide, W_2C . Both compounds may be present in coatings and the proportions can depend on the coating method [137]. The phase diagram of the WC-Co system shows that WC and Co form binary eutectic phase. Phases transformation (so-called carbides phases) can be formed during the thermal spray process. These phases are brittle which is the reason why control of the spray parameters is important to prevent the development of these phases [138].

The WC-Co powders used in this research consist of a mixture of 88% WC and 12% cobalt. This composition is widely used in applications requiring wear resistance, owing to properties imparted to the material by combining a hard ceramic phase (WC) and a tough metal phase (Co) [139]. During the thermal spray, powder particles are partially and/or totally molten before they are projected onto the substrate by a plasma or high-velocity flame gun. The adhesion and properties of the coatings depend on the amount of partial melting of the particles and on the energy (velocity) with which they impinge on the substrate. [140]

At low temperature and low velocity, insufficient melting of the particles and limited reactions between the ingredients occur which result in porosity and poor adhesion. Coatings produced under these conditions tend to have a lower hardness and wear resistance. As the particle temperature (and velocity) increases to a certain extent (optimum conditions), low porosity and higher hardness coatings can be achieved. [141]

At high temperatures, WC decomposes to tungsten and carbon. This can occur during high-temperature thermal spray process, e.g. high velocity oxygen fuel (HVOF) and high energy plasma methods [142]. Oxidation of WC starts at 500–600 °C [143]. The cobalt cladding does not protect the WC from oxidation [144]. Oxidation will result in WC phase transformation.

At high temperatures, not only the amount of partial/total melting occurs but chemical and structural changes in the material were accompanied. The chemical and structural changes were resulted from possible powder reactions during the HVOF and Plasma spray of WC-Co on carbon steel substrates were discussed in this research.

Decarburization of WC:

During spraying WC-Co powder, particles are subjected to chemical reactions which cause a decrease of the total carbon content. This reaction is called "decarburization". Decarburization occurs in both HVOF and plasma spraying, but usually to a much lesser degree in HVOF due to the lower temperatures involved [145]. Decarburization and carbide dissolution occurred to a significant extent during the deposition of the coatings [146].

In the HVOF system, the decarburization of the WC–Co particles requires reaction with oxygen in the hot gas. The stoichiometric combustion reaction is given in Eq. (3.1).



From the equation above, complete combustion reaction requires an oxygen to hydrogen ratio of 75%. A small percentage of O₂ present in the gas within the HVOF spray gun can cause the combustion reaction to initiate but it will not fully develop. [147]

In plasma spraying system, the WC-Co powder tends to undergo decarburization by reaction with the plasma gas. In both systems, powder particles will encounter considerable environmental oxygen levels as they exit the spray gun on their way to the substrate. The combination of high temperature and presence of oxygen in both systems would support decarburization of WC–Co particles.

The decarburization mechanism results in transformation of Tungsten Carbide WC to Tungsten Semicarbid W_2C and formation of Tungsten W would be as per the following reactions [148]:



A portion of WC particle starts to decompose to less hard W_2C and C at a temperature of 1250 °C. When the temperature increases, W_2C melts in the binder phase and some portion undergoes the decarburization reaction (at 2785 °C) to produce W and more carbides.

The free carbon can also react with oxygen to form carbon oxide gasses (CO or CO_2) or can remain dissolved in the cobalt matrix after solidification by cooling. Metallic tungsten W or W_2C can also be dissolved in the cobalt binder or be present (precipitation) on the surface of WC particles [149, 150].

Phase compositions depend on the spray conditions and the heat and mass transfer to in-flight particles prior to coating formation. The tribological behaviour of sprayed coatings compared with microstructure and the phase transformations of the starting material, leads to a wide variation in mechanical properties (Up to 50% of the WC–Co starting material may decompose and transform during the spraying process) [151-153].

3.9 COATING CHARACTERIZATION

To assess the quality of the multilayer thermal spray coating, microstructural characterization of the produced coatings should be investigated. Coating characterization is an essential technique to define the chemical and physical characteristics of the sprayed coatings. These characteristics will help to study the mechanical and corrosion behaviour of the applied coatings during their application. Metallographic preparation for every type of coating was performed prior to characterization. The comparative metallographic results of the various test coatings are discussed in Chapter 5.

3.9.1 Methods of Coating Characterization

In this work, the following methods of coating characterization and techniques were used to evaluate the coating materials:

- Environmental scanning electron microscope (ESEM)
- Energy Dispersive Spectrometry (EDS)
- X-ray powder diffraction (XRD)
- Surface roughness measurement of the coating
- Evaluation of coating porosity and adhesion
- Coating hardness assessment

These techniques will help to anticipate the powder reactions that would have taken place and affecting the quality of the coating. It also helps to study the coating porosity and adhesion to the base metal, which are as discussed in the following sections.

3.9.2 Metallographic Preparation

The objective of this work was to capture the images of topographical or microstructural features on prepared surfaces of coated materials. Thermally

sprayed coatings can be characterized in terms of revealing the coating/substrate interface, coating layer morphology, and thickness. The properties and performance of coating materials may be controlled by studying the microstructures using metallography equipment. Sample sectioning, mounting, grinding and polishing were conducted as per the recommendations from Struers (developer for materiallographic laboratories, Table 3.8 and 3.9). Secotom-10 with the Diamond Cut-off wheel 25 TRE had been used to cut the specimens. The mounting press LaboPress-3 with Multifast were used for mounting. Grinding and Polishing were done using the LaboPol-5 with LaboForce-3 and labo dosers, Figure 3.27 (a).

Table 3.8, Grinding work parameters for metallographic preparation.

Step	PG	FG 1
Surface	SiC-Paper #320	MD-Largo
Abrasive Type		DiaPro Largo
Lubricant Type	Water	
Speed [RPM]	300	150
Force [N]	240	180
Holder direction	>>	>>
Time [min]	1	3

Table 3.9, Polishing work parameters for metallographic preparation.

Step	P 1	OP
Surface	MD-Dac	MD-Chem
Abrasive Type	DiaPro Dac	OP-S, 0.04 μm
Lubricant Type		
Speed [RPM]	150	150
Force [N]	180	90
Holder direction	>>	<<
Time [min]	3	1

The preparation time for the grinding and polishing steps depends very much on the condition of the samples. Once finished, samples were stored under a Nitrogen

blanket to prevent oxidation (Figure 3.27 (b)). PANalytical instrument was used to perform the XRD analysis and to determine the chemical composition and crystallographic structure of the surface coating layer.



(a) Metallographic laboratory equipment



(b) Samples stored under Nitrogen blanket

Figure 3.27, Metallographic Preparation of the coated samples.

3.9.3 Coatings ESEM/EDS Analysis

Backscattered electron images together with EDS spectra were acquired from different parts of the coating samples in order to analyze and evaluate the coating microstructure, composition, and thickness. In backscattered electron images, the larger the tungsten content, the whiter the phase appears, due to the high atomic number of tungsten. WC appears lighter than cobalt, and W_2C appears lighter than WC.

3.9.4 Surface Roughness Measurement of the Coating

WC–Co cermets are widely used by thermal spray processes to deposit protective coatings on engineering surfaces against conditions where abrasion, erosion and other forms of wear exist. Surface roughness is one of the major factors that influence wear rates [154]. The study of quality of surface roughness is an

important requirement for WC-based cermets coatings due to their favourable combination of toughness and hardness.

Studies of surfaces roughness of thermally sprayed coatings have been conducted on sprays that are perpendicular and non-perpendicular to the substrate. These studies investigated the effects of the powder feed rate, the spraying distance, the spray angle, and the gun traverse rate on the surfaces roughness and the effects of the roughness of the substrate and the coating thickness [155- 158].

All of these studies concluded that the spray angle had a large effect on the coating surface roughness. The surfaces roughness of thermally sprayed coatings increased as the spray angle decreased. It showed also that the surface roughness of the coating was small for sprays that were perpendicular to the substrate (compared to non-perpendicular spray angles) and that the effect of the process parameters was small. For a spray angle of 45 ° it has been shown that the coating roughness increases with the coating thickness [159]. Yongzhong, et al, observed that, there is a coarsening tendency of WC powders with the increase of reaction temperature from (1000 -1300 °C). The coarse grain of WC powders results from long time carbonization at high temperature [160]. In general, the coating roughness was found to decrease with decreasing droplet size, decreasing splash fraction and increasing direction angle of the overspray.

A laser profilometer was used to measure the surface profile of the eight coating groups, which scans the coating surface vertically from above. The 3D surface profiler and the area and line scanning features were used to characterize and quantify the surface roughness and topographical features of the coatings Figure 3.28. All measurements were non-destructive, and require no sample preparation. Figure 3.29 shows a micrograph of one of the applied coating 3D roughness measurements.



Figure 3.28, Surface profiler used for Coating roughness measurements.

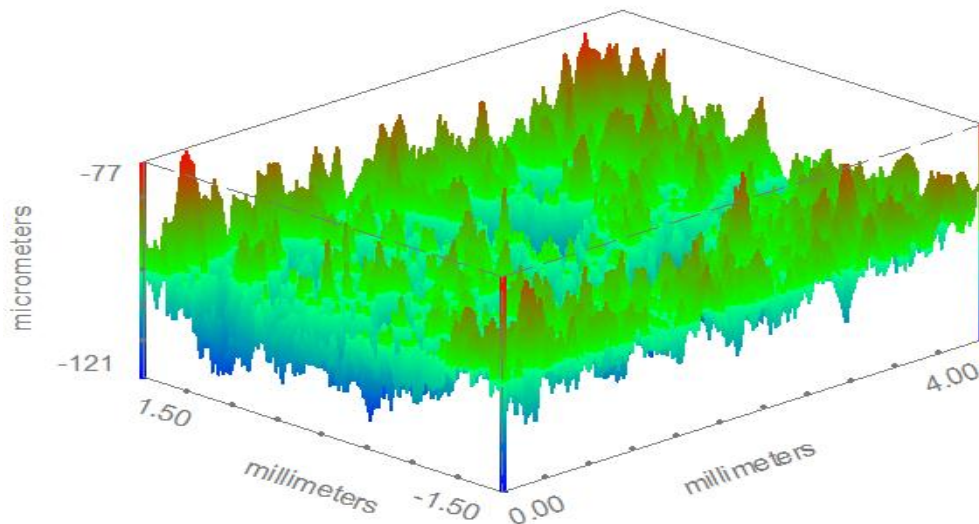


Figure 3.29, Example of 3D roughness measurements.

The results for the coating roughness measurements are presented in terms of the roughness variables, Arithmetical mean deviation R_a , and Maximum peak-to-valley height PV . R_a can be calculated as the average roughness or deviation of all

points from a plane fit to the test part, while PV is obtained by measuring the absolute value between the highest and lowest peaks.

3.9.5 Porosity Measurements

In this work, Scentis software, developed by Struers, was used to conduct the porosity measurement of the produced coatings. This software uses simple methods of coating image processing to obtain the percentage of porosity and that can provide a good indication of the porosity (but should not be 100% accurate value). These values can be used for coatings comparison. Three phase colour contrast method was selected in software to detect voids in the coatings, Figure 3.30. The most important step in this work is the selection of the representative coating spot that can represent the overall porosity. This step should be repeated several times by selecting different spot of the coating until, more consistent results are obtained (then one take an average).

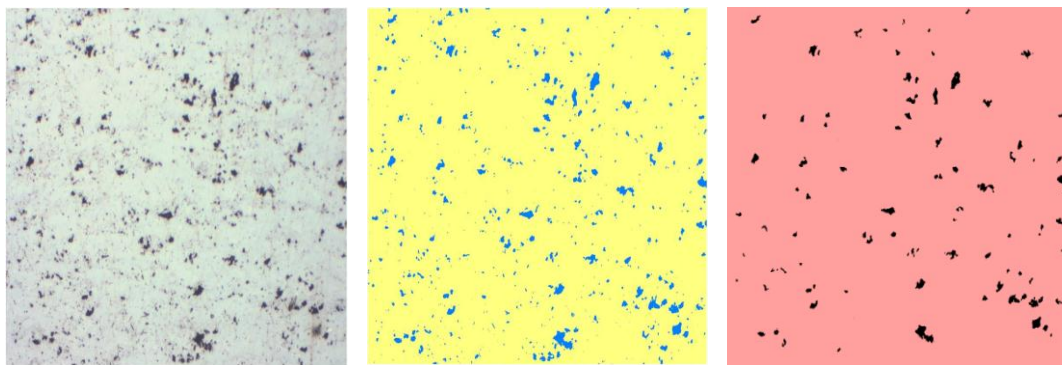


Figure 3.30, Three phase colour contrast method used to detect voids/porosity.

3.9.6 Coating Hardness Assessment

Micro-hardness tests were conducted in order to characterize the produced coatings and determine their resistance to permanent forces. The micro hardness measurement (indentation) was performed to measure the hardness of each layer of coating (5 indents/layer). The measurement was run according to ASTM E384 (The Vickers law method HV [161]) at load/force of 500 g. The LEICA VMHTMOT machine was used to conduct the measurement, Figure 3.31.



Figure 3.31, The LEICA VMHTMOT machine.

3.10 STATIC CORROSION TEST

The salt spray test is a standardized test method used to check corrosion resistance of coated samples. It is an accelerated corrosion test that produces a corrosive attack to the coated samples. The appearance of corrosion products (oxides) is evaluated after a period of time. Test duration depends on the corrosion resistance

of the coating; the more corrosion resistant the coating is, the longer the period in testing without showing signs of corrosion. Some of the characteristics of salt spray test are [162]:

- Considered to be the most useful method for measuring relative corrosion resistance of closely related materials (comparative test).
- Widely used for process qualification and quality acceptance.
- Applicable to most metals/alloys and their coatings.
- Provides a controlled corrosive environment representing accelerated marine type atmospheric conditions (acceleration from prevailing test temperature and/or degree of wetness).
- Reproducibility of results can be affected by specimen type, details surrounding specimen surface condition, evaluation criteria, operating variables and the type of test chamber.
- Correlation of test results to in-service (field) performance only to be considered if supported by results from long term in-service atmospheric exposures.
- Salt spray resistance results tend to differ from resistance to other media - alternative tests are designed for other media.

In this work, the objective of conducting this test was to assess the corrosion resistance of the applied coatings and to prepare test specimens for other tribocorrosion tests.

The test was conducted in accordance to ASTM B 117, [162]. This standard provides a controlled corrosive environment representing accelerated marine type atmospheric conditions. The results were accelerated by the test temperature, the test solution, the degree of wetness.

The salt spray test was performed using a solution of NaCl at a pH of between 6.5 and 7.2. The duration of the test ranged significantly, but typically from 500-1000 hours then given a grade of 1 to 10. There is no direct correlation between

accelerated salt fog testing and real outdoor exposure. The reason for this is that the outdoor environment is inherently variable on a day to day basis. However, general experience has shown that 1000 hours of exposure is equivalent to several years of outdoor exposure. Some industries equate this to a 10 year life. Despite this, salt spray testing is widely used in industry for the evaluation of corrosion resistance of finished surfaces or parts in order to predict relative suitability for use in service or as a quality control test. It is an ideal test to perform when comparing different suppliers or the effectiveness of different coatings. Table 3.10 depicts the scale for grading of the results of the salt spray testing, based on ASTM B117.

Table 3.10: Scale for grading result using salt spray test, [162].

Area Failed %	Rating No.
No failure	10
0 To 1	9
2 To 3	8
4 To 6	7
7 To 10	6
11 To 20	5
21 To 30	4
31 To 40	3
41 To 55	2
56 To 75	1
OVER 75	0

Test Apparatus:

The apparatus for testing consists of a closed testing chamber (Figure 3.32), where a salted solution is atomized by means of a nozzle. This produces a corrosive environment of dense saline fog in the chamber so that parts exposed in it are attacked under this severe corroding atmosphere.

The salt spray chamber is designed to give complete flexibility in the analysis of corrosion resistance for a wide variety of sample types by incorporating the versatility of both Prohesion and Condensation Humidity test methods. Also, the

apparatus used to conduct this test gives complete compliance to all major national standards including ASTM B117, [162].

A digital dual-loop temperature controller enables the operator to independently set the chamber temperature and the temperature of the bubble tower. The chamber is heated by a wrap-around heater jacket which is bonded to the exterior surface of the internal workspace to protect it from damage from the corrosive climate created inside the test chamber. The bubble tower humidifies the compressed air on the way to the salt fog atomizer and is heated by an immersion heater. Both the cabinet and bubble tower are equipped with over-temperature protection safety thermostats.



Figure 3.32, Salt Spray Testing Chamber.

The system is equipped by a separate external salt solution reservoir, where the salt water to be atomized into a fog is mixed and held. Salt fog fall-out is controlled by an adjustable flow control meter located on the control panel. This, coupled with the integrated air pressure regulator and gauge, were used to ensure a uniform and continuous fall-out of salt fog onto the samples were maintained under test (Figure 3.33).

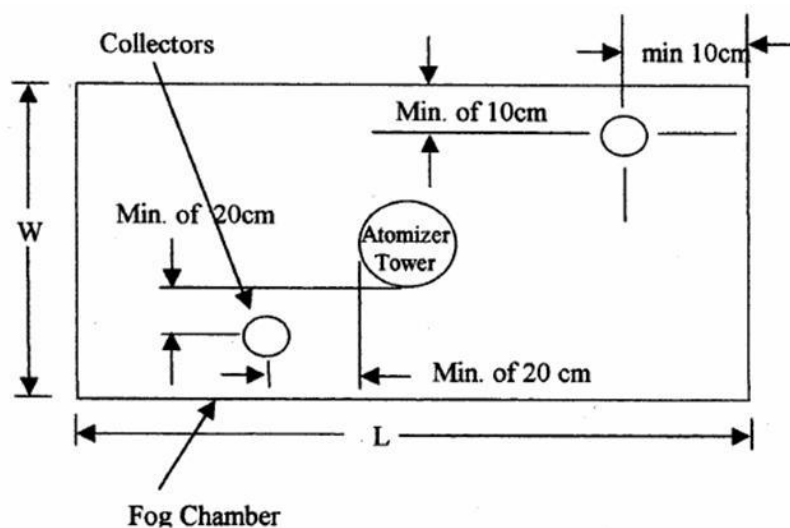


Figure 3.33, Arrangement of Fog Collectors.

Test Procedures:

The salt solution was prepared by dissolving 5 parts by mass of sodium chloride in 95 parts of water. The salt used in this experiment was sodium chloride with not more than 0.3 % mass of total impurities (Figure 3.34). Halides (Bromide, Fluoride, and Iodine) other than Chloride constituted less than 0.1 % by mass of the salt content. The uncoated areas of the test specimens were masked with corrosion-resistant epoxy paint and then protected against the fog using a suitable masking tape. The coated specimens were degreased and washed with de-ionized water prior to testing. Then they were placed in racks at an acute tilt angle. The position of the coated side of the specimens was such that they were supported 15 to 30° from the vertical and parallel to the principle direction of flow of the fog through the chamber (Figure 3.35).

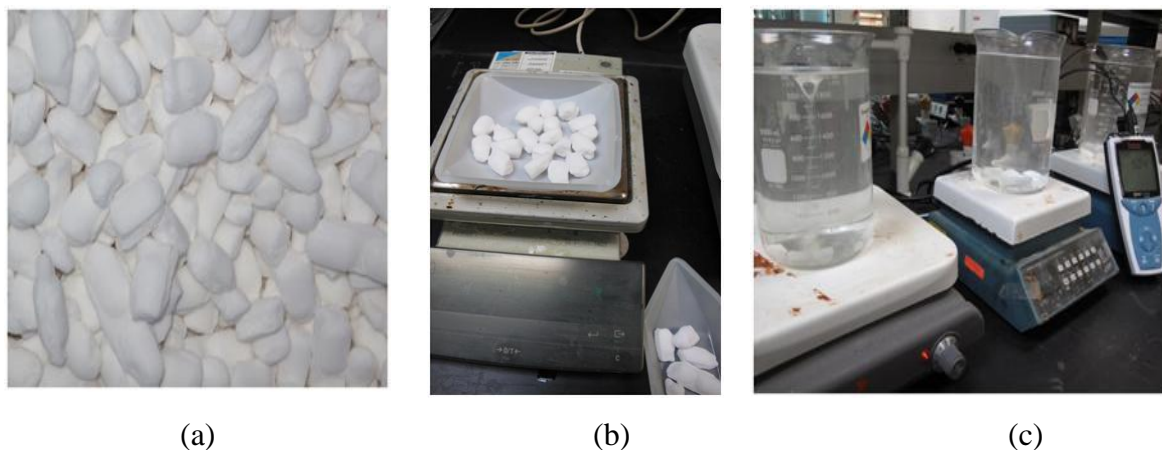


Figure 3.34, Salt used, (b) 5 parts by mass of salt , (c) NaCl solution preparation and pH measurement

The test began when the NaCl solution was mixed with the humidified air at the spray nozzle in the center of the cabinet. The solution atomized to create a fog within the enclosed chamber which contained the coated specimens. Fog flowed at a rate of 3 mL/min. The pH of the salt solution was measured periodically and maintained in the range from 6.5 to 7.2 pH. All test specimens were subjected to static fog. The exposure duration of this test was 720 hours and the temperature was maintained at 35°C during the course of the test. Changes to the coating surface during the test period were recorded such as the growth of number of corrosion pits.

After exposure, all samples were cleaned in running water not warmer than 38°C to remove salt deposits from the surface and then immediately dried with compressed air. After drying, surface corrosion products were removed by polishing the surface with fine sandpaper. Then, they were analyzed by ESEM/EDS. Visual examination was made for all samples which were exposed to the same conditions in order to be compared and rated. Photographs of the corroded specimens were then taken (Chapter 5).

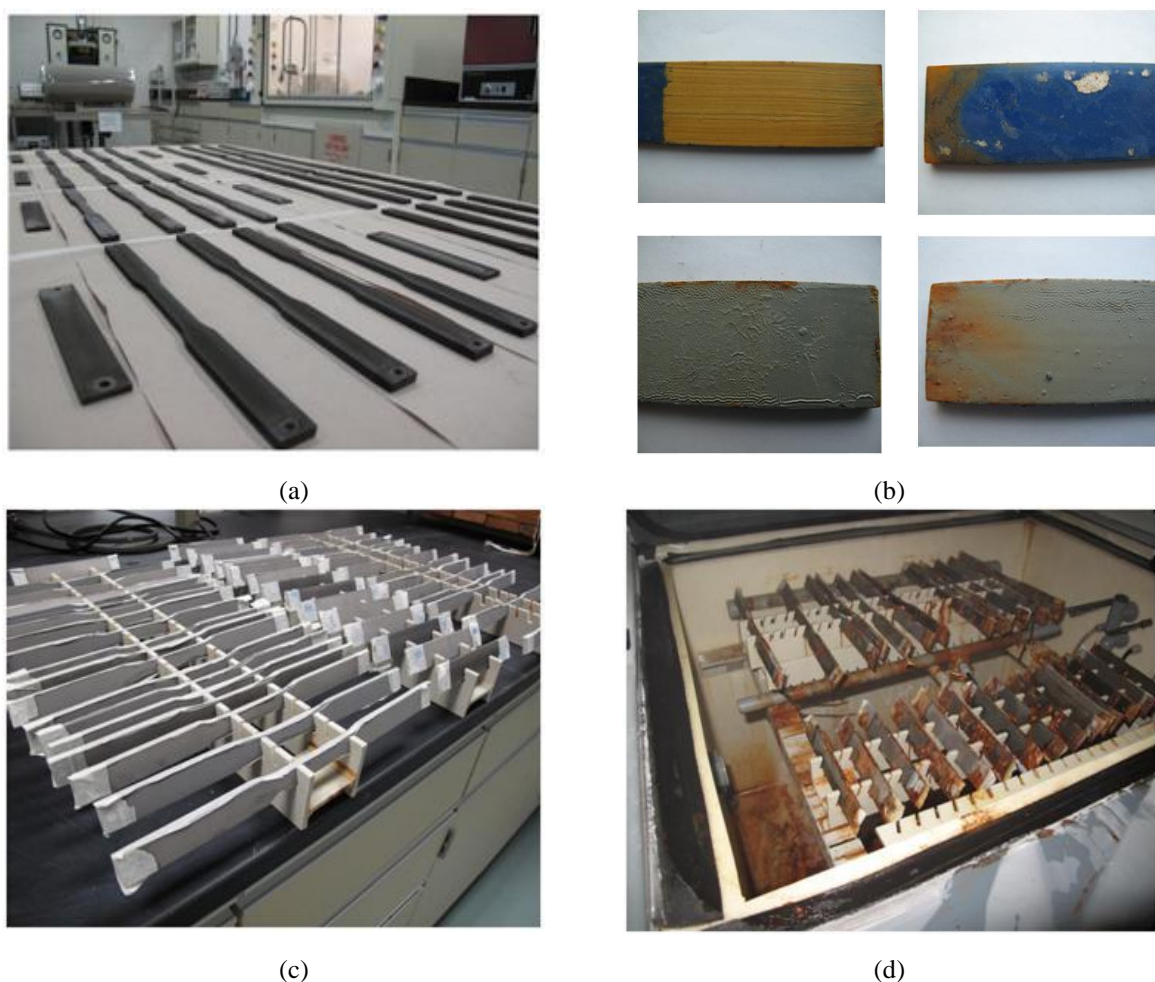


Figure 3.35, Salt Spray Test conducted in the laboratory; (a) Corrosion-resistant epoxy applied to uncoated part of the test specimens, (b) Testing the durability of some epoxies in high corrosive mediums, (c) Test Specimens were placed in racks at an acute tilt angle, (d) Test Specimens after salt spray test in the chamber.

During the corrosion test, fog accumulated on the top surface of the coating specimens and acted as an electrolyte that electrically conduct the anodic part of the corrosion cell to the cathodic part of the coating. The NaCl solution was continually in contact with the top surface of the coating. The electrolyte ions penetrated through the coating via irregularities or defects in the coating if any presented. The extent of penetration depends on coating porosity [163]. After electrolyte penetration, the test specimens began to corrode forming corrosion products that were mainly iron oxides as seen from the EDS analysis. The

corrosion product started to accumulate at the top surface of the coating. Accumulation of the products formed a barrier to the electrolyte penetration, which decreased the rate of corrosion (corrosion products growth).

If the corrosion products accumulated at the coating-substrate interface, this could cause the coating to peel away from the substrate, which was not the case in these tests indicating that the coatings were dense enough to stop the electrolyte penetration to the substrate. Thus, better corrosion resistance was expected for the batches that had low porosity in the coating.

3.11 EROSION-CORROSION BEHAVIOUR OF THERMALLY SPRAYED COATINGS

Erosion–corrosion is one of the common failure mechanisms in oil and gas production facilities [164]. Impingement of high velocity liquid droplets and sand particles cause severe material degradation in gas producing wells.

Material corrosion is an electrochemical phenomenon which leads to material loss. The ion transfer between the anodic and cathodic parts of the corrosion cell can be accelerated by the increased mass transfer or mechanical impacts as a result of an impinging flow. Erosion is mechanical damage due to impacts of a high-energy flow or suspended solids within a flow. The material removal does not involve any corrosion processes.

In applications where WC-based thermal spray coatings were subjected to erosion–corrosion environments, enhanced material damage occurred as a result of the combined effect of corrosion and erosion. Interactions, corrosion enhancing erosion, phenomenon gives rise to a synergistic action, which makes the overall material loss higher than the sum of material loss from corrosion and erosion together [165].

This research addressed the material degradation of WC-Co/AMDRY protective coatings applied to metallic substrates using a high velocity oxy-fuel (HVOF) and Plasma systems. The jet impingement rig was used to study the combined effect of corrosion and erosion (synergy) on the overall material loss in erosion–corrosion environments. The test was performed according to ASTM G73 “Practice for Liquid Impingement Erosion Testing” [166].

The test was carried out in a 1% sand contaminated seawater impingement jet to simulate the effect of particles and fluid high flow on the coated surfaces at the worst summer temperature. Weight loss measurement was considered to provide a measure for the amount of material loss.

Test Procedures:

Synthetic sea water was prepared according to ASTM D 1141 [167] by dissolving 245.34 g of sodium chloride and 40.94 g of anhydrous sodium sulfate in 8 to 9 L of water. The pH then was adjusted to 8.3 with 0.1 *N* sodium hydroxide solution. 1% sand (50 micrometer Alumina) was added to the solution. The jet impingement test rig was used to run the tests, Figures 3.36 and 3.37. The system was operated at a velocity of 40 m/s, temperature of 50 °C, and pressure of 13.8 Bar (17.2 Bar after heating). Teflon holders were used to ensure the prevention of any anticipated leakage. The test duration was 120 hrs for each run (3 samples/run). The jet angle was 90 degree to the top coat surface. The jet nozzle diameter size was 1.5 mm and jet distance was 1 cm. All test specimens were rinsed in acetone, dried and weighed with a precision balance which had an accuracy of ± 0.1 mg. System was purged with Nitrogen to make sure there was no trace of oxygen.

Once each run terminated, the specimen was carefully removed and inspected to determine whether failure to the substrate had indeed occurred. After cleaning with running water and acetone, the specimens were dried and mass measurements were

made. The chemical lab analysis of the water and residuals after test were also conducted.

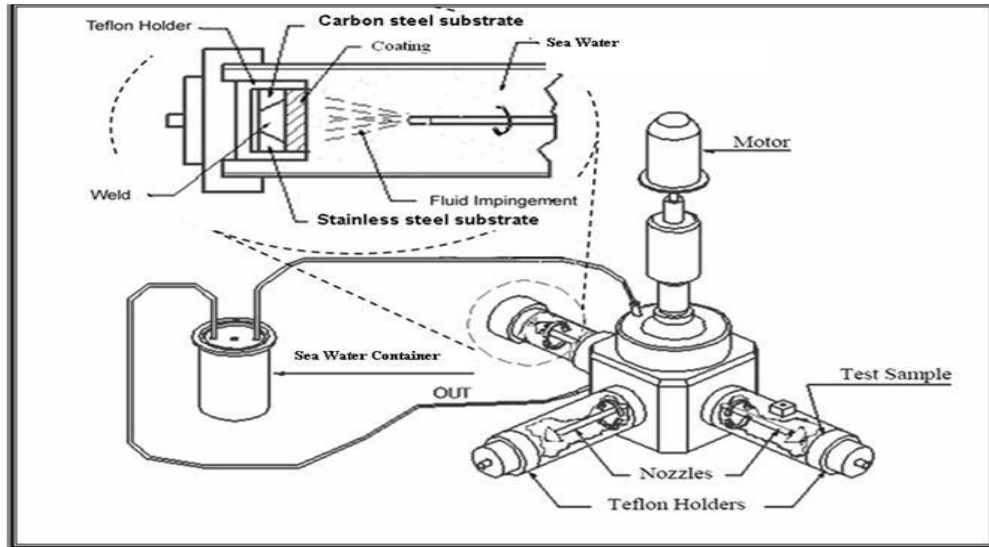


Figure 3.36, Schematic representation of the erosion-corrosion testing rig [128].

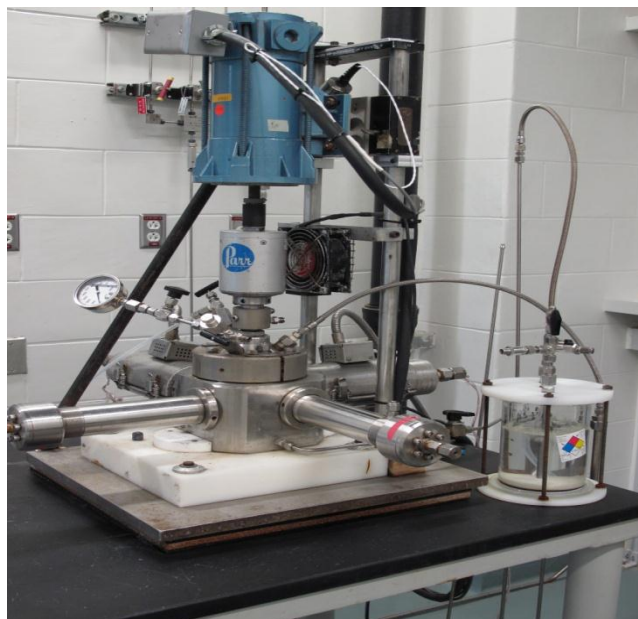


Figure 3.37, The erosion-corrosion testing rig.

3.12 MECHANICAL BEHAVIOUR OF THERMALLY SPRAYED COATINGS

To study the mechanical properties of hard coatings, some mechanical tests were conducted to assess coatings performance and behaviour when force is applied. The aim of these mechanical tests is to show whether the coating is suitable for mechanical applications by measuring elasticity, tensile strength, elongation, hardness, and fatigue limit.

In addition to the hardness test that was previously discussed in the Coating Characterization part of this work, three main mechanical tests; Three points bending test, Tensile test, and Fatigue test; were carried out in this research. The following sections will give explanation of each test in more details.

3.12.1 Three Points Bending Test

The three point bending test had been conducted to study the flexural stress-strain response of the coating. Instron testing instruments, Figure 3.38, were used to run the test. Materials testing software was used to provide automatic test control and data collection.



Figure 3.38, Instron testing instruments used for three point bending test

Test Procedures:

The three point bending method is sensitive to specimen and loading geometry. A micrometer was used for measuring the width and thickness of the test specimen to an incremental discrimination of at least 0.03 mm at the centre of the support span. The testing machine was calibrated before the test and operated at constant rates (the error in the load measuring system did not exceed +/-1 % of the maximum load).

The support span had been determined accordance to ASTM D-790-07 [168] (support span of 80 mm) then marked using a vernier caliper to measure the distance between the supports and the center as described in Figures 3.39 and 3.40 below. The test was carried out at room temperature and each run was conducted at a rate of 1.0 mm/min (4 samples per material type). The specimen lay on a support

span and the load was applied to its center by the loading nose producing three point bending at the specified rate. The test was stopped when the coating fractured or reached 10% deflection



Figure 3.39, Markings on fixed specimen supports.

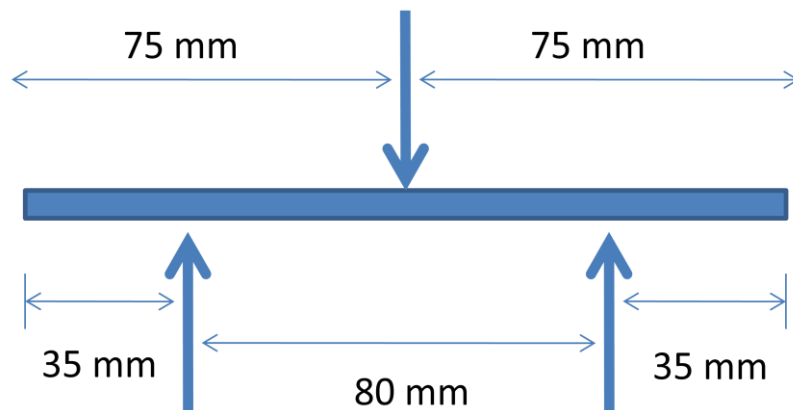


Figure 3.40, Geometry of the three point bending test.

3.12.2 Tensile Test

The objective of this test was to evaluate the tensile bonding strength of the thermally sprayed coating and to determine the stress strain behaviour of the coated materials. This test was also used to determine the point of failure of the coating. The test was performed as per ASTM E8, "Standard Method of Tension Testing of Metallic Materials" [169].

Test Procedures:

The tests were conducted using the Instron testing machine, Figure 3.41. A software program (Excel) was used to acquire stress strain plots for all test specimens (4 samples per material type). The tests were performed under load controlled at a displacement rate of 1.0 mm/min. The test specimen was of dog-bone shape, Figure 3.5. The test was carried out at room temperature and according to ASTM E8 [169]. Test was terminated after 8 mm expansion in the reduced section of the test sample.



Figure 3.41, Photograph of the Instron tensile testing machine with sample attached.

3.12.3 Fatigue Test

The objective of this test was to simulate the behaviour of the coating under which materials were subjected to vibrating or oscillating forces by simply applying cyclic loading to the test specimen to understand how it will perform under similar conditions in actual use. Fatigue testing indicates and predicts the in-service life of coated materials.

Test Procedures:

The ESH 100 KN Fatigue Machine (Figure 3.42) was used to perform this test. All fatigue tests were ramped to a sinusoidal loading of 25 KN at a frequency of 20 Hz by means of hydraulic fatigue testing machine. The main interest was the

determination of the number of fatigue cycles towards failure. Accordingly, a program was set to stop the loading cycles when there was 50% drop in the load. Tests were carried out at ambient temperature. The test specimens were of the same dimension and similar in geometry to specimens used in the tensile test (dog bone shape, Figure 3.5). Four samples per material type were used in this test, the results of which are presented in chapter 5.



Figure 3.42, Photograph of fatigue testing machine.

RESULTS AND DISCUSSION - POWDERS CHARACTERIZATION AND REACTION

4.1 POWDER CHARACTERIZATION

Powders MIX-1 (micro sized WC-12Co) and MIX-2 (nano sized WC-12Co) were used to spray the bond coats of the samples (Chapter 3-Table 3.5).

MIX-1:

MIX-1 EDXRF results showed that powder MIX-1 contained 7 wt. % cobalt and 4.7 wt. % silicon. Some traces of different elements (Ni, Fe, P, S, Cr, Ti, K) were detected by the EDXRF instrument. The weight percentage of WC in the sample was about 84.5 wt.% WC which contained 6.13 wt.% C. As a result of calculation, the MIX-1 powder therefore contained 79.3 wt. % tungsten and 5.2 wt. % carbide, Figure 4.1. The source of the silicon and the detected traced elements are unknown and these were not mentioned in the powders manufacturer specification sheet. They may be considered as contaminations from sample preparation tools in the laboratory.

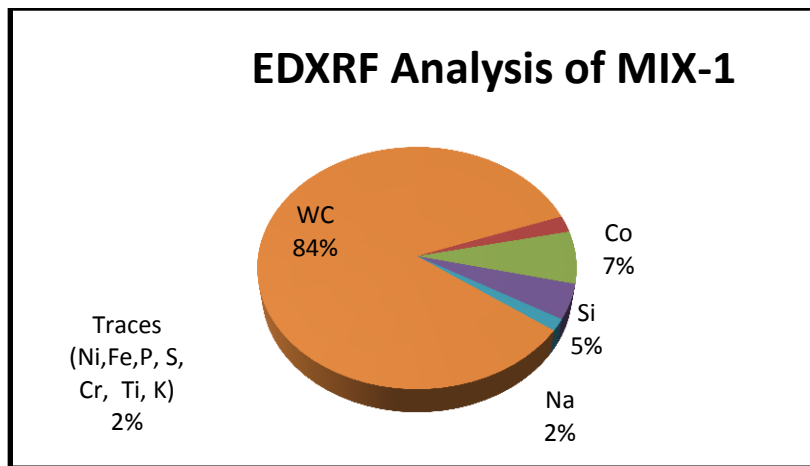


Figure 4.1, EDXRF results of powder MIX-1 in wt. %

The X-ray diffraction of powder MIX-1 revealed that the composition of the powder consists of 86 wt. % tungsten carbide and 14 wt. % cobalt. The XRD result confirms the compound composition of metallic powder and the WC value to very close to the elemental composition obtained from the EDXRF analysis and to the compound composition of powder manufacturer. The diffractogram of the powder with reference patterns of identified compounds is illustrated in Figure 4.2. Using the Mie scattering method of measurements, the powder particle distribution resulted in an average particle size of approximately 38.7 μm which is acceptable considering powder (SM 5812) particle size was -53 +11 μm (-270 mesh +11 μm), Figure 4.3. Particles above 100 μm that are shown in the graph were related to the dispersant (> 100 μm) used to calibrate the measurement (wet test), so these values were ignored.

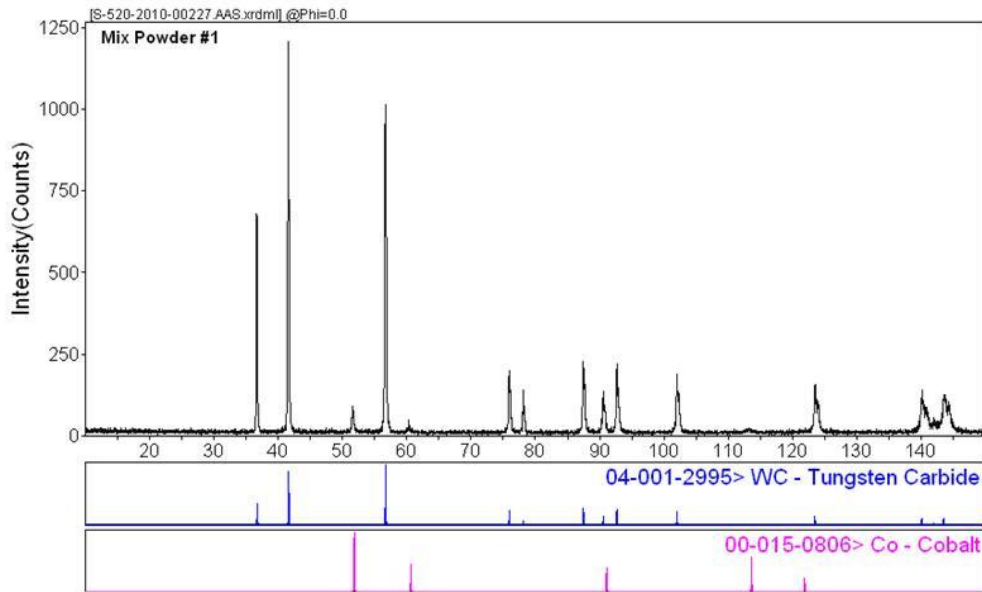


Figure 4.2, XRD Diffractogram of Identified Compounds- Powder MIX-1.

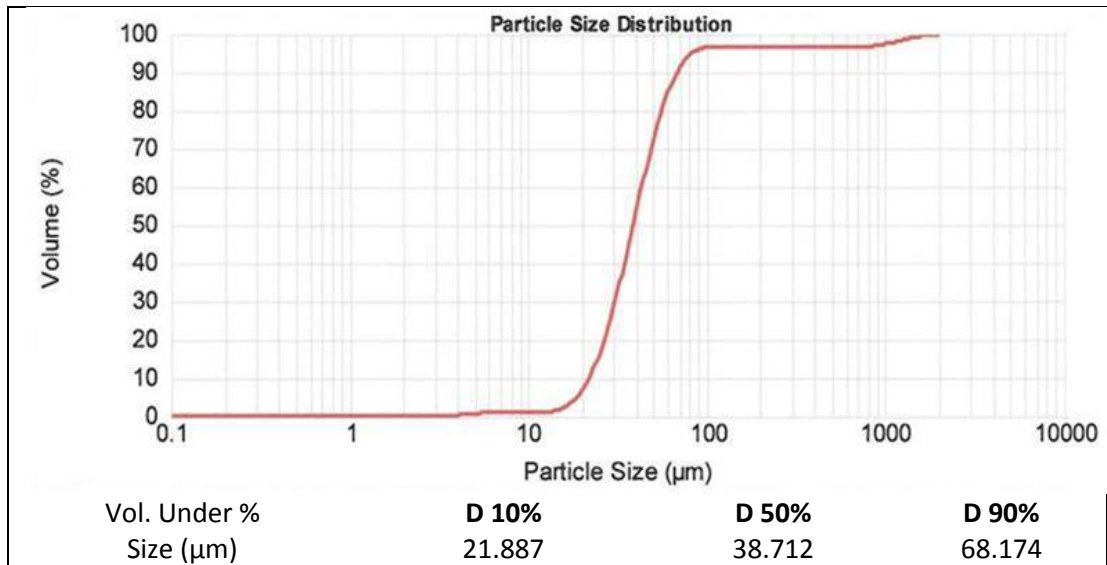


Figure 4.3, Particles Size Distribution of MIX-1.

Figure 4.4 shows the ESEM BSE (backscattered electrons) images taken at 100X, 800X and 3200X and EDS spectrum of powder MIX-1. The BSE images show that the powder particles exhibited a non-spherical shape, and they were in the 8 –45

μm size range. Also, the images at higher magnification (3200X) shows vast fractions of agglomerated loosely joined particles of irregular shape and these were in the 500 nm- 5 μm size range within these large particles. The semi-quantitative analyses (spot analysis) of the particles showed that they were composed of; 73 wt. % W, 14 wt. % C, 9 wt. % Co, 2 wt. % O and traces of Na via EDS X-ray technique.

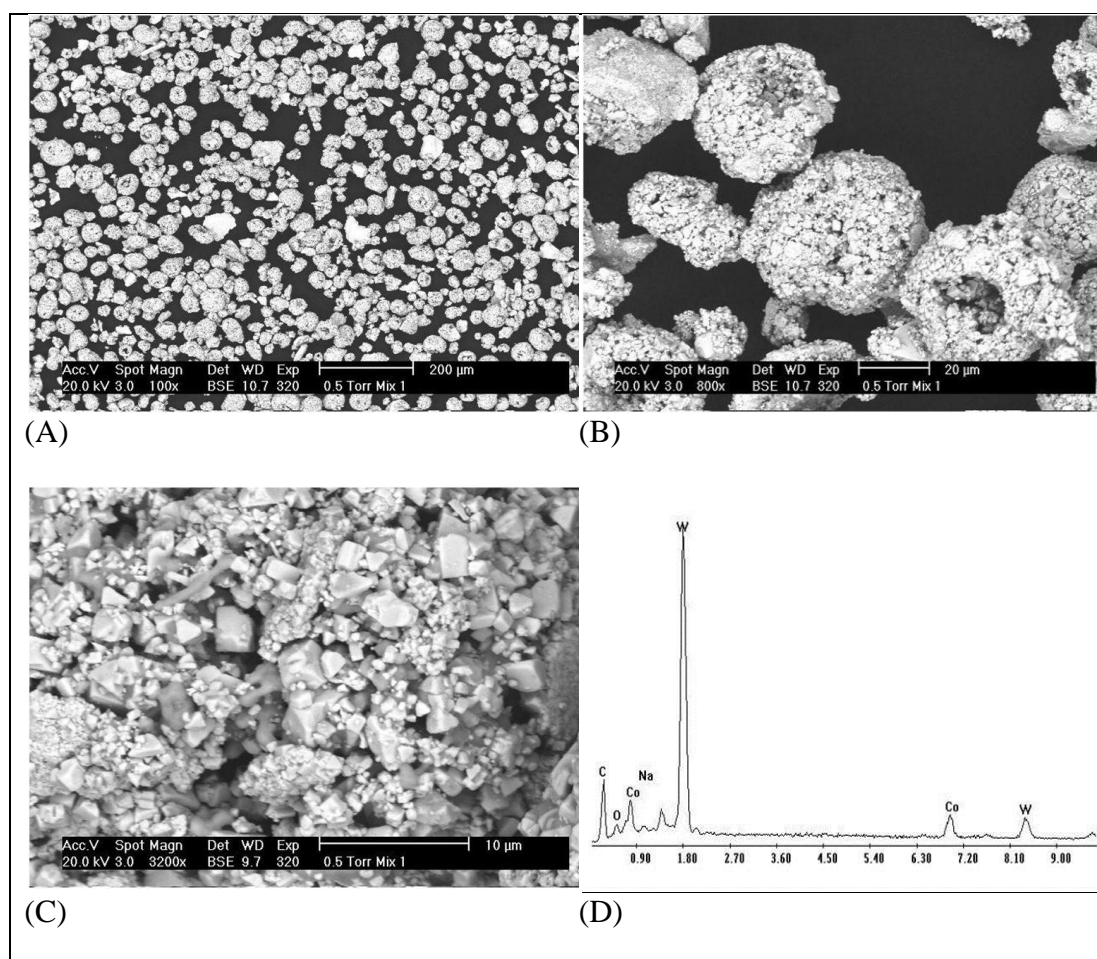


Figure 4.4, MIX- 1: (A) ESEM backscattered electron (BSE) image at 100X showing homogenous mixing of the sample; (B) backscattered electron (BSE) image at 800X showing irregular grain shapes of the powder (C) high magnification image of the same area at Magnification 3200X; (D) EDS X-ray spectrum of the powder.

MIX-2:

MIX-2 EDXRF results showed that powder MIX-2 contained 4.8 wt. % cobalt and 89.2 wt. % of the powder consists of tungsten and carbide (Nano size). By calculation, the weight percentage of W in the sample was about 83.7 wt. % while carbides approximately 5.5 wt. %, Figure 4.5. Some traces of different elements (Ni, Fe, P, S, Cr, Ti) were detected by the EDXRF instrument (< 1.4 wt. %).

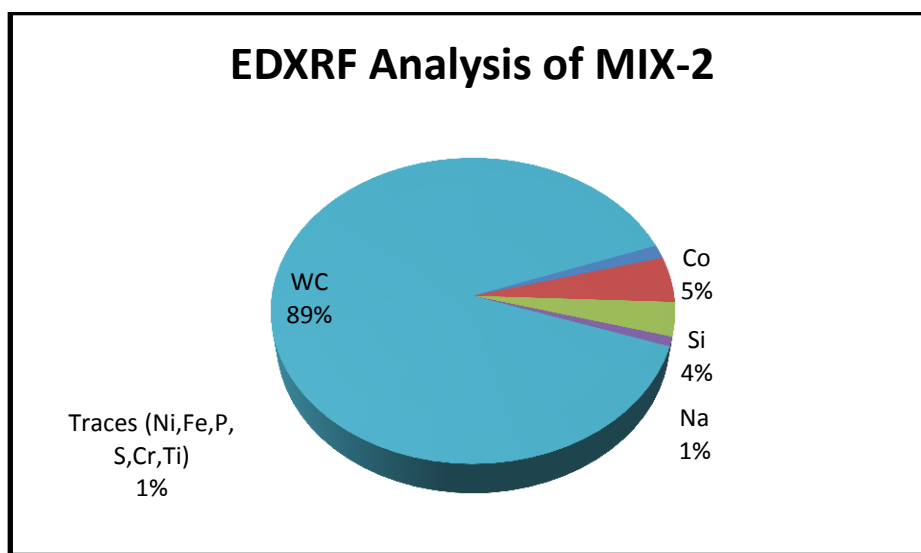


Figure 4.5, EDXRF results of powder MIX-2 in wt. %

The X-ray diffraction of powder MIX-2 revealed that the composition of the powder consist of 89 wt. % tungsten carbide and 11 wt. % cobalt which is same as the elemental composition obtained from the EDXRF analysis and close to the compound composition of powder manufacturer. The diffractograms of the powder with reference patterns of identified compounds are illustrated in Figure 4.6. The particles size distribution of powder MIX-2 revealed that the average particle diameter by mass was approximately 33.1 μm which is acceptable considering powder (S7412) particle size was 50 - 500 nm. The particles size distribution profile is illustrated in Figure 4.7 below. Particles above 100 μm that are shown in

the graph were related to the dispersant (> 100 μm) used to calibrate the measurement (wet test), so these values were ignored.

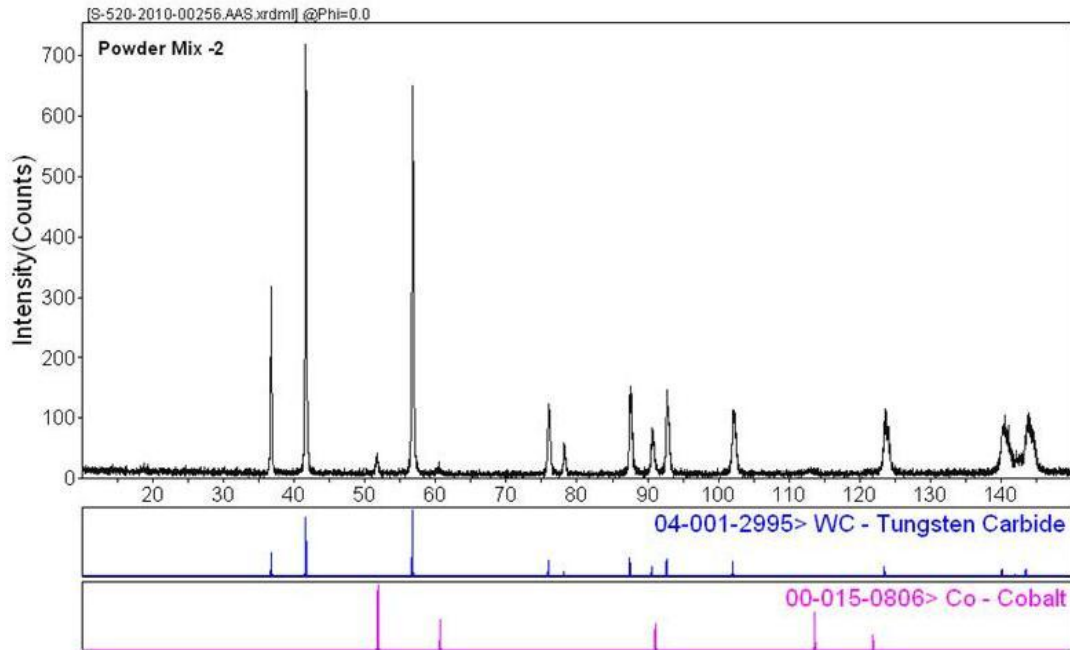


Figure 4.6, XRD Diffractogram with Identified Compounds- Powder MIX-2.

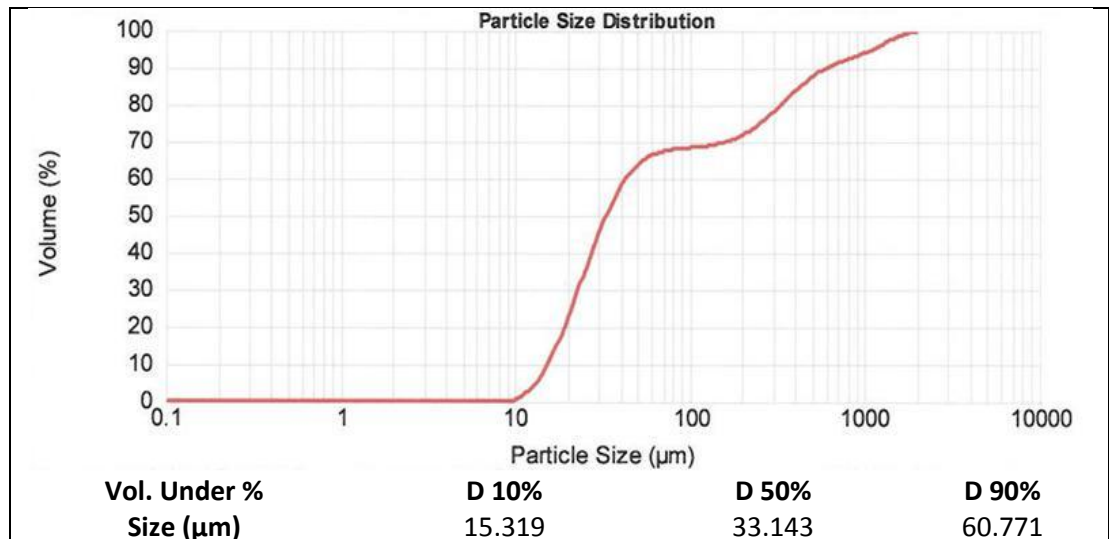


Figure 4.7, Particles Size Distribution of MIX-2.

The ESEM/EDS analysis of powder MIX-2 showed that the powder was composed of spherical particles with higher degree of roundness. Figure 4.8 below, show the ESEM BSE images that were taken at different magnifications (100X, 800X, 3200X) for the metallic powder MIX-2. The BSE images show that the powder particles reveal a higher degree of roundness and they were in the 12-60 μm size range. The particles were more compact and less porous compared to MIX-1. The image at higher magnification 3200 X also shows agglomerated crystals in the 150 nm- 2 μm size range. The semi-quantitative analysis (spot analysis) indicated that the particles were composed of 87 wt% W, 5 wt% Co, 7 wt% C, and 1 wt% O.

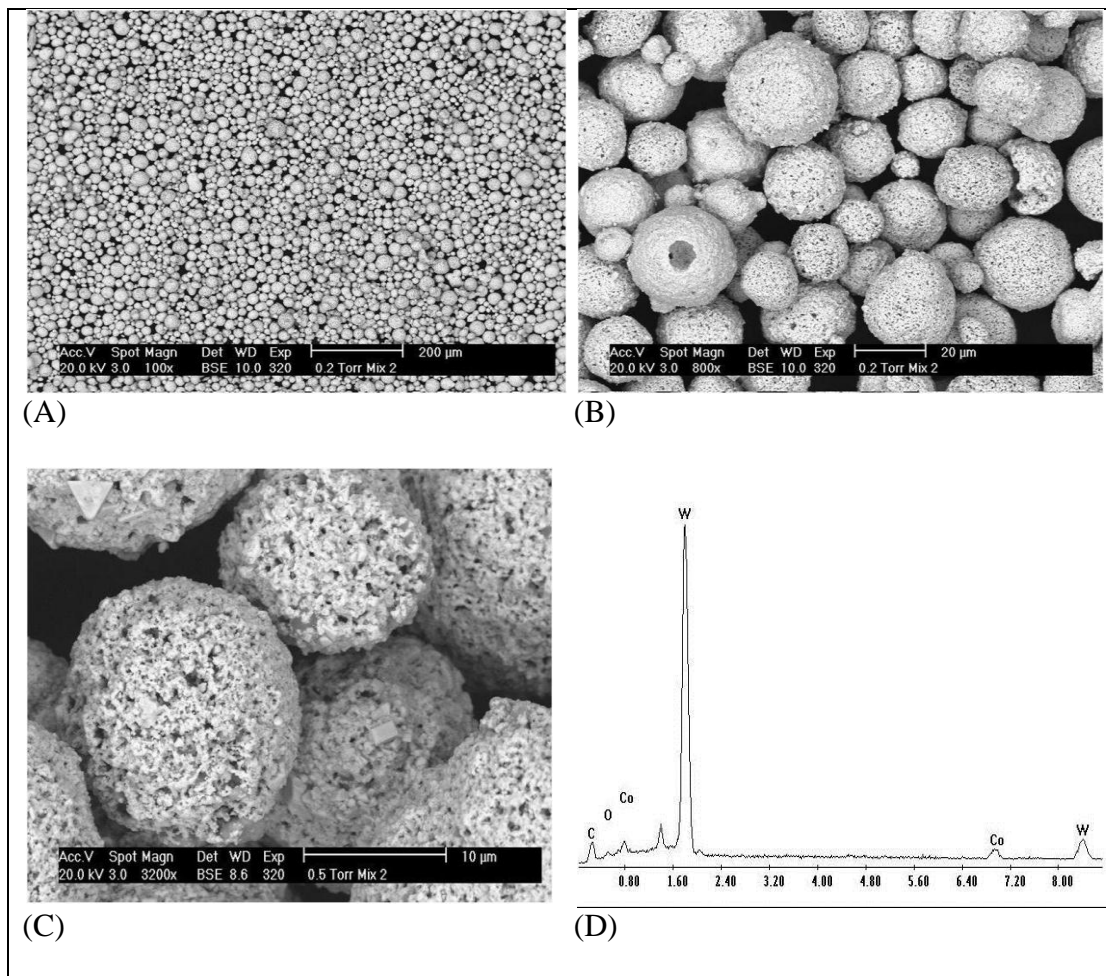


Figure 4.8, Mix No. 2: ESEM images of (A) BS image of coating powder particles showing triple and four point contacts, Magnification 100X; (B) backscattered electron (BSE) image showing the rough nature of coating at Magnification 800X (C) high magnification BSE image of coating powder, Magnification 3200X; (D) EDS X-ray spectrum of the powder. It shows mainly W and traces of Co, and O elements presence in the sample.

Figures 4.8 (B) showed the MIX-2 powder to have a near spherical morphology with particle size distribution ranging from 15 to 60 μm in diameter, which aids flowability and thermal transfer from the flame. The ESEM images Figure 4.8 (C) also showed the particles to exhibit some degrees of porosity. These porosities can be eliminated when sprayed at elevated temperatures.

Powders used to spray the top layers:

Powders MIX-3, 4, 13, and 14, in addition to MIX-1 and 2, were used as feedstock powders to spray the top layer coatings (Chapter 3-Table 3.5).

MIX-3:

MIX-3 EDXRF showed the MIX-3 powder (60 wt.% micro sized WC-12Co + 40 wt.% micro sized AMDRY 9954) to contain more elements than MIX-1 and 2. The tungsten percentage in the sample was found to be 57.6 wt.% while the carbide presented 3.8 wt.% of the sample (WC 61.4 wt.%). It also contained 14.3 wt.% cobalt, 11.1 wt.% chromium, 8.3 wt.% nickel and 2.7 wt.% silicon. Trace elements (P, Fe, Na, S, Y, Ti, K) were also detected by EDXRF. Figure 4.9 shows the elemental distribution of MIX-3.

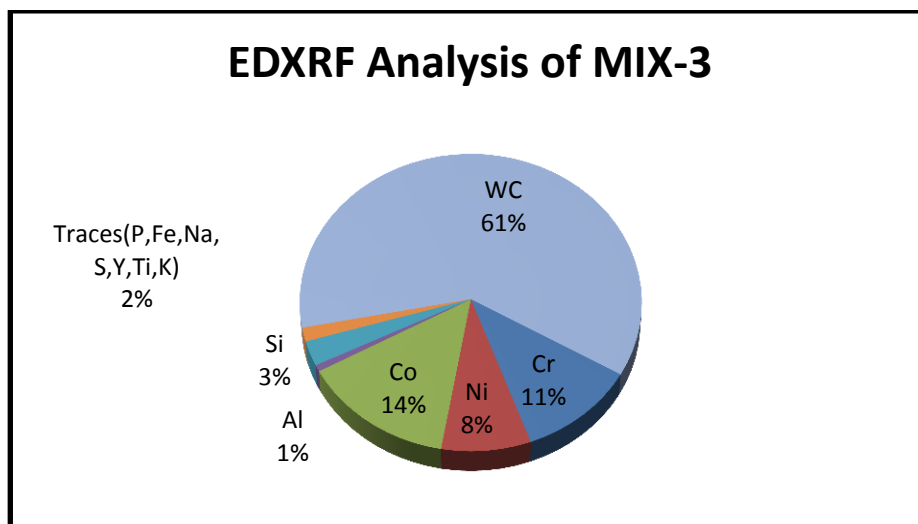


Figure 4.9, Energy dispersive X-ray fluorescence Spectrometry of Powder MIX-3 in wt. %

The X-ray diffraction of powder MIX-3, identify crystalline phases consisting of the combination of Tungsten Carbide [WC], Tungsten Cobalt [WCo], and Chromium [Cr]. The elements of these compounds were detected also by the energy dispersive X-ray fluorescence spectrometry. The diffractogram of the powder with reference patterns of identified compounds are illustrated in Figure 4.10. Using the Particles Size Distribution method the average particle diameter of MIX-3 was 35.95 μm (Figure 4.11) which is acceptable considering mix of powder particle size -53 +11 μm (SM 5812) with -62 + 11 μm (AMDRY 9954).

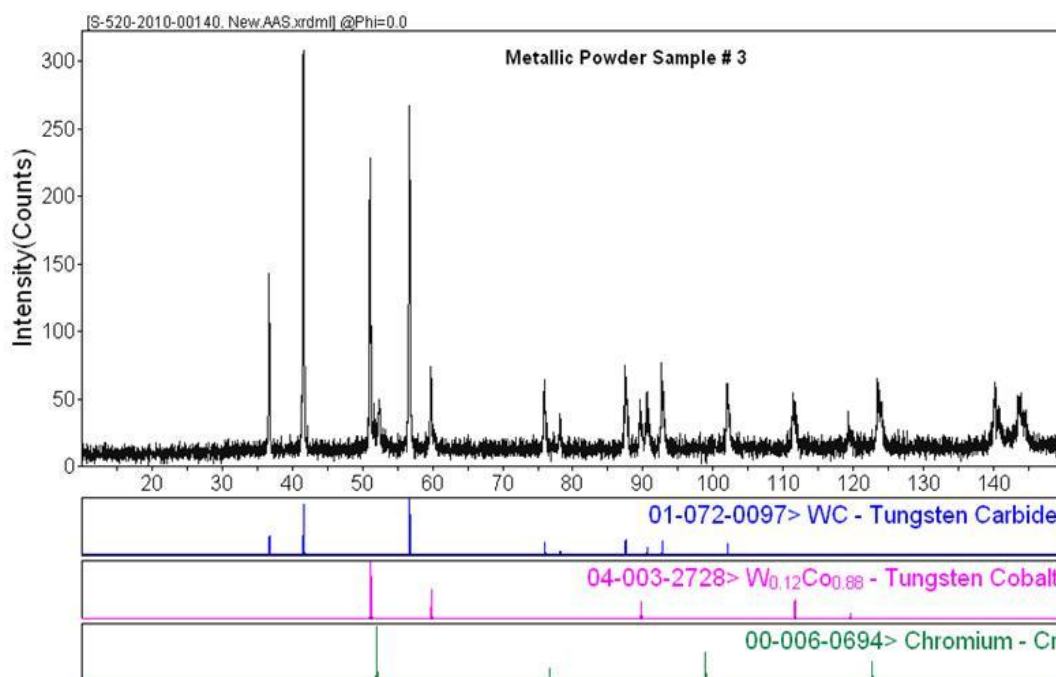


Figure 4.10, XRD Diffractogram with Identified Compounds- Powder MIX-3.

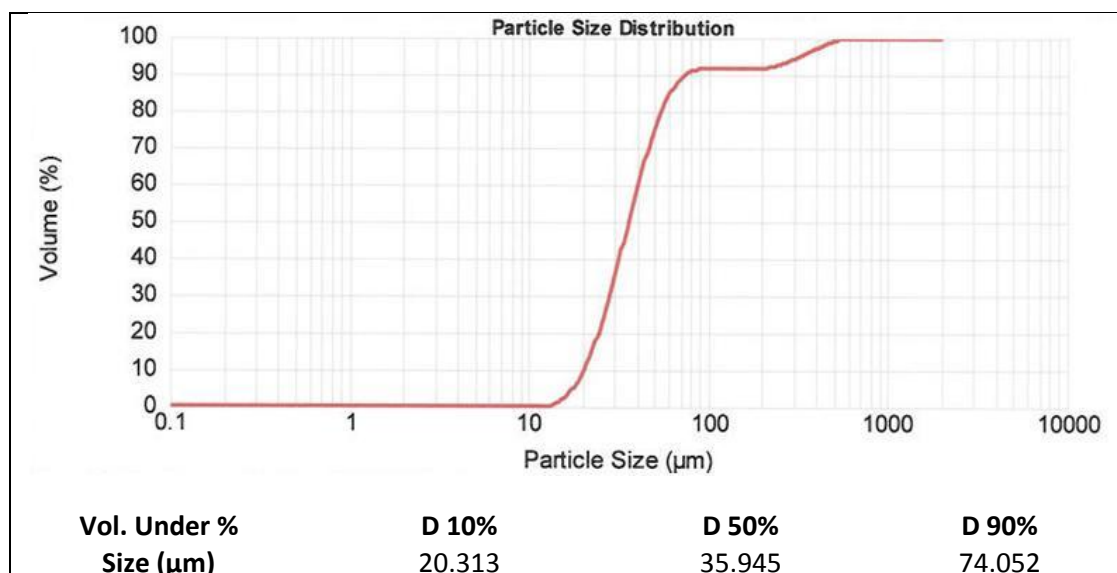


Figure 4.11, Particles Size Distribution of MIX-3.

Figure 4.12 shows the ESEM BSE images taken at 100X, 3200X, and EDS spectrum of the light and dark regions of the powder MIX-3. The BSE images showed dark and light powder particles with a ratio of approximately 40 % to 60 % respectively. The spherical dark particles were nonporous and they were 9- 45 µm in size. The semi-quantitative analysis of the spherical dark particles were 10 wt.% W, 34 wt.% Co, 9 wt.% Al, 19 wt.% Cr, and 29 wt.% Ni (Figure 4.12 (C)). A trace of Na was also found in the samples. The non-spherical light particles displayed high porosity compared to powder MIX-2 and were in the 3- 80 µm size range. The BSE image of the light particles at X 3200 showed agglomerated loosely bonded crystals of irregular shape and they were in the range of 200 nm-3 µm. The chemical composition of the non-spherical bright particles were 87 wt.% W, 9 wt.% Co, 3 wt.% O, and 1 wt.% Na (Figure 4.12 (D)).

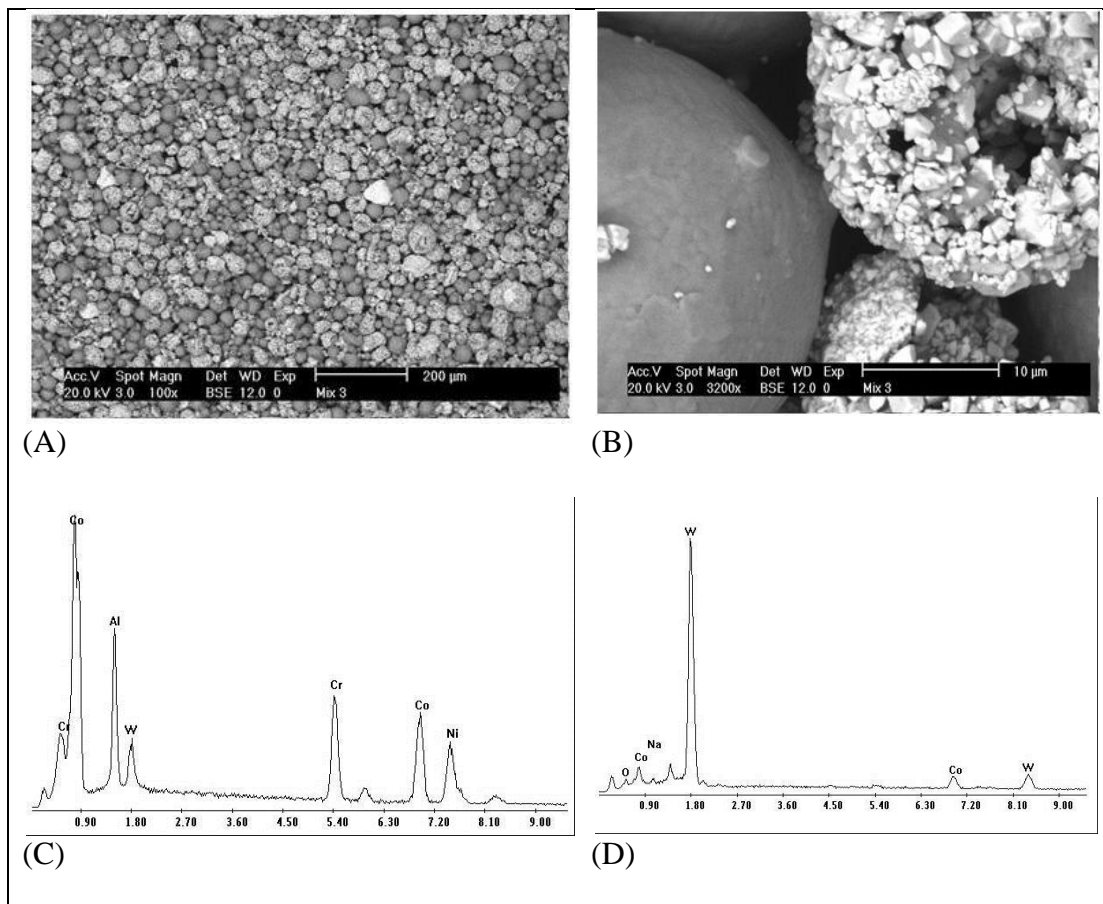


Figure 4.12, Mix No. 3: (A) ESEM backscattered electron (BSE) image at 100X showing the various powders used to produce the sample; (B) backscattered electron (BSE) image at 3200X showing both light and dark powder used to produce the mix; (C) EDS X-ray spectrum of the dark powder shows Co, Al, W, Cr and Ni presence in the sample; (D) EDS X-ray spectrum of the light powder shows W and traces of elements presence in the sample.

MIX-4:

The elemental composition analysis (EDXRF) of powder MIX-4 (60 % nano sized WC-12Co + 40 % micro sized AMDRY 9954) showed the WC percentage in the sample was found to be 54.9% (51.5% W and 3.4% C). The powder also contained 14.4 wt.% chromium, 15.7 wt.% cobalt, and 10.6 wt.% nickel. A small portion of silicon and aluminium was also found in the sample (2.2% and 1.1% respectively), Figure 4.13.

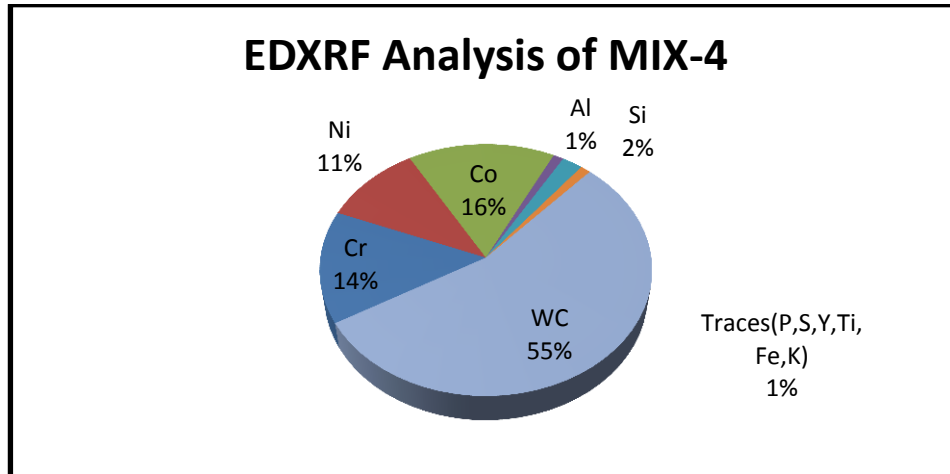


Figure 4.13, Energy dispersive X-ray fluorescence Spectrometry of Powder MIX-4 in wt. %

Three phases were represented when the X-ray powder diffraction analysis was performed on the powder MIX-4. The composition of these phases was Tungsten Carbide [WC], Chromium Nickel [Cr_2Ni_3], and Cobalt [Co]. These phases are represented with reference patterns Figure 4.14 which appear amorphous but it resulted from backscattered electron. The log chart of particle size distribution showed a uniform powder of particle size ranges from 17- 71 μm with a mass-median-diameter of 28.077 μm (Figure 4.15) which is acceptable considering mix of powder particle size 50 - 500 nm (S7412) with -62 + 11 μm (AMDRY 9954).

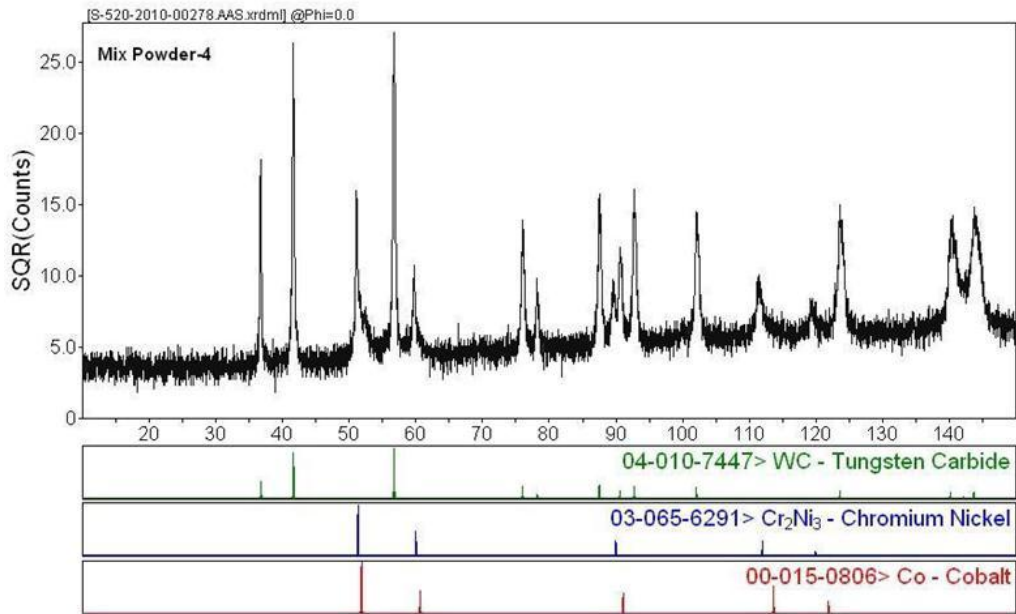


Figure 4.14, XRD Diffractogram with Identified Compounds- Powder MIX-4.

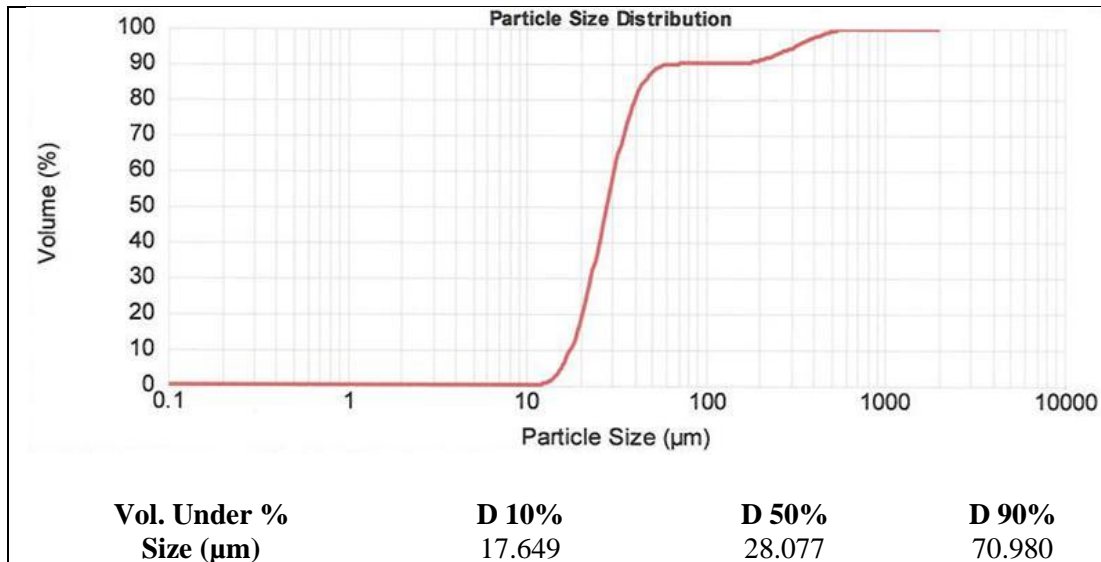


Figure 4.15, Particles Size Distribution of MIX-4.

The BSE images of powder MIX-4 showed dark and light powder particles with a ratio of approximately 75% to 25% respectively. The BSE images also show that the light particles, 4-45 µm size range, were low in porosity compared to powder

MIX-3 and exhibit approximately 45% spherical and the rest are non-spherical in shapes. Figure 4.16 shows the ESEM BSE images taken at 800X and 3200X and EDS spectrum of dark and light powder MIX-4 (Figure 4.16 (A) and (B)). The spherical dark particles are nonporous and measure about 15- 48 μm . The semi-quantitative analysis of the spherical dark particles was, 8 wt.% W, 31 wt.% Co, 8 wt.% Al, 17 wt.% Cr, 5 wt.% C, 4 wt.% O, and 26 wt.% Ni (Figure 4.16 (C)). The BSE image of light particles at X 3200 (Figure 4.16 (B)) shows agglomerated of loosely crystals of irregular shapes and they are in the 200 nm- 3 μm size range. The chemical composition of the light particles was, 88 wt.% W, 8 wt.% Co, 2 wt.% O, and 3 wt.% Cr (Figure 4.16 (D)).

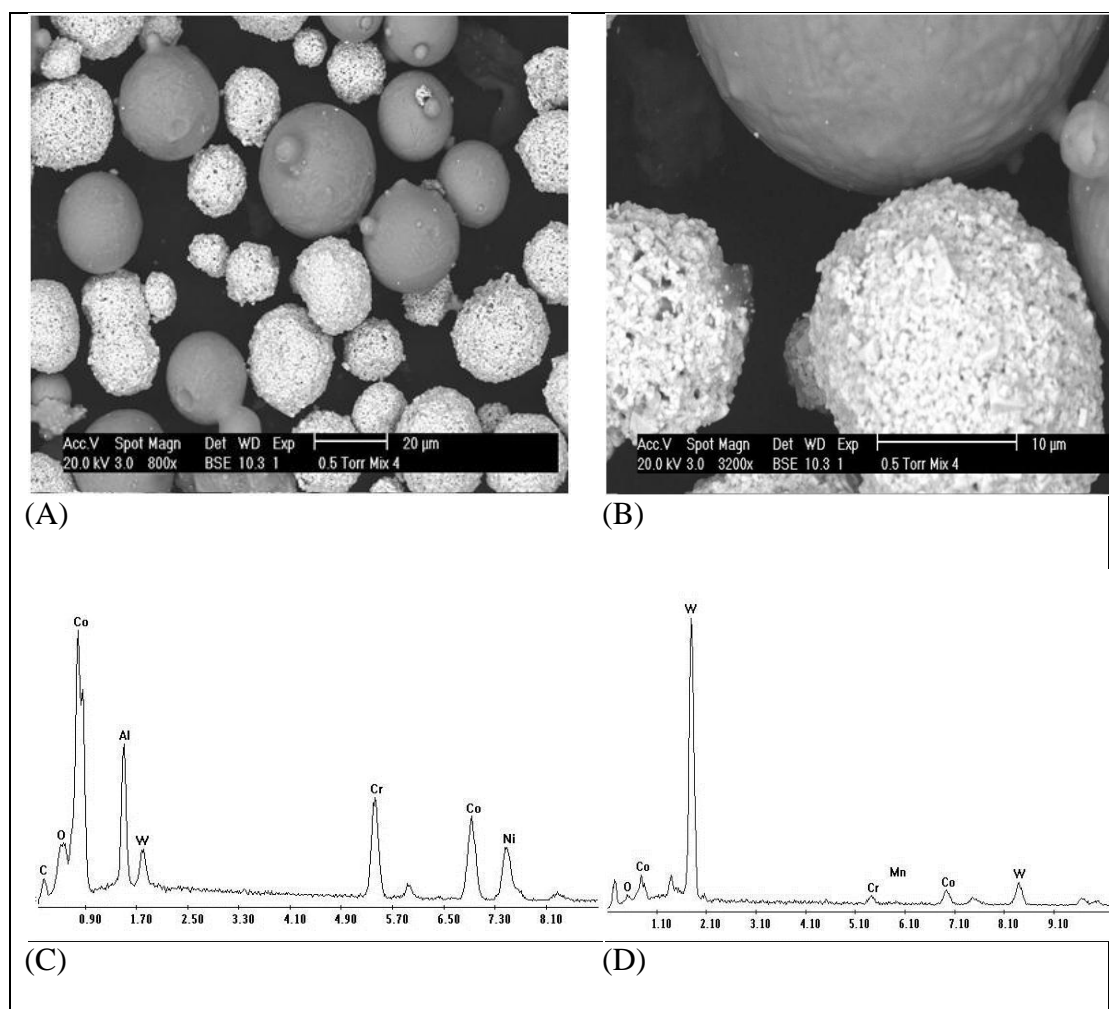


Figure 4.16, Mix No. 4: (A) ESEM backscattered electron (BSE) image at 800X showing differ powders used to produce the sample; (B) backscattered electron (BSE) image at 3200X showing light and dark powder in the mix (C) EDS X-ray spectrum of dark powder. It shows Co, W, Cr and Ni presence in the sample; (D) EDS X-ray spectrum of light powder. It shows W and Cr, and Co in the sample.

MIX-13:

The EDXRF analysis of powder MIX-13 (60 % micro sized WC-12Co + 40 % micro sized AMDRY 995M) resulted in 67.0 wt.% tungsten, and 4.4 wt.% carbide (71.4 wt.% WC) and 11.2 wt.% cobalt. The metallic powder also contains 6.9 wt.% chromium, 5 wt.% nickel, and 3.5 wt.% silicon. Figure 4.17 presents these compositions.

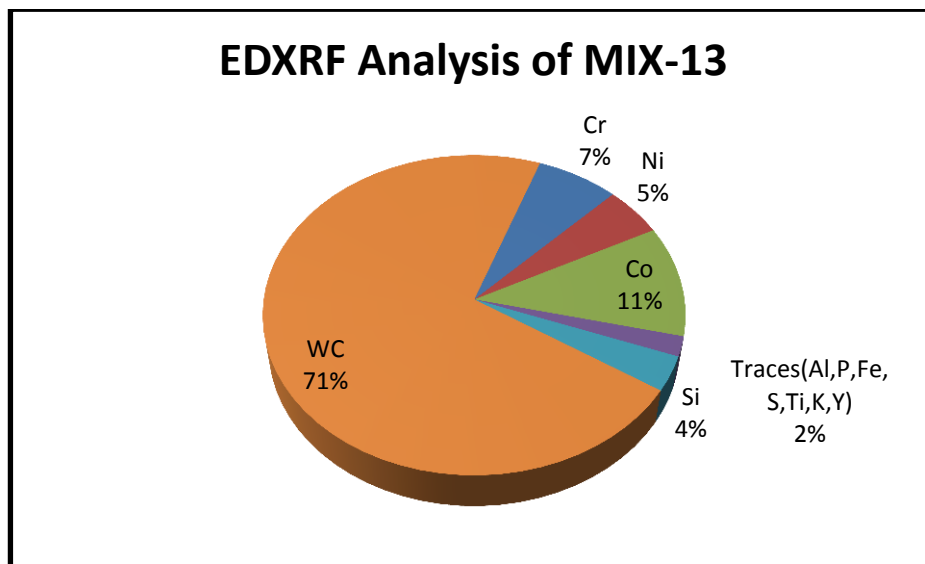


Figure 4.17, Energy dispersive X-ray fluorescence Spectrometry of Powder MIX-13 in wt. %

The XRD composition analysis of powder MIX-13 showed that the powder is mainly consisting of tungsten carbide WC, chromium nickel- Cr_2Ni_3 , and cobalt metal. The Cr, Ni, W, C, and Co elements are the same elements detected by the EDXRF analysis. The patterns of the crystalline phases identified by X-Ray Diffraction are illustrated in Figure 4.18 which appear amorphous but it resulted from backscattered electron. The average particle diameter of MIX-13 was approximately $43.4 \mu\text{m}$ (Figure 4.19) which is acceptable considering mix of powder particle size $-53 +11 \mu\text{m}$ (SM 5812) with $-63 +45 \mu\text{m}$ (AMDRY 995M).

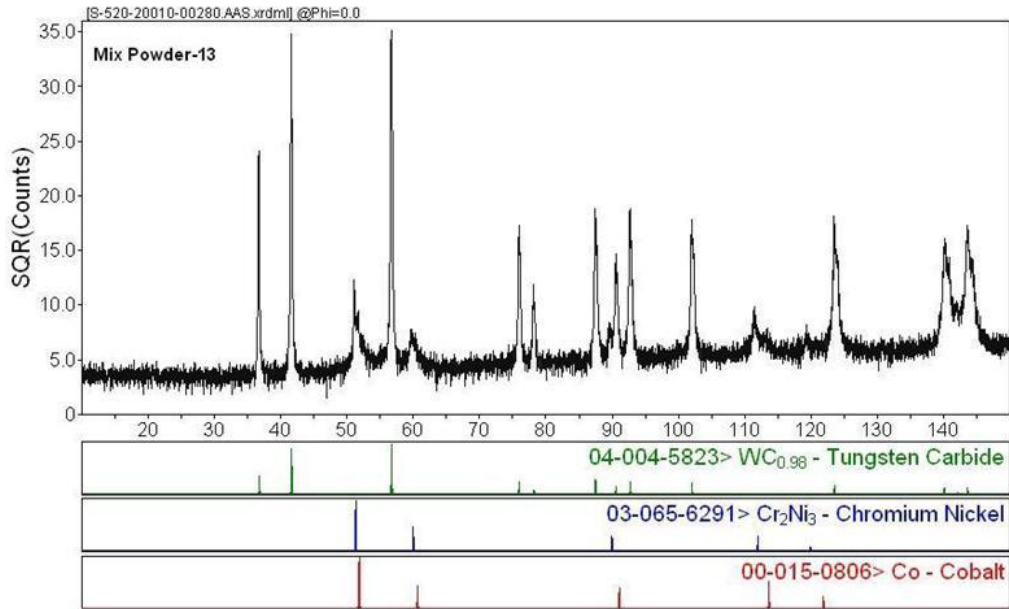


Figure 4.18, XRD Diffractogram with Identified Compounds- Powder MIX-13.

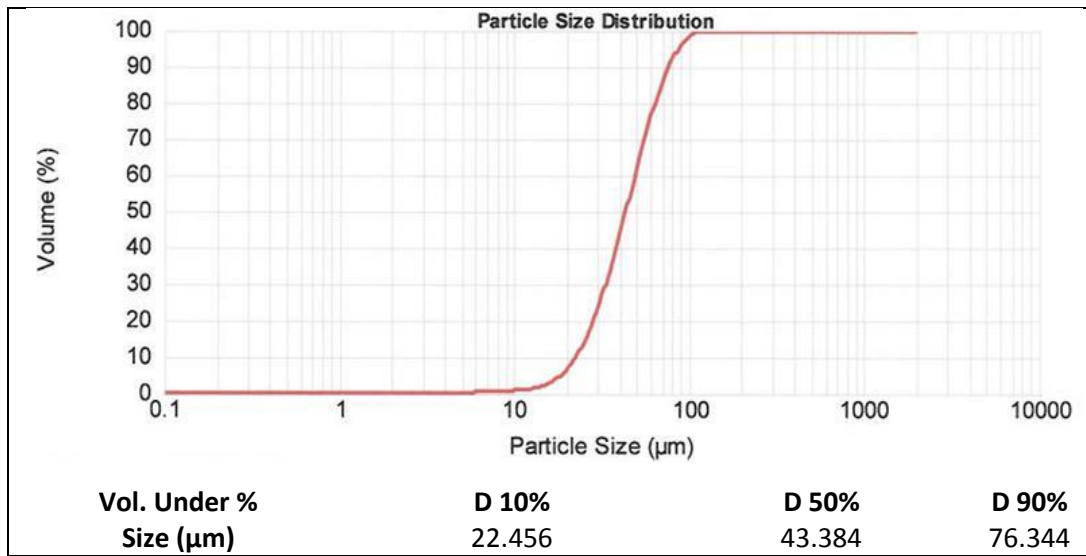


Figure 4.19, Particles Size Distribution of MIX-13.

ESEM BSE images were taken at different magnifications for powder MIX-13. Also, the powder had gone over EDS spectrum analysis. The BSE images as well as the EDS X-ray spectrum are shown in Figure 4.20. The BSE images show dark and light powder particles with a ratio of approximately 70% to 30% respectively. The light particles show roughly 20% spherical and the rest are non-spherical in shape (Figure 4.20 (A) and (B)). The nonporous spherical (50% of the total dark particles) are in the range of 15-70 μm . The chemical composition of the dark particles was 5 wt.% W, 35 wt.% Co, 8 wt.% Al, 20 wt.% Cr, and 32 wt.% Ni (Figure 4.20 (C)). The light particles were in range of (4- 80 μm) with high porosity compared to some other powder mixes. The BSE image at X 3200 shows agglomerated loosely crystals of irregular shapes in the 150 nm- 5 μm size rang. The chemical composition of the bright particles was 92 wt.% W, 8 wt.% Co, and 2 wt.% O (Figure 4.20 (D)).

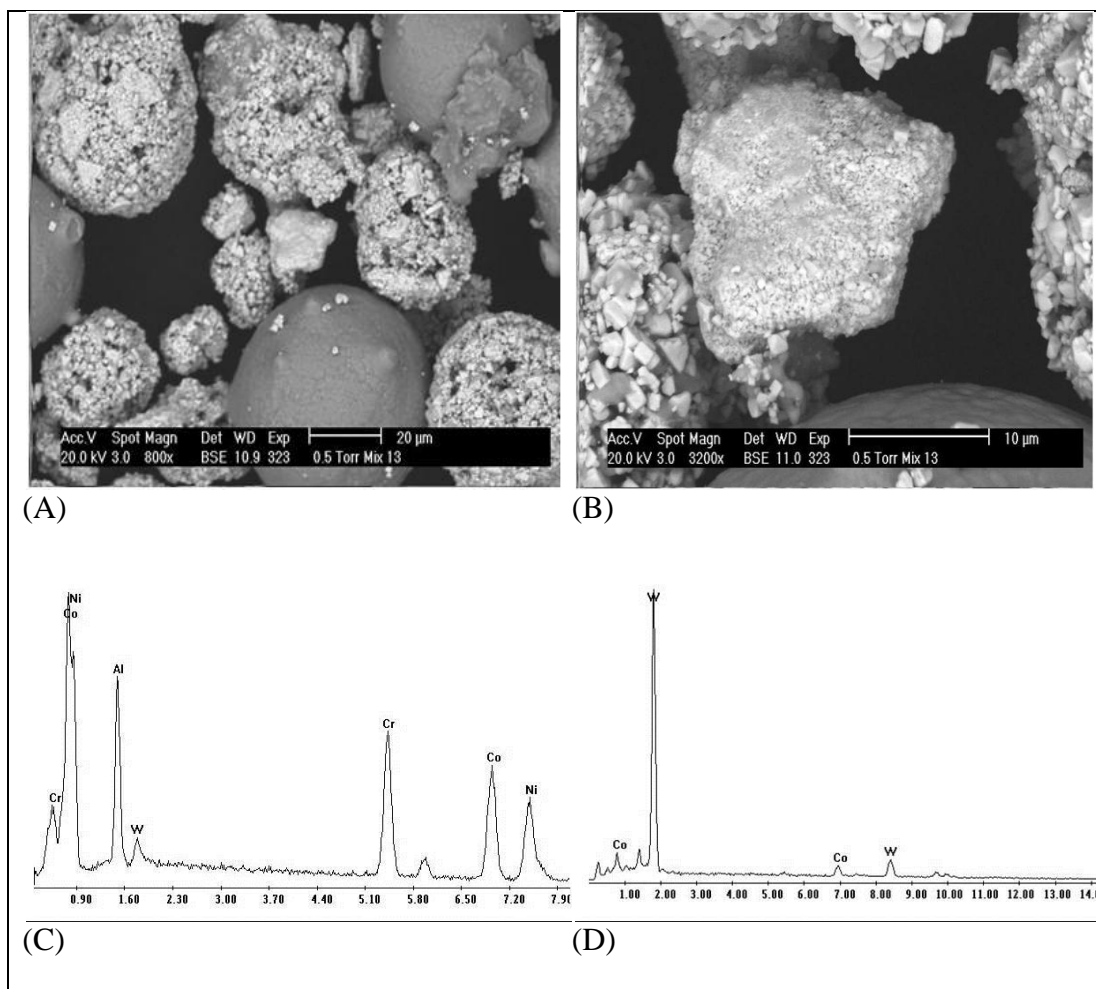


Figure 4.20, Mix No. 13: (A) ESEM backscattered electron (BSE) image at 800X showing heterogeneous mixing; (B) backscattered electron (BSE) image at 3200X showing irregular grains of coating powder (C) EDS X-ray spectrum of dark powder. It shows Ni, Co, Al, W, and Cr presence in the sample; (D) EDS X-ray spectrum of light powder. It shows W and other traces of elements presence in the sample.

MIX-14:

Figure 4.21 represents the result of the elemental analysis of powder MIX-14 (60% nano sized WC-12Co +40% micro sized AMDRY 995M) by the EDXRF. It clearly shows that the metallic powder consists of 65% by weight tungsten carbide

and 12 % of cobalt. Other elements such as chromium (11.4%), nickel (7.4%), and silicon (2.5%) were also detected in the powder.

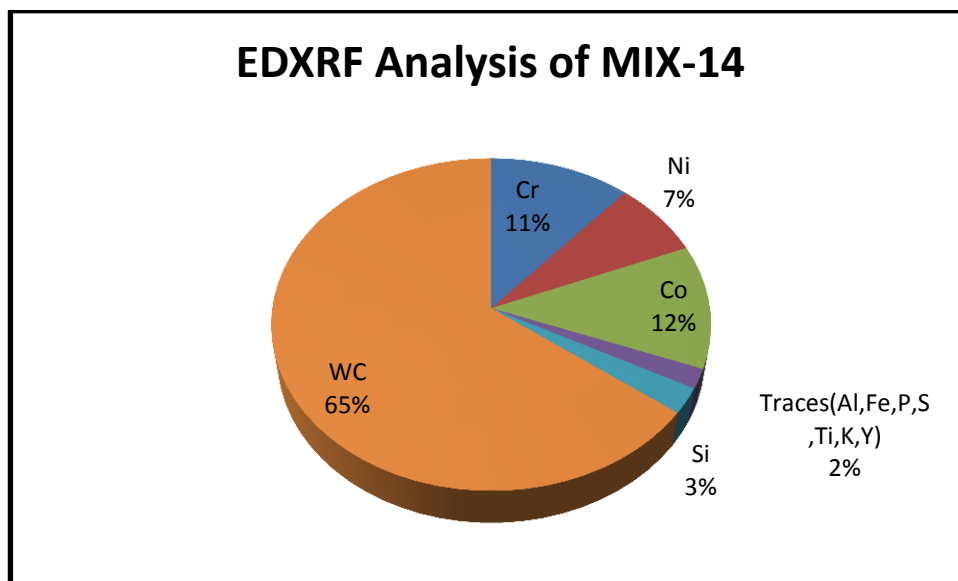


Figure 4.21, Energy dispersive X-ray fluorescence Spectrometry of Powder MIX-14 in wt. %

Similar to powder MIX-13, powder MIX-14 is consisting of chromium nickel- Cr_2Ni_3 , tungsten carbide WC and cobalt metal. Crystalline phases identified by X-Ray Diffraction are represented in Figure 4.22. The measurements of the powder MIX-14 particle size result in minimum size of particles (D10) equal to 16.052 μm , maximum size of particles (D90) equal to 360.585 μm , and an average particle diameter by mass equal to 37.68 μm (Figure 4.23) which is acceptable considering mix of powder particle size 50 - 500 nm (S7412) with -63 +45 μm (AMDRY 995M).

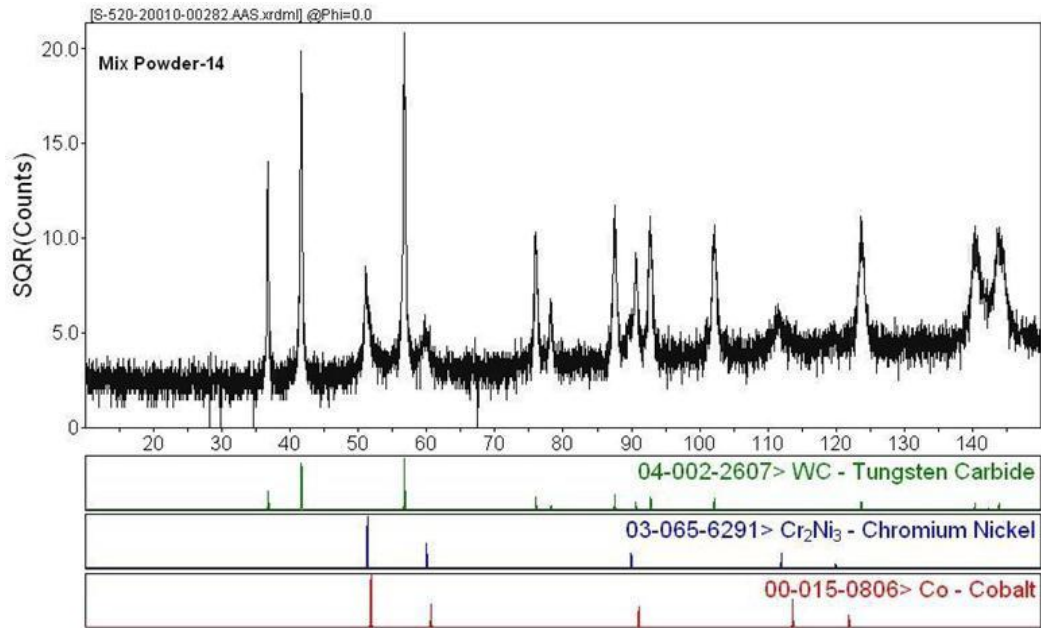


Figure 4.22, XRD Diffractiongram with Identified Compounds- Powder MIX-14

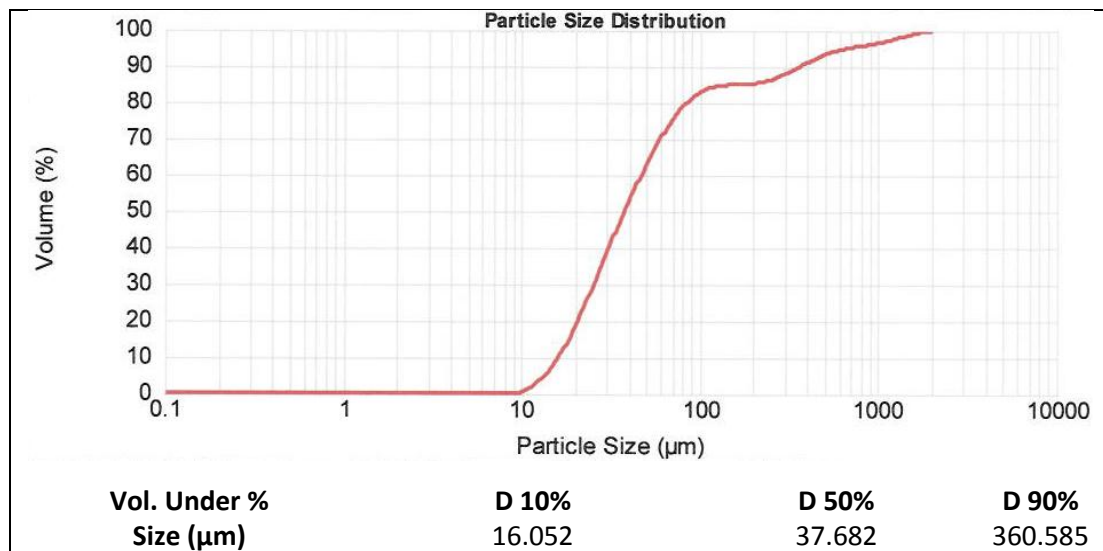


Figure 4.23, Particles Size Distribution of MIX-14.

The ESEM/EDS analyses of powder MIX-14 showed that the powder was composed of dark and light powder particles with a ratio of approximately 80 % to 20 % respectively. Figure 4.24 shows the ESEM BSE images taken at 800X and 1600X and EDS spectrum of dark and light powder MIX-14. The light particles were in the 3-75 μm size range, and reveal roughly 20% spherical and the rest were non-spherical in shapes (Figure 4.24 (A)). BSE image at 1600X of the light particles shows agglomerated loosely crystals of irregular shapes and are in 150 nm- 4 μm in size (Figure 4.244 (B)). The spherical (nonporous) dark particles were in the 30- 90 μm size range. The chemical composition of the spherical dark particles was 30 wt.% Co, 27 wt.% Ni, 17 wt.% Cr, 8 wt.% Al, 7 wt.% W, 6 wt.% C, and 4 wt.% O (Figure 4.24 (C)). The chemical composition of the light particles was 81 wt.% W, 9 wt.% C, 6 wt.% Co, 2 wt.% Cr, and 2 wt.% O (Figure 4.24 (D)).

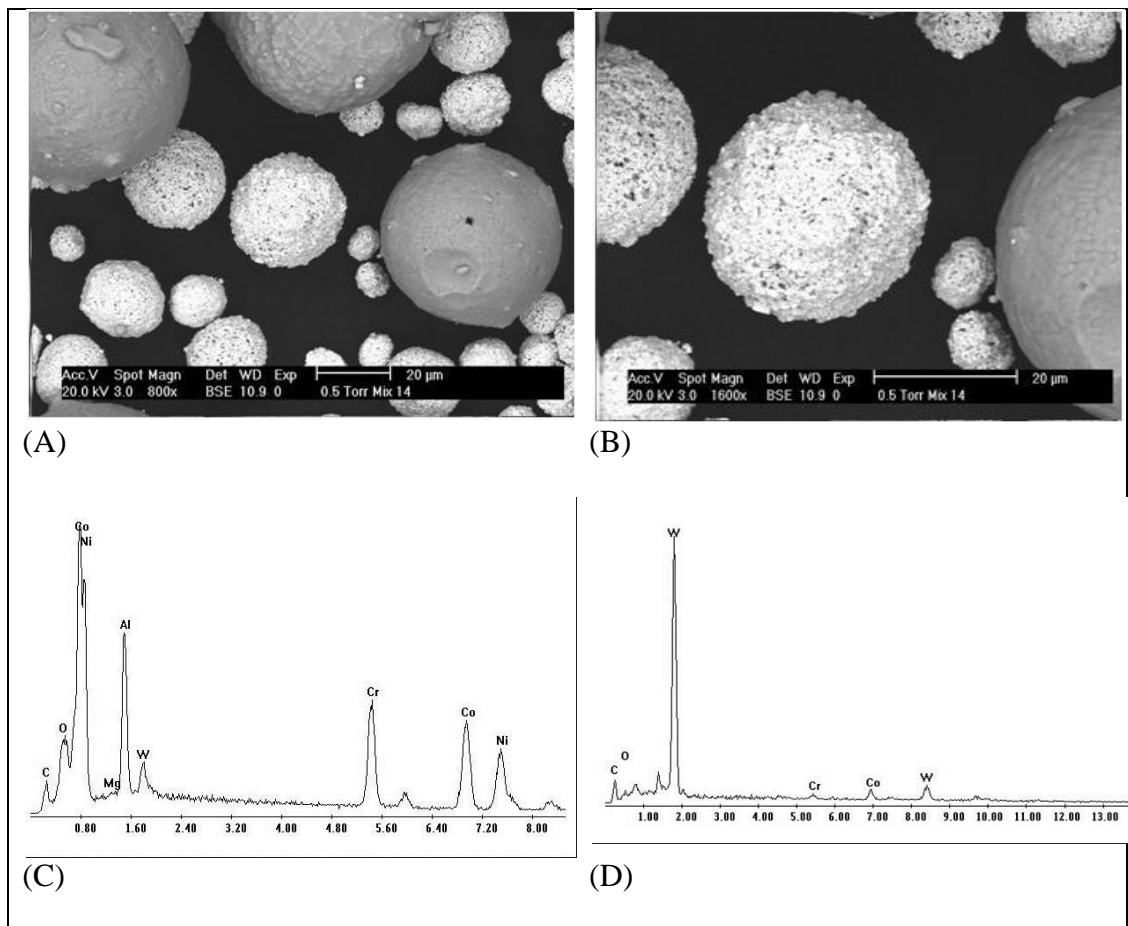


Figure 4.24, Mix No. 14: (A) ESEM backscattered electron (BSE) image at 800X showing heterogeneous mixing of the sample; (B) backscattered electron (BSE) image at 1600X showing coating powder (C) EDS X-ray spectrum of dark powder. It shows Ni, Co, Al, W, and Cr presence in the sample; (D) EDS X-ray spectrum of light powder. It shows W and other traces of elements presence in the sample.

4.2 POSSIBLE POWDER REACTIONS DURING THE HVOF AND PLASMA SPRAY

Based on the chemistry and behaviour of substances during high temperature reactions (e.g. thermal spray) the response of WC-Co powder particles to high temperatures is presented in Figures 4.25 and 4.26 as follows:

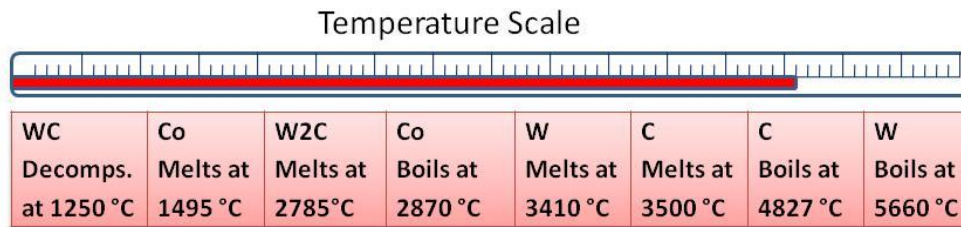


Figure 4.25, Sequence of events of WC-Co responses to high temperatures.

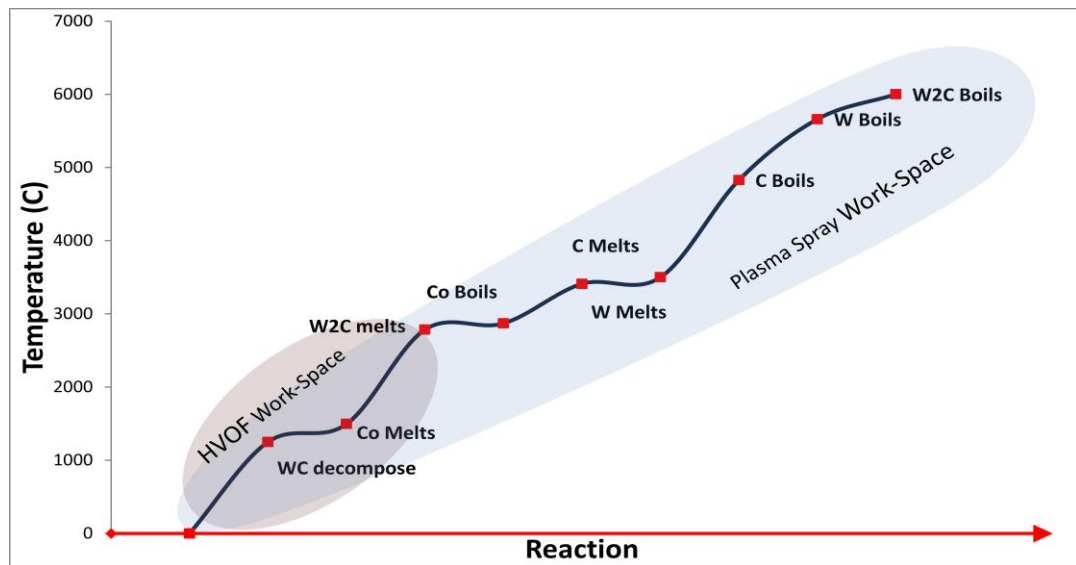


Figure 4.26, Thermal spray work space and WC-Co response.

During the process of thermal spray, the WC-Co particles are either completely or partially molten. At a temperature of 1250 °C, a portion of WC particle starts to decompose to less hard W₂C, W and C while Co starts to form the eutectic binder

phase at 1495°C. When the temperature increases, W_2C melts in the binder phase at 2785 °C in comparison to W melting point of 3410 °C [170–173]. Therefore, by reaching these temperatures, the cobalt completely reduces to a liquid phase and starts to evaporate leaving some free carbon, W, WC, and W_2C impeded in the cobalt matrix. W_2C is stable below 1250 °C [174], however, it can also be found in the coating when the material has been quenched rapidly even if it did not undergo high temperature decarburization [175].

From reactions mechanism above, the anticipated changes to sprayed coating materials in this study are; formation of an amorphous Co binder phase, dissolution of W and C in the Co; phase transformation, decarburization of WC to W_2C , and finally loss of Co and C due to evaporation or oxidation of the powders, and each of these will depend on the process used. Table 4.1 presents the percentage of W, C, and Co before and after reactions at selected top coating spots.

Table 4.1 Percentage of W, C, and Co before and after reactions.

Batch No.	W		C		Co	
	Starting Powder Wt%	Coating Wt%	Starting Powder Wt%	Coating Wt%	Starting Powder Wt%	Coating Wt%
1	79.3	75.22	5.2	10.4	14	10.7
2	83.7	73.07	5.5	15.87	11	8.73
3	57.6	44.42	3.8	5.96	14.3	24.25
4	51.5	50.57	3.4	9.86	15.7	18.63
11	79.3	78.9	5.2	12.3	14	4.97
12	83.7	83.16	5.5	9.41	11	4.93
13	67	54.4	4.4	13.46	11.2	12.26
14	60.8	41.05	4	8.73	12	18.98

4.2.1 Formation of an Amorphous Co Binder Phase

For a binary W-C system, pure WC in the absence of cobalt decomposes into a liquid phase and graphite above 2750 °C where decarburization may take a place at this high temperature. However, the W-C-Co phase diagram, where Co exists, shows WC dissolution can be occur at much lower temperatures than 2750 °C (almost at 1250°C) because the wettability of WC by Co binder is better than that for carbides [176]. This explains the importance of formation of the Co binder phase in order to force the reaction to take place in a lower temperature.

The ESEM analysis of the applied coatings shows the formation the Co binder phase (dark areas) where other coating particles were imbedded and cemented. The ESEM images may indicate that the cobalt binder phase in the plasma sprayed WC-Co coatings producing a lamellar structure whereas this may not be the case in the HVOF sprayed coatings. The cobalt binder phase microstructure in HVOF sprayed coatings may be closer to that of hard metal. In both cases, carbides particles are distributed and dispersed in the cobalt matrix (cemented) as shown by the chemical composition analysis, Figure 4.27.

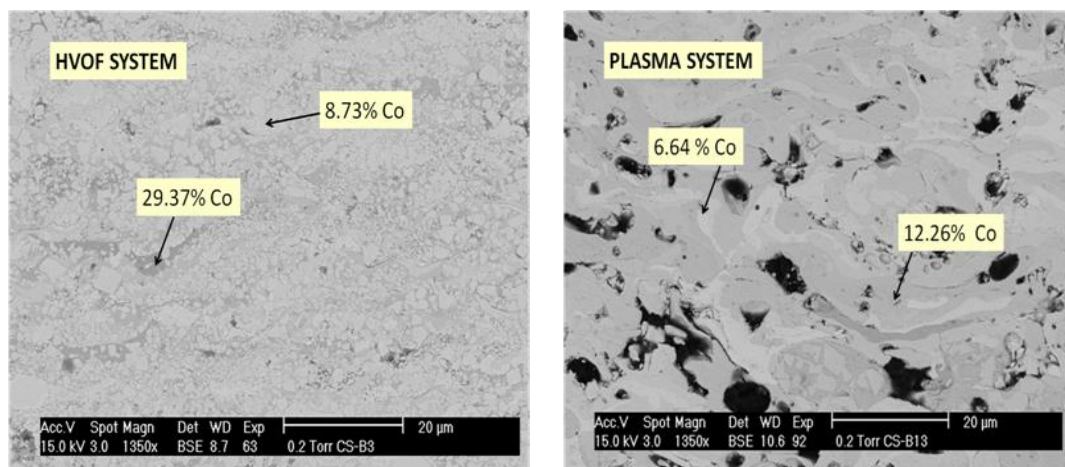


Figure 4.27, ESEM analysis of the applied coatings confirms the formation of the Co binder phase.

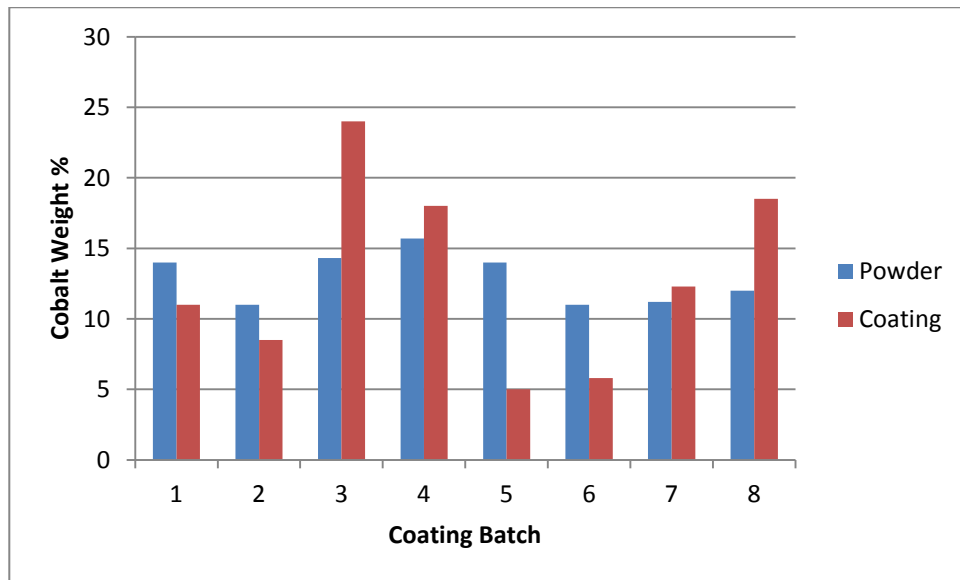


Figure 4.28, Presentation of cobalt both the starting powders and in the top coat layer, obtained from Table 4.1.

It can be concluded from Table 4.1 and Figure 4.28 above that cobalt increased from that found in the powder to that found at the top coating layer in Batch 3, 4, 13, and 14 which may conclude that AMDRY powder reduced the evaporation of the cobalt phase. Evaporation of cobalt was noticed in other coatings and to a greater percentage in plasma coating Batch 11 and 12 (due to high operating temperatures of plasma). The particle size shows no effect in the formation of an amorphous Co binder phase. One important note is that values presented in Table 4.1 are indications of phase transformation that occurred during the powder spray process. The percentage of each element is therefore highly depending on the percentage of the other elements. For example, evaporation of cobalt resulted in less Co percentage in the produced coating; this percentage would change the percentage of other elements.

4.2.2 Dissolution of W and C in the Co

Since WC-based powders contain Co, the dissolution process should be taken into consideration during spraying process. At a temperature of 1495°C, the Co starts molten and WC will begin to rapidly dissolve. In this case and at this temperature, approximately 30 wt. % W and 2.5 wt. % C can dissolve in the binder phase as indicated in the literature [92]. More WC will dissolve as the particle's temperature increases. When an equilibrium state is reached, the binder phase can contain more than 50 wt.% W and 3.5 wt.% C [92].

Spot analysis on the coatings revealed that dissolution of W and C in the Co phase occurred at different ratios. The ratio increased with increasing temperature. More dissolution occurred in the plasma thermal spray than the HVOF system as shown in Figure 4.29, which was expected due to the higher operating temperature of the plasma plume.

If the temperature is increased and a WC decarburization reaction exists, tungsten semicarbide W_2C may also be dissolved in the cobalt binder [149] or be present on the surface of WC particles [139, 142]. Karimi et al. [177] found that almost 30 to 40 wt.% carbides in the cobalt matrix existed as solids and in the form of ternary $CO_xW_yC_z$ carbides [178].

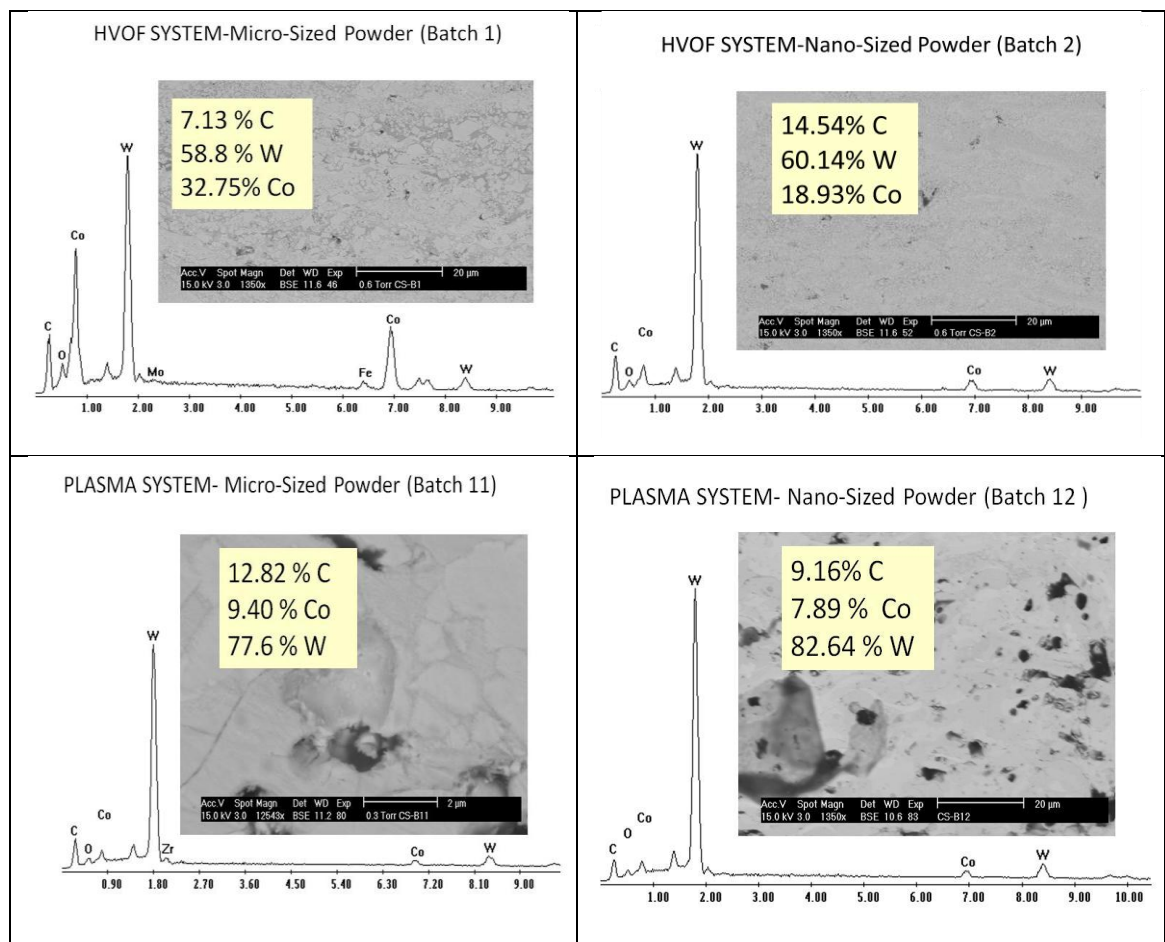


Figure 4.29, Dissolution of W and C in the Co phase post thermal spray.

During the dissolution, carbide particles usually tend to be more or less discrete in the matrix. It can remain dissolved in the cobalt matrix after solidification as confirmed by XRD analysis of the coatings [149]. This may be due to the high cobalt contents in the used starting powder and due to the loss of WC by dissolution in the cobalt matrix during thermal spraying, as discussed earlier [174].

Dissolution of the WC phase in the Co produces a more wear-resistant matrix phase [141]. However the dissolution of the carbide in the cobalt matrix may not be always beneficial. Such a reaction will result in increased levels of other species (e.g., W_2C) that can be detrimental to the wear resistance of the coating. WC contained 6.13% C and had a microhardness of about 2400 kg/mm^2 , while W_2C

contained 3.16% C and has a microhardness of about 3000 kg/mm², but was more brittle than WC [135]. This counterbalances any improvements resulting from the increases in the cohesive strength of the matrix hardening at higher temperatures.

Previous investigations of similar coatings revealed that an increase in cobalt content in the starting powder led to higher degree of dissolution of WC, a reduction in hardness, and a slight increase in toughness [179]. The hard WC particles form the major wear-resistant, while the cobalt binder provides toughness and support [180].

Properties such as the hardness are influenced mainly by the WC particle size and volume fraction and also by varying the carbide and binder phase composition as will be shown in the hardness test section of this study (section 4.3.8).

4.2.3 Phase Transformation

During the melting of WC particles, these particles can be easily transformed to other phases as a result of high-temperature oxidizing/decarburizing conditions generated during thermal spraying. For a given powder, the determination of different phases and their relative proportions in a coating depends on spray parameters of the spray system and on the heat and mass transfer between powder particles [147]. Approximately 75 % of phase transformation of WC during spraying of WC–Co powders occurred during the in-flight stage [181]. The size and distribution of spray particles influence the heating degree and oxidation of in-flight particles and thus the decarburization [182]. Figure 4.30 shows the phase transformation diagram of WC–Co at 1425 °C [183].

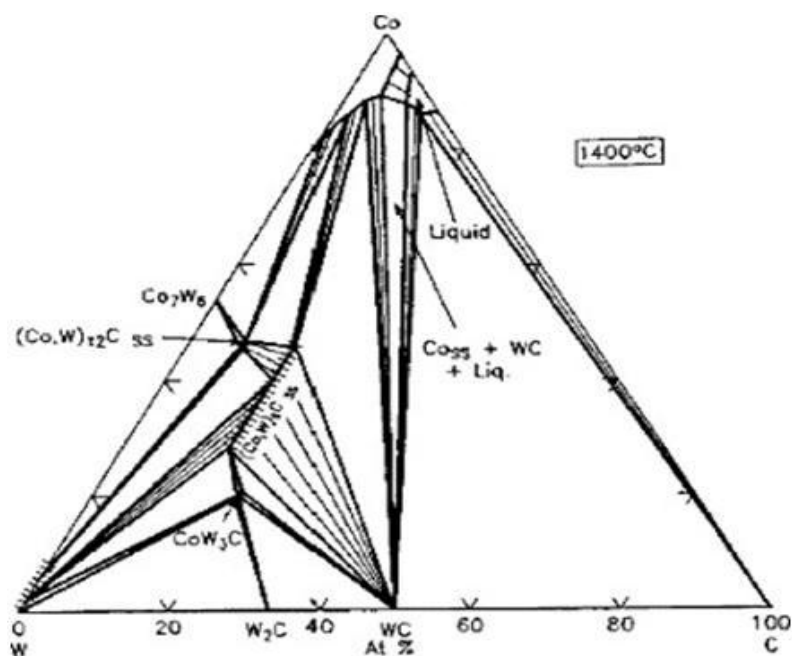


Figure 4.30, Phase transformation diagram of WC–Co at 1425 °C [183].

In this research, many secondary phases were found when the coatings were produced (Table 4.2). The XRD of the coating shows peaks indexed to tungsten semicarbide (W_2C). These peaks were found in all eight groups of coatings. However, the peaks indexed to WC were only found in the HVOF coatings (Batches 1, 2, 3, and 4) and Batch 14 of the plasma sprayed coating. The peaks indexed to WC in the HVOF coatings are almost at the same intensity of W_2C . From XRD patterns, there was no peak indexed to elemental W (in the HVOF produced coatings). The peak indexed to elemental W was found in 3 out of 4 coating groups in the plasma sprayed coating. This confirms the high temperature of plasma sprayed system decarburized the W_2C to W, as will be discussed in more detail in the decarburization study of the powders.

In addition to these peaks, $W_2(C,O)$ and WCo phases were observed in some coatings as shown in Table 4.2. The WCo resulted from the dissolution reaction

between the WC and the cobalt binder metal during spraying. XRD patterns showed more phases in the plasma produced coatings than the HVOF coatings because the WC-Co powder tends to undergo a combination of decarburization, oxidation, and reduction reactions in plasma spraying more than the HVOF spraying [146, 177]. It was also noticed that the HVOF coating phases were similar to the starting powder. This was primarily due to the lower temperatures attained in the HVOF process [145].

Table 4.2, Phase transformations during reactions.

Coatings Batch	Starting Powder			Coating						
	Tungsten Carbide	Cobalt	Chromium Nickel	Tungsten Carbide	Tungsten Semicarbide	Tungsten Oxide Carbide	Tungsten	Tungsten Cobalt	Chromium Nickel	
	WC	Co	Cr ₂ Ni ₃	WC	W ₂ C	W ₂ (C,O)	W	WCo	Cr ₂ Ni ₃	
1	√	√		√	√					HVOF
2	√	√		√	√					
3	√	√	√	√	√			√	√	
4	√	√	√	√	√				√	
11	√	√			√	√	√			PLASM
12	√	√			√	√	√			
13	√	√	√		√	√	√		√	
14	√	√	√	√	√				√	

Although WC can decompose to W₂C, even to metallic tungsten, the decomposition products can also dissolve into metallic C to form more complex carbide, such as Co_xW_yC, if the operating conditions were not optimized and controlled. Additional peak such as Cr₂Ni₃ were determined in the coatings containing AMDRY powders as the starting feedstock. The Cr₂Ni₃ peaks were observed in both starting powders and produced coatings.

Chemical transformations can produce brittle phases that reduce the toughness and wear resistance [170]. Numerous authors [174-180, 184] show that, the decarburization and dissolution of WC in the coatings during the spraying process

causing the formation of amorphous or nanocrystalline phase, and were considered to affect the mechanical properties of the binder phase. The dissolution reaction between the WC and the cobalt binder during spraying process, resulted in the formation of hard and brittle phases such as W_2C and tungsten. It has been shown that W_2C can remain stable below 1250 °C [174] when quenched rapidly by subsidiary cooling air, as it does not undergo high temperature decarburization. [175, 185, 186]

The binder in thermally sprayed WC-Co coatings was mainly amorphous due to rapid post-spraying solidification. Evidence of partial recrystallization of the amorphous binder phase by means of nucleation of crystallites at the WC/Co interface have been documented [149]. These phases can also crystallize from the melt during solidification [187,188], sometimes in the form of very fine (nano) crystallites. Many researchers attributed variations in the properties of thermally sprayed WC-Co to the phase changes that occur in the material during spraying [153, 185, 188- 190].

Generally, the extent of the WC transformation depends on the starting powder type (size, morphology, carbide size), the type of spray process, the amount of oxygen in the environment, and the spray parameters [149, 191, 192]. The higher the enthalpy of the spray stream, the more transformation reactions can be predicted, because more thermal energy is available to drive the process [192, 193].

In both of the HVOF and Plasma systems used in this research, tungsten was combined with carbon to form WC and W_2C during the cooling process of the substrate [171] as shown by the X-ray powder diffraction (XRD), Figures (4.31-4.38). The XRD method was used to determine the composition of the surface coating layer. In all of the coatings produced, the coating composition showed two forms tungsten semicarbide- W_2C and tungsten carbide-WC. The proportions of W_2C and WC in the coatings depended on the coating method used.

The identification of the crystalline phases was achieved using X-Pert HighScore Plus program. The XRD analysis confirmed the existence of the Co binder phase in all types of coatings. Some carbides were found in the matrix for the plasma coatings. They remain dissolved in the cobalt matrix after the solidification process. $W_2(C,O)$ and WCo peak indexes were observed in most plasma coatings. The XRD patterns showed more phases in the plasma coatings than in the HVOF ones, because the WC-Co powder tended to undergo a combination of decarburization, oxidation, and reduction reactions in plasma spraying more than the HVOF spraying. Additional peaks such as Cr_2Ni_3 were found in coatings containing the AMDRY powders in the starting feedstock. The Cr_2Ni_3 peaks were observed in both starting powders and produced coatings. The XRD Diffractograms of the coatings are shown in Figures (4.31-4.38) with reference patterns of identified compounds given to support the finding in Table 4.2. Some Diffractograms appear amorphous but it resulted from backscattered electron.

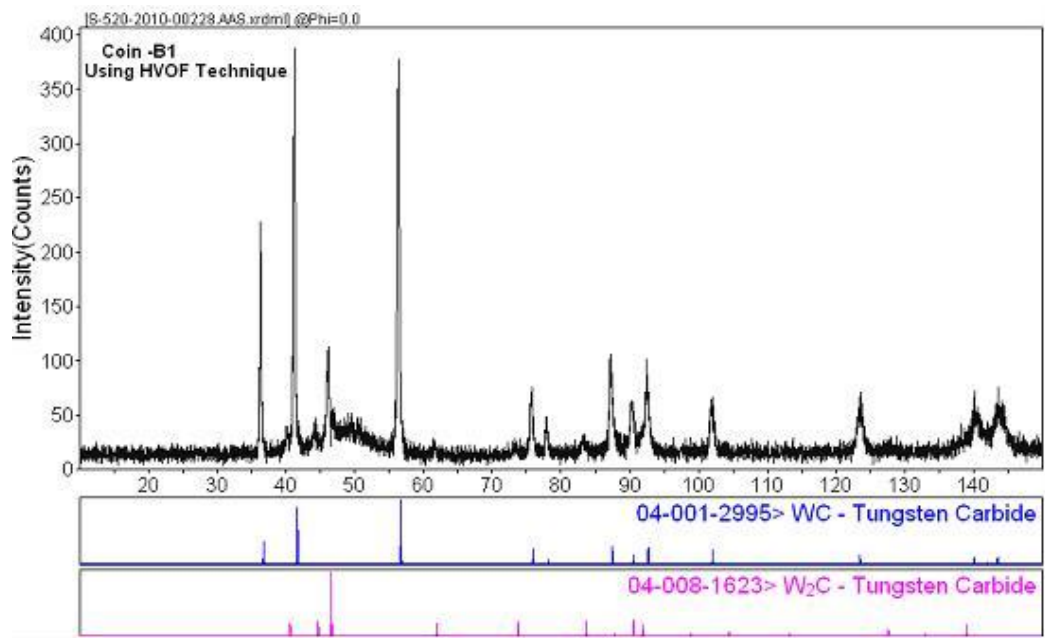


Figure 4.31, XRD Diffractogram with Identified Compounds of Coating of Batch 1.

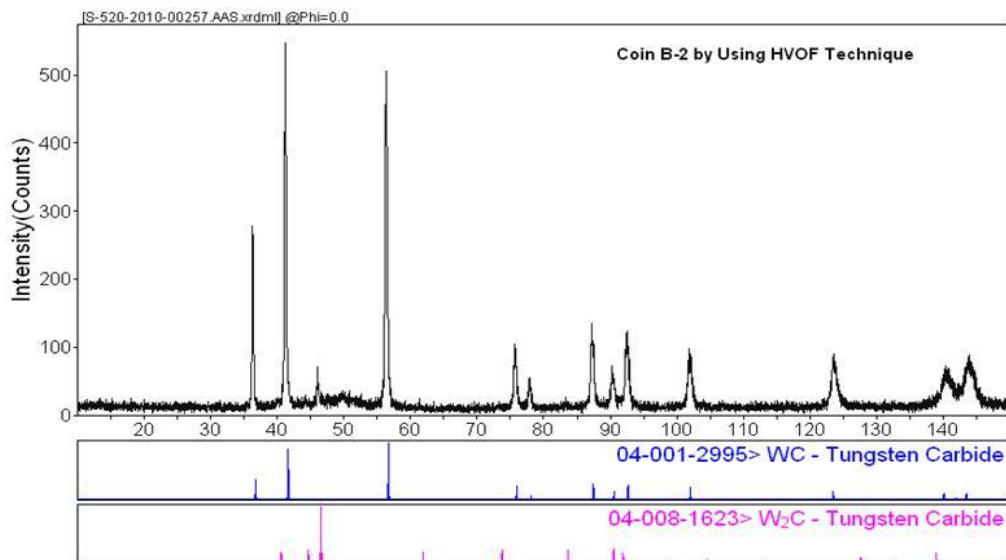


Figure 4.32, XRD Diffractogram with Identified Compounds of Batch 2 Coating.

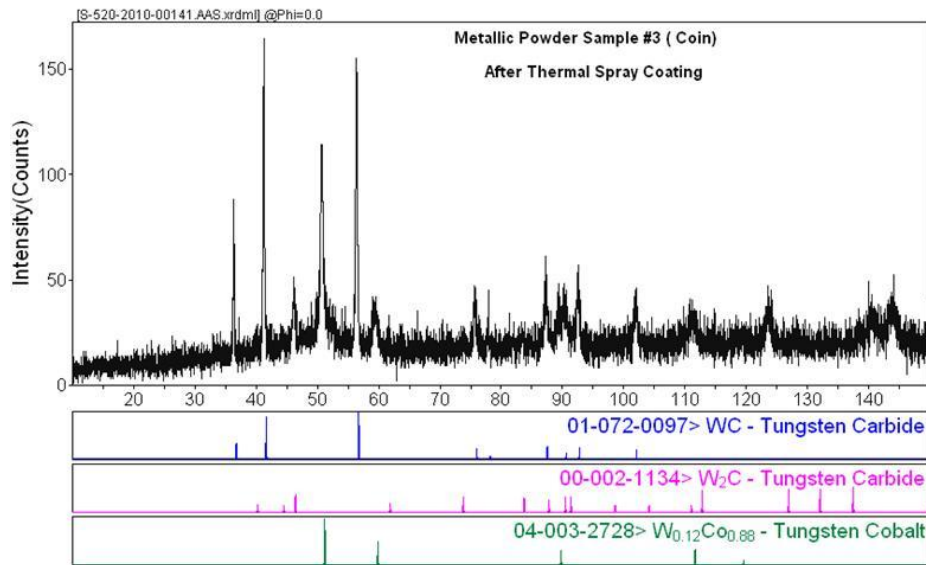


Figure 4.33, XRD Diffractogram with Identified Compounds of Batch 3 Coating.

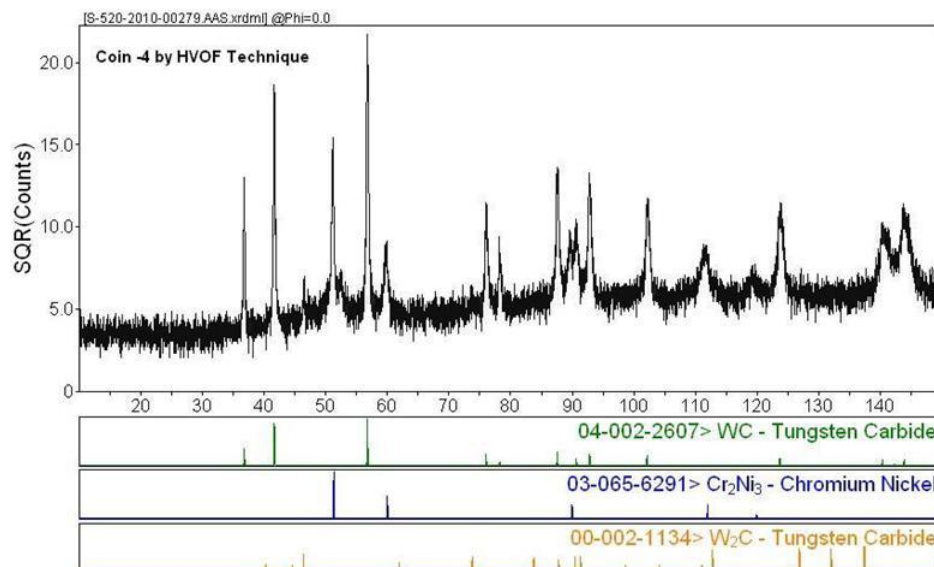


Figure 4.34, XRD Diffractogram with Identified Compounds of Batch 4 Coating.

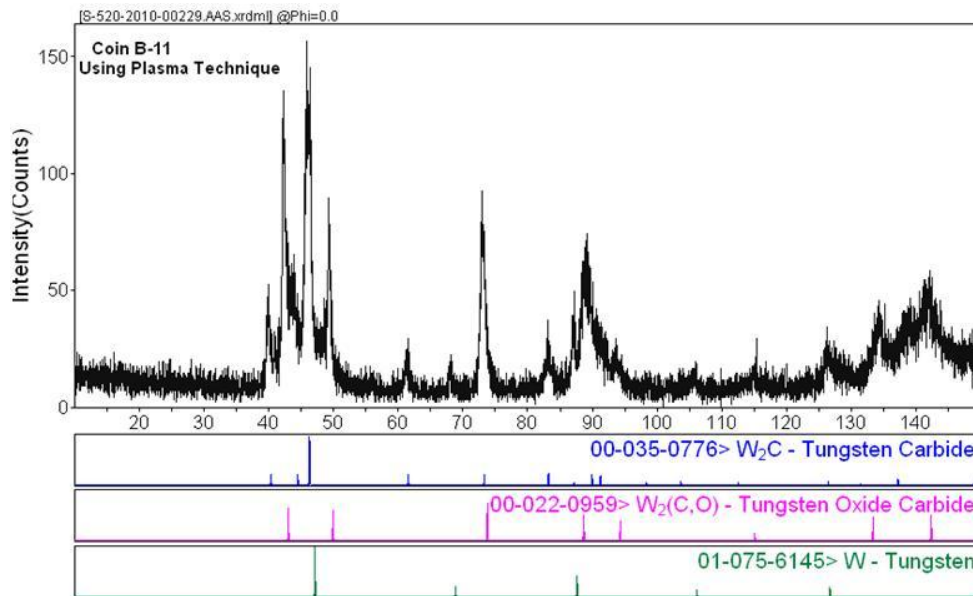


Figure 4.35, XRD Diffractogram with Identified Compounds of Batch 11 Coating.

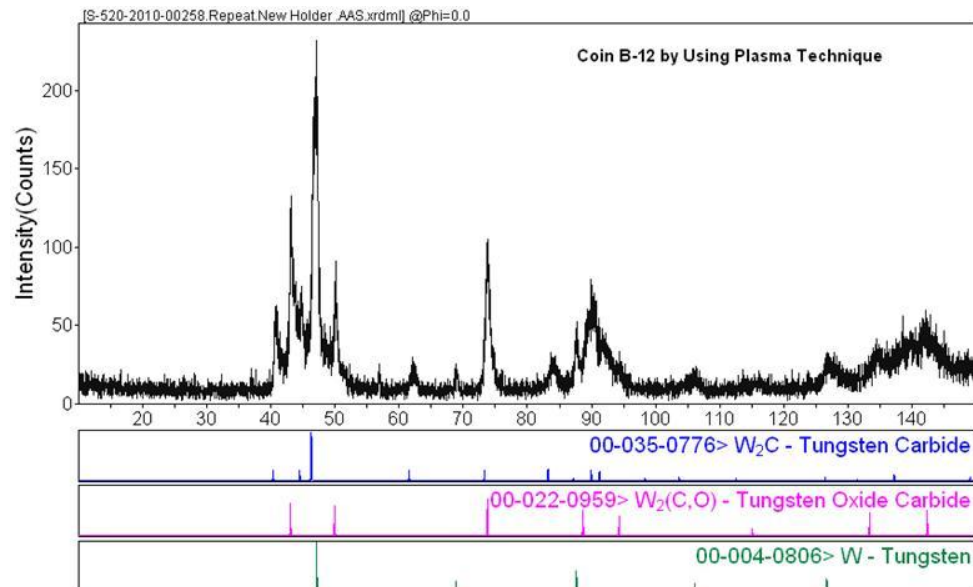


Figure 3.36, XRD Diffractogram with Identified Compounds of Batch 12 Coating.

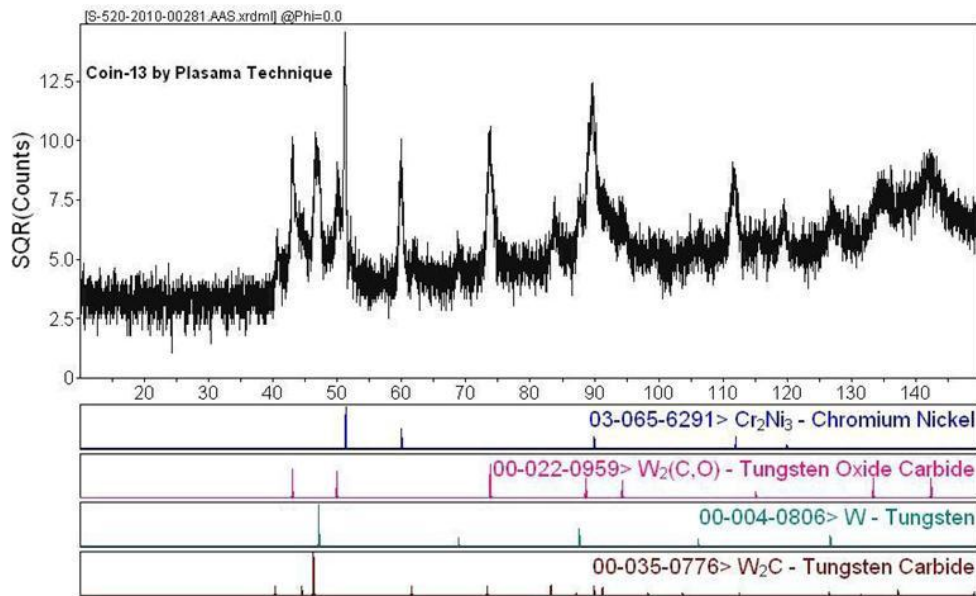


Figure 4.37, XRD Diffractiongram with Identified Compounds of Batch 13 Coating.

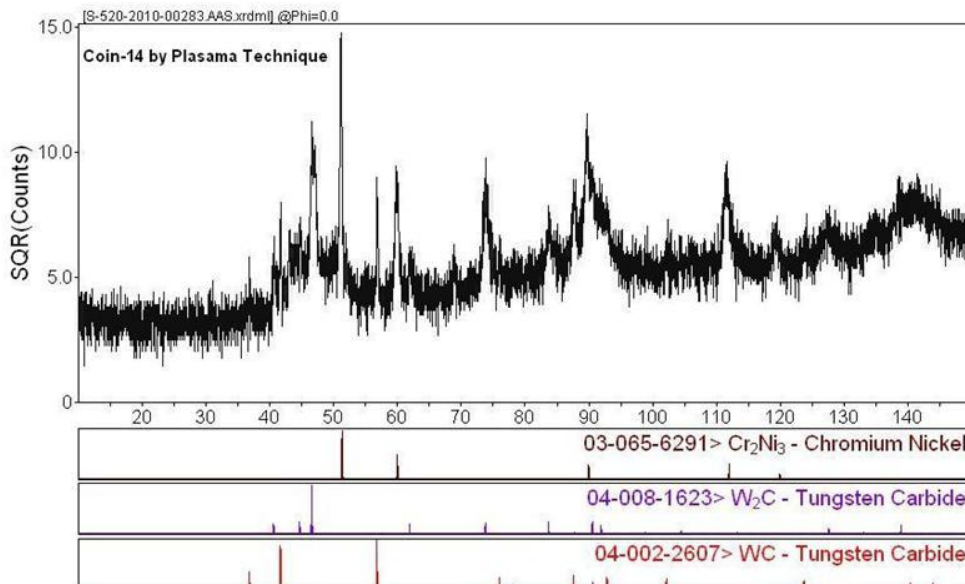


Figure 4.38, XRD Diffractiongram with Identified Compounds of Batch 14 Coating.

In some cases the flame temperature in the HVOF thermal spray system may not have been sufficient to decompose WC directly, but the decomposition occurred throughout the reaction of WC with the cobalt binder instead [176]. It should be noted that a portion of the WC phase would remain solid during the spraying process during HVOF deposition. It is only a fraction of materials that melts [141].

During melting, heat transfer to the internal region of a particle may result in uniform melting and the production of softer particles that are easily incorporated into the coating; whereas, less uniform heat transfer will present harder particles that tend to rebound off the substrate surface. Therefore, it is clear from the foregoing statement that the importance to minimize the decomposition of WC, lies in the optimizing of the process parameters [194].

In plasma spraying, the higher the enthalpy of the plasma gas, the more thermal energy that is available which results in more WC decarburization and reaction with the binder phase. In HVOF spraying, the higher the oxygen-to-fuel ratio or the enthalpy of HVOF jets the greater loss of WC due to decarburization [192].

Thus, an increase in the gas flow in the plasma system usually increases the loss of WC. The use of an Ar or Ar-He plasma usually results in less decarburization than the use of an Ar-H₂ plasma as shown in different studies [188, 192,193].

Likewise in HVOF spraying, it has been approved by Korpiola et al. [193] that less WC is retained in the coatings when a higher flame temperature or greater standoff distance has been used. Therefore, increasing the spray jet energy and/or decreasing its velocity will extend the decarburization of the WC [149].

It has been reported that nano-WC-Co powder experiences more decarburization during HVOF spray than micro-WC-Co powder [195]. The situation is more complicated in the plasma spray due to the high-temperature vaporization of Co

and C. The type and morphology of the nanostructured powder influence its melting characteristics and reaction kinetics. Heterogeneous melting and localized superheating of the high-surface-area powder can be considered as a controlling factor in decarburization.

In a practical way, decarburization can be reduced by controlling the spray parameters carefully. Optimized spray distance limits the contact of the molten WC-Co particles with oxygen. Also, the increase in the gas jet velocity decreases the time available for the reactions to occur (shorter residence time) [193].

The results obtained from the particle size distribution measurements of the starting powder may be used as an indicator of dissolution rate as well as powder decarburization. High surface to volume ratio of the sprayed powder may lead to more decarburization and formation of W_2C as presented in Table 4.3.

Table 4.3, Powders particle size distribution measurements.

Coatings Batch	Specific Surface Area m^2/g	Surface Weighted Mean μm	Volume Weighted Mean μm	Average Particle Diameter by Mass μm	Surface to Volume ratio
1	0.181	33.074	80.841	38.712	1 : 2.4
2	0.186	32.226	202.714	33.143	1 : 6.3
3	0.177	33.918	63.786	35.945	1 : 1.9
4	0.215	27.871	58.775	28.077	1 : 2.1
11	0.181	33.074	80.841	38.712	1 : 2.4
12	0.186	32.226	202.714	33.143	1 : 6.3
13	0.166	36.210	46.720	43.384	1 : 1.3
14	0.184	32.544	131.072	37.682	1 : 4.0

From Table 4.2 above, the powders used to produce coatings Batch 2 and Batch 12 (nano-sized WC-Co) tend to decarburize more and form W_2C than any other mix of powders. While powders used for coatings Batch 3 and Batch 13 (Micro-sized

WC-Co + AMDRY) tend to have less decarburization and formation of W_2C than other powders. On the other hand, the dissolution rate of nano-sized powders was found to be greater than the micro-sized powders as indicated by the volume/surface weighted mean.

RESULTS AND DISCUSSION- COATINGS CHARACTERIZATION

5.1 COATING STRUCTURE

5.1.1 Coating Formation and Build Up

Macroscopic properties of the coating such as hardness, porosity, and surface roughness are determined by its microstructure formation. Attention must be paid to the mechanism of droplet impact on the substrate and solidification conditions. Fast solidification may result in splashing and breakup of the impacting particles. Under cooling may result in less degree of spreading [196]. In some systems, surrounding gas can result in a trap of a bubble under the impacting drop.

In the HVOF system, the powder particles were melted (totally or partially) and then projected to the substrate. Impacting particles (splats) would be in the form of spheres. When splats hit the substrate, they may create lamellar, pancake, or flower shape deposits. The shape of these splats plays a critical role in determining the physical properties of the coating. Splat shapes depend on many factors such as size, velocity, and the degree of melting and solidification of the impacting particles, as well as the topology and physical properties of the substrate [63].

Flower structure gives high surface roughness while the pancake structure gives low roughness so get better adhesion. Figure 5.1 shows the pancake morphology of an obtained HVOF coating and its builds up to the required thickness.

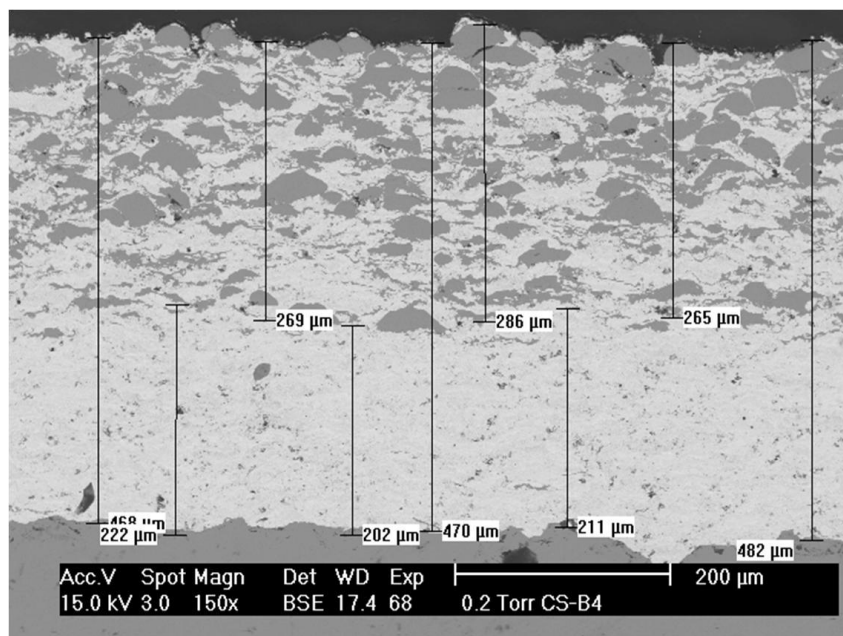


Figure 5.1, Batch 4 coating showing a pancake morphology.

In the Plasma-spray system, a stream of molten, semi-molten, or even some solid particles strike the surface of the substrate where they undergo rapid deformation and solidification to form disc-like splats (thin discs, discs with fingers) [196].

Surrounding gases results from decarburization of the powder (CO and CO_2) or from the plasma gas can result in trap of a bubble under the droplet. Entrapped gases resulted in generation of small voids under the splat which affect the coating porosity. The coating is the buildup of many splats that strike the substrate. After the solidification process of each coating pass, layers of different materials comprise of solidified droplets forming the microstructure of the coating and the buildup of the thickness [63]. Figure 5.2 shows the disc-like morphology that

formed lamellar structured coating (layers of different materials) of the applied plasma spray coatings. It also shows the small voids (porosity) in the coatings.

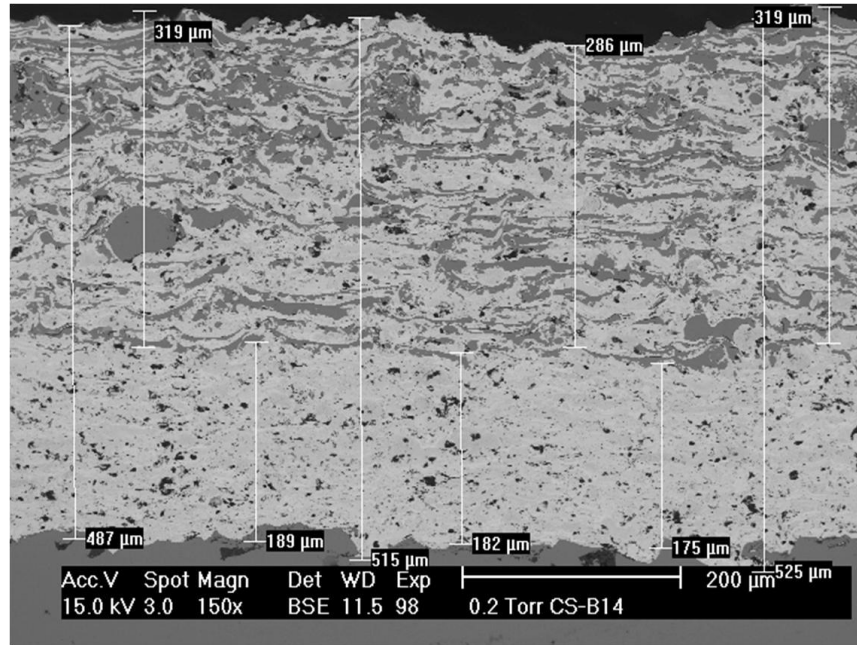


Figure 5.2, Batch 14 coating shows layers of different lamellas.

It is clearly shown from Figures 5.1 and 5.2 that a uniform coating thickness is obtained by moving the thermal spray gun at constant speed along the axis of the sample holder as previously described in the coating procedures part of this work.

5.1.2 Coating Roughness Measurements

Figure 5.3 and Table 5.1 present the coating roughness measurements obtained in this research.

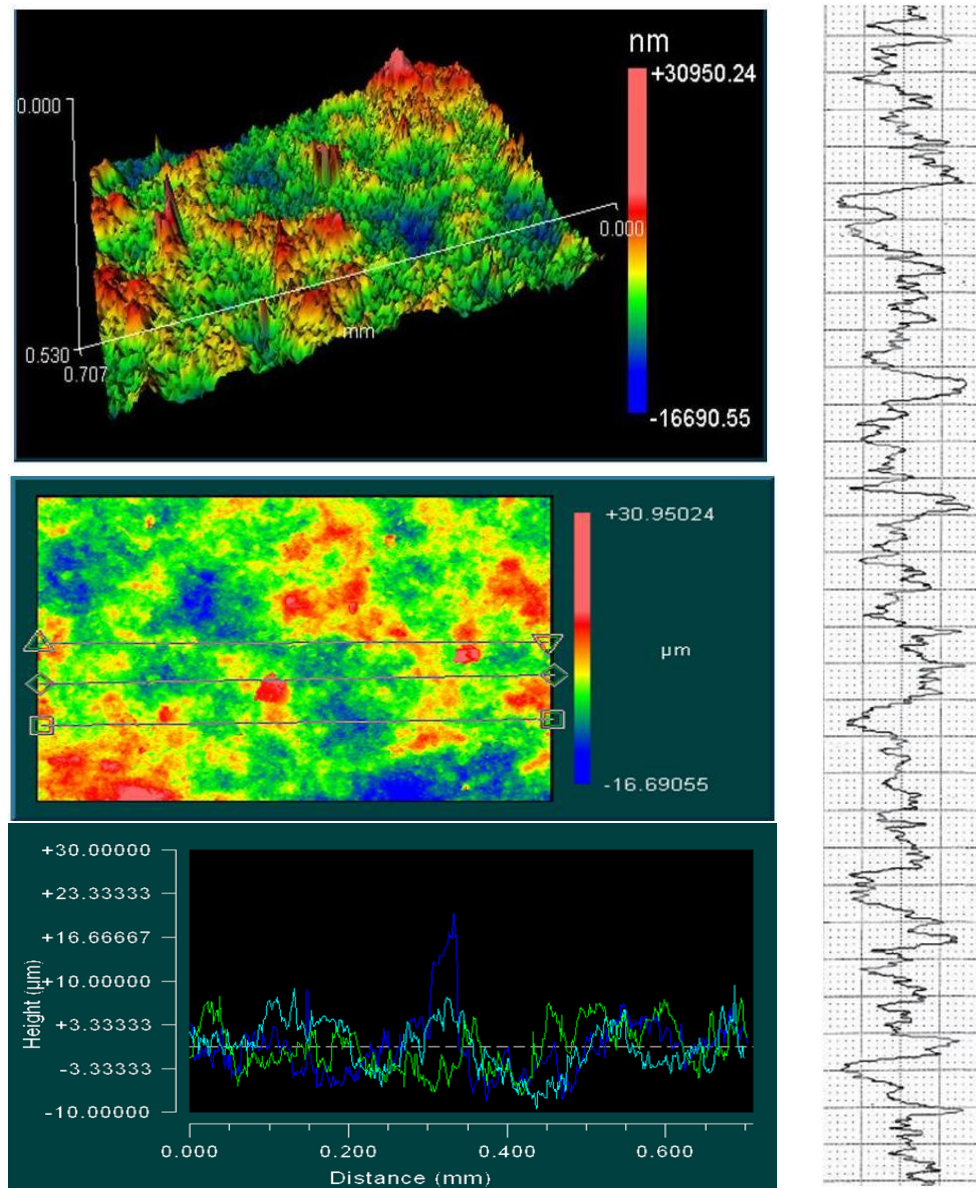


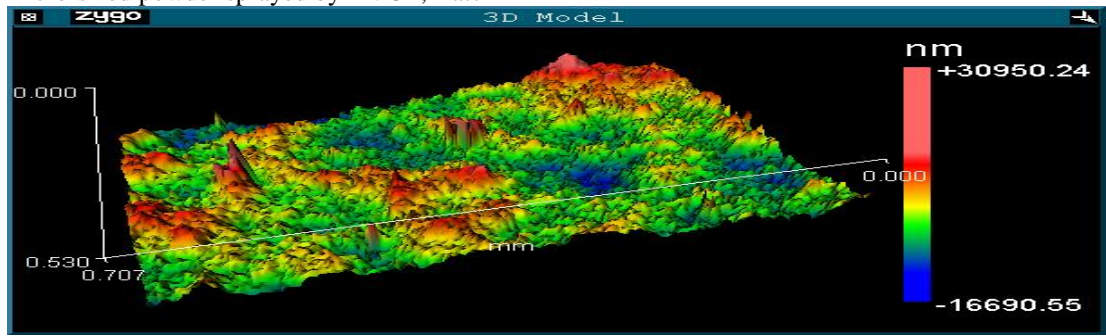
Figure 5.3, Coating roughness measurements for Batch 1 sprayed by the HVOF process.

Table 5.1, Coating roughness measurements.

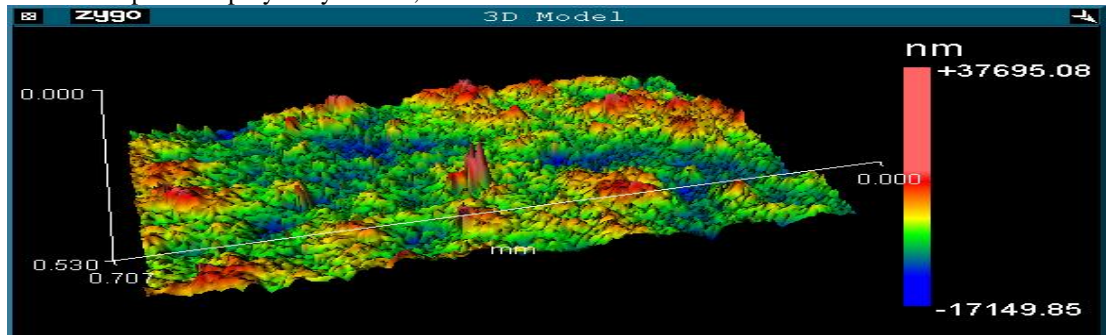
Coating Batch	Coating System	Sprayed powder	Mean Ra μm	Max. PV μm	Standard Deviation
1	HVOF	Micro	3.137	20.832	0.135
2	HVOF	Nano	4.344	25.858	0.661
3	HVOF	Micro+AMDRY	6.138	36.321	0.394
4	HVOF	Nano+AMDRY	7.83	48.269	0.421
11	PLASMA	Micro	5.502	32.911	1.722
12	PLASMA	Nano	4.607	26.908	0.178
13	PLASMA	Micro+AMDRY	6.729	40.74	2.208
14	PLASMA	Nano+AMDRY	8.831	45.597	1.758

The Ra deviation from the mean values revealed that surface roughness of HVOF coatings were lower than the plasma sprayed coatings except for Batch 12, as HVOF produces denser coating which lowers roughness of the surface. From the data collected from the surface roughness measurement, it was concluded that the use of nano-sized powders in the plasma spray system helped to lower the coating roughness (Mean Ra decreased from 5.5 μm to 4.6 μm) however increased the roughness when sprayed by HVOF system (Mean Ra increased from 3.1 μm to 4.3 μm). This is attributed to the total melting of mixed powder in plasma spray system. The addition of AMDRY to the original WC-Co powders increased the surface roughness of the coatings. Figure 5.4 presents the surface roughness profiler of the topographical features of the coatings that resulted when spraying different metallic powders sizes in this research.

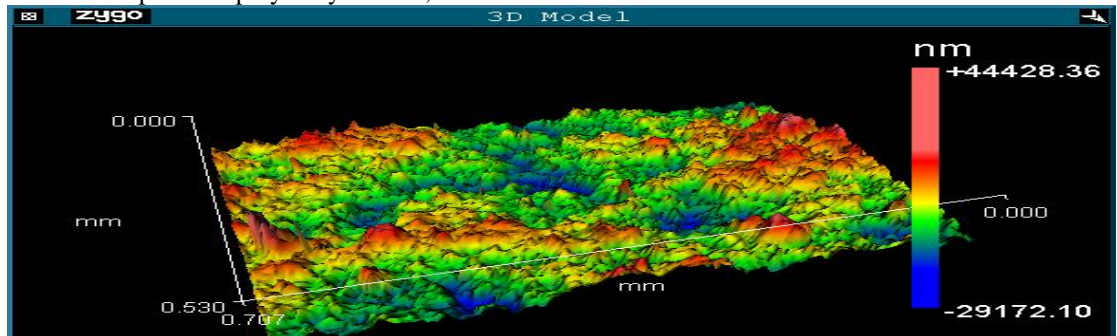
Micro-sized powder sprayed by HVOF, Batch 1



Nano-sized powder sprayed by HVOF, Batch 2



Micro-sized powder sprayed by Plasma, Batch 11



Nano-sized powder sprayed by Plasma, Batch 12

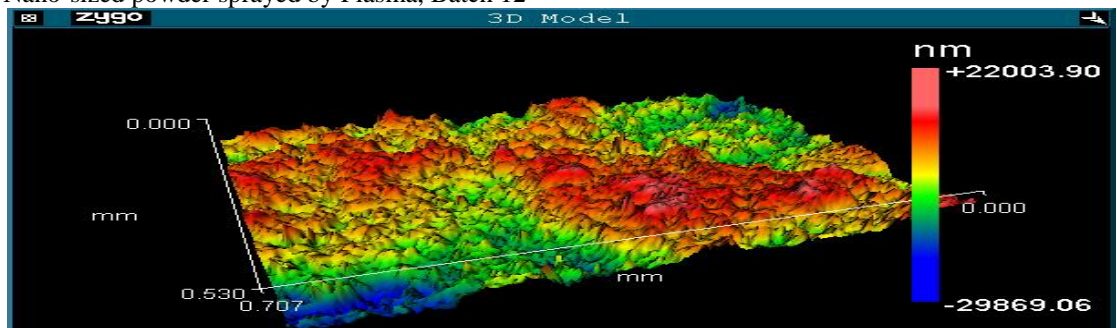


Figure 5.4, Topographical features of the coatings results from spraying different metallic powders sizes show peaks and valleys.

Kanouff et al. [159] demonstrated that the substrate surface roughness had very little effect on the coating roughness for coating thicknesses greater than 100 μm . However the waviness of the thermal spray coatings can be compared to substrate surface waviness; as illustrated schematically in Figures 5.5- 5.7. HVOF coating surface had more peaks than valleys, in contrast plasma produced coatings had more valleys than peaks. Valleys may act as confined places for corrosive particles to penetrate via coating layers in the presence of electrolyte. Figures 5.7 shows that Batch 12 has low mean deviation which confirms the value obtained in Table 5.1 (0.178) thus smoother coating resulted.

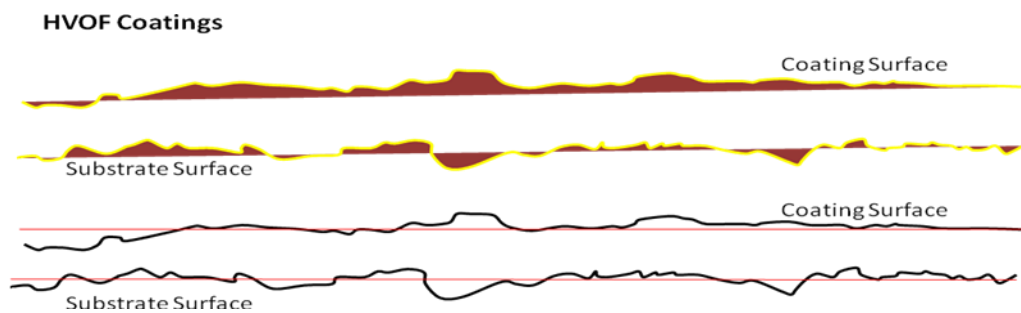


Figure 5.5, Example of waviness of the thermal spray coatings produced by HVOF, Batch 3.

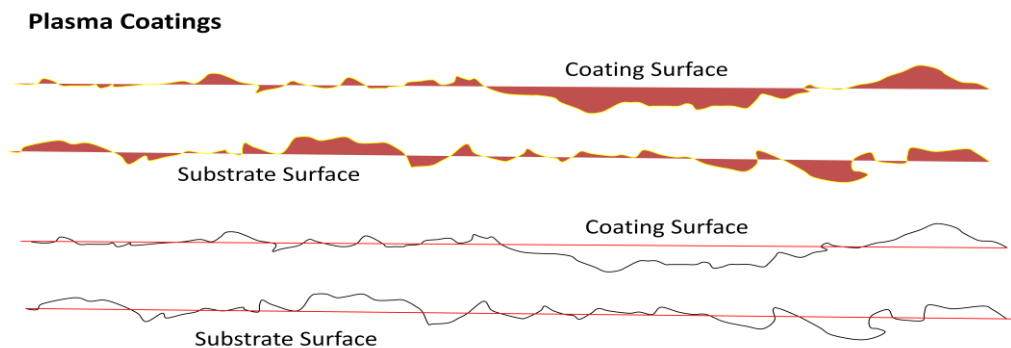


Figure 5.6, Example of waviness of the thermal spray coatings produced by Plasma system, Batch 14.

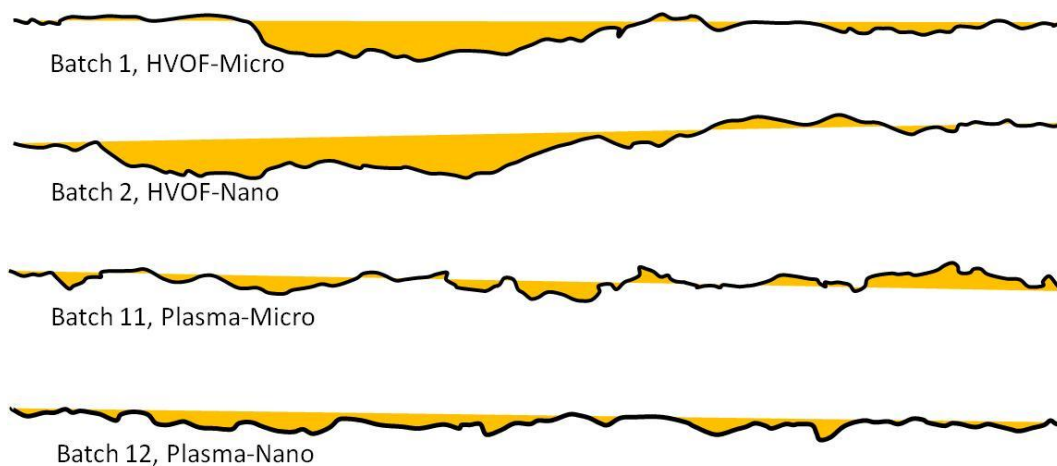


Figure 5.7, Coating waviness produced by HVOF and Plasma thermal spray using different powder sizes.

Effect of Coating Roughness on Corrosion Rate

The most important point in producing corrosion-resistant coating films is to avoid porosity. Munemasa et al. [197] investigated the relationship between the surface roughness and the birth of pinholes and studied the effects of total film thickness and multilayer coatings in order to reduce porosity. As result, they found that when the arithmetical mean deviation (R_a) decreased, the porosity decreased accordingly. They also found that the amount of porosity could be reduced radically by increasing the number of layers in multilayer coatings.

The effect of surface roughness on the corrosion resistance of an oxide layer was studied by Bongyoung et al. [198]. The study showed that the distribution of pores in the oxide layer increased with increasing surface roughness which allowed more penetration of the corrosive materials into the coating layers.

Li et al. [199] studied the influence of surface morphology on corrosion and electronic behaviours, showed that the corrosion rate increased with an increase in surface roughness. Theoretical studies confirmed that the roughness was affected by not only the overall electron work function (EWF) of a surface but also its local EWF fluctuation. It is easier for electrons in the vicinity of a peak to escape than those in a valley, so that the peak would be corroded preferentially, Figure 5.8. An increase in roughness may also support the formation of corrosion cell that could further accelerate corrosion of a rough surface.

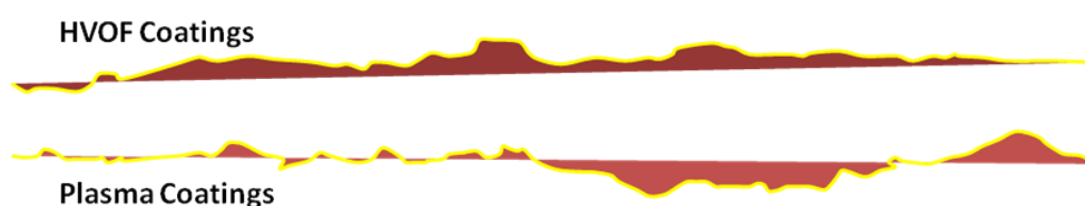


Figure 5.8, Comparison of peaks and valleys of HVOF and Plasma coating conducted in this research.

The deviation from the mean Ra values revealed that surface roughness of HVOF coatings were lower than the plasma sprayed coatings. This was due to the fact that HVOF produces denser coating which helps to lower roughness of the surface. From the data of the surface roughness measurement, it is concluded that the use of nano-sized powders in the plasma spray system helped to lower the coating roughness while it increased the roughness when sprayed by the HVOF system. The addition of AMDRY to the original WC-Co powders increased the surface roughness of the coatings.

5.1.3 Analysis of HVOF Produced Coatings

It can be clearly seen from BSE ESEM images as well as the EDS spot analysis that the HVOF coatings were very dense (porosity < 1.3%) and had very low oxide content (less than 1.69%). There was good contact with the substrate, indicating good bonding to the substrate. The WC particles distribute uniformly within the coating. Cemented areas were mostly cobalt. The sharp irregular shapes of the small particles indicated that these particles were not molten during spraying (Figure 5.9). Therefore, it can be assumed that portion of the metal binder was partly but not fully melted.

Typical coating microstructure were produced, consisting of adjacent bands of dark and light areas of materials. The microstructure of the dark areas were revealed to be mostly Co particles with aggregate of WC. In contrast, the microstructure of the light areas was composed mostly of sintered aggregate WC particles.

The coatings showed low porosity structure (porosity < 1.3%) compared to the plasma coatings. No subsurface cracks in the coating were observed. Good adhesion between the coating layers was also observed at high magnification.

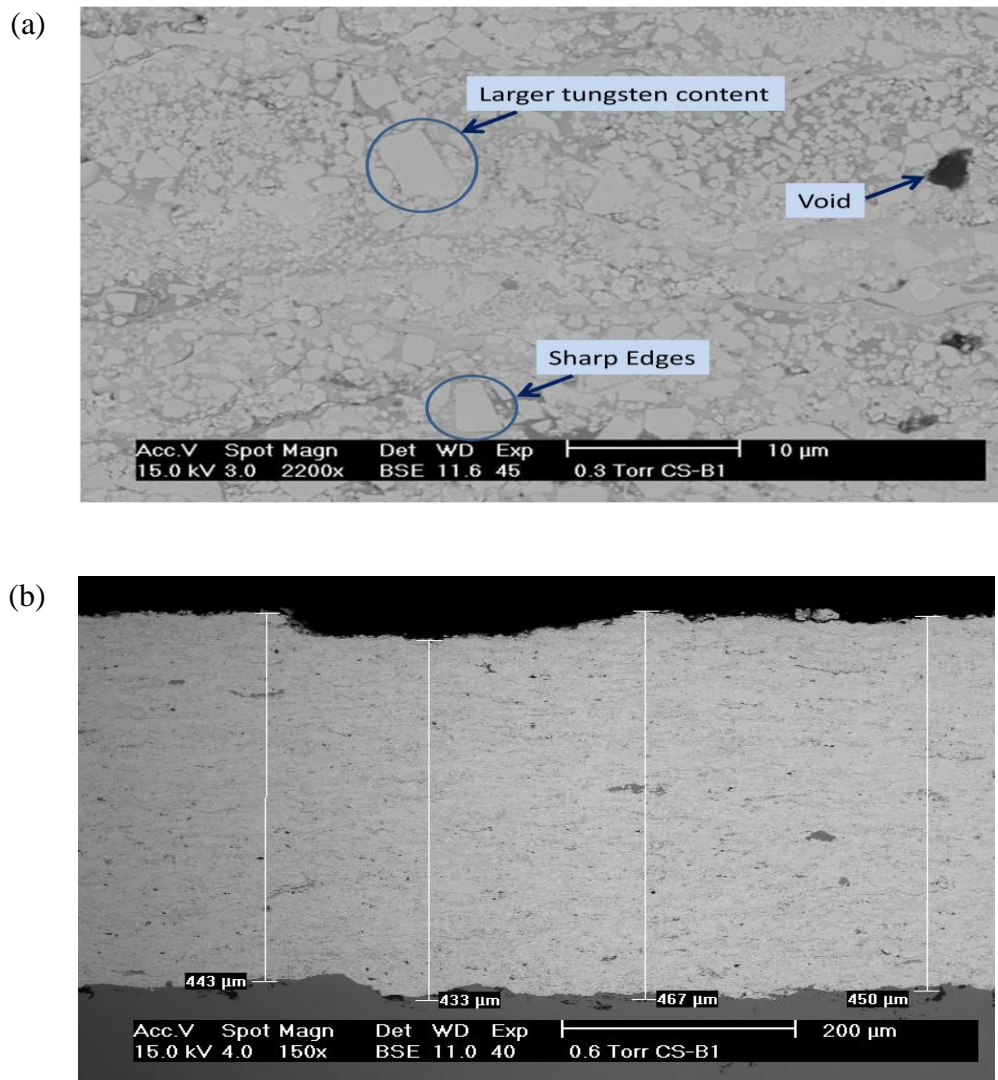


Figure 5.9, Example of HVOF coatings produced in this work, Batch 1; (a) Sharp edges; (b) Coating thickness.

Powder Size Effect on HVOF Coatings:

Relative to the coatings produced by HVOF micro-sized powders, coatings produced by nano-sized powders had more uniform distribution of WC particles in the Co matrix phase. They show better melting of the powder contents, resulting in very dense coatings which eliminated most of the sharp irregular shapes. Increased dissolution of WC particles in the liquid Co was found compared to coatings

produced by the HVOF micro-sized powders. This was due to the low surface area of contact in micro-sized powders used to perform the coatings.

It can be clearly seen from the images both at same magnifications (Figure 5.10 (A) and (B)) that coatings produced by HVOF system using nano-sized powder produced a heterogeneous microstructure. They display slightly lower overall porosity, but the pore percentage of elongation was larger than HVOF coatings obtained from micro-sized powders. Different samples showed different amounts of microporosity. However, the difference was not particularly large; as no major difference in structure was highlighted.

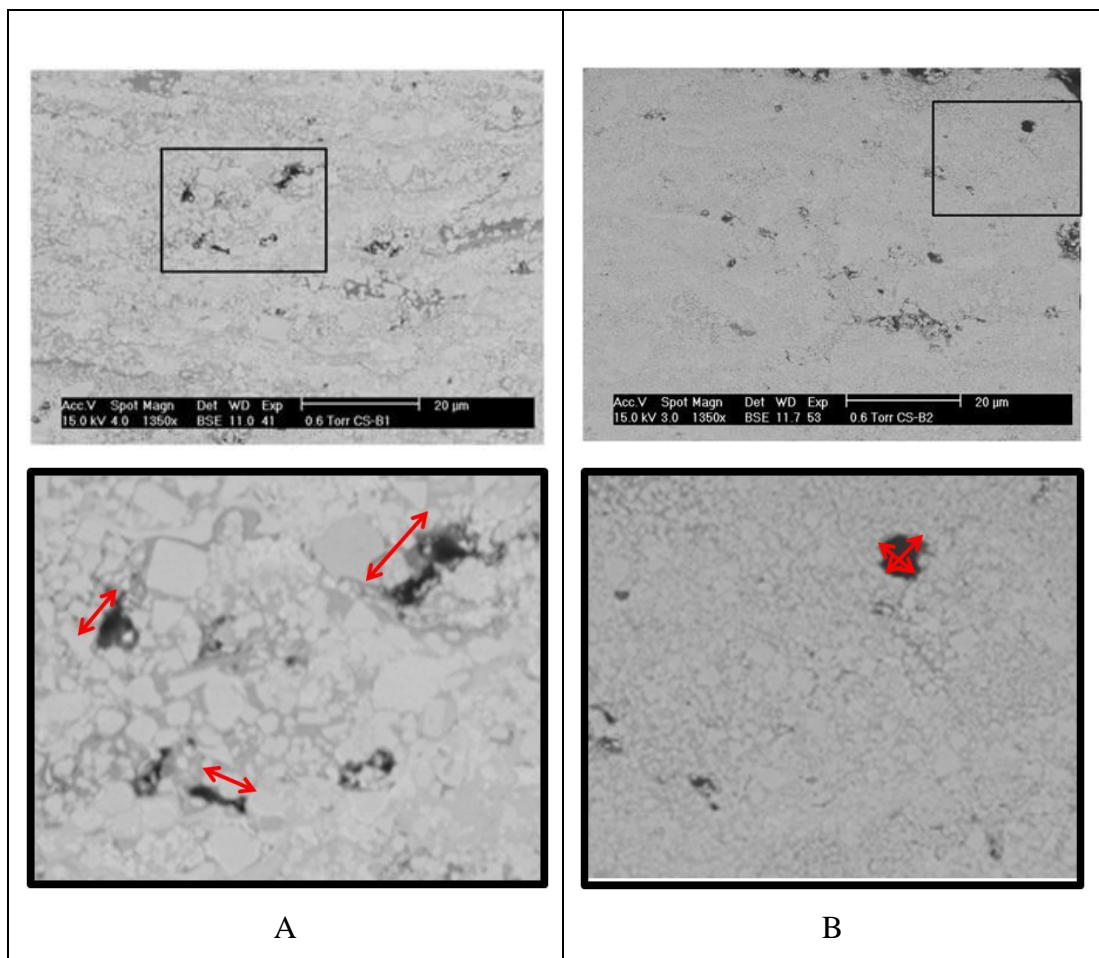


Figure 5.10, HVOF coatings produced by different powder size: A) Batch 1, B) Batch 2, shows pore elongation, and shape at the same magnification, 1350X.

The extent of decarburization observed from the percentage of carbon also by EDS analysis (Figure 5.11) of the nano-sized powder (15.87 wt.%), was a little bit higher than the micro-sized powder (14.54 wt.%). This was due to the higher degradation and larger degree of melting of nano-sized powder. Surface to volume ratio effects contributed to this issue. Close examination of light areas of coatings of the nano-sized powder showed very small WC particles which appeared to be at different stages of coalescence, forming larger particles.

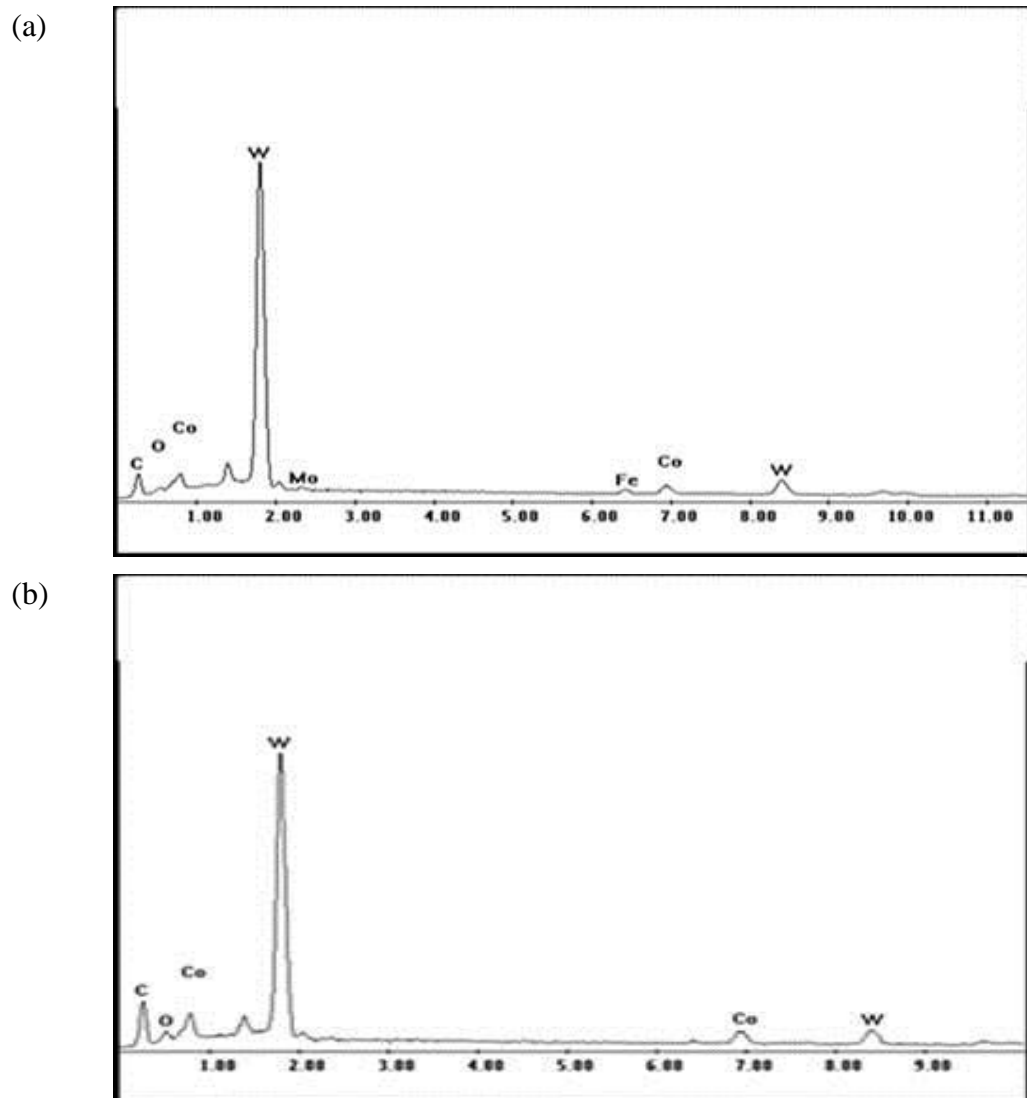


Figure 5.11, EDS Analysis of HVOF coatings produced by different powder size: (a) Batch 1, (b) Batch 2.

5.1.4 Analysis of Plasma Produced Coatings

BSE ESEM images illustrated that all of the plasma produced coatings were well adhered to the base metal and had very good contact with the substrate. Much higher porosity (4-7 %) and lower density was observed compare to the HVOF coatings. Evolution of carbon oxide gas from the coating may be considered to be the largest contributor to porous coatings. Only a few rounded edges, semi-melted, particles of original powder were found in the coatings and complete dissolution of the cobalt binder phase due to high operating temperatures was observed.

EDS analysis showed that W and C were present in the structure. Also, less cobalt phase (4 wt.% Co) was produced by plasma spray in the coatings compared to the coatings produced by HVOF thermal spray (8-10 wt.%). This may be due to evaporation of cobalt phase at higher operating temperatures. Higher decarburization was realized in the plasma produced coatings relative to HVOF produced coatings. It can clearly be seen from BSE SEM images (Figure 5.12) that there were no cracks initiation or propagation in the coatings.

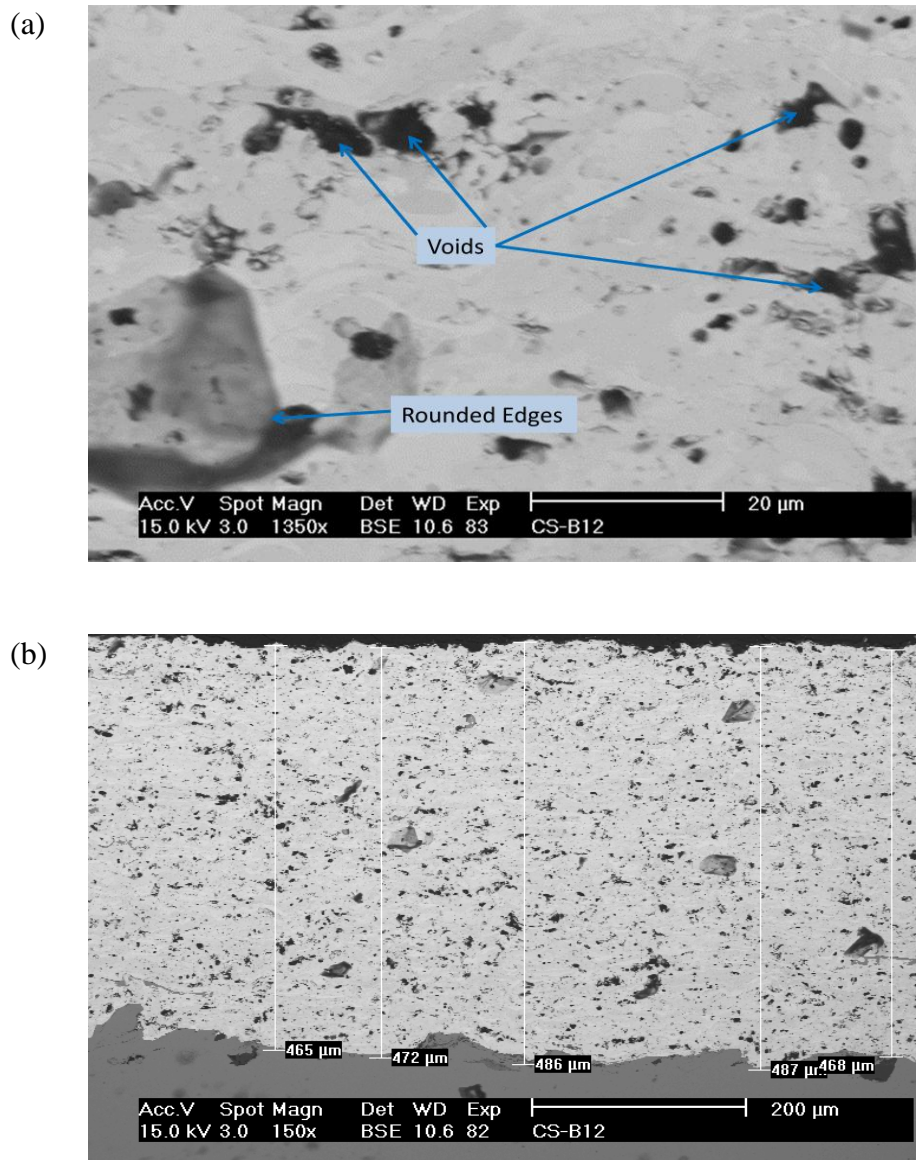


Figure 5.12, Plasma coatings produced in this research; (a) Voids and rounded edges; (b) Coating thickness.

Powder Size Effect on Plasma Spraying Coatings:

Due to the high temperature of the plasma spraying system, heterogeneous melting of powder particles was expected, which led to WC particle dissolution and decomposition. The dissolution rate of WC in the coatings of the nano-sized sprayed powders was found to be higher as indicated by the weight percentage of

WC in the cobalt phase (13-32 % WC dissolution). The particle size did not produce any clear effect in the evaporation of an amorphous Co binder phase, but the higher tungsten weight percentages in the area analysis of the nano produced coatings, which may have attributed to cobalt evaporation and degradation in the binder phase.

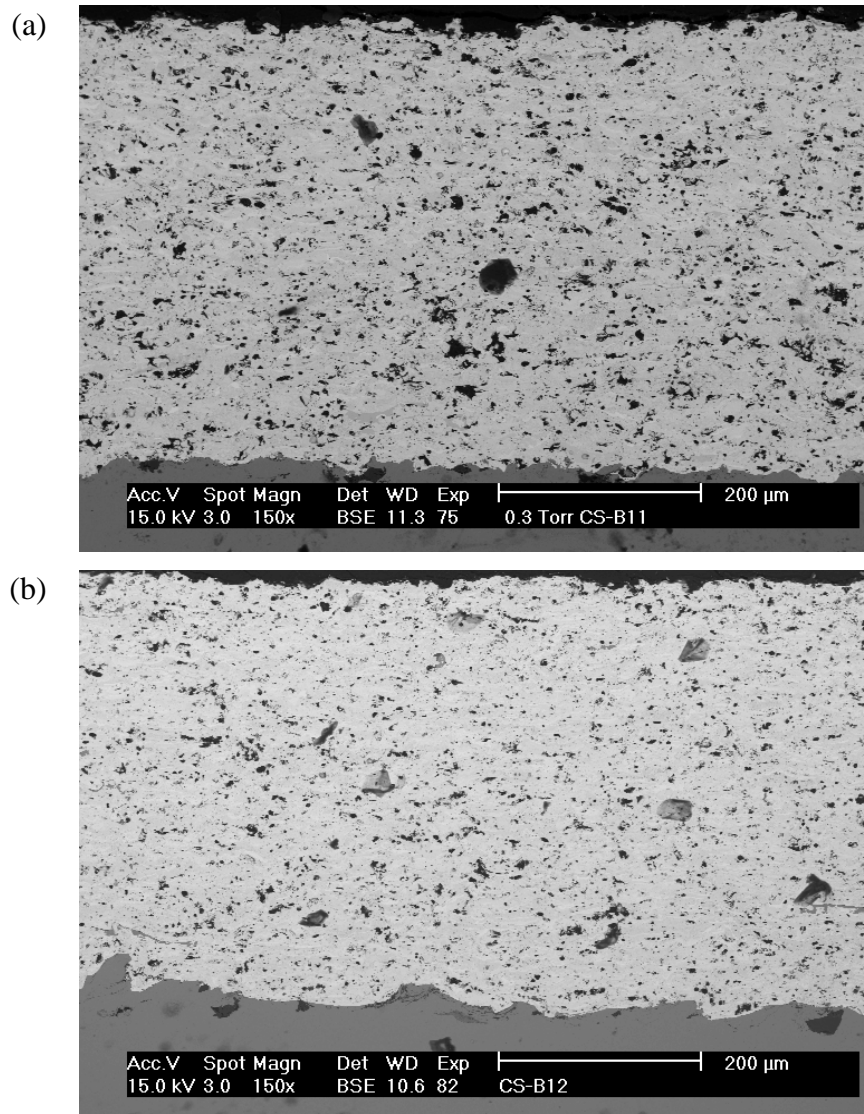


Figure 5.13, Plasma sprayed coatings at different powder size: (a) Batch 11- Micro, (b) Batch 12- Nano.

The EDS analysis, Figure 5.14, did not show any significant increase in decarburization of coatings produced by the nano-sized powders, but led to the formation of W_2C compared to the other powders, as anticipated. However the high surface area of the nano-sized WC/Co particles facilitates all types of high-temperature reactions, which causes greater degree of decarburization encountered in the produced coatings.

Variations in WC particle size and distribution in the light areas of the microstructure were observed in some samples. This may be due to the high operating temperature of the plasma system and the rapid dissolution of the WC nano-particles into the liquid Co.

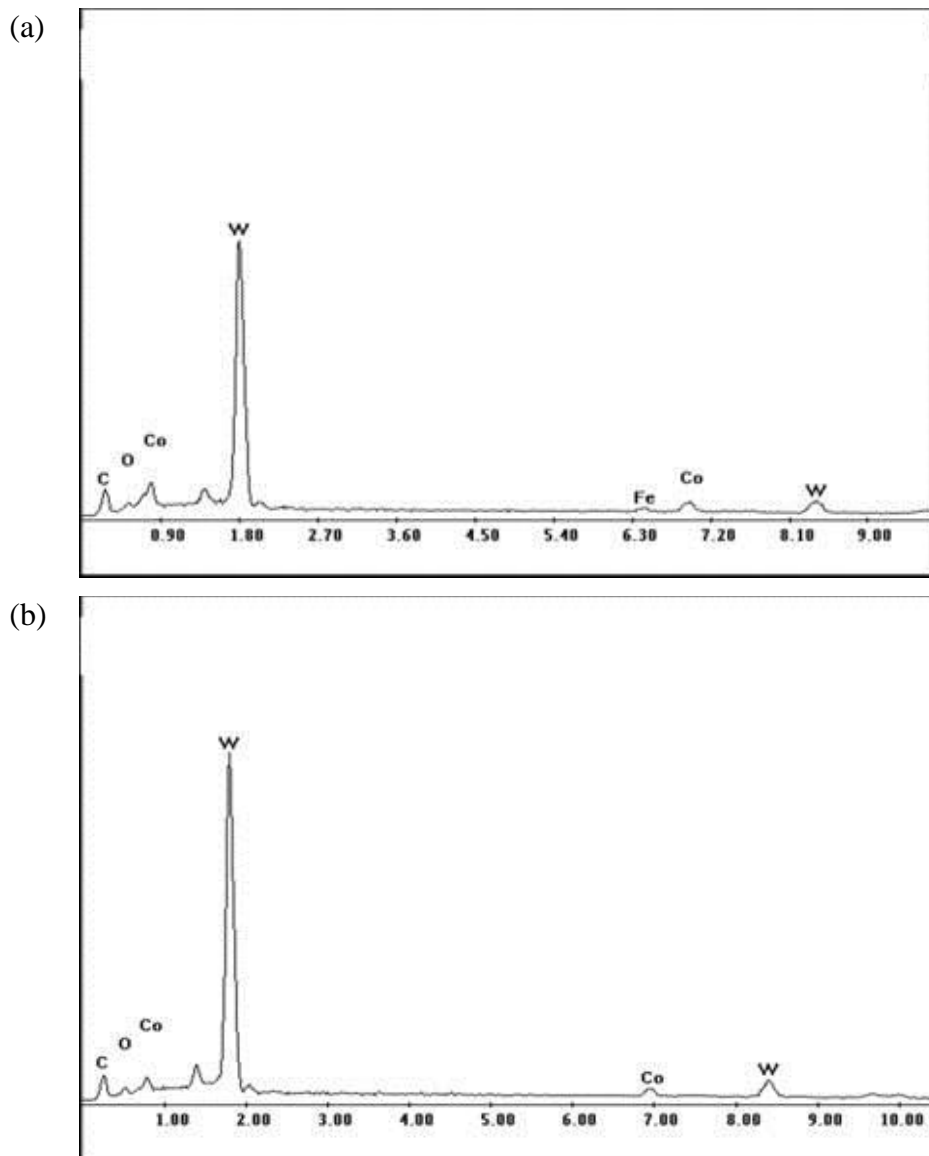


Figure 5.14, EDS Analysis of Plasma spray coatings produced by different powder size; (a) Micro-sized; (b) Nano-sized.

5.1.5 Effect of Addition of AMDRY Powder to the Original WC-Co Powder

The EDS analysis showed that the tungsten content 83-75 wt.% decreased to 41-54 wt.% in these coating as coating layers increased in coating thickness (from 160 micron to 480 micron) which confirms the coating technique that was adapted in the scope of this work. Different morphology of different coating layers were

found in the BSE images. Generally, all coatings had good interface between coating layers and adhered well to the substrate, Figure 5.15.

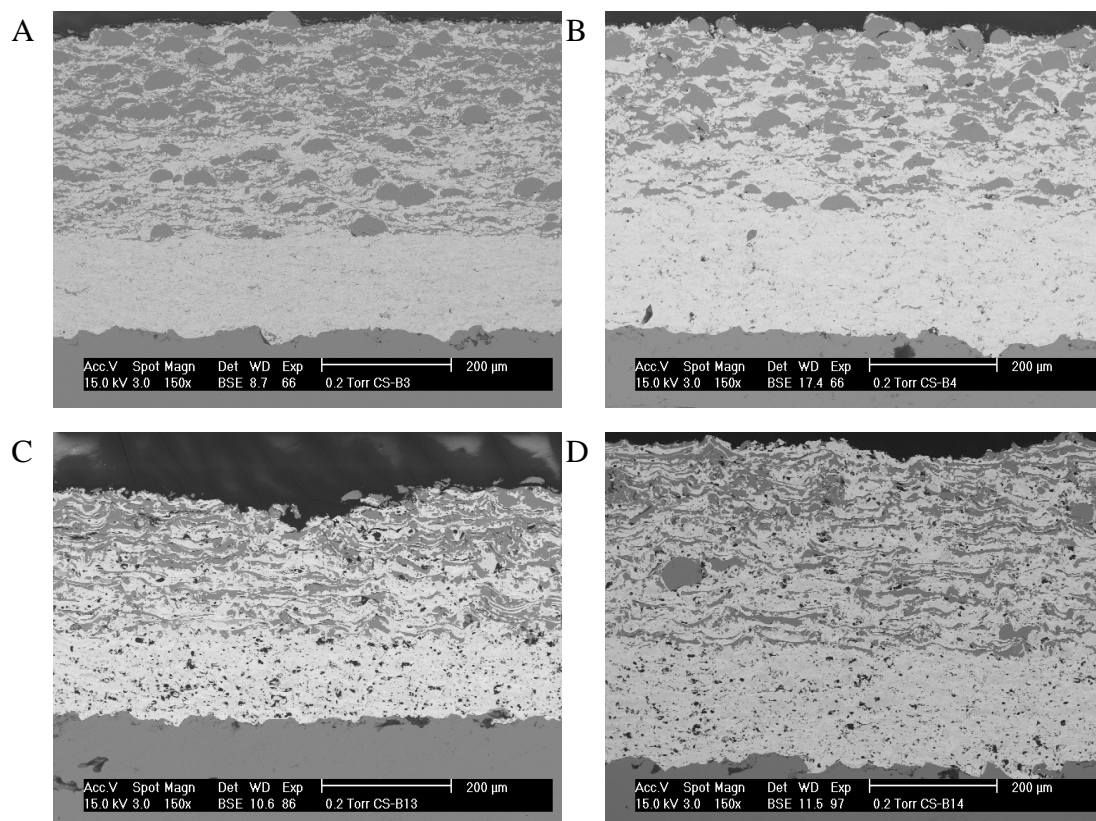


Figure 5.15, Multilayers structures showing the effect of AMDRY powders on the top layer: A) HVOF-Micro, B) HVOF-Nano, C) Plasma-Micro, D) Plasma-Nano.

More cobalt weight percentages (24 %) were detected by the EDS analysis in the coatings containing AMDRY powders and the micro-sized WC-Co powder mix. The addition of AMDRY powder could be responsible for minimizing the Co evaporation in both HVOF and plasma systems. The addition of AMDRY powder to nano-sized WC-Co powder had no significant effect on Co evaporation in both systems. There was no clear evidence that addition of AMDRY powder to the original WC-Co powders had major effect on WC decarburization. In these coatings, Co and Ni formed surrounding the WC grains in the matrix. White areas

were rich in tungsten while dark areas consist mainly of Co, Ni, Cr, and Al. Large areas rich in Co precipitation were detected in the HVOF coatings.

These coatings represented the coating structures observed from different systems (HVOF and plasma) used in this work. Adjacent regions of the microstructure consisted of distributed speckled areas for the HVOF coatings, while on the other hand, banded layers developed the lamellar structured deposits in the plasma sprayed coatings.

5.1.6 Evaluation of Coating Porosity

Coating porosity can be detrimental in coatings with respect to corrosion and its response to mechanical tests. The mechanical properties of the coating such as strength, hardness and wear characteristics can all be affected by coating porosity.

Coating thermal spray process at low temperatures limits reaction between the constituents in the coating which results in poorly bonded splats that can be easily removed or debond. As the process temperature (and velocity) increases, low porosity, well-bonded structure, and higher-hardness coatings are produced. The adhesion of the coating to the substrate and its hardness increased while the porosity decreased [200]. Also, the dissolution of the WC phase in the Co increased with increasing temperature. This produces a more wear-resistant matrix phase. The porosity level of the used powders can contribute to the produced coating porosity if powder particles are not fully melted during the deposition process.

The use of HVOF/Plasma thermal spraying systems to spray micro/nano-sized powders with the intention of achieving very dense, low porous coating and preventing decarburization has remained a challenge. High temperature reactions of WC can produce other species (e.g. W_2C and W) that are detrimental to the wear resistance of the coating. Therefore it is a complex combination of different

processes, different powder sizes, and different mechanical and chemical properties of the coating that promotes wear resistance.

The porosity measurements revealed that the average overall porosity of the HVOF coatings produced by spraying the micro-sized powders was about 1.3%. Coatings produced by HVOF system using nano-sized powder showed slightly lower overall porosity of 1.2%. On the other hand, plasma coatings show very high porosity compared to the HVOF coatings of 6.6 % for Micro and 6.3% for Nano. Table 5.2, lists the average overall porosity percentages of the produced coatings.

The addition of the AMDRY powder to the original WC-Co powders at different ratios (20% and 40% AMDRY) helped to lower coating porosity and produce more denser coatings (as illustrated in Figure 5.16 and 5.17) especially at 40% AMDRY 995M.

Table 5.2, Average overall porosity percentages of the produced coatings.

	<u>HVOF System</u>	<u>Plasma System</u>
Micro-Sized Powder	1.3039 % (Batch-1)	6.6038 % (Batch-11)
Nano-Sized Powder	1.1999 % (Batch-2)	6.3559 % (Batch-12)
AMDRY + Micro-Sized Powder	1.3039 % (First Layer of B-3) 1.2652% (Second Layer of B-3) 1.1571% (Third Layer of B-3)	6.6038 % (First Layer of B-13) 5.6525% (Second Layer of B-13) 5.2893% (Third Layer of B-13)
AMDRY + Nano-Sized Powder	1.1999 % (First Layer of B-4) 1.1864 % (Second Layer of B-4) 1.1530 % (Third Layer of B-4)	6.3559 % (First Layer of B-14) 5.2508 % (Second Layer of B-14) 4.9893 % (Third Layer of B-14)

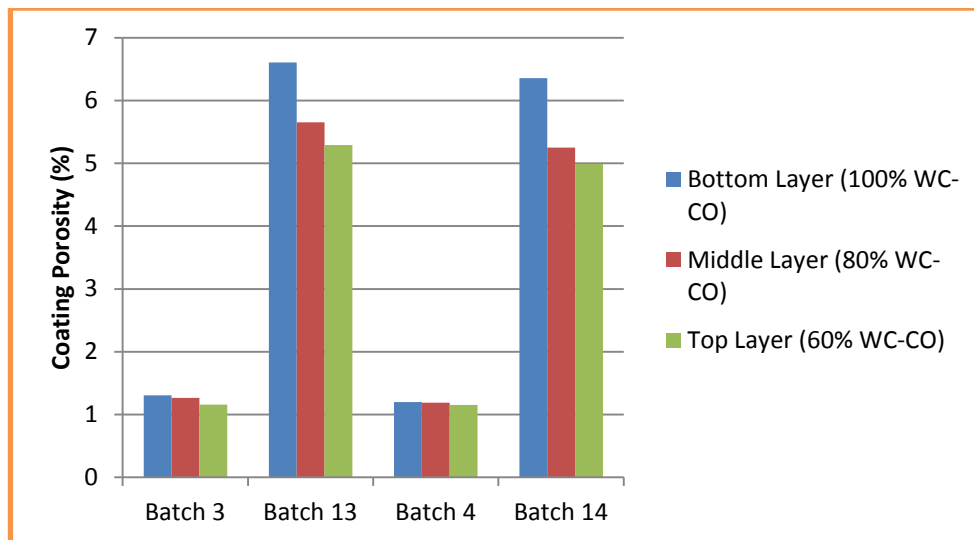


Figure 5.16, Effect of addition of AMDRY powders on overall layers porosity.

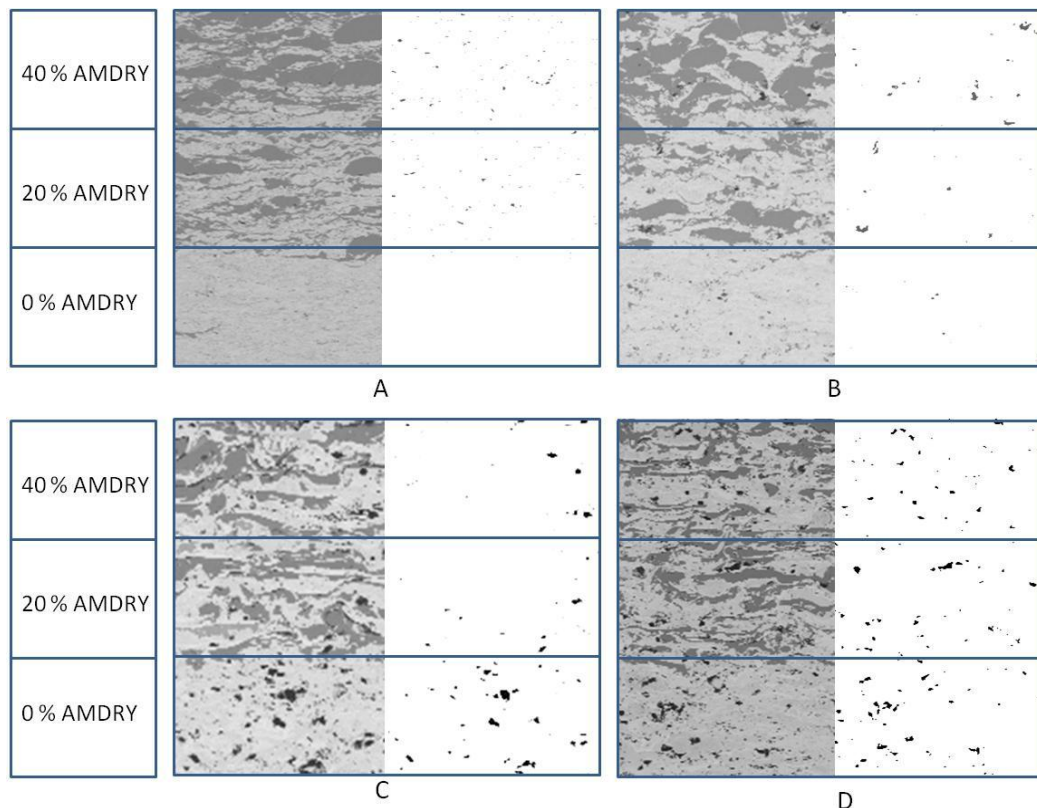


Figure 5.17, The addition of the AMDRY powder to the original WC-Co powders at different ratios (20% and 40% AMDRY), (A) Batch 3, (B) Batch 4, (C) Batch 13, (D) Batch 14.

The ESEM images collected in this work showed many porosity features observed in the coatings such as, rounded pores that formed due to gas evolution from the coating at high temperatures, which remain dissolved in the cobalt matrix after solidification by cooling [145]; and irregular shapes of pores that may be created as a result of improper stacking between splats, un-melted or semi-melted particles. In the Nano produced coatings, elongated pores were also found. It was observed that the pores in the plasma coatings seemed more destructive than HVOF-sprayed ones Figures 5.18 and 5.19.

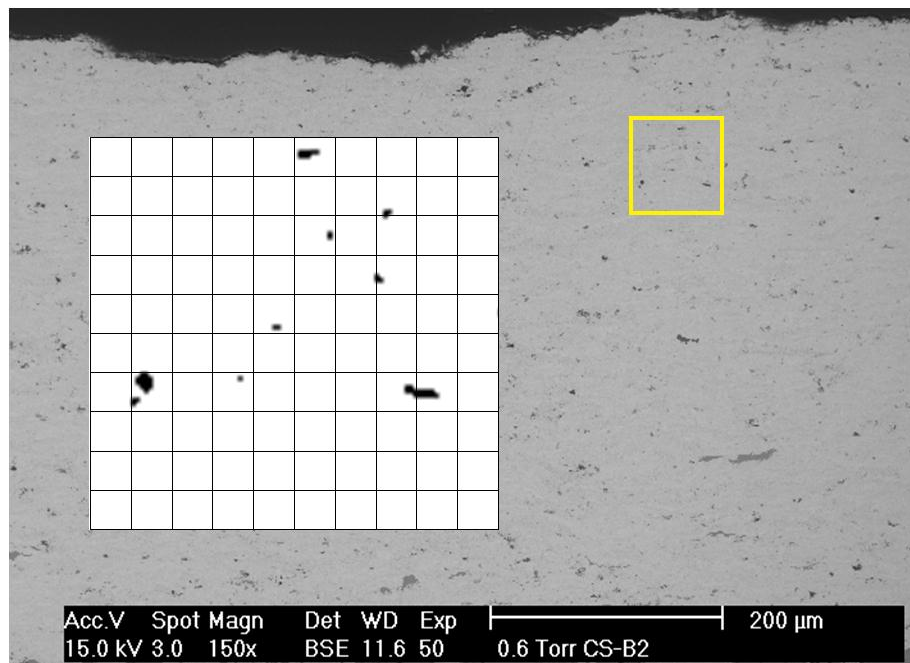


Figure 5.18, Example of pores features of HVOF produced coatings, Batch 2.

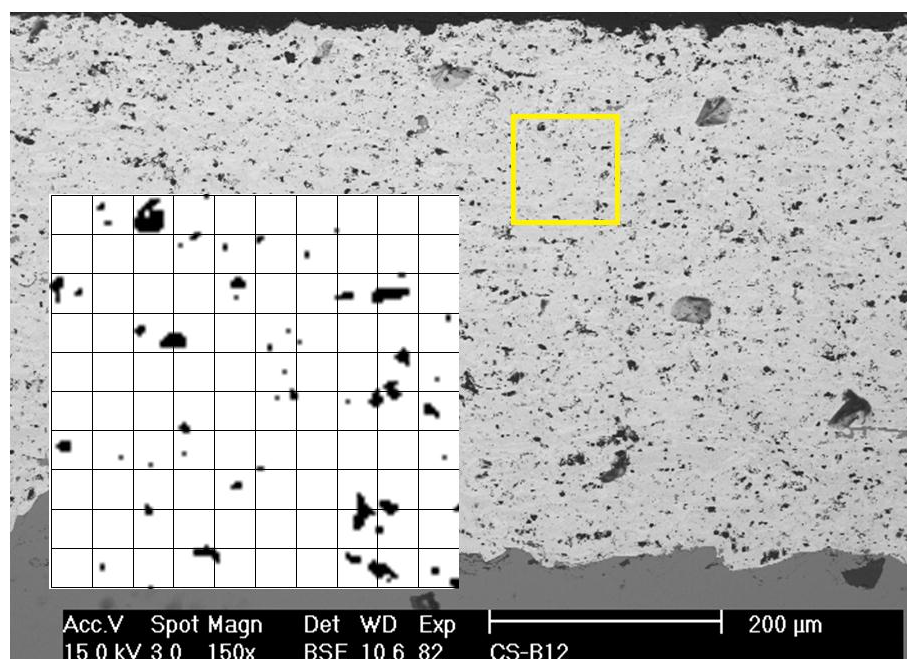


Figure 5.19, Example of pores features of Plasma produced coatings, Batch 12.

The porosity was higher for plasma sprayed coatings than that for HVOF, as would be expected, because in the plasma system it is very difficult to compromise between low porosity and the retention of WC particles (that is preventing decarburization and gas evolution) at high temperatures.

Melting of the cobalt phase at high plasma temperature and expansion of the enclosed gases resulting from decarburization of the powder, resulted in the trapping of gas bubbles under the cobalt liquid phase which would have affected the coating porosity [201, 202].

The use of nano-sized powders provide moderate improvement in lowering coatings porosity over the use of the micro-sized powders because of their higher degree of melting compared to the other powders. However the improvements were not significant.

5.1.7 Evaluation of Coating Adhesion

Physical observation showed good adhesion between the multi-layers themselves and the bottom layer with the substrate material in all coatings. No coating interfacial crack propagation was initiated, and no failure mechanism was noticed in all coatings specimens. This is due to the good surface preparation of the base metal that required grit blasting to roughen the surface and allow mechanical interlocking. It also describes the superior wettability of the coating materials that was obtained by controlling the number of heating/cooling passes during the spray process, thus excellent solidification was achieved and the number of cooling passes selected was found to be optimal to slow the solidification process in order to allow penetration of melting material into surface cavities and to form stronger bonds.

Voids created at the coating-substrate interface may reduce adhesion [203]. An increase in coating porosity would result in a decrease in coating adhesion and hardness [200]. So, it is expected that the HVOF coatings would have better adhesion than the plasma spray coatings as it propels the particles at higher speed, thus stronger interlocking of substrate and previously laid down particles are achieved. For future work, an adhesion test such as “scratch test” may be recommended for the investigation of adhesion of WC-based coatings sprayed on carbon steel substrate since the adhesion observation in this work was based on optical microscope and ESEM examination, Figure 5.20-5.22.

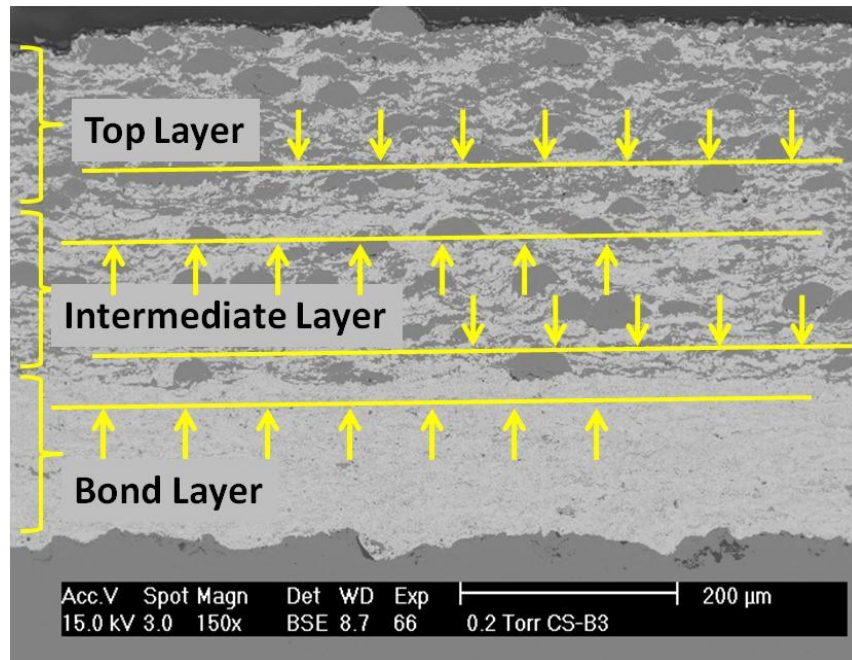


Figure 5.20, Multilayer coating interface and adhesion, Batch 3.

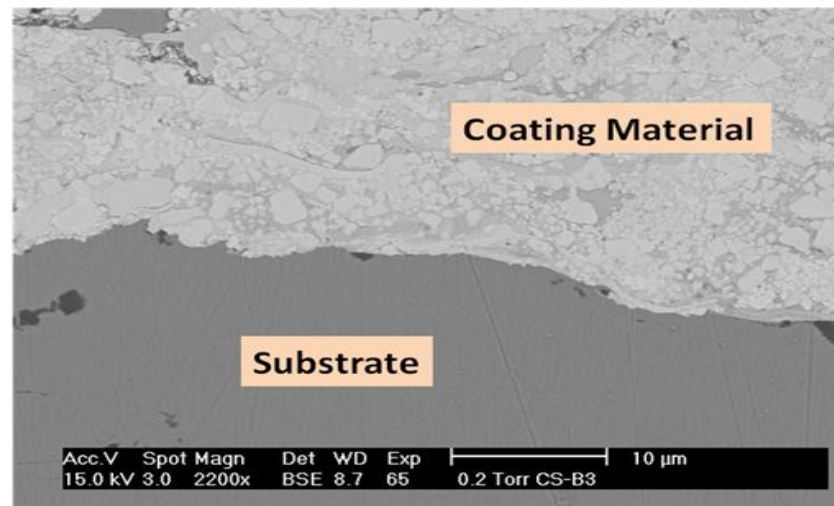


Figure 5.21, Coating adhesion in the base metal, Batch 3 at 2200X.

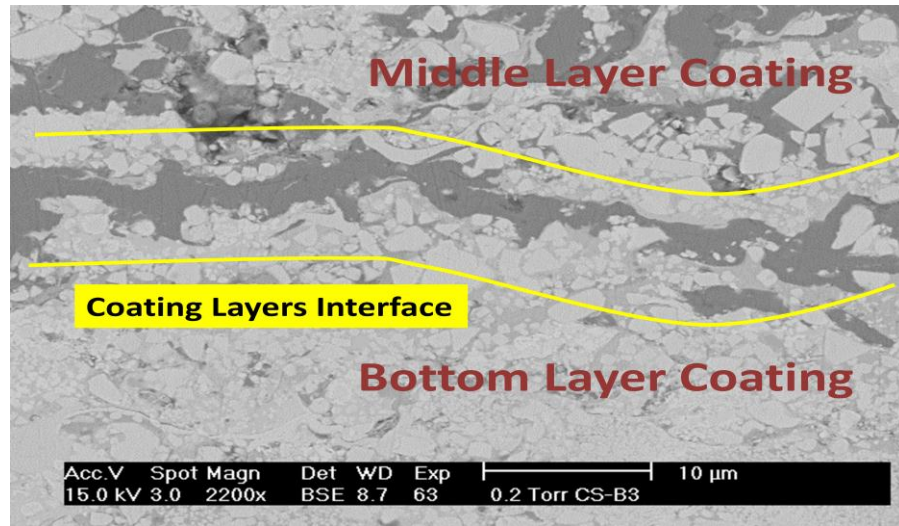


Figure 5.22, Bottom-Middle layer interface and adhesion, Batch 3 at 2200X.

5.1.8 Coating Hardness Assessment

The measurements show that the average hardness value (5 indentations) of the coatings produced by spraying micro-sized powder via HVOF was 1066 HV (Batch 1) compared to 1367 HV for the coatings produced by HVOF spraying of nano-sized powder (Batch 2). In the plasma system, the average hardness value for the coatings produced by spraying the micro-sized powder was approximately 826 HV (Batch 11), whereas the nano-sized powder (Batch 12) was approximately 837 HV. Table 5.3 below summarizes the measurements.

Table 5.3, Hardness test measurements.

Average Hardness Values of all Layers (WC-Co)			Multi-Layer Hardness (WC-Co + AMDRY)			
Powder Type	Process		Batch	Hardness HV		
	HVOF	Plasma		Bond Layer	Intermediate Layer	Top Layer
Micro-Sized Powder	Batch 1=	Batch 11=	3	1171	905	836
	1066 HV	826 HV	4	1273	990	968
Nano-Sized Powder	Batch 2=	Batch 12 =	13	840	638	618
	1367 HV	837 HV	14	977	709	625

Effect of Particle Size on Coating Hardness

As previously mentioned in the powder reactions section of this research, the WC particle size and volume fraction influence the hardness of the coating. The sprayed powder surface area and the carbides distribution in the matrix, and also the hardening effect of W and C dissolution in the Co matrix can affect the hardness of the produced coating [134]. The measurement results revealed that the coating produced by spraying the nano-sized WC-Co powder showed higher hardness than coatings produced by spraying the micro-sized powders; HVOF demonstrating a more significant increase. The nano-sized powders have higher surface area and finer distribution of nanostructured carbides in the matrix. Therefore, coatings produced by spraying the nano-sized powders showed higher hardness compared to the coatings produced by the micro-sized powders, Table 5.4.

The plasma sprayed micro and nano coatings display almost similar hardness values for the pure WC-Co coatings with higher values for Nano-sized structured powders. This may be due to the higher temperature of the system which led to decomposition of the powders and formation of brittle carbide phases.

Table 5.4, Powders surface area effect on coating hardness.

Coating Group	Specific Surface Area m ² /g	Ave. Particle Diameter μm	% of nano-sized WC-Co in top coat	Top Layer Hardness HV
1	0.181	38.712	0	1066
2	0.186	33.143	100	1367
3	0.177	35.945	0	836
4	0.215	28.077	60	968
11	0.181	38.712	0	826
12	0.186	33.143	100	837
13	0.166	43.384	0	618
14	0.184	37.682	60	625

Coating Process Effect Hardness

The obtained hardness measurements clearly confirmed that the powder used in the plasma spraying experienced decarburization reactions more than the HVOF spraying which resulted in formation of hard and brittle phases, Figure 5.23. The hardness increased with increasing content of W_2C in the coatings because the W_2C phase is harder than the WC phase [135], and due to the high operating temperature of the plasma system, where powder particles absorbed larger heat during the flight resulting in larger decomposition of the hard WC to less hard products of other carbide phases, and consequently reduced the coating hardness [105]. The presence of microporous structure within the plasma coatings contributed to the decrease in the hardness values of the coatings. The increase of the hardness of the HVOF coatings compared to the plasma coatings can be associated to the increased particle velocity, the low porosity of the dense coating and low degree of decarburization.

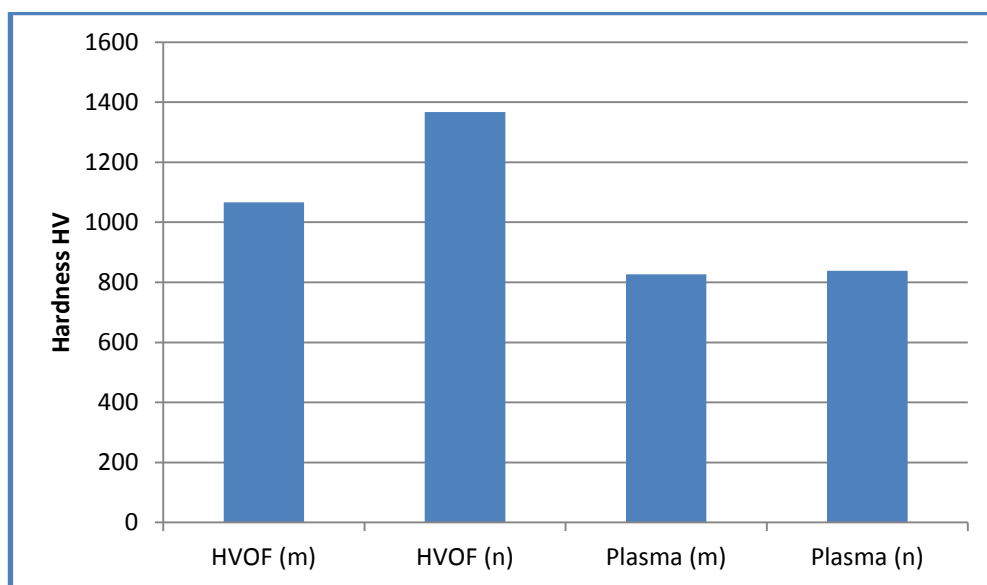


Figure 5.23, Hardness of coatings produced by different systems (HVOF/Plasma) using different powder particle size (micro/nano).

Effect of AMDRY Powder on Coating Hardness

The results of coatings hardness measurements for multilayered coatings revealed that the addition of AMDRY powder at both 20% and 40% to the WC-Co powder resulted in lowering the hardening layers (Figure 5.24). The hardness decreased as the percentage of the nano-sized powder decreased. The addition of AMDRY powder helped to lower the degree of decarburization and Co evaporation in both HVOF and plasma systems. At same time, it lowers the percentage of the hard materials such as tungsten and carbide in the started powders and increased the cobalt phase in the produced coatings (Co is softer than W and C). The use of high percentage of WC-Co powder in the bottom layer would provide harder coating for wear resistance while the addition of the AMDRY powder would aim to improve the coating corrosion resistance. However the multilayered coatings with Nano-sized WC-Co yield higher hardness in both HVOF (938 HV) and plasma (625 HV) compared to those for Micro-sized WC-Co (HVOF at 836 HV and plasma at 618 HV). HVOF sprayed Nano WC-Co and AMDRY 9954 (Batch 4) produced higher hardness of 938 HV.

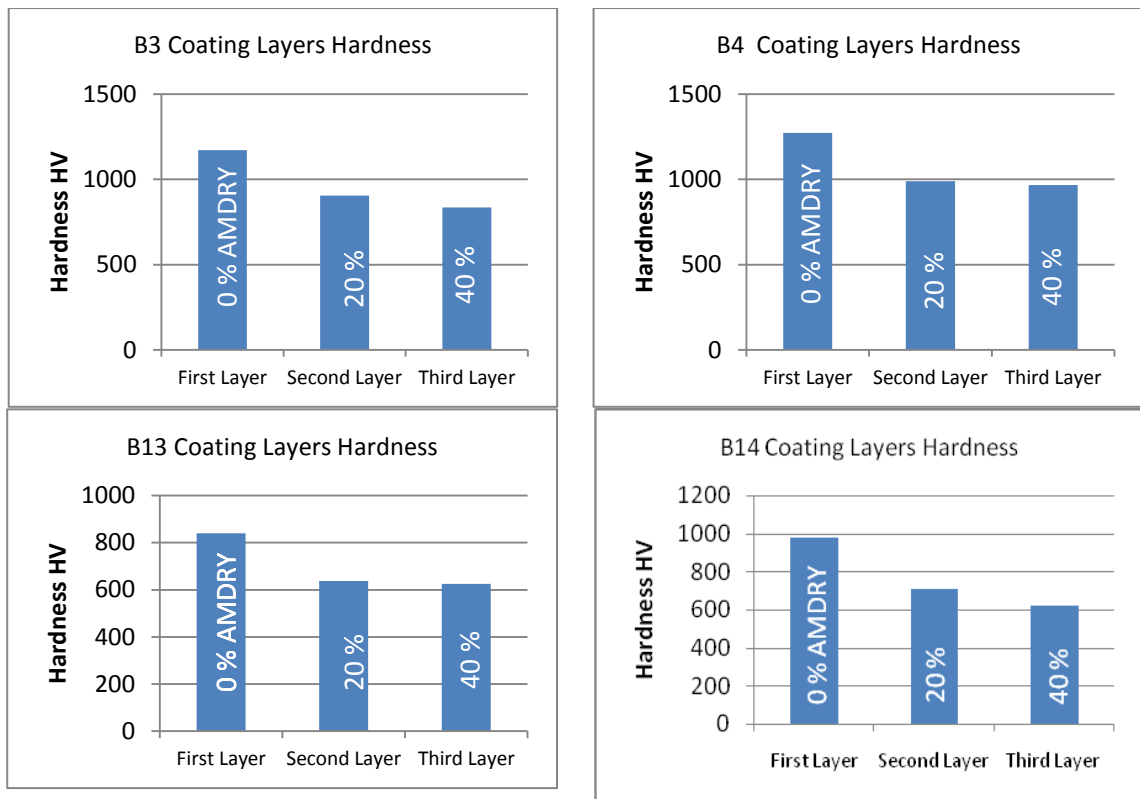


Figure 5.24, Effect of AMDRY powder on coating hardness for HVOF and Plasma sprayed samples.

5.2 CORROSION BEHAVIOUR OF APPLIED COATINGS

During the corrosion test, corrosion products (e.g. rust, oxides,..) were generated on the coating surface under the conditions of salt spray chamber. As the test time proceeded, initially the corrosion products grew rapidly but then grew at a slower rate (Figure 5.25). The corrosion products did not cover the entire coating surface covering only certain spots of the surface. In addition, not all test specimens were found to have corroded. Therefore, the formation of corrosion products was likely to be related to some factors such as coating type, density of coatings, and the condition inside the testing chamber. The pH of the solution kept in the desired range (pH 6.5-7.2), Figure 5.26, up to the test period of 720 hrs.

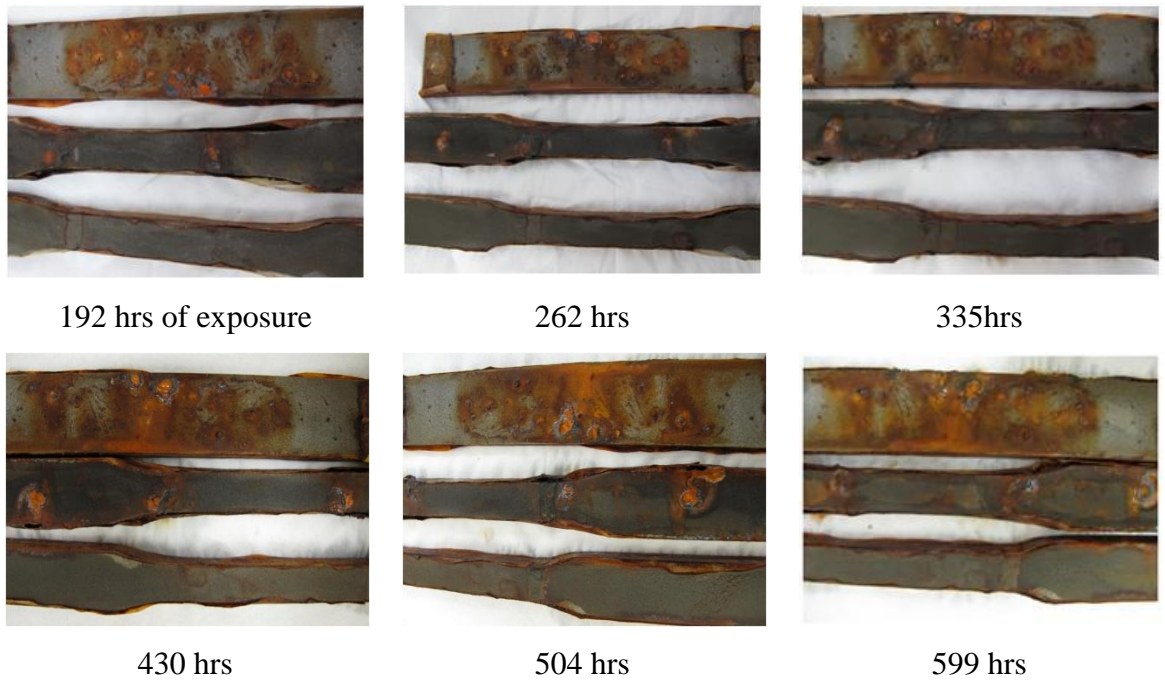


Figure 5.25, Corrosion products growth on selected samples representing the coating response to the corrosive medium.

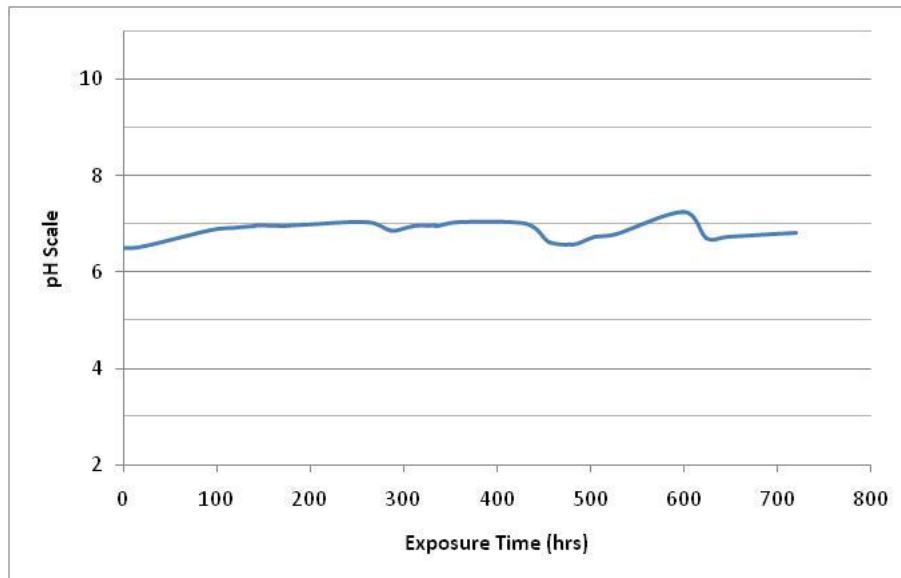


Figure 5.26, Solution pH during the course of the test.

The corrosion products of each batch of the coating were collected for further analysis. They were tagged as; CP-Batch 1, CP-Batch 2, CP-Batch 3, CP- Batch 4,

CP-Batch 11, CP-Batch 12, CP-Batch-13, and CP-Batch 14. CP represented the Corrosion Product of the coated batch (Figure 5.27).



Figure 5.27, Collected corrosion products.

The backscattered electron images along with the EDS X-ray spectra that were acquired from the examined samples showed that portions of samples were covered by the corrosive products. The general EDS analysis indicated that the eight samples were mainly composed of Fe and O which corresponds to iron oxide (Iron-rich oxides with the presence of NaCl), Figures 5.28-5.35. Table 5.5, shows the elements of corrosion products detected by EDS.

Table 5.5, Elements of corrosion products detected by EDS

Element	C	Fe	O	Cl	Na	Ca	W
CP-B1	√	√	√	√	√		
CP-B2	√	√	√	√	√	√	√
CP-B3	√	√	√	√			√
CP-B4	√	√	√	√	√	√	√
CP-B11	√	√	√	√		√	√
CP-B12	√	√	√	√	√		√
CP-B13	√	√	√	√	√	√	√
CP-B14	√	√	√	√	√	√	√

Backscattered electron images at the micrometer scale of the corrosion products in sample numbers: CP-Batch 1, CP-Batch 2 and CP-Batch 13 revealed that they had the same morphology (Figures 5.28, 5.29 and 5.34). The EDS analysis of the plate shaped formation, in CP-Batch 1, fiber-like in CP-Batch 2 and needles in CP-Batch 13 showed that they mainly contained Fe and O which corresponded to iron oxide. In addition, W, Ca, Na and Cl were detected in the three samples. However, the EDS analysis of sample number CP-Batch 13 showed that it also contained significant amounts of NaCl. In case of samples number CP-Batch 3 and CP-Batch 4, the backscattered electron images revealed the same morphology in the corrosion products. The EDS analysis of the cubic shaped (crystallized) particles in both samples indicated that they mainly contained Fe and O (iron oxide) with the presence of Na, Cl and W (Figures 5.30 and 5.31). Likewise, the backscattered electron images of samples number CP-Batch 11 and CP-Batch 12 showed similar morphology in the corrosion products but different to the other samples which were mainly composed again of Fe and O, plus presence of W, Na and Cl (Figures 5.32 and 5.33).

In regards to sample number CP-Batch 14, the backscattered electron image and corresponding EDS spectrum revealed a unique morphology (flower like) corrosion product which again composed of Fe and O with the presence of Na, Cl and W (Figure 5.34). In all samples no cobalt was detected by the EDS analyses.

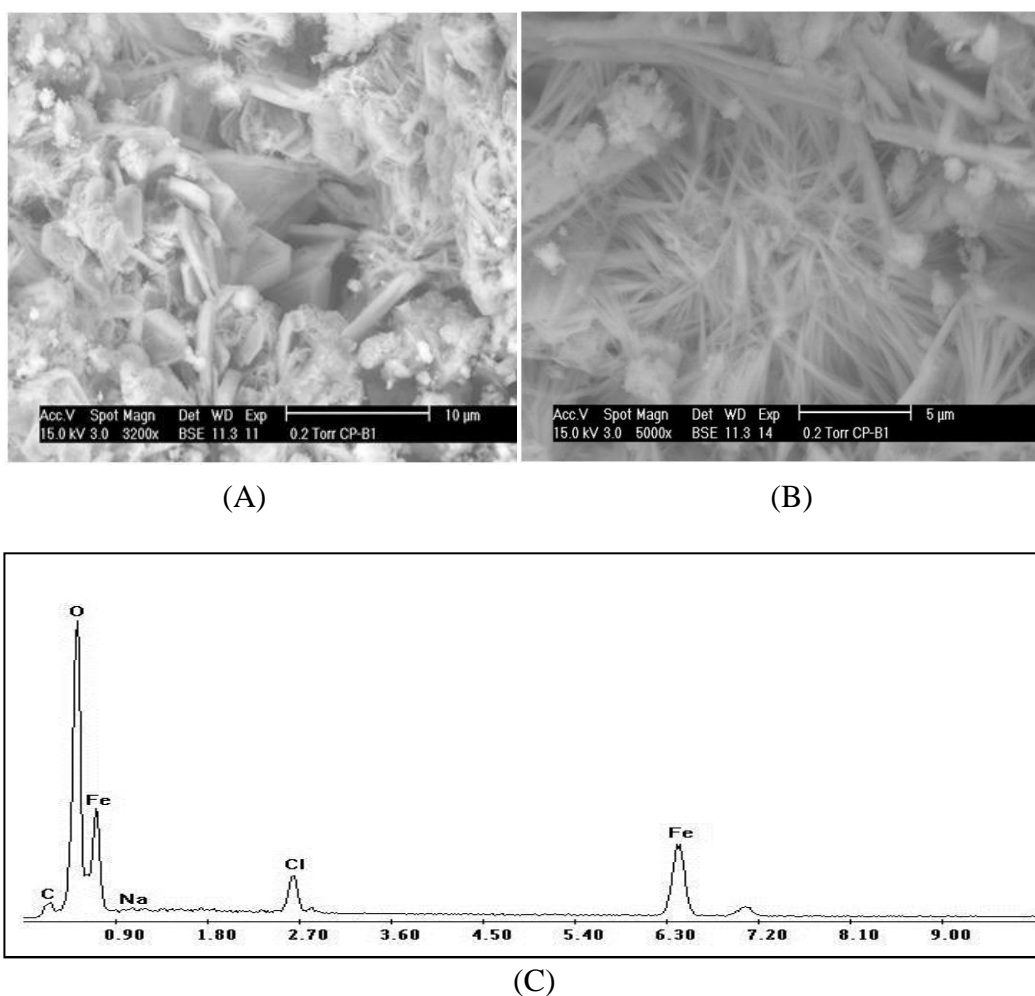
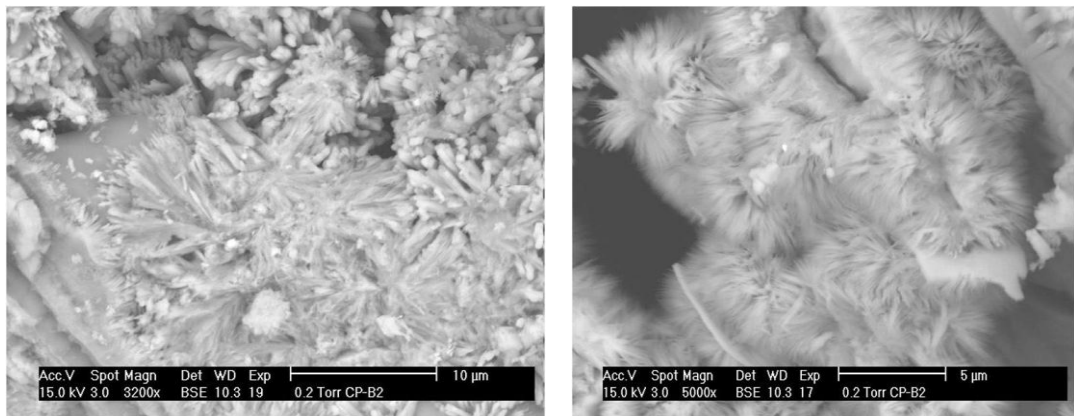


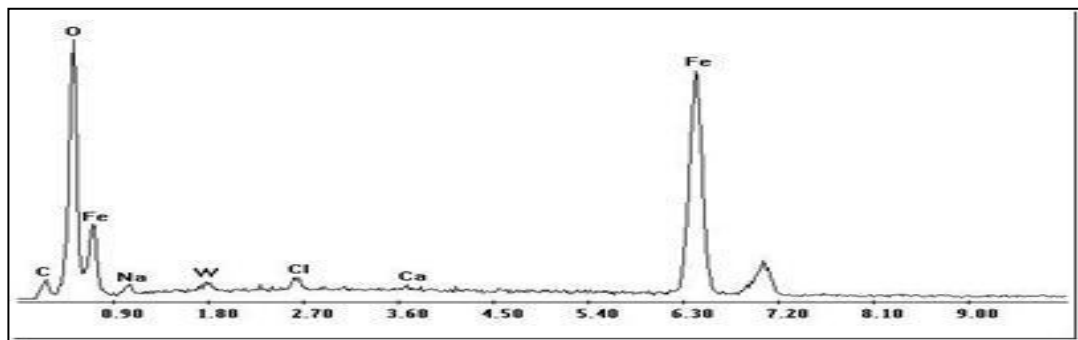
Figure 5.28, Corrosion Products of CP-Batch 1; (A) BSE image at 3200x (plate shape), (B) BSE image at 5000x (Needle like), (C) EDS spot analysis from the needle shape structures.

The general elemental analysis of corrosion products showed that 52 wt.% was mainly Fe and 29 wt.% was oxides. The needle shape was rich of FeO, NaCl, and small amount of FeCl while the plates shape is rich of FeCl. Visual examination was made after the completion of the tests and the coating groups were rated as shown in Table 5.6 and Figure 5.36.

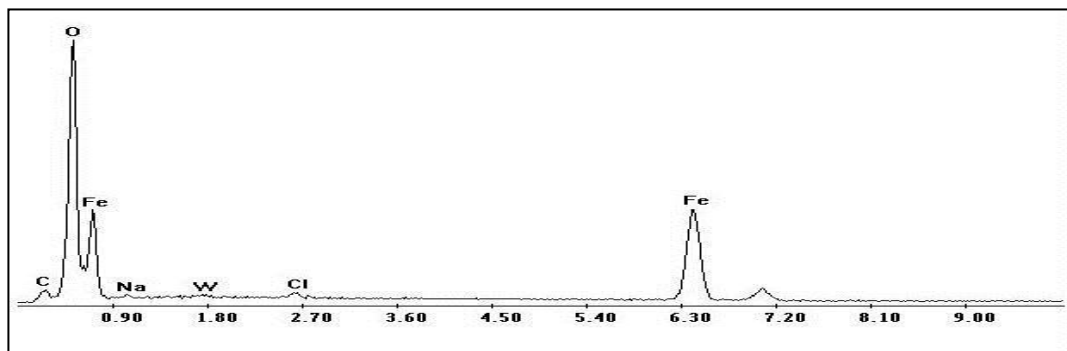


(A)

(B)



(C)



(D)

Figure 5.29, CP-Batch 2 BSE images and corresponding EDS spectra; (A) BSE image at 3200X, (B) BSE image at 5000X (fiber like), (C) General EDS analysis, (D) EDS analysis from the fiber like structures.

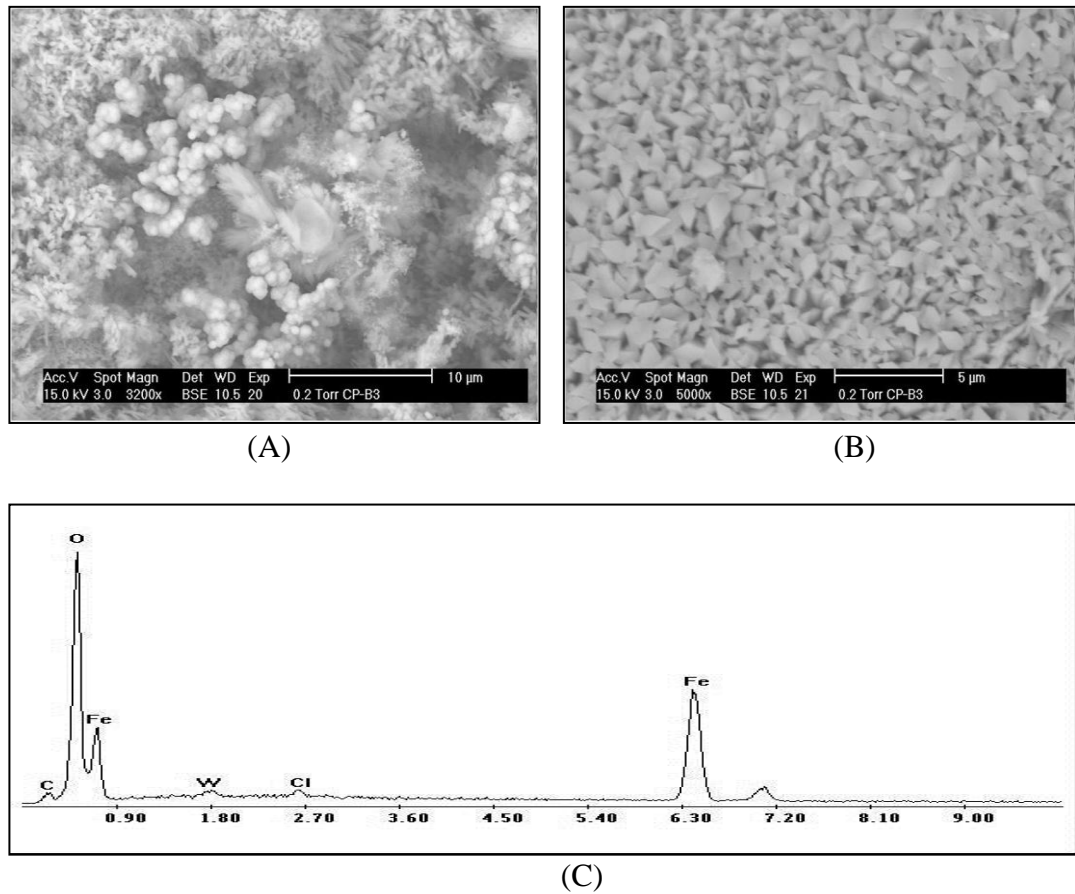


Figure 5.30, CP-Batch 3: BSE images and corresponding EDS spectrum; (A) BSE image at 3200X, (B) BSE image at 5000X, (C) EDS general analysis of the cubic shaped structured.

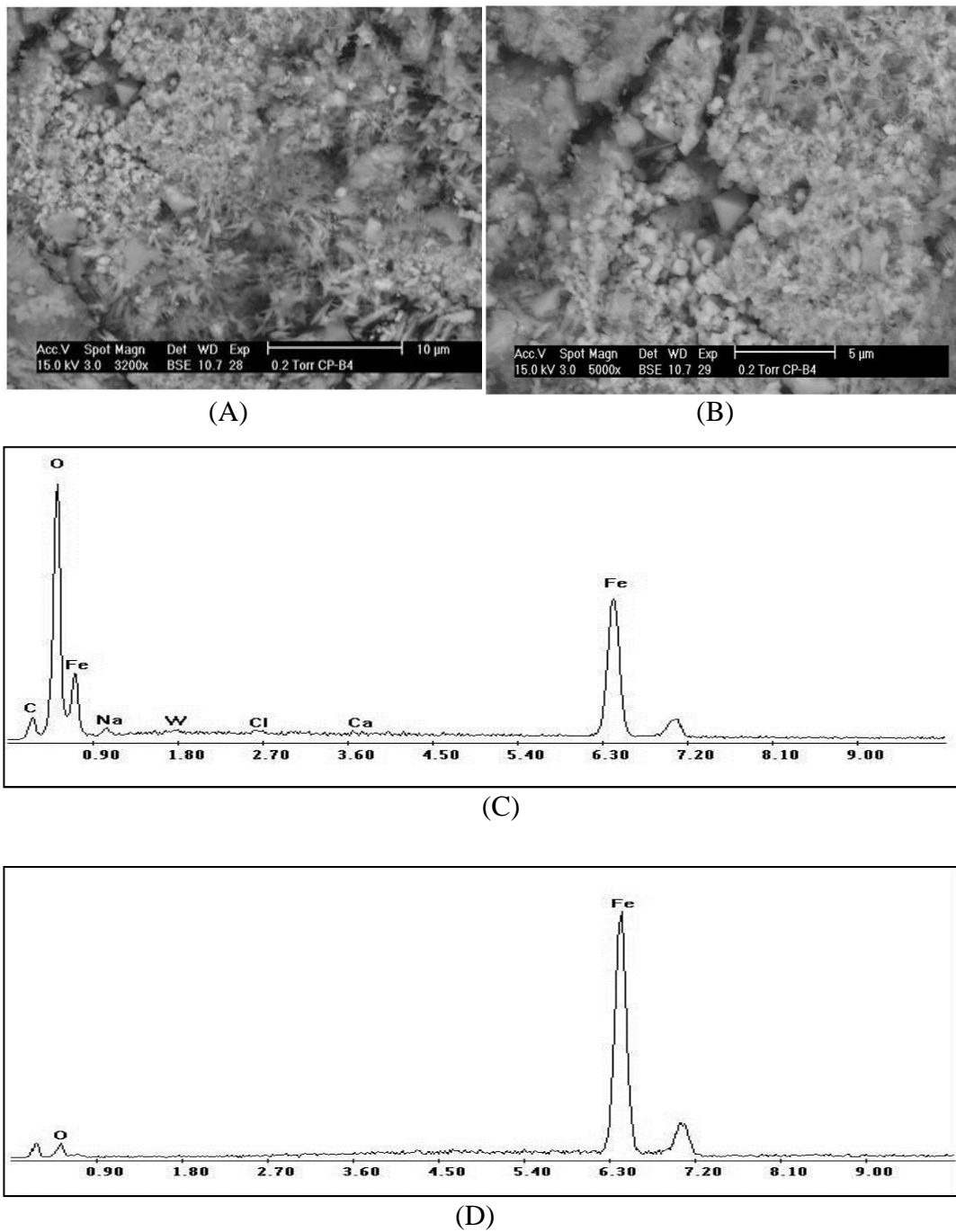


Figure 5.31, CP-Batch 4: BSE images and corresponding EDS spectra; (A) BSE image at 3200X, (B) BSE image at 5000x (shows irregular particle), (C) EDS general analysis, (D) EDS analysis of the cubic shaped structured.

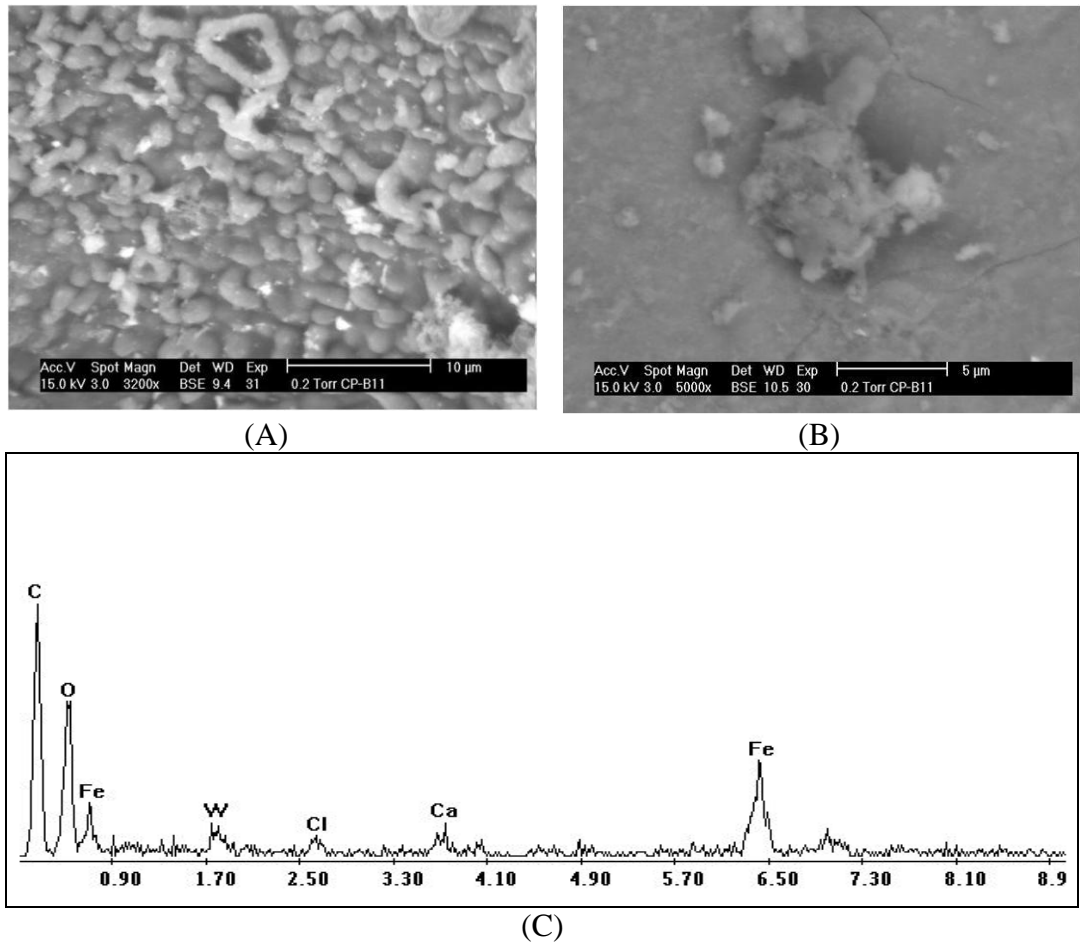


Figure 5.32, CP-Batch 11 BSE images and corresponding EDS spectrum; (A) BSE image at 3200X, (B) BSE image at 5000X, (C) EDS general analysis of irregular shaped particles.

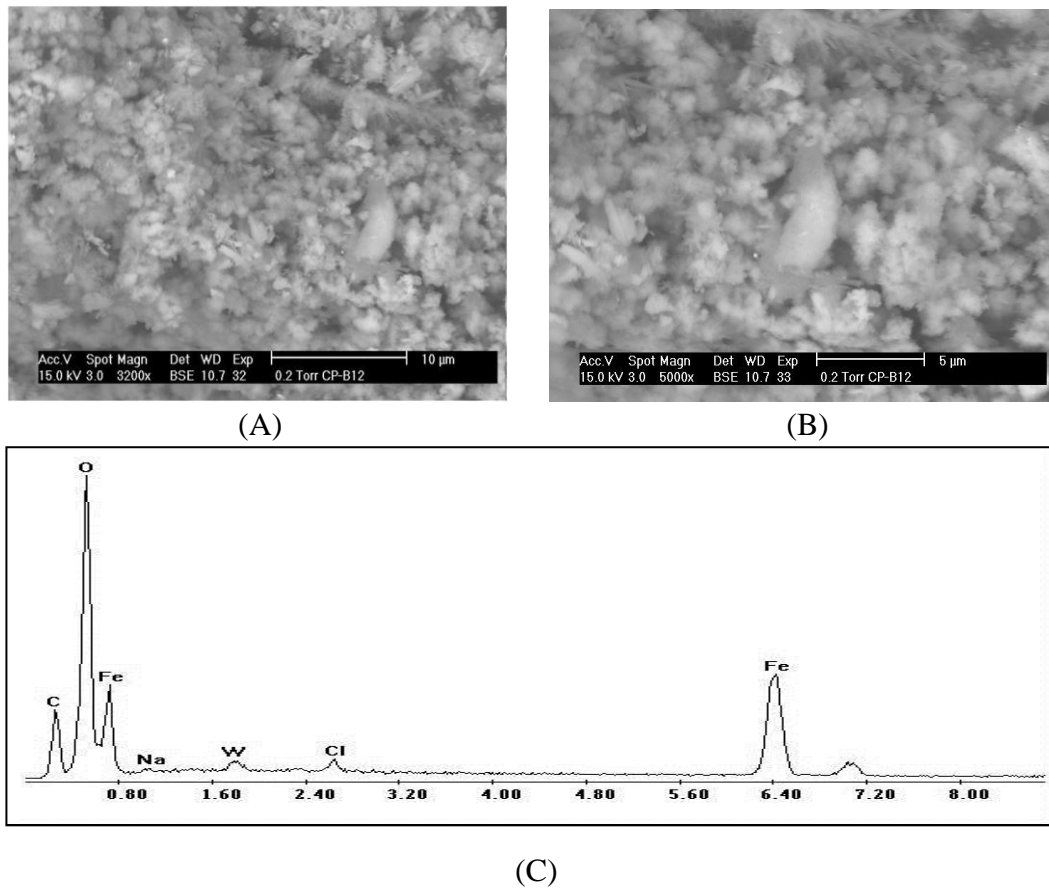
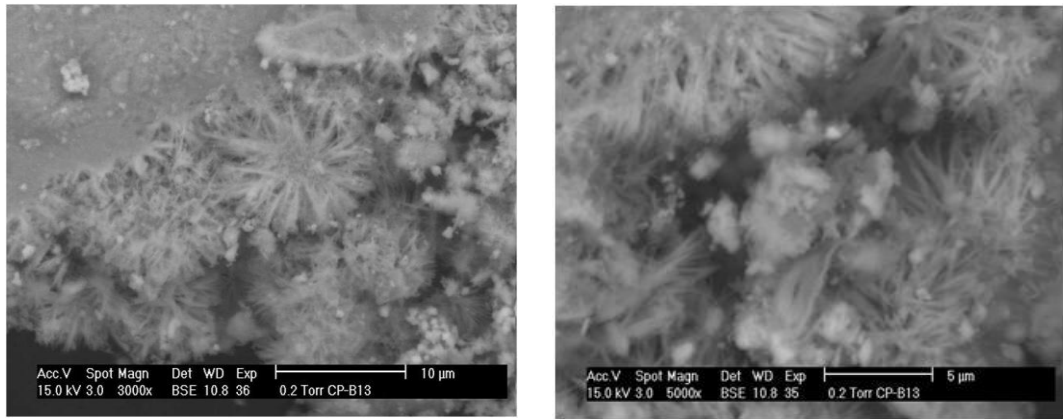
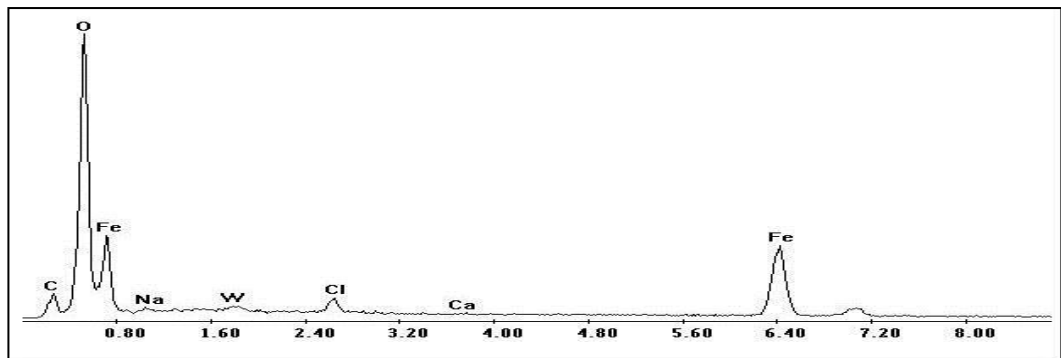


Figure 5.33, CP-Batch 12 BSE images and corresponding EDS spectrum; (A) BSE image at 3200X, (B) BSE image at 5000X, (C) EDS general analysis of irregular shaped particles.

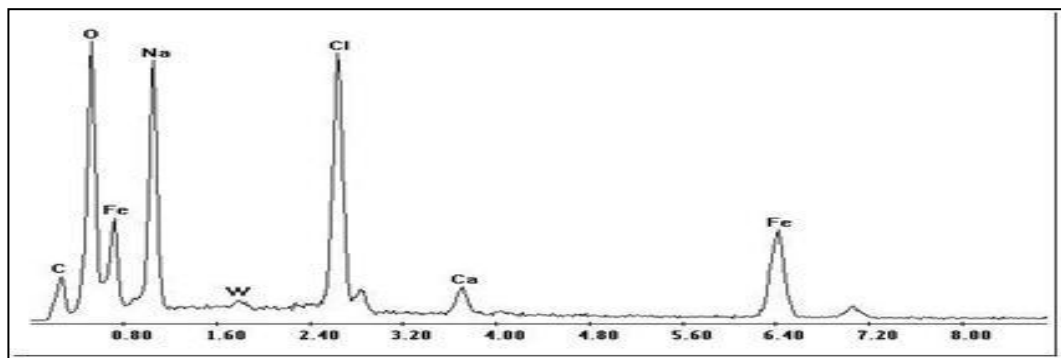


(A)

(B)



(C)



(D)

Figure 5.34, CP-Batch 13 BSE images and corresponding EDS spectra; (A) BSE image at 3000X, (B) BSE image at 5000X (needle shape), (C) EDS general analysis, (D) EDS analysis from the needle shaped structured.

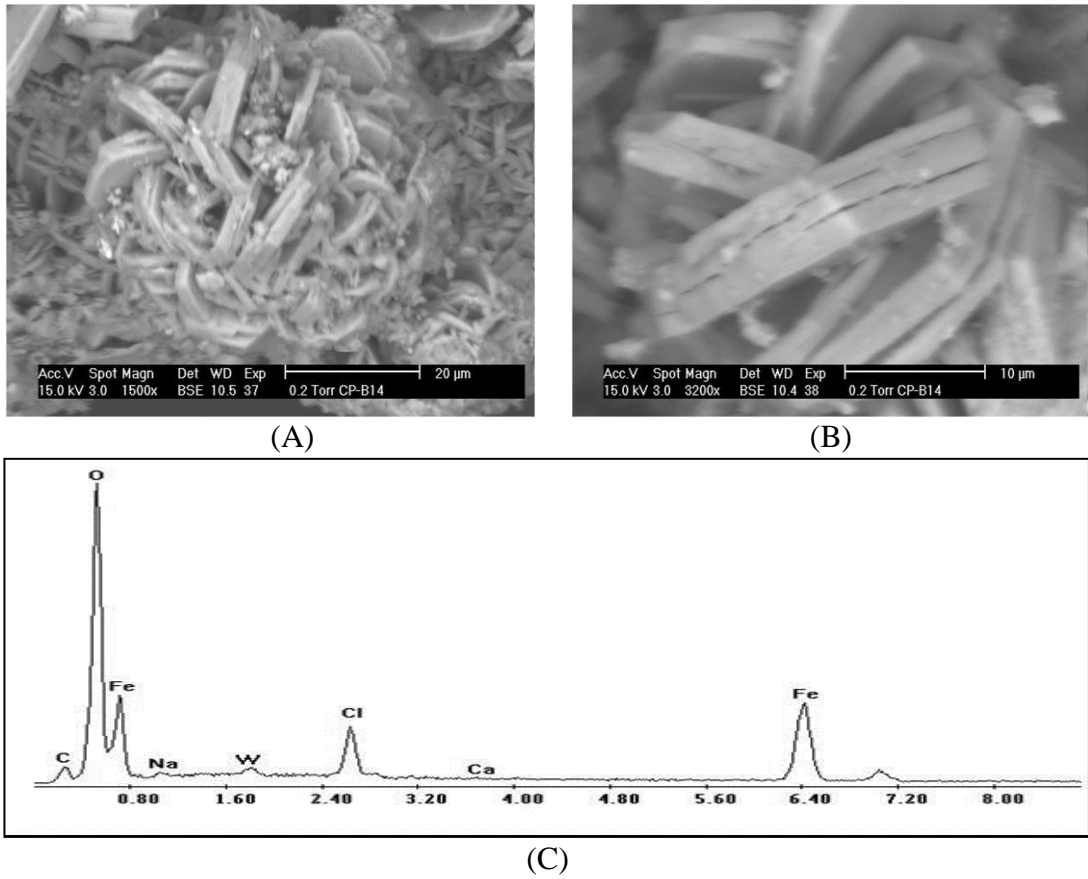


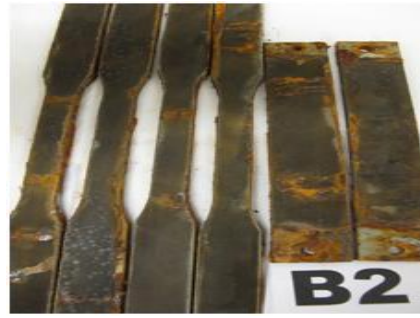
Figure 5.35, CP-Batch 14 BSE images and corresponding EDS spectrum; (A) BSE image at 1500X, (B) BSE image at 3200X, (C) EDS general analysis of the structures.

Table 5.6, Coating groups rating according to ASTM B 117 [162].

Area Failed %	Rating No.	Coating Batch
No failure	10	
0 To 1	9	
2 To 3	8	3, 4
4 To 6	7	1
7 To 10	6	2
11 To 20	5	13, 14
21 To 30	4	11
31 To 40	3	12
41 To 55	2	
56 To 75	1	
OVER 75	0	



Area Failed % 4 To 6= Rating No.7



Area Failed % 7 To 10= Rating No.6



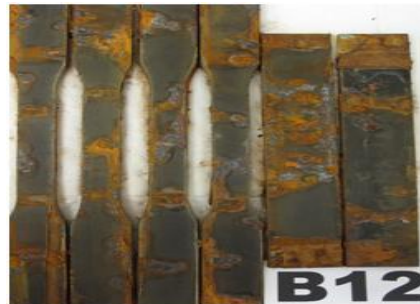
Area Failed % 2 To 3= Rating No.8



Area Failed % 2 To 3= Rating No.8



Area Failed % 21 To 30= Rating No.4



Area Failed % 31 To 40= Rating No.3



Area Failed % 11 To 20= Rating No. 5



Area Failed % 11 To 20= Rating No. 5

Figure 5.36, Visual Examination and corresponding rating of each coating batch.

WC–Co coatings have complex compositions that may lead to corrosion activity between the different microstructure and the composition of the coating (micro-galvanic corrosion) [153, 204]. The cobalt binder phase can form a galvanic coupling inside the coating structure. Thus the coupled cobalt-WC can affect the corrosion process [205, 206].

Due to this coupling, uniform corrosion may occur in the binder materials of WC–Co (between the WC particles and the Co binder) [206]. This test did not concentrate on studying the micro-galvanic corrosion however it may have existed.

5.2.1 Dissolution of the Binder Phase In the NaCl Solution

It was noticed from previous literature that Co can dissolve in NaCl at low percentages [208]. Cobalt is considered a strong oxidizing agent. It can exist in the +2 and +3 oxidation states (Baes and Mesmer [209]). Under oxidizing and moderately reducing conditions, the dominant cobalt aqueous species can be predicted by the use of Potential/pH diagram if the pH value of the solution is known. Potential/pH diagram is a thermodynamic diagram which shows the ability of metals to be attacked, dissolved or corroded at various pH and oxidation conditions. Thus it gives a guide to the stability of a particular metal in a specific environment.

The likely states of W and Co to be corroded for the pH range studied (pH= 6.5-7.2), as described in their Potential/pH diagrams (Figure 5.37 and 5.38), are when (Co^{2+}) and (WO_4^{2-}) are formed [210]. The laboratory analysis of the post test solution that was taken from the chamber drain showed that cobalt did not appear to form any important complexes with dissolved chloride obtained from NaCl nor carbonates that were obtained from base metal substrate or the powders, (Table 5.7).

This was due to the low acidity of the NaCl solution used in the test. Chemical analyses also showed that tungsten did not undergo any significant dissolution. However tungsten was detected in low percentages in the corrosion product using the EDS analysis. This concluded that the dissolution of the tungsten carbide binder phase in NaCl solution (pH 6.5-7.2) during the corrosion test was almost negligible.

Table 5.7, Post test solution analysis.

Bicarbonate	< 3.47 %
Calcium	< 0.9 %
Bromide	< 0.1 %
Chloride	< 3.1 %
Copper	< 0.3 %
Nickel	< 0.001%
Fluoride	< 0.1 %
Iodide	< 0.1 %
Potassium	< 0.001%
Sulfate	< 0.02%
Sodium	<1.9%
Magnesium	< 0.1%
Iron	< 1.94%
Total Impurities	< 0.27 %

Conductivity @ 25°C= 20 μ S/cm
Specific gravity @ 15.5 °C =1.0325

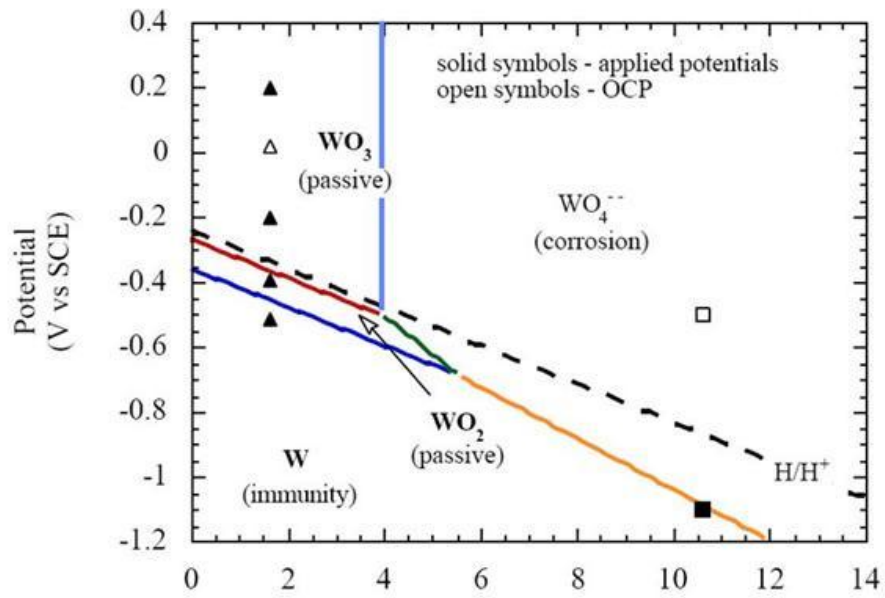


Figure 5.37, Potential/pH diagram for tungsten [211].

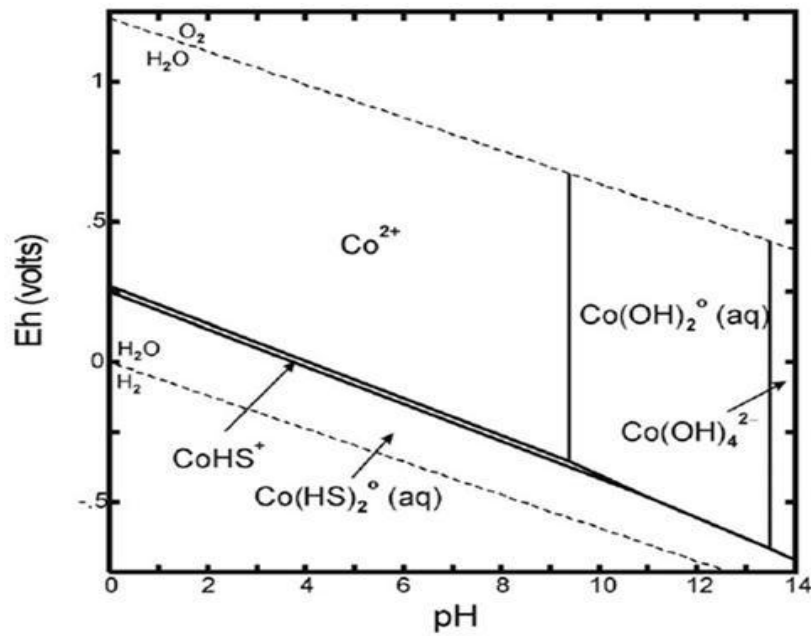


Figure 5.38, Eh-pH Diagram of dissolved cobalt in the presence of dissolved chloride, nitrate, sulfate, and carbonate [212].

5.2.2 Corrosion Mechanism

Tungsten was detected in small percentages in all samples. The source of W was not mainly due to corrosion. It could be from the mills when using sand paper to collect the corrosion products. Since there was no cobalt detected by the EDS analysis, this indicated that no dissolution of the tungsten carbide binder occurred during the corrosion test. The source of the Na and Cl came from the salt solution. Ca is a contamination that would have come from the coated epoxy materials used to protect the uncoated areas of the substrate.

Iron (Fe) was detected in the solution of all coatings after salt spray tests. The iron content in the solution indicated that the substrate was exposed to the solution due to the breakup of the protected epoxy layer during the test and the attack of the corrosive solution on the base metal. ESEM showed different morphology of corrosion product such as platelet-like, fiber-like, needles, irregular, and flower shaped which depended on type of oxides and tungsten carbides in the samples.

During the HVOF or Plasma thermal spray processes, oxidation occurred on the surface of the coatings [213]. As the oxidation of the particle surfaces during HVOF thermal spray occurs in an oxygen/fuel environment and at high temperatures in the plasma spray, a particular oxide layer can be formed. The oxide layers on the particle surfaces can form a network inside the coating [214], and can form an oxide layer that covers the top surface of the coated specimens. The oxide layer can act as an anticorrosion film. This film is subject for removal when the test specimens were degreased using acetone before they placed in the salt spray chamber.

The density of a coating is very important for resistant oxide layers network. HVOF sprayed particles possess higher speed with lower temperature. Such particles impinge onto a target substrate often in the semi-molten state and build up

to form coatings. Denser coatings can be fabricated by the HVOF process with compare to plasma spray process. [215]

The denser the coating the less porosity and the more resistant it is to corrosion [216]. Table 5.6 and Figure 5.36 clearly show that coating groups Batches 1, 2, 3, and 4 which were coated using the HVOF system have fewer spots of corrosion products than coating groups Batches 11, 12, 13, and 14 which were coated by the Plasma system, subjected to same conditions in spite of Batches 13 and 14 contained AMDRY which indicates that coating porosity is the main factor in resisting corrosive particles to penetrate to the base metal, promoting HVOF in this case.

The coating thickness also influences the type of corrosion that takes place in thermally sprayed coating systems. As coating thickness increases, the number of interconnecting porosity leading to the coating/substrate interface decreases [84]. However in this study, the coating thickness effect was eliminated because all coating specimens have almost the same coating thickness (total of approximately 460 microns).

5.2.3 WC-Co Powder Size Effect

Some previous studies [208] on the effect of WC grain size on the corrosion resistance of WC-Co concluded that the corrosion rate of the coating with smaller WC grain size was lower than that of the coating with larger WC grain size. Hence, WC-Co coating with the smaller WC grain size showed a higher corrosion resistance. In this study and based on results obtained, the effect of WC grain size on the corrosion resistance could not be confirmed when comparing Batch 1 to Batch 2 or Batch 11 to Batch 12 (Table 5.6 and Figure 5.36). It can be concluded that WC grain size was not a major contributor to the corrosion resistance, compared to the porosity of the coating.

5.2.4 AMDRY Powder Effect

Coating groups that numbered Batches 3, 4, 13, and 14 provided very effective protection against corrosion in NaCl solution compared to other groups of coatings coated by same system (HVOF/plasma) but had no AMDRY. This may be related to the existence of NiCrAl elements in the AMDRY powder that were mixed with the WC-Co powder. NiCrAl was reported by Godoy et al [84], to have high corrosion resistance when used in a duplex coating system. This system also has superior abrasive wear resistance than the non-duplex WC-Co system, under both severe and mild wear conditions. However, WC-Co HVOF sprayed micro and nano (Batch 1 and 2) were better than multilayered plasma Batch 13 and 14 due to lower porosity.

Results confirmed that mixing AMDRY powder with WC-Co powder enhanced the corrosion resistance of the WC-Co cermet coating by reducing the affected areas of the coating and minimizing the corrosion products (Table 5.6 and Figure 5.36). Amongst the eight coated groups, coatings produced by HVOF and mixed powders were the most effective coating systems in preventing corrosion (rated 8 out of 10). Figure 5.36 shows that Batch 3 and 4 were equally rated despite use of micro and nano sized WC-Co however.

5.3 EROSION-CORROSION BEHAVIOUR OF THERMALLY SPRAYED COATINGS

The test results revealed that no significant erosion-corrosion damage was observed in all coatings after exposure to the erosion-corrosion environment applied for about 120 hours. There were no propagation of sub-surface cracks found. The coating material losses obtained from the mass measurement were very small (maximum loss = 0.035 gram). This was confirmed by measuring the chemical analysis of the fluid and residuals (scale deposit after filtration) after each test, (Table 5.8 and Figure 5.42). There was no indication of precipitation of

coating materials in the medium. Chemical analysis showed that some of the materials related to leak sealed materials, salts, and erodent's.

Figure 5.39, shows the average mass loss recorded for the HVOF and Plasma coatings. More coating material losses (almost 3 times) were exhibited in plasma sprayed coatings compared to the HVOF coatings for WC-Co only deposits. The coating porosity and hardness play an important role in this regard. The addition of the AMDRY powders helped to decrease the coating material loss in three out of four coatings. This was due to AMDRY acting as anticorrosion (barrier) and the coating material loss recorded in these coatings can be assumed to be attributed to the erosion effect of the jet system. Coating produced by the deposition of micro WC-Co and AMDRY by plasma (Batch 13) was the best over plasma produced coatings in resisting the erosion-corrosion (Figure 5.40). However, the coating produced by the deposition of nano WC-Co and AMDRY by HVOF (Batch 4) performed the best behaviour in resisting the erosion-corrosion among all HVOF and plasma coatings (Figure 5.41). This is due to its high density (due to Nano particles), low porosity (1.15%), and had AMDRY added to its original powders.

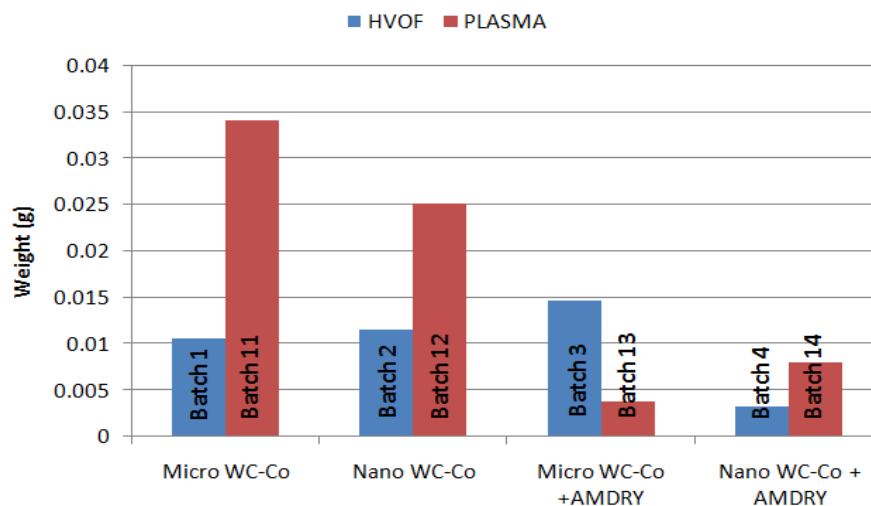
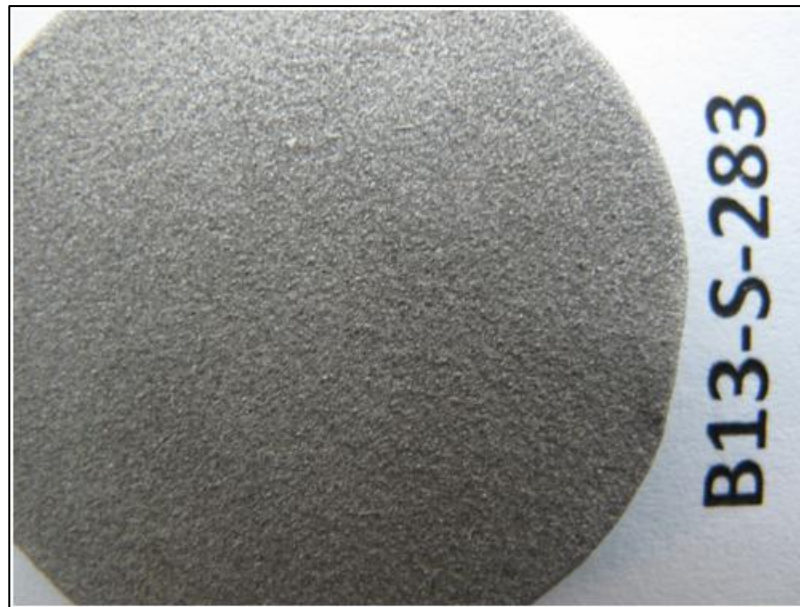


Figure 5.39, Coating materials losses due to erosion–corrosion combined effect.

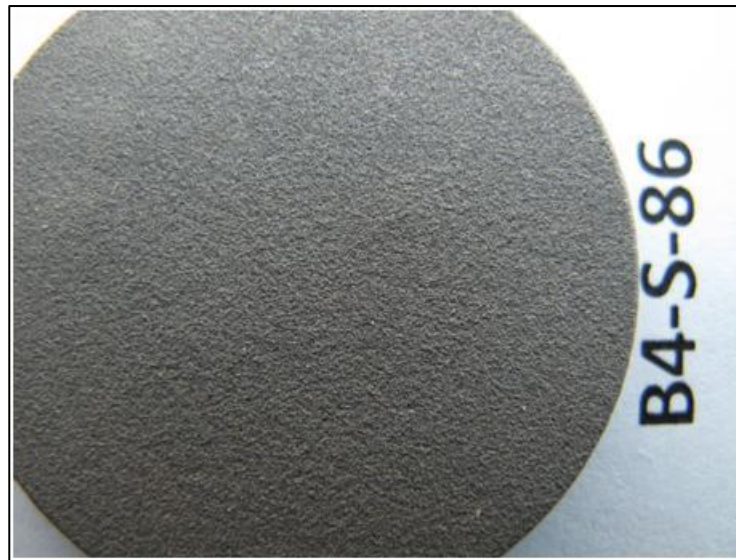


A- Pre- test

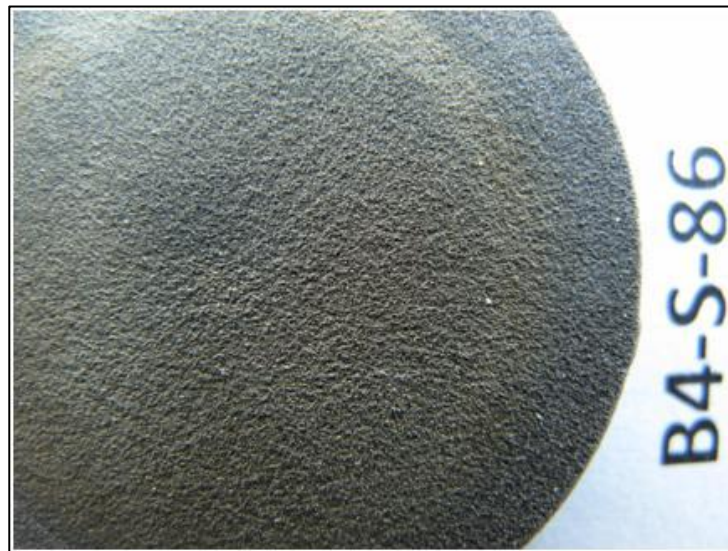


B- Post- test

Figure 5.40, Plasma coatings (Batch 13), pre and post test erosion corrosion.



A- Pre-test



B- Post-test

Figure 5.41, HVOF coatings (Batch 4), pre and post test erosion corrosion.

The expected erosion mechanism that governs the mass loss in these coatings can be related to the very high impact energies of the jet eroding particles which removed parts of exposed soft binder materials of the coating. The eroding particles can also work to weaken the interface of the hard coating materials (W_2C) and cobalt matrix after repeated solid particle impacts. This may lead to loss of hard coating materials as well [217].

Table 5.8, Analytical report of the jet fluid after test termination.

	Value	Unit
Bicarbonate	109	mg/L
Carbonate	0	mg/L
Hydroxide	0	mg/L
Chloride	18153	mg/L
Sulfate	2705	mg/L
Calcium	307	mg/L
Potassium	370	mg/L
Magnesium	1088	mg/L
Sodium	9884	mg/L
Conductivity @ 25 C	>1000	Micro omhs
pH @ 25 C	7.6	
Total Dissolved Solids	32246	mg/L
Specific Gravity @ 60 F	1.0259	

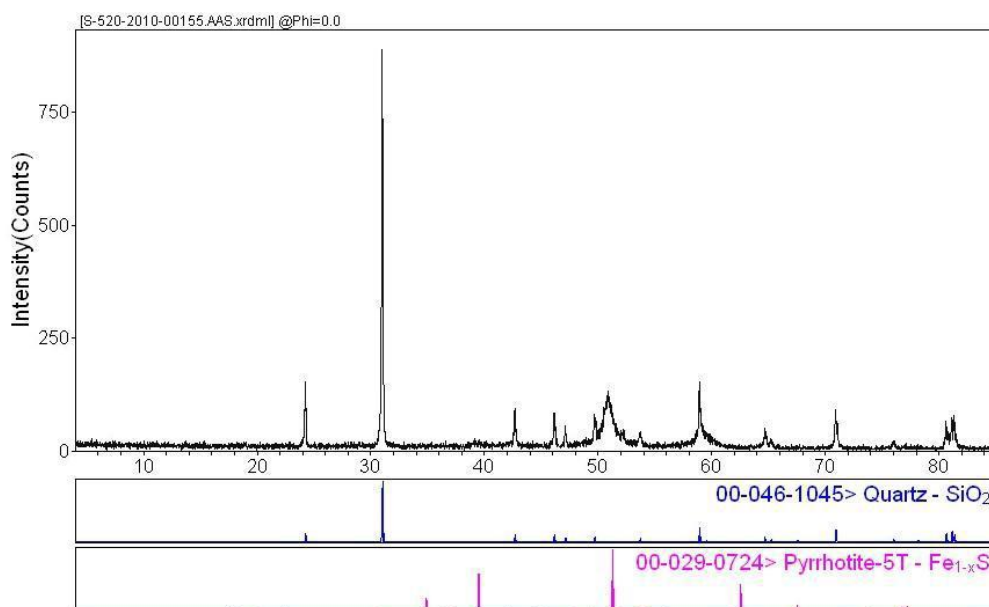


Figure 5.42, Scale sample analysis by XRD, collected after jet impingement test, showing no coating materials in the residual product.

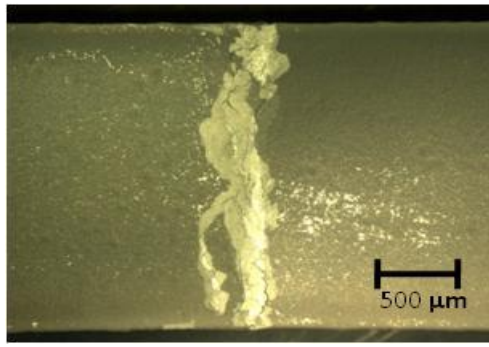
5.4 MECHANICAL BEHAVIOUR OF THERMALLY SPRAYED COATINGS

5.4.1 Three Points Bending Test

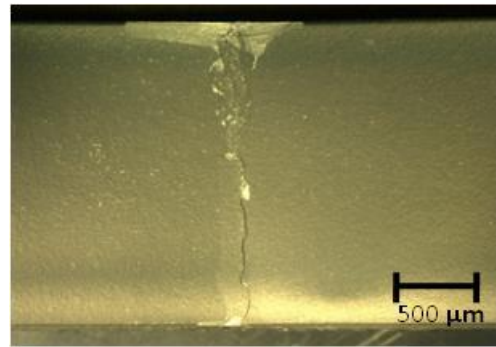
In all of the tested coatings, the crack initiated at the coating top surface due to the bending force and propagated through the coating thickness. Close examination of the coatings revealed that no major deformation was observed due to the strong bonding to the base metal. Only small coating delamination was noticed around the coating edge of some plasma sprayed coatings. No defects were detected in the coating/substrate interface.

More cracks in coatings produced by spraying the nano-powders compared to coatings produced from the micro-size powders. However, wider cracks (20-50 μm) resulted from coatings produced from the micro-size powders. The crack extended straight along the coating surface. Crumbling of the coating material was not noticed, the cracks resulted from coating material separation (binder phase).

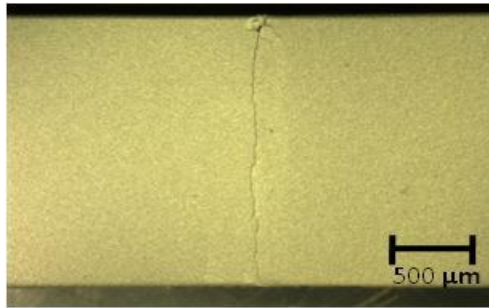
The addition of AMDRY powder reduced the number of cracks in coatings but created more cracks in the coatings produced by plasma coating. This may add more ductility to the coatings and strengthen the bonding force between the coating particles. Figures 5.43 and 5.44 show the inside and outside bend shape of some of the tested specimens after the three points bending test.



HVOF-Micro-WC-Co



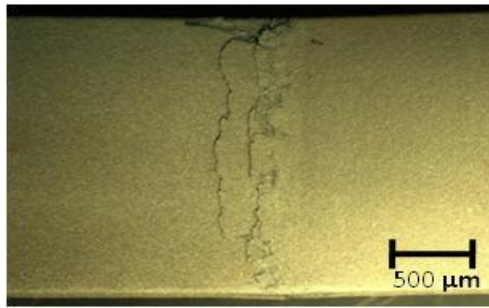
HVOF-Nano-WC-Co



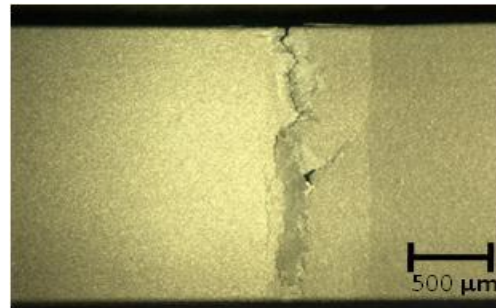
HVOF-Micro-WC-Co + AMDRY



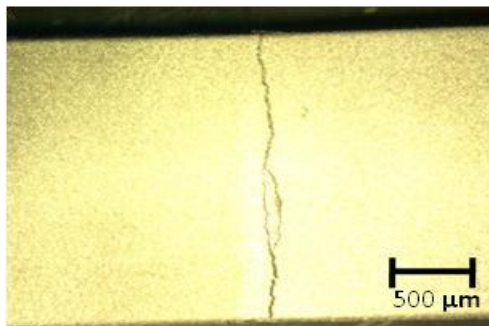
HVOF-Nano-WC-Co + AMDRY



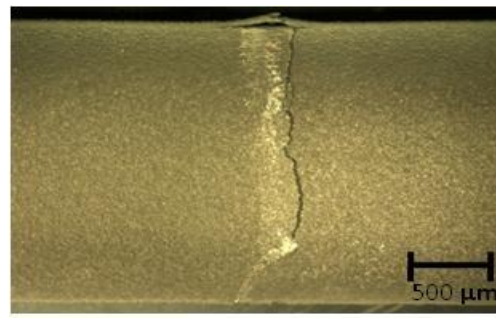
Plasma-Micro-WC-Co



Plasma-Nano-WC-Co

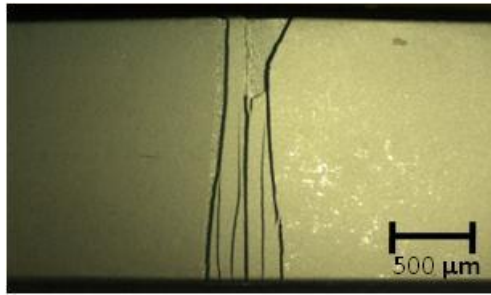


Plasma-Micro-WC-Co + AMDRY

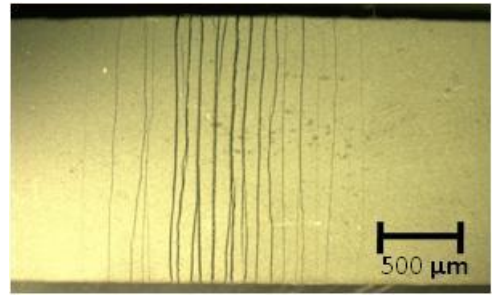


Plasma-Nano-WC-Co + AMDRY

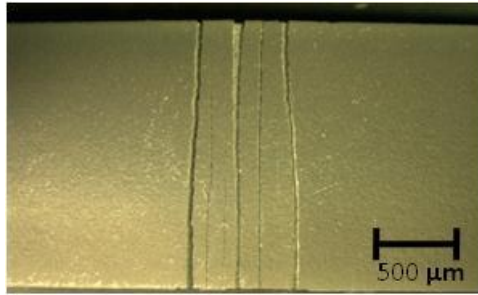
Figure 5.43, Test specimens after the three points bending test which show coatings cracks on the inside bend (U-shape).



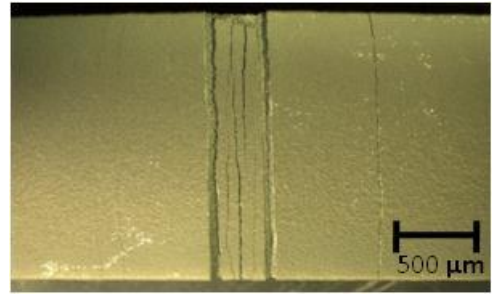
HVOF-Micro-WC-Co



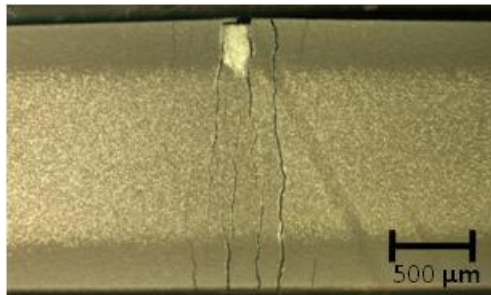
HVOF-Nano-WC-Co



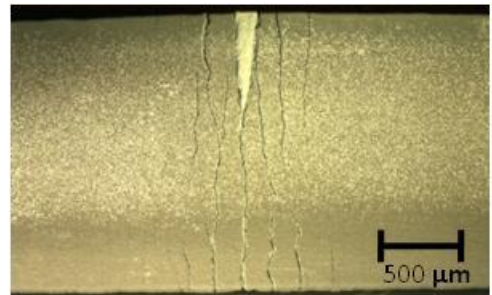
HVOF-Micro-WC-Co + AMDRY



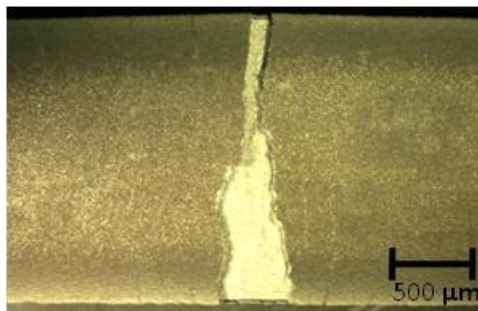
HVOF-Nano-WC-Co + AMDRY



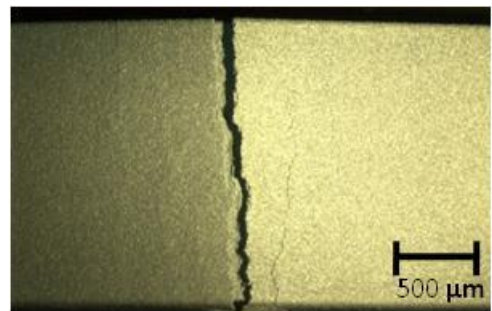
Plasma-Micro-WC-Co



Plasma-Nano-WC-Co



Plasma-Micro-WC-Co + AMDRY



Plasma-Nano-WC-Co + AMDRY

Figure 5.44, Test specimens after the three points bending test, the outside bend.

The stress-strain curves (Figures 5.45- 5.48) showed similar behaviour for the same coatings sprayed using the same coating systems. Almost the same bending force was required for the three points bending test for all thermal coatings that were generated by the same coating system. More force was required to bend HVOF thermal coatings compared to plasma thermal sprayed coatings (700-900 MPa for HVOF coatings and 500-600 MPa for Plasma coatings, 400 MPa for the substrate base metal). HVOF coatings are very dense and have less porosity than plasma coatings. The coatings that were produced by the nano-size powders particles required more load fracture/bend than the coatings produced by micro-size powders (5-10 % more). The applied load can be related to coating hardness. It was observed that, as the hardness of the coating increased, more load was required for the three bending test.

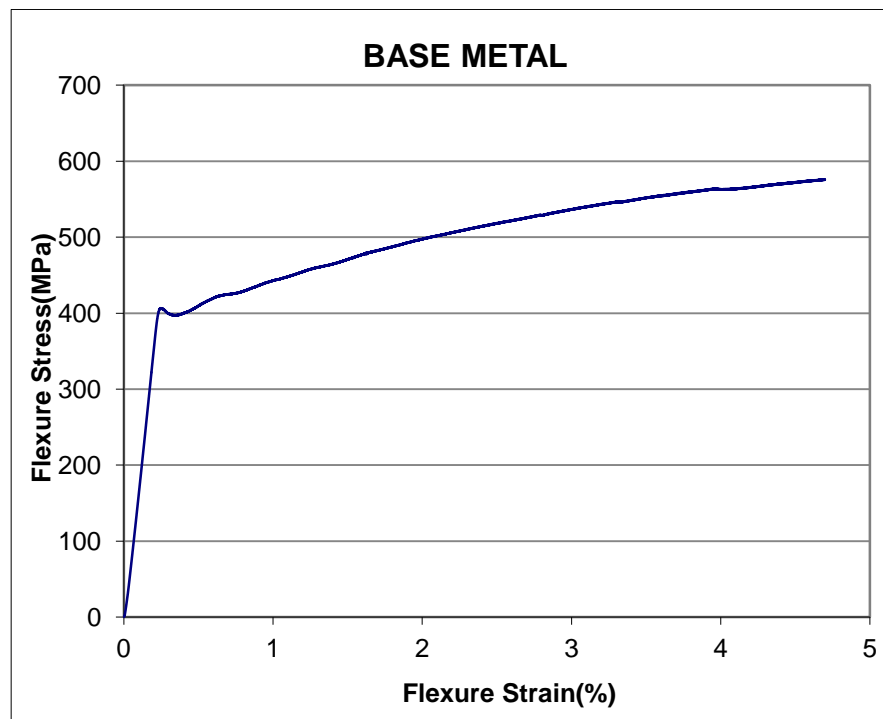


Figure 5.45, Flexural propriety resulted from applying the three points bending test on substrate base metal.

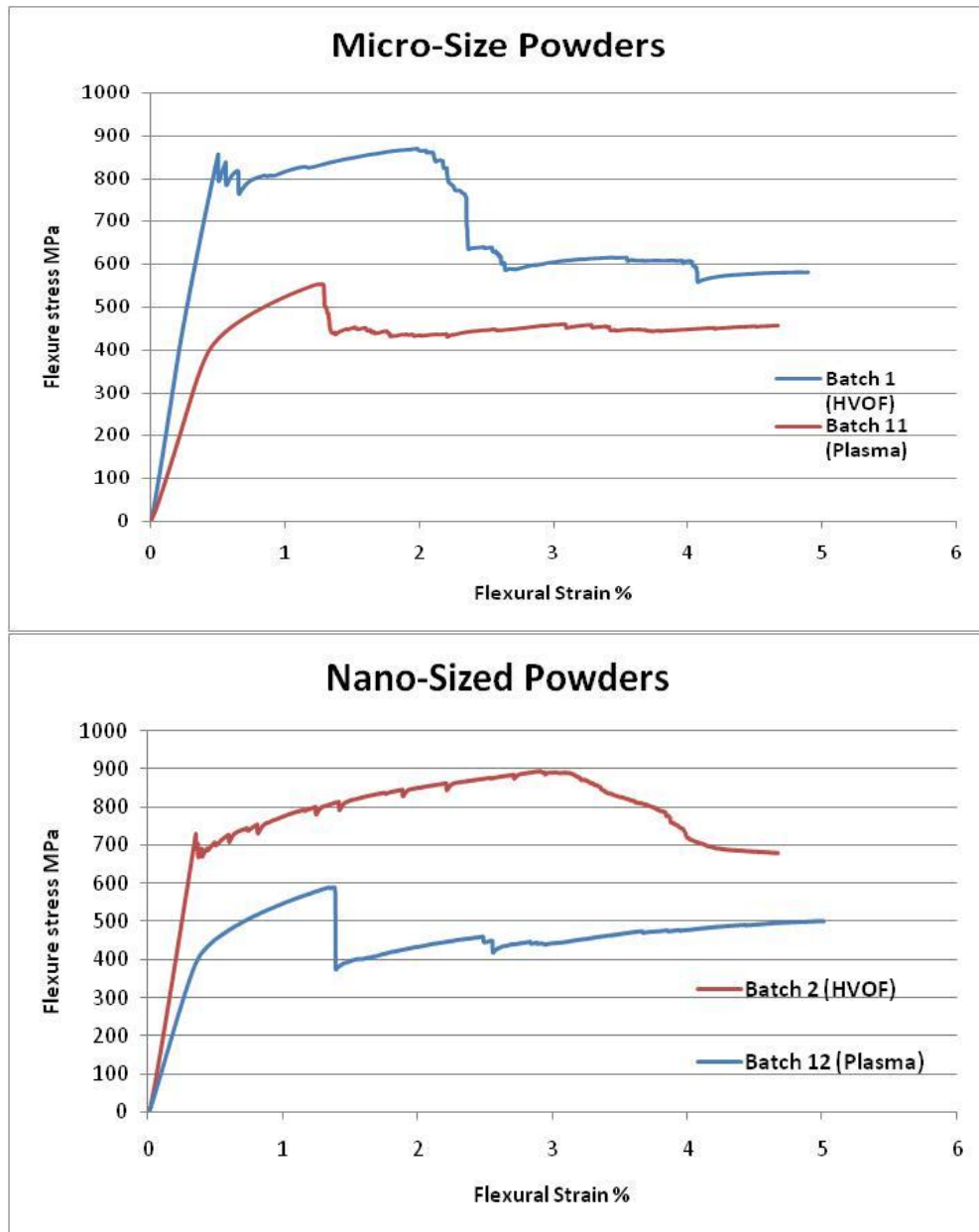


Figure 5.46, Process effect on coating flexural propriety resulted from applying the three points bending test using different powder size.

Figure 5.46 shows that higher yield strength (834 MPa) of coatings produced by spraying the micro-sized WC-Co by HVOF compared to coatings produced by spraying same powder by plasma system (yield strength = 437 MPa). The graph shows that Batch 1 coatings are stiffer than Batch 11. Similarly when nano-sized

WC-Co was used, HVOF coatings (Batch 2) had a yield strength of 712 MPa and stiffer than plasma coating Batch 12 (yield strength = 413 MPa). It can be concluded that nano-sized powders gave lower yield strength for the produced coatings but slightly stiffer than the coatings produced by deposition of micro-sized WC-Co powders.

The addition of the AMDRY coating to the main WC-Co powder seems to provide more ductility to the coating as shown in Figures 5.47 and 5.48. Flexural extension was higher when AMDRY was added to the WC-Co powders. Almost same load required for bending but more flexural strain (2-4%) resulted from AMDRY addition (flexural modulus can be used as an indication of coating stiffness). AMDRY added coatings showed slightly lowered yield strength in both HVOF and plasma coatings and it did not affect stiffness by a significant degree. AMDRY powders had lower effect in terms of coatings yield strength and stiffness in plasma coatings when compared to HVOF coatings. Micro-sized HVOF coatings (Batch 1) had the best yield strength, stiffness were almost the same for coatings.

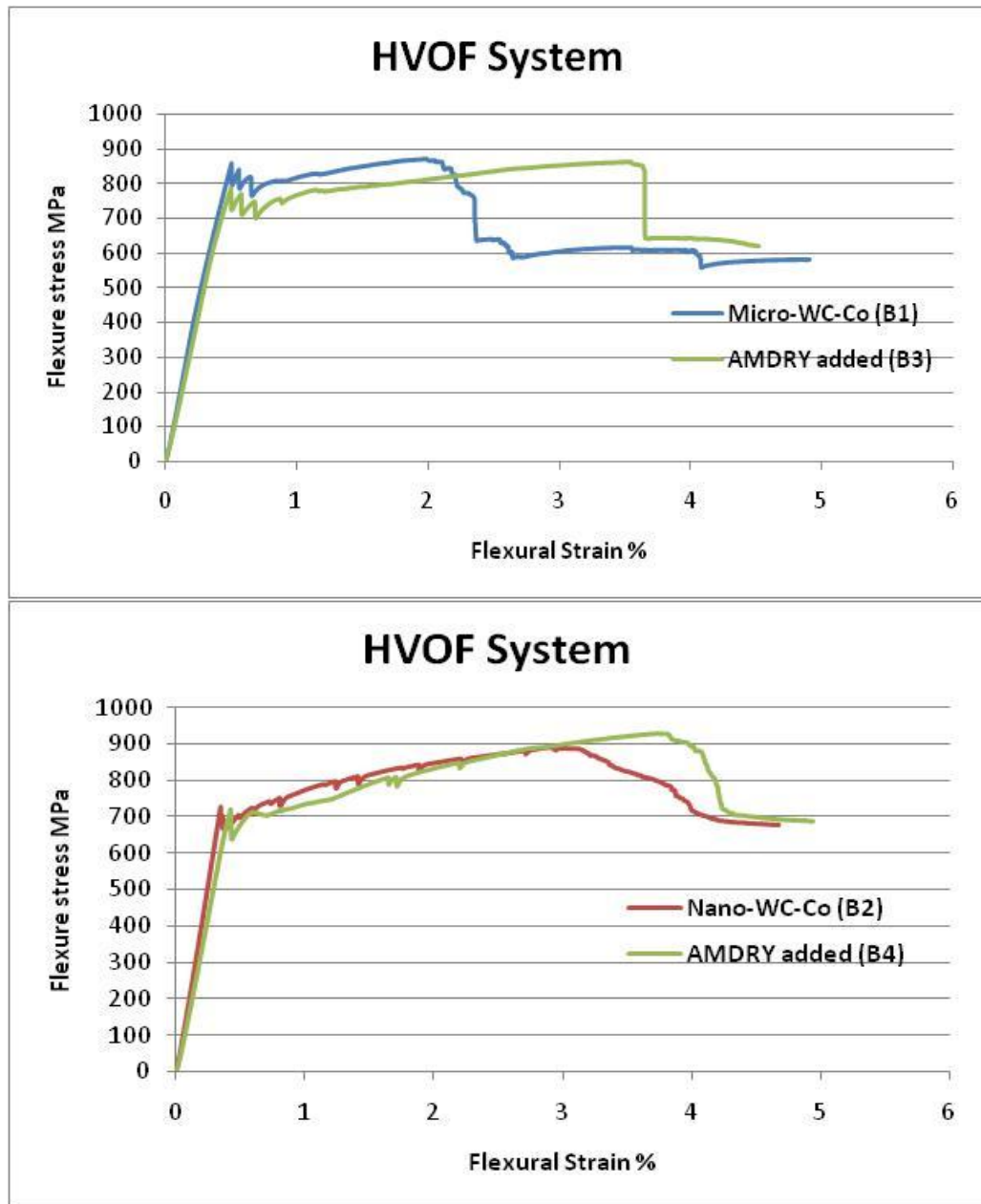


Figure 5.47, AMDRY powder effect on HVOF coating flexural propriety resulted from applying the three points bending test.

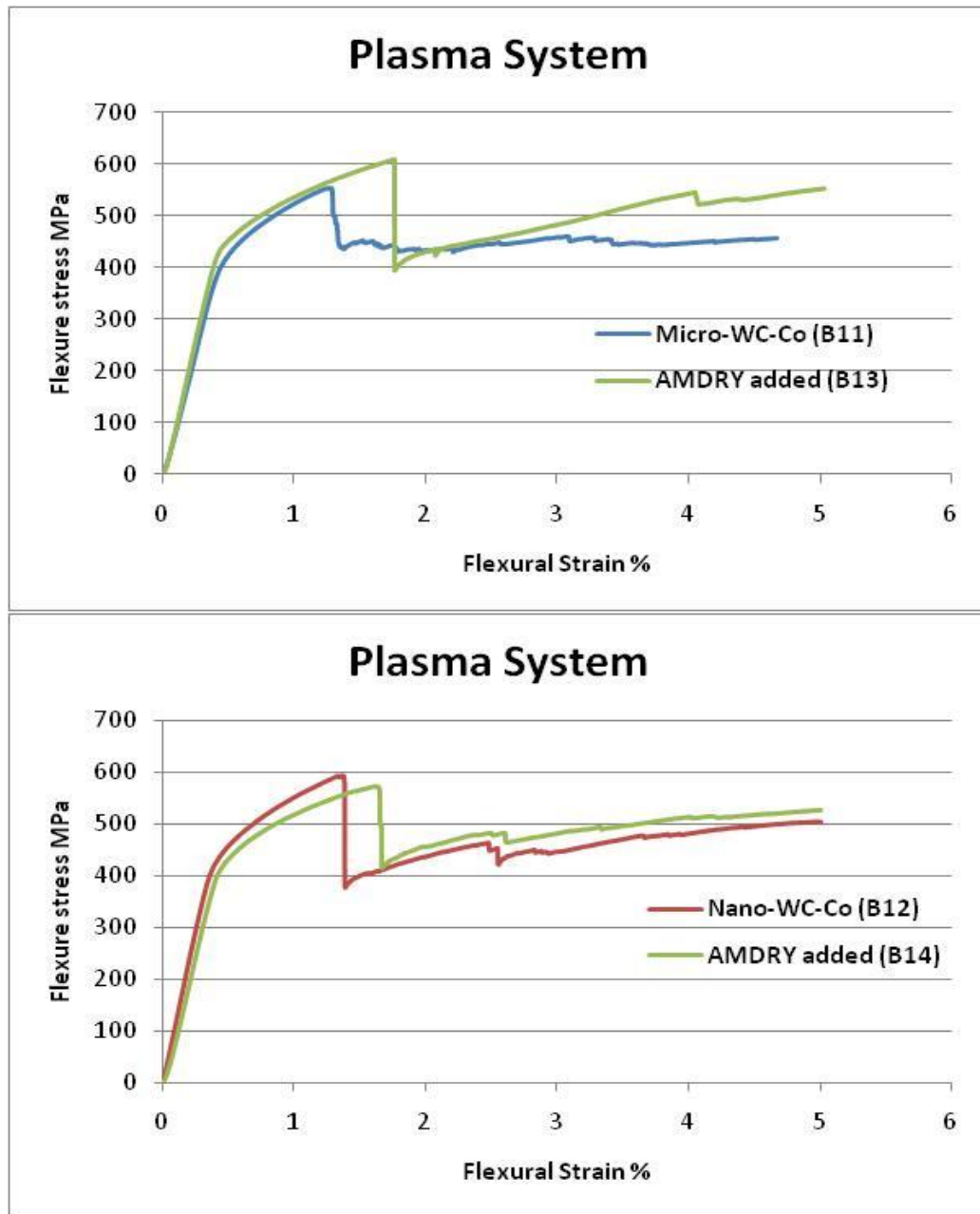


Figure 5.48, AMDRY powder effect on plasma coating flexural propriety resulted from applying the three points bending test.

Corrosion effect versus coating flexural strength property

Investigating the effect of corrosion of thermally sprayed coatings when subjected to a three-point bending test can be represented by comparing the load and flexural displacement characteristics obtained from the three-point bending tests for as coated and corroded specimens.

In all HVOF types of coatings, fewer loads (6-16 % less) were required for the corroded samples to undergo the three points bending test, Figure 5.49. Since the plasma coatings were affected more by corrosion during the corrosion test, it underwent the bending test when two third of the force was applied. The penetration of corrosive electrolyte ions through the coating via irregularities or defects in the coating and forming the iron oxides weakens the coating layers and decreased its bending force [163]. Higher loads were required to bend the corroded sample of the HVOF Batch 2 coatings than other corroded samples. Batch 3 reduced in load supported by the least for any coating combination.

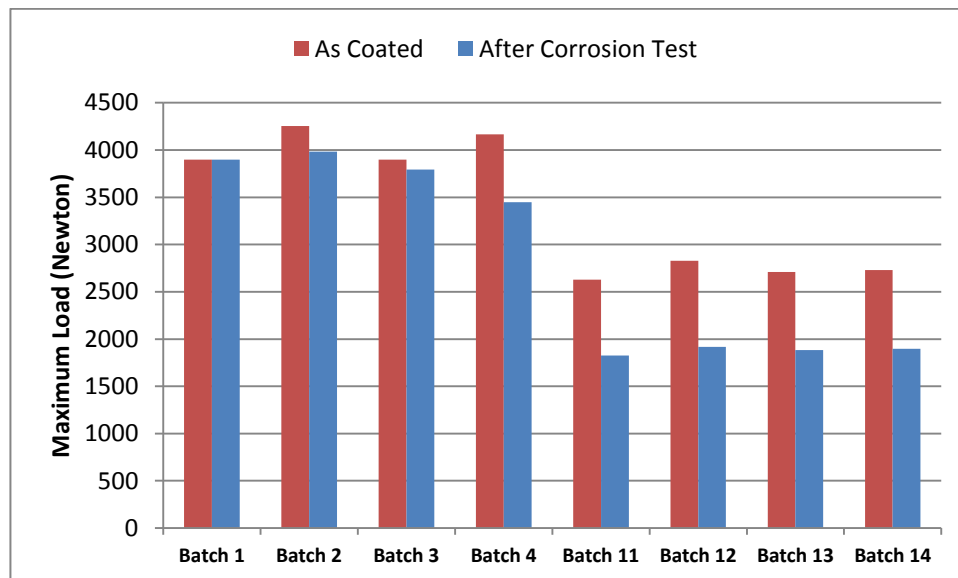


Figure 5.49, Maximum load required to undergo the bending test.

5.4.2 Tensile Test

The tensile yield strength of substrate material is shown in Figure 5.50 (280 MPa). The Stress-Strain curves (Figure 5.51 and 5.52) show that the HVOF sprayed micro and nano WC-Co powders exhibit almost the same behaviour. The tensile bonding strength of the nano coatings was 5% more than the tensile bonding strength of the micro coatings. During the test, both coatings displayed good behaviour; there were no fractures/peeling of the coating materials when the coatings underwent extensions of 8 mm. Only small cracks initiated and propagated horizontally along the spaceman width. Coating delamination was not observed during the testing of HVOF-micro/nano coatings.

In the plasma produced coatings, identical tensile behaviours were obtained for coatings produced by micro and nano WC-Co powers. During the tensile process, many small cracks were initiated in the coatings. Once both coatings passed the 8 mm extension, small pieces of coatings fractured. No coating delamination was noticed at the coating/substrate interface.

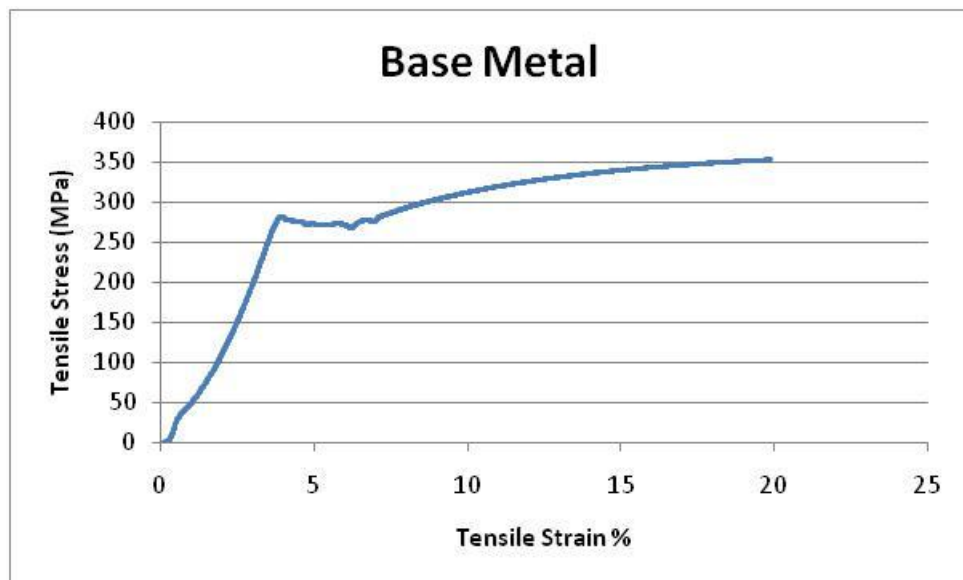


Figure 5.50, Stress-Strain curve resulted from tensile test applied on uncoated substrate.

Process and powder size effect on tensile behaviour:

In both HVOF and plasma coatings, Figures 5.51 and 5.52 showed that both micro and nano sized produced coatings had the same stiffness when subjected to tensile forces but the micro-sized coatings had higher yield strength than the nano-sized coatings. Batch 2 coating which resulted from deposition of the nano-sized WC-Co powder using HVOF gave the best yield strength of 305 MPa.

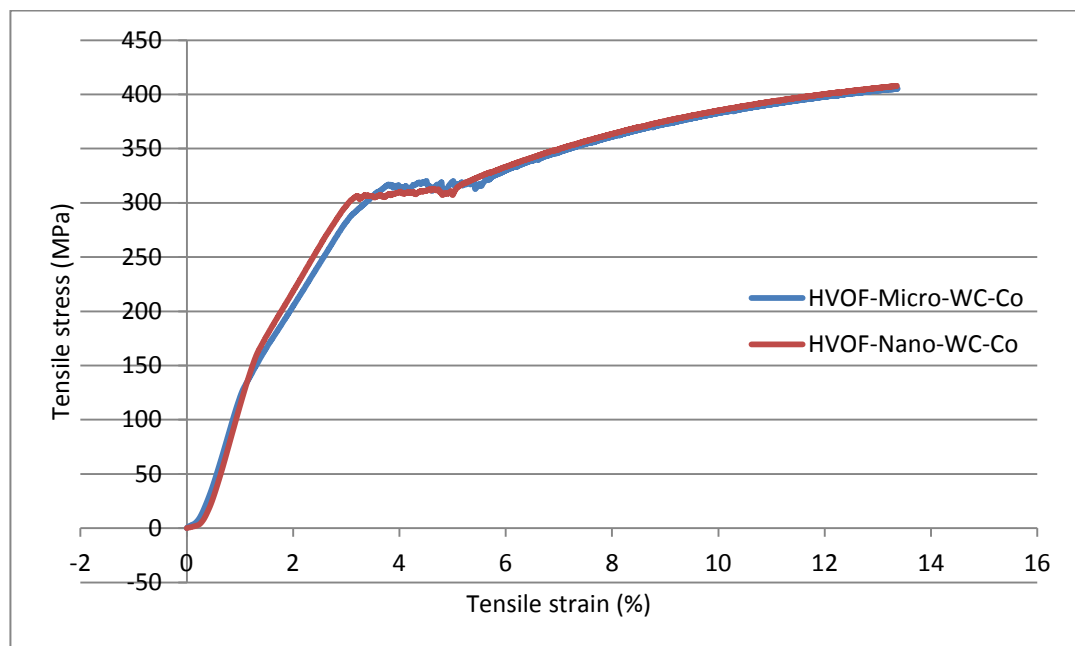


Figure 5.51, Stress-Strain curve resulted from tensile test showing powder size effect on HVOF coating.

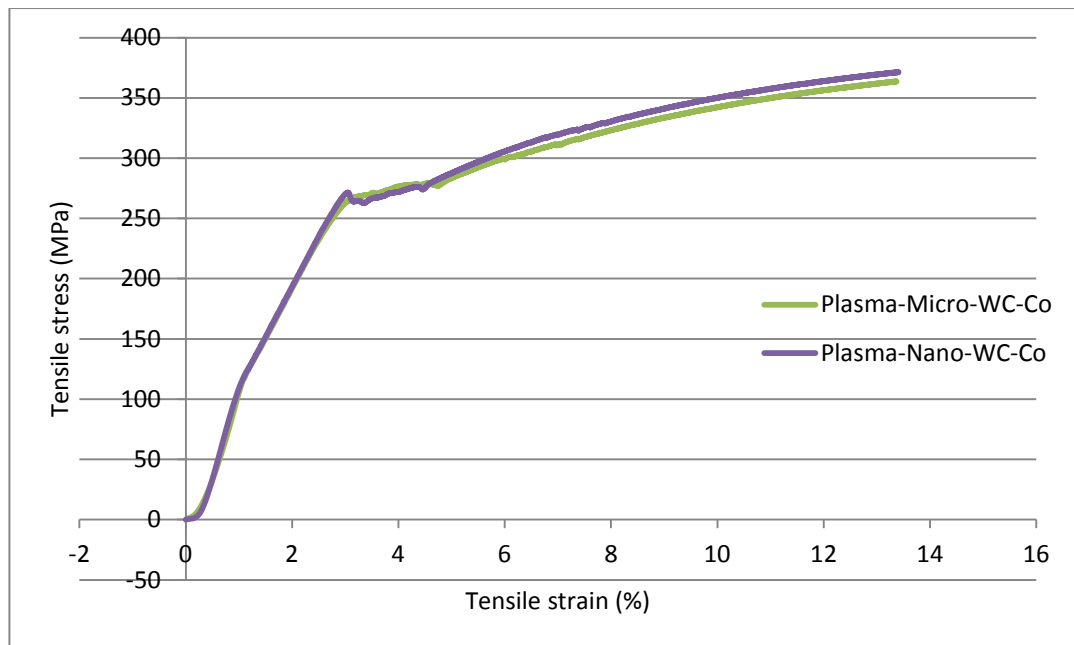


Figure 5.52, Stress-Strain curve resulted from tensile test showing powder size effect on plasma coating.

AMDRY powder effect on tensile behaviour:

Figures 5.53 and 5.54 shows the Stress-Strain curve for AMDRY added coatings for both HVOF and plasma. As the results obtained from the bending test, the addition of AMDRY powders to the micro-sized WC-Co powder gave higher yield stress for HVOF coatings than the coatings resulted from the addition of AMDRY powders to the nano-sized WC-Co however both showed similar stiffness. In plasma system, addition of AMDRY had no significant effect on nano sized WC-Co produced coatings but it slightly increased the yield strength of when added to the micro-sized WC-Co powders. Overall, no significant effect of AMDRY on coating stiffness of plasma produced coatings. Batch 1 which had no AMDRY added showed higher yield strength than other AMDRY added coatings.

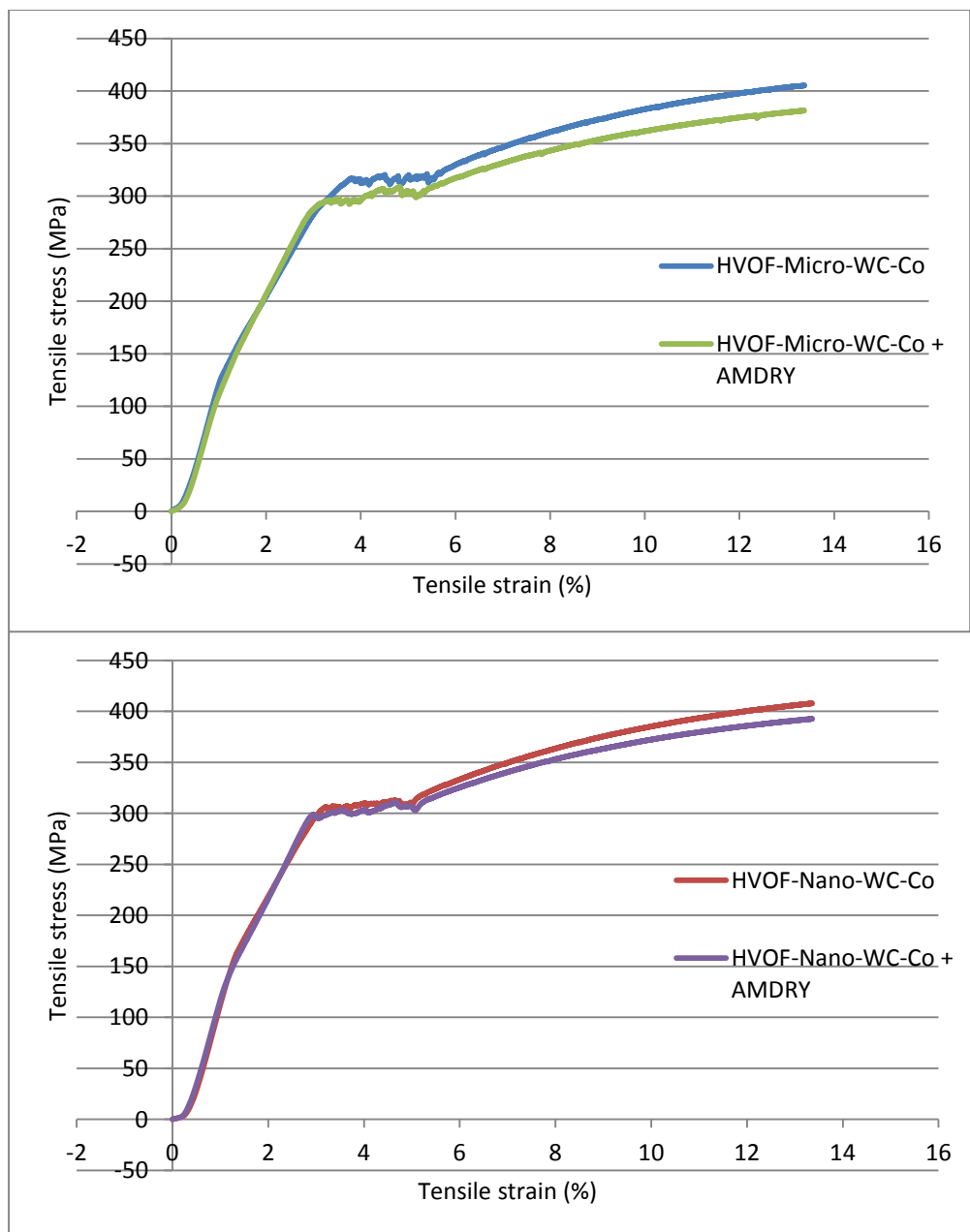


Figure 5.53, Stress-Strain curve resulted from tensile test showing AMDRY effect on HVOF coatings.

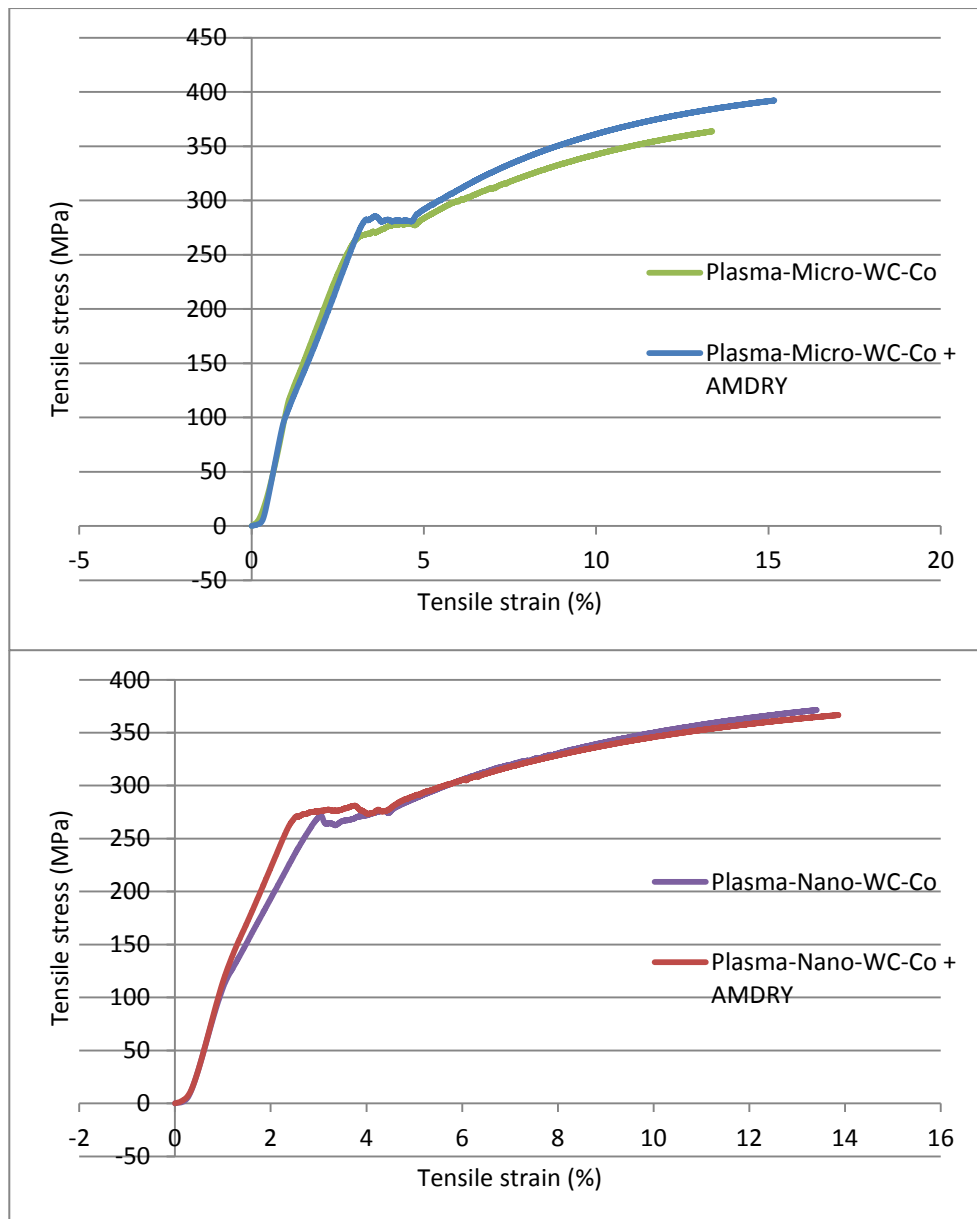
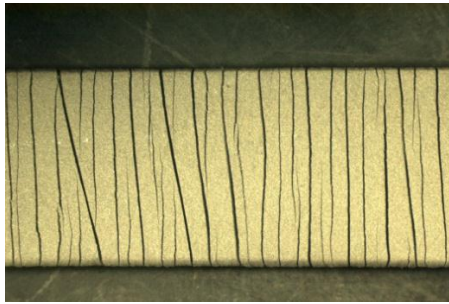
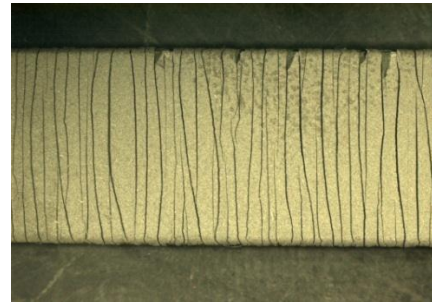


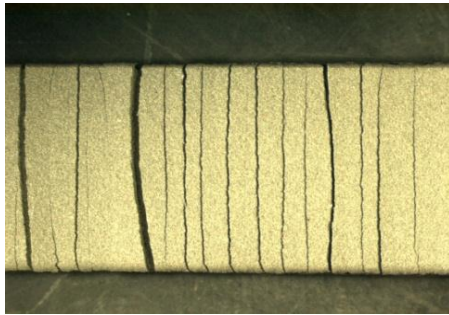
Figure 5.54, Stress-Strain curve resulted from tensile test showing AMDRY effect on plasma coatings.



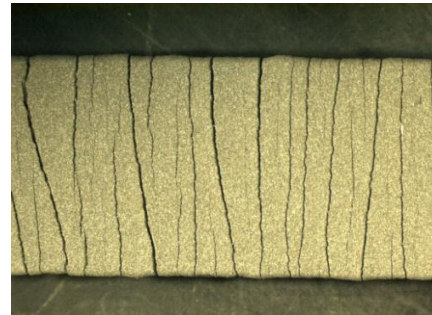
HVOF-Micro-WC-Co



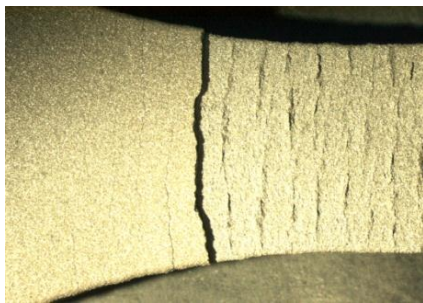
HVOF-Nano-WC-Co



HVOF-Micro-WC-Co + AMDRY



HVOF-Nano-WC-Co + AMDRY



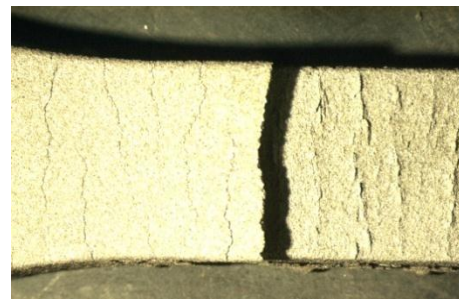
Plasma-Micro-WC-Co



Plasma-Nano-WC-Co



Plasma-Micro-WC-Co + AMDRY



Plasma-Nano-WC-Co + AMDRY

Figure 5.55, Coatings crack shapes post tensile test.

The test results also revealed that more tensile forces were required for HVOF produced coatings compared to Plasma sprayed coatings for both types of sprayed powder size. High kinetic energy of the HVOF thermal spraying helps to increase the bonding strength of the HVOF coatings due to the energy gained from high velocity impacts of the sprayed particles. HVOF coatings are denser and have lower porosity than the plasma coatings as discussed in the Coating Characterization part of this research. The bonding strength of HVOF coatings was higher than the plasma ones thus requiring more tensile force as illustrated in Figures 5.51 and 5.52.

The surface topography and microstructure of the plasma and HVOF coatings were different, as explained previously, which will contribute to define the bonding strength of the coating. Temperature difference used by both systems also play an important role in determining the reaction and the thermal energy during the spray which affect the bonding strength and adhesion of the coating.

In HVOF coatings, the tensile bonding strength was reduced to two-third in both coatings produced by the nano and micro-size powders for coatings contain AMDRY powders. The addition of AMDRY powder to WC-Co powder reduced the hardness of the coatings. This result was obtained from the hardness test in this research. Addition of AMDRY powder helped to increase the elasticity of the coatings which was confirmed by elasticity modulus calculation of the coatings (Figure 5.56). Batch 4 coating that resulted from the addition of AMDRY to nano-sized WC-Co showed the highest modulus of elasticity.

In the plasma coatings, the situation was more complex. It was observed that the addition of AMDRY powder to micro-size WC-Co powder helped to increase the tensile bonding strength and decrease the elasticity modulus of the coating. The reason for this may be due to the homogeneous melting at high temperature of the same particle size of powders that helped to enhance the bonding strength of the coating materials.

There were no coating defects or delamination observed in any of the AMDRY added coatings produced by the HVOF thermal spray coatings. However, there were some coating delamination observed in the plasma thermal spray coatings. Although, fewer cracks initiated compared to coatings with no AMDRY added. It was noticed in some samples that cracks were initiated from coating edges (not from the middle), thus causing them to propagate and the coatings failed as one piece.

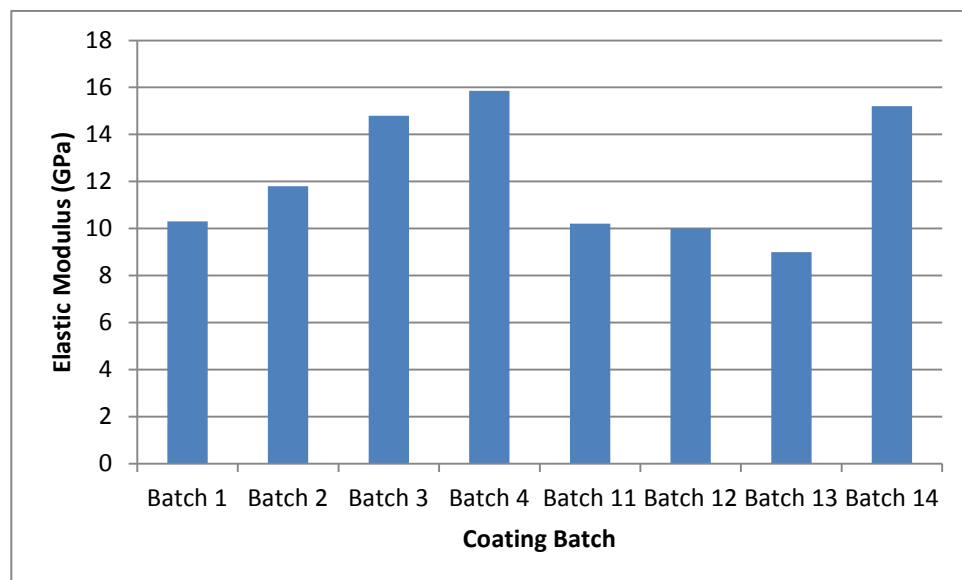


Figure 5.56, Elastic modulus of coatings.

Corrosion Effect Versus Tensile Bonding Strength of the Coatings

Figure 5.57, compares the ultimate stress that was required to complete the tensile test for as coated and corroded test specimens. Generally, lower loads were required for corroded samples. All of the corroded samples showed the same behaviour as the As-Coated samples. In the HVOF thermal spray coatings, the coating produced by mixing micro-WC-Co and AMDRY demonstrated excellent behaviour compared to the other types of HVOF coatings. While in the plasma

coatings, coatings produced by spraying the micro-size WC-Co powder were superior. Defects in the corroded plasma coatings were observed when they were subjected to the tensile test, this was due to dual effect of the tension force applied (mechanical interlocking) and corrosion effect (chemical interlocking). Figure 5.57 clearly shows that Batch 3 had almost the same ultimate stress before and after the corrosion test of about 380 MPa.

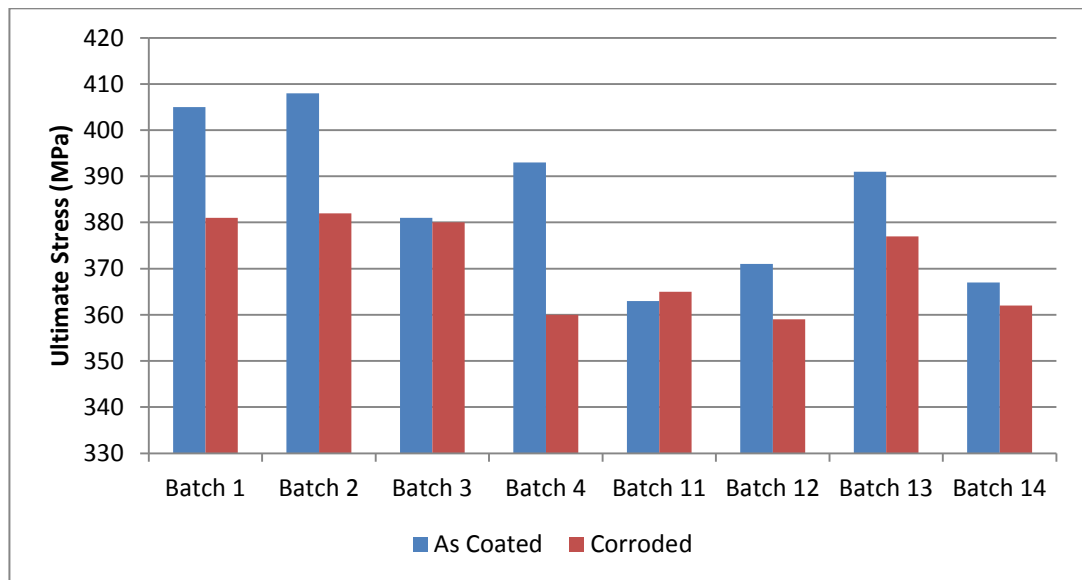


Figure 5.57, Ultimate stress of the coatings before and after the corrosion test.

5.4.3 Fatigue Test

Figure 5.58 shows an example of the cyclic loading applied on to a coated specimen. To determine the fatigue life of the coating, it was chosen when the number of cyclic loading when 50% of load drop was obtained for all coatings.

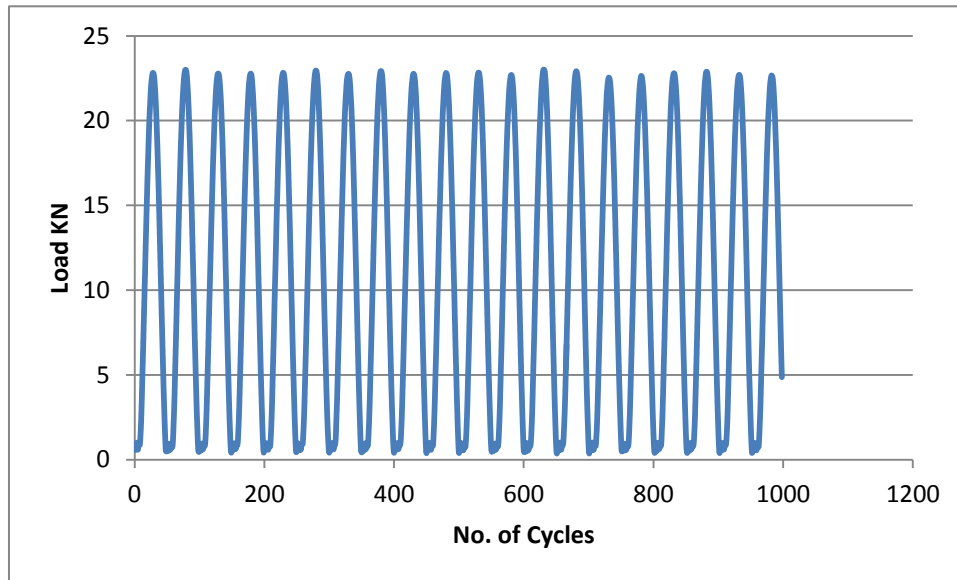


Figure 5.58, Example of the cyclic loading applied on to a coated specimen.

Figure 5.59, represents the powder size effect on fatigue property of the coating for HVOF and plasma coatings. There was about 65% increase of number of cyclic loading for coatings produced by spraying the nano-size powders compared to coatings produced by spraying the micro-size powders. The elastic modulus of the nano-coatings were higher than the micro-coatings (11.7 GPa and 10.4 GPa respectively) which may help to increase the fatigue life of the coating. Similarly, coatings produced by plasma spraying of nano-size powders exhibit good behaviour compare to other coatings. The coating process effect on fatigue life was deemed not as important as the powder type. However, the plasma coatings show better behaviour compare to HVOF coatings.

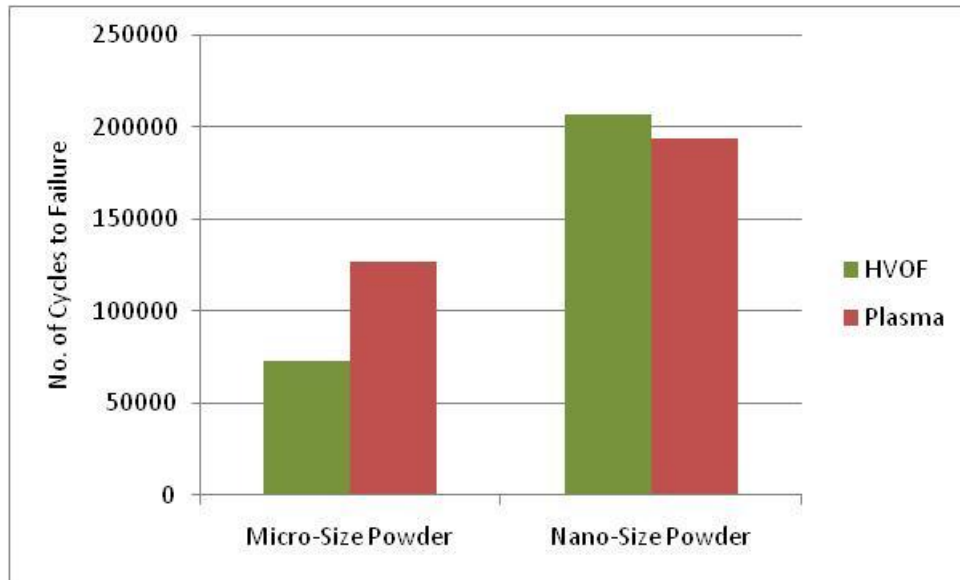


Figure 5.59, Powder size effect on fatigue propriety of the coating for HVOF and plasma coatings.

The addition of AMDRY powder to the WC-Co powder, had slightly effect on the nano coatings produced by the HVOF thermal spray system but increased the number of loading cycles in the plasma coatings significantly for micro-size powders by about 34%, (Figure 5.60). On the other hand, the number of loading cycles in the plasma coatings produced by nano-size powder was reduced by 25%. The degree of nano powder decarburization and evaporation of coating material in plasma system due to high operating temperature may be attributed to this conflict in addition to homogenous mixing of powder particles of same size. Coating Batch 4 (HVOF-nano-AMDRY) required more load cycles to failure compared to the rest of coating batches.

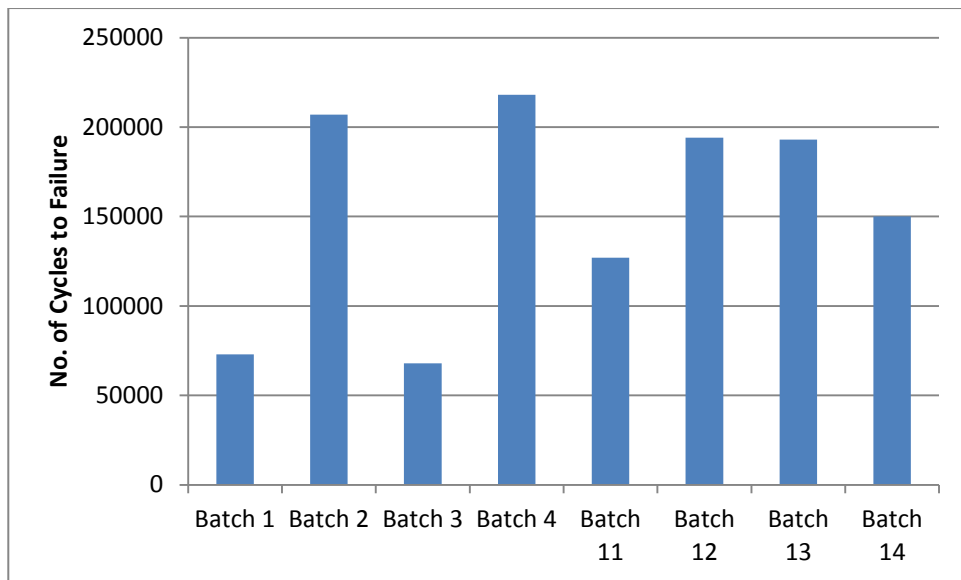


Figure 5.60, Number of cycles to coating failure.

All of the samples subjected to the corrosion test recorded lower number of loading cycles to failure when compared to the as-coated samples, (Figure 5.61). The plasma micro coating exhibited excellent behaviour compared to other types of coatings. Batch 3 and 4 were rated as best corrosion resistance in the static corrosion test however Figure 5.61 showed a big drop in the number of cycles exhibited by the corroded sample of Batch 4. This is due to the formation of brittle phase during the spraying of nano powders more than the micro powders.

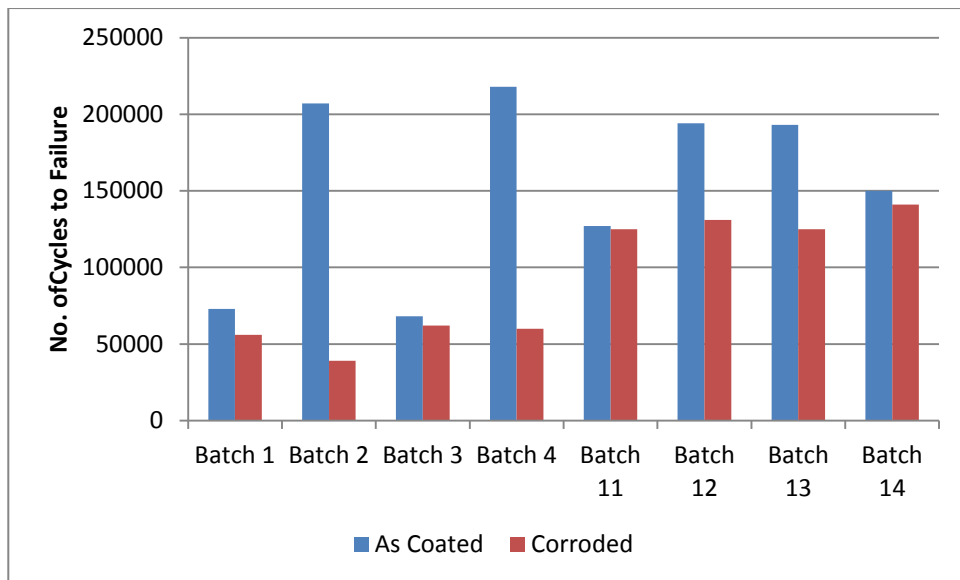


Figure 5.61, Corrosion effect on number of cycles to coating failure.

5.5 RESULTS SUMMARY:

Table 5.9 summarizes the overall findings found in chapter 5. The coatings behaviour, with respect to some desired coating properties, were compared and ranked from 1 to 8, where 1 represent the best behaviour and 8 is the lowest behaviour.

Table 5.9, Summary of tests results.

Property	HVOF Coatings				Plasma Coatings			
	Batch 1	Batch 2	Batch 3	Batch 4	Batch 11	Batch 12	Batch 13	Batch 14
Porosity	4	3	2	1	8	7	6	5
Hardness	2	1	4	3	5	4	7	6
Corrosion resistance	2	3	1	1	5	6	4	4
Load under corrosion	1	3	2	4	5	5	5	5
Tension under corrosion	3	3	1	5	4	4	4	2
Fatigue under corrosion	4	7	2	6	1	3	3	1
Erosion-Corrosion	4	5	6	1	8	7	2	3
Roughness	2	3	4	5	6	1	8	7
Bending yield strength	1	3	2	4	8	4	5	7
Tensile yield strength	1	1	3	2	4	5	6	7
Fatigue	6	2	7	1	5	3	3	4
Stiffness	3	1	5	5	3	3	5	5
Elasticity	5	4	3	1	5	6	7	2

From Table 5.9, coating Batch 1 (HVOF, Micro WC-12Co) was found to have best behaviour for application where a corrosive medium and load may be applied onto protected carbon steel. Also, it was seen as a good performer for applications requiring coatings of high yield strength (Bending/Tensile).

Coating Batch 2 (HVOF, Nano WC-12Co) was an alternative selection for applications involving fatigue but it presented the best behaviour for coatings subjected to tensile force, stiffness, and hardness. Based on results obtained from corrosion, corrosion-erosion, and mechanical tests, coating Batch 3 (HVOF, 60% Micro WC-12Co and 40% Micro AMDRY 9954) was one of the best amongst the other applied coatings in corrosion resistance applications.

For erosion-corrosion applications or for applications subjected to high fatigue cycles, Batch 4 (HVOF, 60% Nano WC-12Co and 40% Micro AMDRY 9954) can give high elasticity, high tensile strength, low porosity, high corrosion resistance.

Coating Batch 11 (Plasma, Micro WC-12Co) was suited for applications where the metal is surrounded by corrosive environment and subjected to fatigue cycles. Coating Batch 12 (Plasma, Nano WC-12Co) could be used for applications that require smooth surfaces and moving parts to avoid friction, but little else.

Coating Batch 13 (Plasma, 60% Micro WC-12Co and 40% Micro AMDRY 995M) is an alternative selection for erosion-corrosion applications, and can be used for application subjected to medium fatigue cycles. Batch 14 (Plasma, 60% Nano WC-12Co and 40% Micro AMDRY 995M) can be used for fatigue applications where is the metal subjected to corrosion and to tensile forces.

5.6 COST OF COATING MANUFACTURING:

Some coating applications are already used in the Oil and Gas industry. Critical pipe segments are coated using nonorganic paints. The first 10 inches (254 mm) of heat exchangers are electroplated using chrome. Thermal spray coating using HVOF and plasma deposition has not been tested by Saudi Aramco Oil Company to date. To assess the cost of such coatings applications, many factors should be put in considerations. Figure 5.62 presents the coating manufacturing main steps.

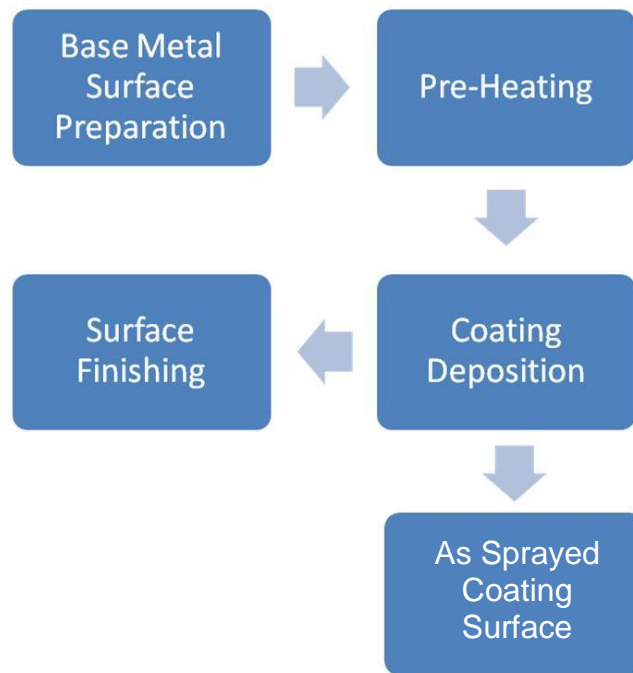


Figure 5.62, Coating manufacturing main steps.

The capital cost of HVOF and Plasma equipment is about € 300K and € 500K respectively. Capital costs may not be a concern to Saudi Aramco because of the outsourcing and contracting policy they adapted recently. The main concern is the possibility of applying the on-site coating to avoid the cost of disassembling, assembling, and shipment of the components to the working shop. The portability of HVOF coating booth may be possible if transferred by a truck. The high voltage requirement for the plasma equipment may be considered as a limitation to the on-site application. Stokes [218] estimated the cost of producing cylindrical component coating (12 mm diameter with 0.5 mm thickness) using HVOF is about € 4.00. The cost is doubled for producing the same by plasma equipment. Additional cost should be added for surface finishing. The distribution of costs in the production of a cylindrical component is shown in Figure 5.63. These costs can be recovered by extending the life time of the current plants material. The expected life time of carbon steel that is subject to the corrosive environment in the Gulf

area is 5 years. For each year extend in material life, there is 20% saving in material replacement costs.

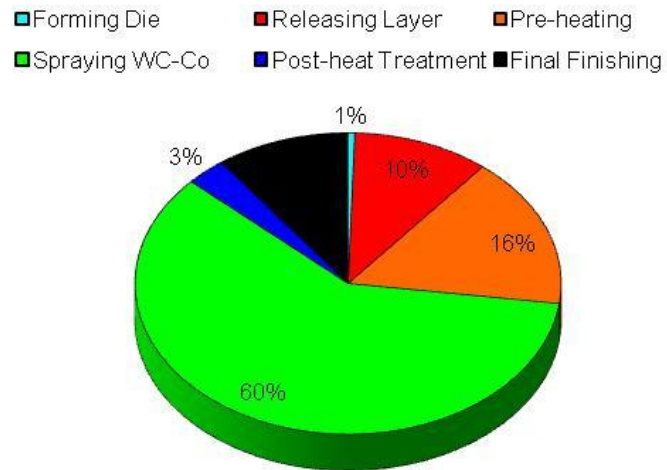


Figure 5.63, Costs distribution in the production of a cylindrical component (12 mm diameter, 5 mm thick) [218].

CONCLUSION AND RECOMMENDATIONS

6.1 CONCLUSION

The present research focused on producing coating materials that provides superior corrosion and corrosion-erosion resistance. The objective was to identify a single thermal spray method and coating combination capable of producing a multi-layer coating by blending micro and nano tungsten carbide cobalt powders with AMDRY powders deposited by HVOF and Plasma spray equipment onto carbon steel substrates to address issues in the oil and gas industry.

Based on results obtained from this research, coating produced by the deposition of the multilayer 60% Micro WC-12Co and 40% Micro AMDRY 9954 onto a 80% Micro WC-12Co and 20% Micro AMDRY 9954 onto a 100% Micro WC-12Co first layer by HVOF was the best coating application to protect the critical areas in the Oil and Gas plants that have material degradation due to corrosion problems. This compositional coating can be applied to plants vessels, tanks, pipes, and flare tip locations. For areas where erosion is the dominant concern, Nano WC-12Co should be used to replace the Micro WC-12Co (throughout) as this will produce a harder coating that stops material removal due to corrosion-erosion effect. For other tested coatings in this research, Table 6.1 lists some of recommended coating applications.

Table 6.1, Recommended coating applications.

Coating Batch	Coating Composition	Recommended Application
1	HVOF, Micro WC-12Co	Corrosion + load applied, Bending, Tensile, and hardness applications.
2	HVOF, Nano WC-12Co	Tensile and hardness applications
3	HVOF, 60% Micro WC-12Co and 40% Micro AMDRY 9954	Corrosion, Corrosion + Load, porosity, tension under corrosion, fatigue under corrosion, and bending applications.
4	HVOF, 60% Nano WC-12Co and 40% Micro AMDRY 9954	Corrosion, erosion-corrosion, low porosity, fatigue, elasticity, and tension applications.
11	Plasma, Micro WC-12Co	Fatigue under corrosion
12	Plasma, Nano WC-12Co	Friction prevention , low roughness.
13	Plasma, 60% Micro WC-12Co and 40% Micro AMDRY 995M	Medium erosion-corrosion
14	Plasma, 60% Nano WC-12Co and 40% Micro AMDRY 995M	Tensile and fatigue under corrosion and elasticity.

It can also be concluded from this research that the addition of the AMDRY powders to WC-Co powders mainly enhanced the corrosion behaviour of coatings and improved the overall erosion–corrosion performance. Depositing the nanostructured powder (particle size effect) improved the coatings hardness and extended its life by increasing the number of cycles to failure due to fatigue when compared to conventional micro sized powder. Also, it can be concluded that HVOF coatings outperformed much better than plasma coatings. HVOF produced

harder coatings that acted better in mechanical applications (bending, tensile, and fatigue) and resisted corrosion better than plasma coatings.

6.2 RECOMMENDATIONS FOR FUTURE WORK

By the completion of this work, further research and development steps that would contribute to the subject of this research have been identified. Followings are recommendations for future work:

- In this research, powder mixing was based on weight percentage. With recent technology development, a recommended research is to mix powders based on volumetric rate by using the recent developed two feeder coating equipment. One powder volumetric rate increases from 0% to 100% and the second powder its volumetric rate decreased from 100% to 0% so smooth graded one layer coating can be achieved.
- In this research, the powder mixing % ratio for top coat was 60:40, Design of Experiment (DOE) techniques may be used to optimize the powders blending ratios to give better results.
- Micro-galvanic corrosion was not investigated closely. It is proposed to investigate micro-galvanic corrosion that may occur between coating particles and base metal in the existence of corrosive environment.
- Preventing decarburization is a key factor to produce excellent coatings. Selection of the optimal deposition parameters for plasma system to prevent decarburization and cobalt phase evaporation requires more efforts and extensive study. Better optimization of best coating gives better results.
- An adhesion test such as “scratch test” may be recommended for the investigation of adhesion of WC-based coatings sprayed on carbon steel substrate since the adhesion observation in this work was based on optical microscope and ESEM examination.

PUBLICATIONS ARISING FROM THIS WORK

Journals

1. **Sultan Al-Mutairi**, J. Stokes, M.S.J. Hashmi, and B.S. Yilbas “Microstructural Characterization of HVOF/Plasma Thermal Spray of Micro/Nano WC-12%Co Blended with AMDRY 995M/9954 Powders”, Journal of Surface and Coatings Technology, (2013).
2. **Sultan Al-Mutairi**, J. Stokes, M.S.J. Hashmi, and B.S. Yilbas “Corrosion Behaviour of Tungsten Carbide-Cobalt Micro/Nano WC-12%Co - AMDRY 995M/9954 Multi Layered HVOF and Plasma Thermal Spray Coatings”, Journal of Surface and Coatings Technology, (2013).
3. **Sultan Al-Mutairi**, J. Stokes, M.S.J. Hashmi, and B.S. Yilbas “Mechanical Behaviour of Tungsten Carbide-Cobalt Micro/Nano WC-12%Co - AMDRY 995M/9954 Multi Layered HVOF and Plasma Thermal Spray Coatings Post Corrosion Effects”, Journal of Surface and Coatings Technology, (2013).

REFERENCES

- [1] Tems R.D. and Al Zahrani, “Cost of Corrosion in Oil Production and Refining”, Saudi Aramco Journal of Technology, (Summer 2006), pp. 2-14.
- [2] Saudi Aramco World, “Sweetening Up the Crude”, (January 1960), pp. 3-5.
- [3] http://www.ife.no/no/ife/avdelinger/material_og_korrosjonsteknologi/prosjekter/kloc, [online], (accessed date January 12, 2013).
- [4] <http://www.icorr.org/news/180/index.phtml> , [online], (accessed date January 12, 2013).
- [5] NACE MR0175/ISO 15156-1, “Materials for use in H₂S-containing environments in oil and gas production”, Petroleum and natural gas industries, (2009).
- [6] http://www.masteel.co.uk/hydrogen_induced_cracking.htm, [online], (accessed date January 12, 2013).
- [7] L. Casteletti, A. Lombardi Neto, G. Totten, “HVOF Production of Hard Chromium Substitution Coatings for Improved Wear”, International Journal of Thermal Technology, (January 8, 2008), pp. 1-5.

- [8] G. Bolelli, L. Lusvarghi, T. Manfredini and F. Pighetti Mantini, "Comparison Between Plasma- And HVOF-Sprayed Ceramic Coatings", *International Journal of Surface Science and Engineering*, (2007), Vol. 1, No. 1, pp. 38-61.
- [9] R.C. Souza, H.J.C. Voorwald, M.O.H. Cioffi, "Fatigue strength of HVOF sprayed Cr₃C₂-25NiCr and WC-10Ni on AISI 4340 steel", *Surface and Coatings Technology*, (25 November 2008), Volume 203, Issues 3-4, pp. 191-198.
- [10] H.J.C. Voorwald, R.C. Souza, W.L. Pigatin, M.O.H. Cioffi, "Evaluation of WC-17Co and WC-10Co-4Cr thermal spray coatings by HVOF on the fatigue and corrosion strength of AISI 4340 steel", *Surface and Coatings Technology*, (21 January 2005), Volume 190, Issues 2-3, pp. 155-164.
- [11] Protective Coating Failure Analysis, <http://www.matcoinc.com>, (Accessed 3 May 2012).
- [12] J. D. Nuse, "Surface Finishing of Tungsten Carbide Cobalt Coatings Applied By HVOF for Chrome Replacement Applications", *Airline Plating and Metal Finishing Forum in Cincinnati, OH*, (March 27, 2000), pp. 119.
- [13] D. Landolt, "Electrochemical and Materials Aspects of Tribocorrosion Systems", *Journal of Physics: Applied Physics*, (2006), Vol. 39, pp. 1-7.
- [14] A. Fischer, S. Mischler, "Tribocorrosion: fundamentals- materials and applications", *Journal of Physics: Applied Physics*, (2006), pp. 39.
- [15] E. Rabinowicz, "Friction and Wear of Materials", New York, John Wiley and Sons, (1995), p. 65.

-
- [16] M. Stemp, S. Mischler and D. Landolt, “The Effect of Mechanical and Electrochemical Parameters on the Tribocorrosion Rate of Stainless Steel in Sulphuric Acid”, *Wear*, (2003), Vol. 255, pp. 466–475.
- [17] S. Mischler, A. Spiegel, M. Stemp and D. Landolt, “Influence of Passivity on the Tribocorrosion of Carbon Steel in Aqueous Solutions”, *Wear*, (2001), Vol. 251, pp. 1295–1307.
- [18] P. Ponthiaux, F. Wenger, D. Drees, J. P. Celis, “Electrochemical Techniques for Studying Tribocorrosion Processes”, *Wear*, (March 2004), Vol. 256, Issue 5, pp. 459-468.
- [19] S. Mischler, “Tribocorrosion of Passive Metals: Third Body Considerations”, Ecole Polytechnique Fédérale de Lausanne, Lausanne EPFL, Switzerland, (Report 2004), p. 1.
- [20] W. Gwidon, Stachowiak, W. Andrew, W. Batchelor, *Engineering Tribology*, Third Edition, ISBN 0750673044, (2006), pp. 254-262.
- [21] N. Thomas, Farris, *Tribology: Rules of Thumb for Mechanical Engineers*, ISBN: 9780884157908, Gulf Publishing Co., (1996), pp. 226-237.
- [22] M. Jones, D. Scott, Eds., *Industrial Tribology: the practical aspects of friction, lubrication, and wear*. ISBN 0898640652, New York, Elsevier Scientific Publishing Company, (1983).

- [23] K. Osara, T. Tiainen, "Three-body impact wear study on conventional and new P/M + HIPed wear resistant materials", *Wear*, (October 2001), Vol. 250, Issues 1-12, , pp. 785-794.
- [24] M.K. Muju, A. Ghosh, "Effect of a magnetic field on the diffusive wear of cutting tools", *Wear*, (January 1980), Vol. 58, Issue 1, pp. 137-145.
- [25] G. Bregliozzi, A. Di Schino, S.I.-U. Ahmed, J.M. Kenny, H. Haefke, "Cavitation wear behaviour of austenitic stainless steels with different grain sizes", *Wear*, (January 2005), Vol. 258, Issues 1-4, pp. 503-510.
- [26] X. C. Lu, K. Shi, S. Z. Li, X. X. Jiang, "Effects of surface deformation on corrosive wear of stainless steel in sulfuric acid solution", *Wear*, (April 1999), Vol. 225-229, Part 1, pp. 537-543.
- [27] J. Williams, "Wear and wear particles - Some fundamentals", *Tribology International*, Issue 38, Vol. 10, pp. 863-870.
- [28] N. Frees, "Characterizing and solving of industrial wear problems", *Wear*, (March 1987), Vol. 115, Issues 1-2, pp. 193-202.
- [29] M.J. Neale, *Lubrication and Reliability Handbook*, Library of Congress, ISBN 0750651547, USA, (2001), pp. A5.5-A7.1.
- [30] M.J. Neale, *Tribology Handbook, Second Edition*, ISBN 0750611987, Antony Rowe Ltd., UK, (1995), pp. C7-12.
- [31] E. Rabinowicz, *Friction and Wear of Materials*, New York, John Wiley and Sons, ISBN 0471830844, USA, (1995), pp. 143-188.

-
- [32] Aludra, www.aludra.nl, [online], (accessed date October 20, 2012).
- [33] Daros, www.daros.se, [online], (accessed date October 20, 2012).
- [34] G. W. Stachowiak, and A. W. Batchelor, "Abrasive, Erosive and Cavitation Wear", *Engineering Tribology*, (2006), pp. 501-551.
- [35] W. A. Glaeser, *Characterization of Tribological Materials*, Materials Characterization Series. ISBN 0750692979, Butterwoth-Heinemann, Boston, (1993).
- [36] E. Rabinowicz, *Friction and Wear of Materials*. New York, John Wiley and Sons, ISBN 0471830844, USA, (1995), pp. 191-235.
- [37] ASM Handbook, *Friction, Lubrication and Wear Technology*. ISBN 0871703807, ASM International, U.S.A., Volume 18, (2002).
- [38] FMA International, www.thefabricator.com, [online], (accessed date October 20, 2012).
- [39] ASTM, *Standard Terminology Relating to Wear and Erosion*, Annual Book of Standards, (1987), Vol 03.02, pp. 243-250.
- [40] M. Bingley, S. Schnee, "A Study of The Mechanisms of Abrasive Wear For Ductile Metals Under Wet and Dry Three-Body Conditions", *Wear*, (January 2005), Vol. 258, Issues 1-4, pp. 50-61.

-
- [41] M. Barge, G. Kermouche, P. Gilles, J. M. Bergheau, "Experimental and Numerical Study of The Ploughing Part of Abrasive Wear", *Wear*, (August-September 2003), Vol. 255, Issues 1-6, pp. 30-37.
- [42] M.S. Bingley, S. Schnee, "A Study Of The Mechanisms Of Abrasive Wear For Ductile Metals Under Wet And Dry Three-Body Conditions", *Wear*, (January 2005), Vol. 258, Issues 1-4, pp. 50-61.
- [43] M.V. Leite, "Analysis of the Wear Mechanisms in Contact Fatigue, Case Study: Austempered Ductile Iron, Dissertation", Federal University of Technology, Paraná, Curitiba-Brazil, (2005), p. 90.
- [44] Noria, www.noria.com, [online], (accessed date October 20, 2012).
- [45] SME, sme-metalworkingfluids.blogspot.com, [online], (accessed date May 3, 2012).
- [46] C. Brunetti, M.V. Leite, G. Pintaude, "Effect of Specimen Preparation on Contact Fatigue Wear Resistance of Austempered Ductile Cast Iron", *Wear*, (10 September 2007), Vol. 263, Issues 1-6, pp. 663-668.
- [47] H. Endo, E. Marui, "Studies on Fretting Wear: Influence of Rubbing Surface Materials and Some Considerations", *Wear*, (October 2002), Vol. 253, Issues 7-8, pp. 795-802.
- [48] POETON, <http://www.poeton.co.uk/w1/p-solver/fretting.htm>, [online], (accessed date January 10, 2013).

- [49] Mamata Kumari Padhy and R.P. Saini, "A review on silt erosion in hydro turbines, Renewable and sustainable energy reviews, (2008), issue 12, vol. 7, p. 1974.
- [50] T. Sinmaz Celik and I. Taskiran, "Erosive Wear Behaviour of Polyphenylenesulphide (PPS) Composites", Materials in engineering, issue 28, (2007), Vol. 9, pp. 2471-2477.
- [51] M. A. Al-Bukhaiti, S.M. Ahmed, F.M.F. Badran, K.M. Emara, "Effect of Impingement Angle on Slurry Erosion Behaviour and Mechanisms of 1017 Steel and High-Chromium White Cast Iron", Wear, (10 April 2007), Vol. 262, Issues 9-10, pp. 1187-1198.
- [52] ASTM Book of Standards, Metals Test Methods and Analytical Procedures: Wear and Erosion; Metal Corrosion, ASTM International, (2004), Vol. 03, p. 02.
- [53] Saudi Aramco Engineering Encyclopedia; [online], Corrosion, (accessed date May 3, 2012).
- [54] Z. Ahmad, Principles of Corrosion Engineering and Corrosion Control, ISBN 0750659246, Elsevier, UK, (2006), pp. 479-545.
- [55] J.C. Earthman, Smithells Metals Reference Book, Eighth Edition, (2004), pp. 2-13.
- [56] NACE International, Corrosion Costs and Preventive Strategies in the United States, (2002), pp. 62-66.

- [57] Sun W and Nestic S, "A Mechanistic Model of H₂S Corrosion of Mild Steel". Proceeding of NACE Corrosion, (2007), Paper No.07655.
- [58] Muhammad Shahid and Muhammad Faisal, "Effect of Hydrogen Sulfide Gas Concentration on the Corrosion Behavior of "ASTM A-106 Grade-A" Carbon Steel in 14% Diethanol Amine Solution", The Arabian Journal for Science and Engineering, (2009), Vol. 34, No.2C, p. 181.
- [59] E. Abelev , J. Sellberg , T. A. Ramanarayanan, S. L. Bernasek, "Effect of H₂S on Fe corrosion in CO₂-saturated brine", Journal of Materials Science, (2009), Vol. 44, pp. 6167–6181.
- [60] Shoesmith D.W, "The Formation of Ferrous Monosulfide Polymorphsduring the Corrosion of Iron by Aqueous Hydrogen Sulfide at 210C", Electrochemical Society, (1980), Vol. 127(5), pp. 1007-1015.
- [61] James G. Edmondson, "Wet H₂S Corrosion and Inhibition", Water and Process Technologies, (2006), p.9.
- [62] T. Sahraoui, N. Fenineche, G. Montavon and C. Coddet, "Alternative to Chromium: Characteristics and Wear Behavior of HVOF Coatings for Gas Turbine Shafts Repair (heavy-duty)", Journal of Materials Processing Technology, (2004), Vol. 152 (1), pp. 43-55.
- [63] J. Stokes, The Theory and Application of High Velocity Oxy-Fuel (HVOF) Thermal Spray Process, ISBN: 1-87232-753-2, Dublin City University, (2008).
- [64] J. Berget, "Influence of Powder and Spray Parameters on Erosion and Corrosion Properties of HVOF Sprayed WC-Co-Cr coatings", Ph.D. Thesis, Norwegian

- University of Science and Technology, Engineering Material Science, Norway, (1998), pp. 90.
- [65] Interfinish' 96 World Congress, Birmingham , Royaume-Uni (10/09/1996) 1997, vol. 75 (3), pp. 108-112.
- [66] C. Rupprecht, G. Reisel, E. Friesen, “Development and trends in HVOF spraying technology”, *Surface & Coatings Technology*, (2006), Vol. 201, pp. 2032–2037.
- [67] A. Papyrin, V. Kosarev, S. Klinkov, A. Alkimov, V. Fomin, *Cold Spray Technology*, ISBN-10: 0080451551, (2007), pp. 248-323
- [68] H. Gruner, J.P. Langagne, A.R. Nicoll, “Equipment performance and coating quality in modern vacuum plasma spraying (VPS)”, *Materials Science and Engineering*, (April 1987), Volume 88, p. 349.
- [69] J.K.N. Murthy, B. Venkataraman, “Abrasive wear behaviour of WC–CoCr and Cr₃C₂–20(NiCr) deposited by HVOF and detonation spray processes”, *Surface and Coatings Technology*, (24 January 2006), Volume 200, Issue 8, pp. 2642-2652.
- [70] Z. Yin, X. Xiang, J. Zhu, and Z. Lai, “Microstructure characteristic of plasma sprayed ZrO₂ /NiCoCrAlY graded coating”, *Functionally Graded Materials*, Elsevier Science, Amsterdam, The Netherlands (1997) pp. 269-274.
- [71] S. Alam, S. Sasaki, H. Shimura, “Friction and Wear Characteristics of Aluminum Bronze Coatings on Steel Substrates Sprayed By a Low Pressure Plasma Technique”, *Wear*, (March 2001), Vol. 248, Issues 1-2, pp. 75-81.

- [72] Maelena M. García, “Optimizing the Sintering of Cr₂O₃-Nano Powders”, *Ciencia E Ingeniería De Materiales E Ingeniería Química*, (2012), pp: 23-38.
- [73] S. C. Sharma, B. M. Satish, B. M. Girish, D. R. Somashekar, “Wear Characteristics of Phosphor–Bronze/Silicon Carbide Particulate Composites”, *Journal of Materials Processing Technology*, (3 December 2001), Volume 118, Issues 1-3, pp. 65-68.
- [74] M.J. Neale, “Bearing Surface Treatments and Coatings”, *Tribology Handbook*, Second Edition, ISBN 0750611987, (1996).
- [75] H. Chen, I. M. Hutchings, “Abrasive Wear Resistance of Plasma-Sprayed Tungsten Carbide–Cobalt Coatings”, *Surface and Coatings Technology*, (10 September 1998), Volume 107, Issues 2-3, pp. 106-114.
- [76] M. M. Lima, C. Godoy, P. J. Modenesi, J. C. Avelar-Batista, A. Davison, A. Matthews, “Coating Fracture Toughness Determined By Vickers Indentation: an Important Parameter in Cavitation Erosion Resistance of WC–Co Thermally Sprayed Coatings”, *Surface and Coatings Technology*, (30 January 2004), Vol. 177-178, , pp. 489-496.
- [77] D. Toma, W. Brandl, G. Marginean, “Wear and corrosion behaviour of thermally sprayed cermet coatings”, *Surface and Coatings Technology*, (16 April 2001), Vol. 138, Issues 2-3, pp. 149-158.
- [78] Z. Panossian, L. Mariaca, M. Morcillo, S. Flores, J. Rocha, J. J. Peña, F. Herrera, F. Corvo, M. Sanchez, O. T. Rincon, G. Pridybailo, J. Simancas, “Steel cathodic protection afforded by zinc, aluminium and zinc/aluminium alloy coatings in the

- atmosphere”, *Surface and Coatings Technology*, (21 January 2005), Volume 190, Issues 2-3, pp. 244-248.
- [79] A.K. Basak, J.P. Celis, M. Vardavoulias, P. Matteazzi, “Effect of nanostructuring and Al alloying on friction and wear behaviour of thermal sprayed WC–Co coatings”, *Surface & Coatings Technology*, (2012), Vol. 206, pp. 3508–3516.
- [80] T. R. Tan, J. R. Cheng, J. H. Wang, J. G. Duh, H. C. Shih, “Surface and Coatings Technology”, *Wear*, (1998), Vol. 110, pp. 194-199.
- [81] T. Try, “Nickel alloy coating”, *Tribology International*, (1978), Volume 11, Issue 1, p. 76.
- [82] Three-layer metal pipe coating composition, *Metal Finishing*, (2001), Volume 99, Issue 9, p. 118.
- [83] Y. Gao, X. Xu, Z. Yan, G. Xin, “High Hardness Alumina Coatings Prepared By Low Power Plasma Spraying”, *Surface and Coatings Technology*, (15 May 2002), Vol. 154, Issues 2-3, pp. 189-193.
- [84] Cellard, V. Garnier, G. Fantozzi, G. Baret, P. Fort, “Wear resistance of chromium oxide nanostructured coatings”, *Ceramics International*, (March 2009), Volume 35, Issue 2, pp. 913-916 A.
- [85] R. Doring, J. VaBen, D. Linke, D. Stover, “Properties of Plasma Sprayed Boron Carbide Protective Coatings For The First Wall In Fusion Experiments”, *Journal of Nuclear Materials*, (December 2002), Vol. 307-311, Part 1, pp. 121-125.

- [86] Saudi Aramco Engineering Encyclopedia, [online], Coating, (accessed date May 3, 2012).
- [87] C. Godoy, M.M. Lima, M.M.R. Castro, J.C. Avelar-Batista, "Structural changes in high-velocity oxy-fuel thermally sprayed WC-Co coatings for improved corrosion resistance", *Surface and Coatings Technology*, (November-December 2004), Volumes 188-189, pp. 1-6.
- [88] R.W. Smith, R. Knight, "Powder consolidation from coating to forming", *Journal of Metals*, (1995), Vol. 47, pp. 32-39.
- [89] Harun Mindivan, "Wear behavior of plasma and HVOF sprayed WC-12Co+6% ETFE coatings on AA2024-T6 aluminum alloy", *Surface & Coatings Technology*, (2010), Vol. 204, pp. 1870-1874.
- [90] V.V Sobolev, J.M Guilemany, J.A Calero, "Heat transfer during the formation of an HVOF sprayed WC-Co coating on a copper substrate, *Journal of Materials Processing Technology*, (1999), Vol. 96, Issues 1-3, pp. 1-8.
- [91] H. Kreye, R. Schwetzke, S. Zimmerman, "High velocity oxy-fuel flame spraying-process and coating characteristics", proceeding of ASM International, (1996), pp. 451- 456.
- [92] D.A. Stewart, P.H. Shipway, D.G. McCartney, "Microstructural evolution in thermally sprayed WC-Co coatings: comparison between nanocomposite and conventional starting powder", *Acta Materialia*, (2000), Vol. 48, pp. 1596-1604.
- [93] Y. Qiao, Y.R. Liu, T.E. Fischer, "Sliding and abrasive wear resistance", *Journal of Thermal Spray Technology*, (2001), Vol 10, pp. 118-125.

-
- [94] C. Zhu, T. Liu and C.X. Ding, “Structural characterization of TiO₂ ultrafine particles”, *Journal of Materials*, (1999), Vol. 14, p. 442.
- [95] Mirva Eriksson, Mohamed Radwan, Zhijian Shen, “Spark plasma sintering of WC, cemented carbide and functional graded materials”, *International Journal of Refractory Metals and Hard Materials*, (2012), Article in printing, doi:10.1016/j.ijrmhm.2012.03.007.
- [96] D.H. Pearson and A.S. Edelstein, “Gas condensation of ultrafine silicon particles using dc magnetron sputtering”, *Nanostructure Materials*, (1994), Vol. 4, , p. 883.
- [97] M.L. Lau, H.G. Jiang and E.J. Lavernia, *Proceedings of the 15th International Thermal Spray Conference, Nice, France, May 25–29, 1998*, p. 379.
- [98] Y.C. Zhu and C.X. Ding. “Plasma spraying of porous nanostructured TiO₂ film”. *Nanostructure Materials*, (1999), vol. 11, p. 319.
- [99] A.K. Akasawat, *Proceedings of the 15th International Thermal Spray Conference, Nice, France, (May 1998)*, p. 281.
- [100] H.L. de Villiers Lovelock, P.W. Richter, J.M. Benson and P.M. Young. *J. Thermal Spray Tech.*, (1998), Vol. 7, p. 97.
- [101] K. Jia and T.E. Fischer, “Abrasion resistance of nanostructured and conventional cemented carbides”, *Wear*, (1996), Vol. 200, p. 206.

- [102] P.P. Bandyopadhyay, D. Chicot, B. Venkateshwarlu, V. Racherla, “Mechanical properties of conventional and nanostructured plasma sprayed alumina coatings”, *Mechanics of Materials*, (2012), Vol. 53, pp. 61–71.
- [103] K. Jia and T.E. Fischer, “Sliding wear of conventional and nanostructured cemented carbides”, *Wear*, (1997), Vol. 203–204, p. 310.
- [104] D.A. Stewart, P.H. Shipway and D.G. McCartney, “Abrasive wear behaviour of conventional and nanocomposite HVOF-sprayed WC–Co coatings”. *Wear*, (1999), Vol. 225–229, p. 789.
- [105] T.Y. Cho , J.H. Yoon, K.S. Kim , K.O. Song , Y.K. Joo, W. Fang, S.H. Zhang, S.J. Youn ,H.G. Chun, S.Y. Hwang, “A study on HVOF coatings of micron and nano WC–Co powders”, *Surface & Coatings Technology*, (2008), Vol. 202, pp. 5556–5559.
- [106] Chang-Jiu Li, Guan-Jun Yang, “Relationships between feedstock structure, particle parameter, coating deposition, microstructure and properties for thermally sprayed conventional and nanostructured WC-Co”, *International Journal of Refractory Metals and Hard Materials*, (2012), p.16.
- [107] Andrew Siao Ming Ang, Christopher C. Berndt, Philip Cheang, “Deposition effects of WC particle size on cold sprayed WC–Co coatings”, *Surface & Coatings Technology*, (2011), Vol. 205, pp. 3260–3267.
- [108] B.R. Marple, M.M. Hyland, Y.-C. Lau, C.-J. Li, R.S. Lima, and G. Montavon, “Effect of Microstructure of HVOF-Sprayed WC-Co Coatings on Their

- Mechanical Properties”, Proceeding of Thermal Spray 2007: Global Coating Solutions, ASM International, Ohio, USA, (2007)
- [109] P. Chivavibul, M. Watanabe, S. Kuroda, “Mechanical Properties of the Coating The microhardness, Young’s modulus and fracture toughness values of the coatings”, National Institute for Materials Science, Tsukuba, Ibaraki. (2007).
- [110] S. Kamnis, S. Gu, T.J. Lu, C. Chen, “Numerical modeling the bonding mechanism of HVOF sprayed particles”, Computational Materials Science, (2009), Vol. 46, Issue 4, pp. 1038-1043.
- [111] H. D. Steffens, B. Wielage, J. Drozak, “Interface Phenomena And Bonding Mechanism Of Thermally-Sprayed Metal And Ceramic Composites”, Surface and Coatings Technology, (May 1991), Vol. 45, Issues 1-3, pp. 299-308.
- [112] Y. Y. Wang, C.-J. Li, A. Ohmori, “Influence Of Substrate Roughness On The Bonding Mechanisms Of High Velocity Oxy-Fuel Sprayed Coatings”, Thin Solid Films, (August 2005), Vol. 485, Issues 1-2, pp. 141-147.
- [113] H. Assadi, F. Gartner, T. Stoltenhoff, H. Kreye, “Bonding Mechanism in Cold Gas Spraying”, Acta Materials, (September 2003), Vol. 51, Issue 15, pp. 4379-4394.
- [114] C. Grujicic, L. Zhao, W. S. DeRosset, D. Helfritch, “Adiabatic Shear Instability Based Mechanism For Particles/Substrate Bonding In The Cold-Gas Dynamic-Spray Process”, Materials & Design, (December 2004), Vol. 25, Issue 8, pp. 681-688.

- [115] M. Boulos, P. Fauchais and E. Pfender, Thermal plasma: Fundamentals and applications, (1994), Vol. 1, ISBN 0306446073, Plenum press, New York, pp. 38-43.
- [116] L. Pawlowski, The Science And Engineering Of Thermal Spray Coatings, ISBN 0471490490, John Wiley & Sons, Chichester, (1995), pp. 221-284.
- [117] X. Chu, M.S. Wong, W.D. Sproul, S.L. Rohde, S.A. Barnett, "Deposition and Properties of Polycrystalline TiN/NbN Superlattice Coatings", Journal of Vacuum Science & Technology, (1992), Vol. A 10, pp. 1604-1609.
- [118] L. Hultman, L.R. Wallenberg, M. Shinn, S.A. Barnett, "Formation of Polyhedral Voids at Surface Cusps During Growth of Epitaxial TiN/NbN Superlattice and Alloy Films", Journal of Vacuum Science & Technology, (1992), issue 4, Vol. A 10, pp. 1618-1624.
- [119] X. Chu, S.A. Barnett, M.S.Wong, W.D. Sproul, "Reactive Unbalanced Magnetron Sputter Deposition of Polycrystalline TiN/NbN Superlattice Coatings", Surface Coating Technology, (1993), Vol. 57, pp. 13-18.
- [120] J. Walkowicz, J. Smolik, K. Miernik and J. Bujak., "Anti-wear properties of Ti(C,N) layers deposited by the vacuum arc method", Surface Coating Technology, (1996), Vol. 81, pp. 201.
- [121] C.W. Lee , J.H. Han, J. Yoon, M.C. Shin, S.I. Kwun, "A study on powder mixing for high fracture toughness and wear resistance of WC-Co-Cr coatings sprayed by HVOF", Surface & Coatings Technology, (2010), Vol. 204, pp. 2223-2229.

- [122] K. Holmberg, H. Ronkainen and A. Matthews, "Tribology of thin coatings", *Ceramic International*, (2000), Vol. 26, pp. 787–795.
- [123] C. Donnet and A. Erdemir, "Historical Developments and New Trends in Tribological and Solid Lubricant Coatings", *Surface Coating Technology*, (2004), Vol. 180–181, pp. 76–84.
- [124] W. Schintlmeister, W. Wallgram, J. Kanz and K. Gigl, "Cutting Tool Materials Deposited By Chemical Vapor Deposition", *Wear*, (1984), Vol. 100, pp. 153–169.
- [125] H.A. Jehn, "Improvement of the Corrosion Resistance of PVD Hard Coating-Substrate Systems", *Surface Coating Technology*, (2000), Vol. 125, pp. 212–217.
- [126] S. Fouvry, B. Wendler, T. Liskiewicz, M. Dudek, L. Kolodziejczyk, "Fretting Wear Analysis of TiC/VC Multilayered Hard Coatings: Experiments and Modelling Approaches". *Wear*, (2004), Vol. 257, pp. 641–53.
- [127] Praxair Technology Inc., www.praxair.com, [online], (accessed date June 5, 2012)
- [128] H. Y. Al-Fadhli, "Analysis of the Effect of Bending, Fatigue, Erosion-Corrosion, and Tensile on HVOF Coating of Metallic Surfaces", Ph.d. Thesis, Dublin City University, Mechanical Engineering, Dublin, (2005).
- [129] Laiwu Steel Group, LTD, steel manufacturer, China.
- [130] ASTM International, *Standard Test Methods and Definitions for Mechanical Testing of Steel Products*, A 370, 2008.
- [131] Sulzer Metco, www.sulzermetco.com, [online], (accessed date June 5, 2012).

- [132] Inframat, www.inframat.com, [online], (accessed date June 5, 2012).
- [133] Clean Blast, www.clean-blast.com, [online], (accessed date June 5, 2012).
- [134] J.M. Guilemany, "The enhancement of the properties of WC-Co HVOF coatings through the use of nanostructured and microstructured feedstock powders", *Surface & Coatings Technology*, (2006), Vol. 201, pp. 1180–1190.
- [135] W. Schedler, *Hard Metals for Practical Users*, VDI-Verlag, Diisseldorf, (1988), pp. 5-29.
- [136] http://www.engineeringtoolbox.com/young-modulus-d_417.html, [online], (accessed date June 5, 2012).
- [137] Jacobs, L.; M. M. Hyland; M. De Bonte, "Comparative study of WC-cermet coatings sprayed via the HVOF and the HVAF Process". *Journal of Thermal Spray Technology*, (1998), Vol. 7, pp. 213–218.
- [138] Ettmayer, Peter; Walter Lengauer, *Carbides: transition metal solid state chemistry encyclopaedia of inorganic chemistry*, John Wiley & Sons. ISBN 0471936200, (1994).
- [139] Yunfei Qiao, YouRong Liu, and Traugott E. Fischer; "Sliding and Abrasive Wear Resistance of Thermal-Sprayed WC-CO Coatings", *Journal of Thermal Spray Technology*, (March 2001), Vol. 10, p.119.

- [140] H.J. Kim, Y.G. Kweon, and R.W. Chang; “Wear and Erosion Behavior of Plasma-Sprayed WC-Co Coatings”, *Journal of Thermal Spray Technology*, (1994), Vol 3 (No. 2), pp. 169-178.
- [141] Basil R. Marple and Rogerio S. Lima, “Process Temperature/Velocity-Hardness-Wear Relationships for High-Velocity Oxyfuel Sprayed Nanostructured and Conventional Cermet Coatings”, *Journal of Thermal Spray Technology*, (2005), Vol. 14, Number 1, pp. 67-76.
- [142] Nerz, J., B. Kushner; A. Rotolico, “Microstructural evaluation of tungsten carbide-cobalt coatings”, *Journal of Thermal Spray Technology*, (1992), Vol. 1 (No. 2), pp. 147–152.
- [143] Pierson, Hugh O., *Handbook of Chemical Vapor Deposition (CVD): Principles, Technology, and Applications*, William Andrew Inc.. ISBN 0815513003, (1992).
- [144] L.C. Mei, W.H. Yang, D.M. Du, and L.W. Huang, “Characteristics of Two Types of WC-Co Thermal Spraying Powder”, *Proceeding of International Conference of Modern Developments in Powder Metallurgy*, (1985), Vo117, pp. 251-271.
- [145] J.R. Fincke, W.D. Swank, and D.C. Haggard, “Comparison of the Characteristics of HVOF and Plasma Thermal Spray, *Thermal Spray Industrial Applications*”, ASM International, (1994), pp. 325-330.
- [146] Giovanni Bolelli, Valeria Cannill, Luca Lusvarghi , Roberto Rosa , Alfredo Valarezo, Wanhuk B. Choi, Ravi Dey, Christopher Weyant, Sanjay Sampath; “Functionally graded WC–Co/NiAl HVOF coatings for damage tolerance, wear

- and corrosion protection”; *Surface & Coatings Technology*, (2012), Vol. 206, pp. 2585–2601.
- [147] E. Celik E., O. Culhaa, B. Uyulgana, N.F. Ak Azema, I. Ozdemira, and A. Turkc, “Assessment of microstructural and mechanical properties of HVOF sprayed WC-based cermet coatings for a roller cylinder”, *Surface & Coatings Technology*, (2006), Vol. 200, pp.4320– 4328.
- [148] H. Li, K.A. Khor, L.G. Yu, P. Cheang, “Microstructure modifications and phase transformation in plasma-sprayed WC–Co coatings following post-spray spark plasma sintering”, *Surface & Coatings Technology*, (2005), Vol. 194, pp. 96 – 102.
- [149] S. Rangaswamy and H. Herman, “Metallurgical Characterization of WC-Co Coatings”, *Advances in Thermal Spraying*, (1986), pp. 101-110.
- [150] Cecilia Bartuli, Teodoro Valente, Fabio Cipri, Edoardo Bemporad, and Mario Tului, “Parametric Study of an HVOF Process for the Deposition of Nanostructured WC-Co Coatings”, *Journal of Thermal Spray Technology*, (June 2005), Vol. 14 (No.2), p. 193.
- [151] Tahar Sahraoui, Sofiane Guessasma, M. Ali Jeridane, Mohamed Hadji, “HVOF sprayed WC–Co coatings: Microstructure, mechanical properties and friction moment prediction”, *Materials and Design*, (2010), Vol. 31, pp. 1431–1437.
- [152] Makoto Watanabe , Masayuki Komatsu, Seiji Kuroda, “Multilayered WC–Co/Cu coatings by warm spray deposition”, *Surface & Coatings Technology*, (2011), Vol. 205, pp. 5358–5368.

- [153] Robert J.K. Wood, "Tribology of thermal sprayed WC-Co coatings", *Int. Journal of Refractory Metals & Hard Materials*, (2010), Vol. 28, pp. 82-94.
- [154] Li CJ, Ohmori A, Harada Y, "Formation of an amorphous phase in thermally sprayed WC-Co", *Journal of Thermal Spray Technology*, (1996), Vol. 5 (No 1), pp. 69-73.
- [155] L Steeper, G. Irons, W.R. Kratochvil, D.J. Varacalle, Jr., G.C. Wilson, R.W. Johnson, and W.L.Riggs, "A Taguchi Experiment Design Study of Twin-Wire Electric Arc Sprayed Aluminum Coatings", *Thermal Spray: International Advances in Coatings Technology*, ASM International, (1992), pp. 427-432.
- [156] Y. Matsubara and A. Tomiguchi, "Surface Texture and Adhesive Strength of High Velocity Oxy-Fuel Sprayed Coatings for Rolls of Steel Mills", *Thermal Spray: International Advances in Coatings Technology*, ASM International, (1992), pp. 637-641.
- [157] A. Hasui, S. Kitahara, and T. Fukushima, "Relation between Properties of Coating and Spraying Angle in Plasma Jet Spraying", *Transactions of National Research Institute for Metals*, (1970), Vol 12, pp. 9-20.
- [158] M.F. Smith, R.A. Neiser, and R.C. Dykhuizen, "An Investigation of the Effects of Droplet Impact Angle in Thermal Spray Deposition", *Thermal Spray Industrial Applications*, ASM International, (1994), pp. 603-608.
- [159] M.P. Kanouff, R.A. Neiser, Jr., and T.J. Roemer, "Surface Roughness of Thermal Spray Coatings Made with Off-Normal Spray Angles", *Journal of Thermal Spray Technology*, (1998), Vol. 7 (No. 2), p. 219.

- [160] Yongzhong Jin, Xinyue Li, Dongliang Liu, Chunhai Liu, Ruisong Yang, “Phase and microstructure evolution during the synthesis of WC nanopowders via thermal processing of the precursor”, *Powder Technology*, (2012), Vol. 217, pp. 482–485.
- [161] ASTM International, *Standard Test Method of Knoop and Vickers Hardness of Materials*, E384, 2008.
- [162] ASTM B 117 *Standard Practice for Operating Salt Spray (Fog) Apparatus*, American Society of Testing and Materials, 2009.
- [163] Cavaleiro, Christopher M. A. Brett, in: L. Faria (Ed.), *Proceedings of EUROMAT’98*, Sociedade Portuguesa dos Materiais, Lisbon, (1998), p. 233.
- [164] P. Andrews, T.F. Illson, S.J. Matthews, “Erosion–corrosion studies on 13 Cr steel in gas well environments by liquid jet impingement”, *Wear*, (1999), pp. 233–235.
- [165] *Annual Book of ASTM standards 2002*, Section 03, 03-02, G119-93 ISSN: 0192-2998 (2002).
- [166] ASTM International, *Standard Practice for Liquid Impingement Erosion Testing*, G73, 2004.
- [167] ASTM International, *Standard Practice for the Preparation of Substitute Ocean Water*, D 1141, 2003.

- [168] ASTM International, Standard Test Method for Flexural Properties of Unreinforced and Reinforced Plastics and Electrical Insulating Materials, D 790, 2007.
- [169] ASTM International, Standard Test Method for Tension Testing of Metallic Materials, E 8, 2004.
- [170] R. Davis, Handbook of Thermal Spray Technology, ASM International, USA, ISBN 0-87170-795-0, 2004, p. 1.
- [171] B.D. Sartwell, K. Legg, B. Bodger, AESF/EPA Conference for Environmental Excellence, vol. 231, 1999, p. 1.
- [172] Yafang Han, Fusheng Pan, Jianmao Tang, Chungeng Zhou, "Surface Modification by HVOF Coating of Micron-Sized WC-Metal Powder and Laser-Heating of the Coating", Materials Science Forum, (2011), pp. 654-686.
- [173] A.W. Adamson, Physical Chemistry of Surfaces, 4th Ed., John Wiley and Sons, ISBN-10: 0471148733, 1982, p. 404.
- [174] H.E. Exner, "Physical and Chemical Nature of Cemented Carbides", International Metals Reviews, (1979) , Vo124, p 149.
- [175] C. Verdon, "Microstructure and Erosion Resistance of WC Coatings Deposited by HVOF Thermal Spraying", Ph.D. Thesis No. 1393, Switzerland, 1995.
- [176] Akesson, "An Experimental and Thermodynamic Study of the Co-W-C System in the Temperature Range 1470-1700 K", Science of Hard Materials, Proceeding of Int. Conf., (Aug 1983), pp. 71-82.

- [177] A. Karimi, Ch. Verdon, and G. Barbezat, "Microstructure and Hydroabrasive Wear Behaviour of High Velocity Oxy-Fuel Thermally Sprayed WCCo(Cr) Coatings", *Surface Coating Technology*, (1993), Vol. 57, pp. 81-89.
- [178] V.V. Sobolev, J.M. Guilemay, and J.A. Calero, "Formation of Structure of WC-Co Coatings on Aluminium Alloy Substrate During High-Velocity Oxy-Fuel (HVOF) Spraying", *Journal of Thermal Spray Technology*, (1995), Vol 4 (No. 4), pp. 401- 407.
- [179] P. Chivavibul, M. Watanabe, S. Kuroda, "Effect of Microstructure of HVOF-Sprayed WC-Co Coatings on Their Mechanical Properties", *Proceeding of Thermal Spray 2007: Global Coating Solutions*, ASM International, 2007
- [180] H.L. de Villiers Lovelock, "Powder/Processing/Structure Relationships in WC-Co Thermal Spray Coatings", *Journal of Thermal Spray Technology*, (1998), Vol. 7 (No.3), p. 357.
- [181] Qing Zhan, Ligen Yu, Fuxing Ye, Qunji Xue, Hua Li, "Quantitative evaluation of the decarburization and microstructure evolution of WC-Co during plasma spraying", *Surface & Coatings Technology*, (2012), Vol. 206, pp. 4068–4074.
- [182] Li C-J, Yang G-J, "Relationships between feedstock structure, particle parameter, coating deposition, microstructure and properties for thermally sprayed conventional and nanostructured WC-Co", *Int. Journal of Refractory Metals and Hard Materials*, (2012), doi:10.1016/j.ijrmhm.2012.03.014.

- [183] H. Li, K.A. Khor , L.G. Yua, P. Cheang, “Microstructure modifications and phase transformation in plasma-sprayed WC–Co coatings following post-spray spark plasma sintering”, *Surface and Coatings Technology*, (2005),Vol 194, pp. 96–102.
- [184] S. Basinski-Pampuch and T. Gibas, “Observations on Some Plasma Sprayed Metal Carbides”, *Ceramic International*, Vol 3 (No. 4), 1977, pp. 152-158.
- [185] Y. Wang and P. Kettunen, “The Optimization of Spraying Parameters for WC-Co Coatings by Plasma and Detonation-Gun Spraying”, *Proceeding of Thermal Spray: International Advances in Coatings Technology*, ASM International, 1992, pp. 575-580.
- [186] L.-M. Berger, B. Schultrich, A. Oswald, and H. Preiss, “Influence of Carbide Powder Composition on Decarburization and Properties of Air Plasma Sprayed Coatings”, *Proceeding of Thermal Spray: International Advances in Coatings Technology*, ASM International, 1992, pp. 253-258.
- [187] M.G.S. Naylor, “Development of Wear-Resistant Ceramic Coatings for Diesel Engine Components”, *National Technical Information Service, U.S. Dept. of Coinmerce*, Vol 1, 1992.
- [188] J.E. Nerz, B.A. Kushner, and A.J. Rotolico, “Effects of Deposition Methods on the Physical Properties of Tungsten Carbide-12 wt% Cobalt Thermal Spray Coatings”, *The Minerals, Metals and Materials Society*, 1990, pp. 133-143.

- [189] S.Y. Hwang, B.G. Seong, and M.C. Kim, "Characterization of WC-Co Coatings Using HPP-HVOF Process", *Proceeding of Thermal Spray: Practical Solutions for Engineering Problems*, ASM International, 1996, pp. 107-112.
- [190] M.S.A. Khan and T.W. Clyne, "Microstructure and Abrasion Resistance of Plasma Sprayed Cermet Coatings", *Proceeding of Thermal Spray: Practical Solutions for Engineering Problems*, ASM International, 1996, p 113-122
- [191] S.E Wayne and S. Sampath, "Structure/Property Relationships in Sintered and Thermally Sprayed WC-Co", *Journal of Thermal Spray Technology*, (1992), Vol 1 (No. 4), pp. 307-315.
- [192] C.-J. Li, A. Ohmori, and Y. Harada, "Effect of Powder Structure on the Structure Of Thermally Sprayed WC-Co Coatings", *Journal of Material Science*, (1996), Vol 31, pp. 785-794.
- [193] K. Korpiola and P. Vuorislo, "Effect of HVOF Gas Velocity and Fuel to Oxygen Ratio on the Wear Properties of Tungsten Carbide Coating", *Proceeding of Thermal Spray: Practical Solutions for Engineering Problems*, ASM International, 1996, p 177-184
- [194] C Tekmen, H Cetinel, A Turk, E Celik, "Wear behaviour of plasma sprayed WC-Ni coatings", *Euro Ceramics VIII*, PTS 1-3 (2004), pp. 264-268.
- [195] B.H. Kear, R.K. Sadangi, M. Jain, R. Yao, Z. Kalman, G. Skandan, and W.E. Mayo, "Thermal Sprayed Nanostructured WC/Co Hardcoatings", *Journal of Thermal Spray Technology*, (2000), Vol. 9 (No. 3), p. 99.

- [196] Javad Mostaghimi and Sanjeev Chandra, "Splat formation in plasma-spray coating process", *Pure And Applied Chemistry*, (2002), Vol. 74 (No. 3), pp. 441–445.
- [197] J. Munemasa and T. Kumakiri, "Effect of the surface roughness of substrates on the corrosion properties of films coated by physical vapour deposition", *Technology Development Centre, Hyogo 651-22, Japan*, 22 August 2002.
- [198] Bongyoung Yoo, Ki Ryoung Shin, Duck Young Hwang, Dong Heon Lee, Dong Hyuk Shin, "Effect of surface roughness on leakage current and corrosion resistance of oxide layer on AZ91 Mg alloy prepared by plasma electrolytic oxidation Original Research Article *Applied Surface Science*", (2010), Vol. 256, Issue 22, pp. 6667-6672.
- [199] W. Li, D.Y. Li, "Influence of surface morphology on corrosion and electronic behavior", *Acta Materialia*, (2006), Vol. 54, Issue 2, pp. 445-452.
- [200] N. I. Smirnov, M. V. Prozhega, and N. N. Smirnov, "Study of Tribological Properties of Detonation Nanostructured WC-Co-Based Coatings", *Journal of Friction and Wear*, (2007), Vol. 28 (No. 2), pp. 200–205.
- [201] H. Kreye, D. Fandrich, H.H. Miiller, and G. Reiners, "Microstructure and Bond Strength of WC-Co Coatings Deposited by Hypersonic Flame Spraying (Jet Kote Process)", *Advances in Thermal Spraying ,Proceeding of Thermal Spray Conf.*, Sept 1986 (Montreal, Canada), pp. 121-128.
- [202] N. Wagner, H. Kreye, and H. Kestel, "Production of Wear Resistant WC-Co Coatings Using Hypersonic Flame Spraying", *Z. Werkstofftech*, (1985), Vol 16, pp. 55-60.

- [203] V. Pershin, M. Lufitha, S. Chandra, and J. Mostaghimi, "Effect of Substrate Temperature on Adhesion Strength of Plasma-Sprayed Nickel Coatings", *Journal of Thermal Spray Technology*, (2003), Vol. 12 (No. 3), pp. 370-376.
- [204] Chenghong Yi, Hongyuan Fann, Ji Xiong, Zhixing Guo, Guangbiao Dong, Weicai Wan, Hongsheng Chen, "Effect of WC content on the microstructures and corrosion behavior of Ti(C,N)-based cermets", *Ceramic International*, (2012), Vol. 39, p. 902.
- [205] C. Monticelli, A. Frignani, and F. Zucchi, "Investigation on the Corrosion Process of Carbon Steel Coated By HVOF WC/Co Cermets in Neutral Solution", *Corrosion Science*, (2004), Vol. 46, pp. 1225–1237.
- [206] C. Monticelli, A. Balbo, F. Zucchi, "Corrosion and tribocorrosion behaviour of cermet and cermet/nanoscale multilayer CrN/NbN coatings", *Surface & Coatings Technology*, (2010), Vol. 204, pp. 1452–1460.
- [207] Cho JE, Hwang SJ, Kim KY, "Corrosion Behaviour of Thermal Sprayed WC Cermet Coatings Having Various Metallic Binders in Strong Acidic Environment", *Surface Coating Technology*, (2006), pp. 2653–62.
- [208] Imasato Shuichi, Shigeya Sakaguchi, Taikou Okada and Yasunori Hayashi, "Effect of WC Grain Size on Corrosion Resistance of WC-Co Cemented Carbide", *Journal of the Japan Society of Powder and Powder Metallurgy*, (2001), Vol.48 (No 7), pp. 609-615.
- [209] Charles F. Baes, Robert E. Mesmer, *The hydrolysis of cations*, Wiley, New York, ISBN-0471039853, 1976.

- [210] Pourbaix Marcel, Atlas of electrochemical equilibria in aqueous solutions. 2nd Edition, Pergamon press, Houston, USA: NACE- 1974.
- [211] R. S. Lillard, G. S. Kanner, and D. P. Butt, "The Nature of Oxides on Tungsten in Acidic and Alkaline Solutions", Journal of Electrochemical Soc., (1998), Vol. 145 (No. 8), pp. 2718-2725.
- [212] K. M. Krupka, R. J. Serne, "Geochemical Factors Affecting the Behavior of Antimony, Cobalt, Europium, Technetium, and Uranium in Vadose Sediments", Pacific Northwest National Laboratory; (December 2002), p.32.
- [213] Chang-Jiu Li, Gang-Chang Ji, Yu-Yue Wang, Keiji Sonoya, "Dominant effect of carbide rebounding on the carbon loss during high velocity oxy-fuel spraying of Cr₃C₂-NiCr", Thin Solid Films, (2002), Vol. 419, pp. 137-143.
- [214] Feng Tanga, Leonardo Ajdelsztajna, George E Kimb, Virgil Provenzanoc, and Julie M Schoenunga, "Effects of surface oxidation during HVOF processing on the primary stage oxidation of a CoNiCrAlY coating", Surface & Coatings Technology, (2004), Vol. 185, pp. 228-233.
- [215] S. Kuroda T. Fukushima, M. Sasaki and T. Kodama, "Microstructure and Corrosion Resistance of HVOF Sprayed 316L Stainless Steel and Ni Base Alloy Coatings", Proceeding of Thermal Spray: Surface Engineering via Applied Research, ASM International, OH, 2000, pp. 455-462.
- [216] Swank W. D., Fincke J. R., Haggard D. C., "HVOF Particle Flow Field Characteristics", Proceeding of Thermal Spray: Industrial Application, ASM International, 1994, pp. 319-324.

- [217] Bjordal M, Bardal E, Rogne T, Eggen TG., “Erosion and corrosion properties of WC coatings and duplex stainless steel in sand-containing synthetic sea-water”, *Wear*, (1995), pp.186–187.
- [218] J. Stokes, “Production of Coated and Free-Standing Engineering Components Using the HVOF (High Velocity Oxy-Fuel) Process” , Ph.D thesis, Dublin City University, (2003), p. 248-9.

APPENDIX

Coating Process Parameters A2-A17

BATCH No.= 01**First Layer Coating Data Sheet**

Powder Used in this layer Percentage
 SM-5812 100%

Initial Coating Layer Thickness (microns) 0 Targeted Coating Layer Thickness (microns) 160
 Coating System : HVOF Time to complete one pass (second): 17
 Spray Distance (in) : 15 Pass length (mm): 200
 Gun Speed (%): 30 Radial Speed RPM: 90

Coating Process Data

Cycle No.	No. of Spray Passes	No. of Cooling Passes	Actual No. of Spray Passes	Spray Operating Parameters						
				Oxygen Flow (cft/hr)	Fuel Rate (gal/hr)	Feeder Speed RPM	Powder Feed Rate (g/min)	Spray Temp. (C)	Cooling Temp. (C)	Thickness (microns)
1	2	4	2	1950	6.0	8.8	77	180	59	
2	2	4	4	1950	6.0	8.8	77	160	46	40
3	2	4	6	1950	6.0	8.8	77	138	58	
4	2	4	8	1950	6.0	8.8	77	135	65	
5	2	4	10	1950	6.0	8.8	77	127	61	
6	2	4	12	1950	6.0	8.8	77	138	44	80
7	4	4	16	1950	6.0	8.8	77	203	79	
8	3	4	19	1950	6.0	8.8	77	193	43	110
9	3	4	22	1950	6.0	8.8	77	168	54	
10	3	4	25	1950	6.0	8.8	77	174	66	
11	3	4	28	1950	6.0	8.8	77	137	46	150
12	2	full cool	30	1950	6.0	8.8	77	145	38	160

Second Layer Coating Data Sheet

Powder Used in this layer Percentage
 SM-5812 100%

Initial Coating Layer Thickness (microns) 160 Targeted Coating Layer Thickness (microns) 320
 Coating System : HVOF Time to complete one pass (second): 17
 Spray Distance (in) : 15 Pass length (mm): 200
 Gun Speed (%): 30 Radial Speed RPM: 90

Coating Process Data										
Cycle No.	No. of Spray Passes	No. of Cooling Passes	Actual No. of Spray Passes	Spray Operating Parameters						
				Oxygen Flow (cft/hr)	Fuel Rate (gal/hr)	Feeder Speed RPM	Powder Feed Rate (g/min)	Spray Temp. (C)	Cooling Temp. (C)	Thickness (microns)
1	3	4	3	1950	6.0	8.8	77	130	46	
2	3	4	6	1950	6.0	8.8	77	148	70	
3	3	4	9	1950	6.0	8.8	77	146	56	
4	3	4	12	1950	6.0	8.8	77	127	47	200
5	3	4	15	1950	6.0	8.8	77	140	57	
6	3	4	18	1950	6.0	8.8	77	115	46	
7	3	4	21	1950	6.0	8.8	77	148	60	240
8	3	10	24	1950	6.0	8.8	77	147	67	
9	2	4	26	1950	6.0	8.8	77	133	63	
10	2	4	28	1950	6.0	8.8	77	124	62	
11	2	4	30	1950	6.0	8.8	77	124	46	290
12	2	4	32	1950	6.0	8.8	77		64	
13	2	4	34	1950	6.0	8.8	77	140	67	
14	2	4	36	1950	6.0	8.8	77	107	56	
15	2	4	38	1950	6.0	8.8	77	124	39	330

Third Layer Coating Data Sheet

Powder Used in this layer Percentage
 SM-5812 100%

Initial Coating Layer Thickness (microns) 330 Targeted Coating Layer Thickness (microns) 480
 Coating System : HVOF Time to complete one pass (second): 17
 Spray Distance (in) : 15 Pass length (mm): 200
 Gun Speed (%): 30 Radial Speed RPM: 90

Coating Process Data										
Cycle No.	No. of Spray Passes	No. of Cooling Passes	Actual No. of Spray Passes	Spray Operating Parameters						
				Oxygen Flow (cft/hr)	Fuel Rate (gal/hr)	Feeder Speed RPM	Powder Feed Rate (g/min)	Spray Temp. (C)	Cooling Temp. (C)	Thickness (microns)
1	4	6	4	1950	6.0	8.8	77	160	77	
2	4	6	8	1950	6.0	8.8	77	168	67	
3	4	6	12	1950	6.0	8.8	77	136	55	390
4	4	6	16	1950	6.0	8.8	77	142	85	
5	4	6	20	1950	6.0	8.8	77	153	56	
6	4	6	24	1950	6.0	8.8	77	149	45	440
7	4	6	28	1950	6.0	8.8	77	134	67	
8	4	6	32	1950	6.0	8.8	77	137	76	468
9	2	full cool	34	1950	6.0	8.8	77	115	39	480

BATCH No.= 02**First Layer Coating Data Sheet**

Powder Used in this layer Percentage
S-7412 100%

Initial Coating Layer Thickness (microns) 0 Targeted Coating Layer Thickness (microns) 160
Coating System : HVOF Time to complete one pass (second): 30
Spray Distance (in) : 15 Pass length (mm): 305
Gun Speed (%): 30 Radial Speed RPM: 90

Coating Process Data

Cycle No.	No. of Spray Passes	No. of Cooling Passes	Actual No. of Spray Passes	Spray Operating Parameters						
				Oxygen Flow (cft/hr)	Fuel Rate (gal/hr)	Feeder Speed RPM	Powder Feed Rate (g/min)	Spray Temp. (C)	Cooling Temp. (C)	Thickness (microns)
1	4	10	4	1950	6.0	7.2	90	185	55	41
2	4	10	8	1950	6.0	7.2	90	178	38	80
3	4	10	12	1950	6.0	7.2	90	190	35	121
4	2	10	14	1950	6.0	7.2	90	170	37	161

Second Layer Coating Data Sheet

Powder Used in this layer Percentage
S-7412 100%

Initial Coating Layer Thickness (microns) 161 Targeted Coating Layer Thickness (microns) 320
Coating System : HVOF Time to complete one pass (second): 30
Spray Distance (in) : 15 Pass length (mm): 305
Gun Speed (%): 30 Radial Speed RPM: 90

Coating Process Data

Cycle No.	No. of Spray Passes	No. of Cooling Passes	Actual No. of Spray Passes	Spray Operating Parameters						
				Oxygen Flow (cft/hr)	Fuel Rate (gal/hr)	Feeder Speed RPM	Powder Feed Rate (g/min)	Spray Temp. (C)	Cooling Temp. (C)	Thickness (microns)
1	4	10	4	1950	6.0	7.2	90	170	60	201
2	4	10	8	1950	6.0	7.2	90	176	55	241
3	4	10	12	1950	6.0	7.2	90	178	57	281
4	4	10	16	1950	6.0	7.2	90	170	60	321

Third Layer Coating Data Sheet

Powder Used in this layer Percentage
 S-7412 100%

Initial Coating Layer Thickness (microns)	321	Targeted Coating Layer Thickness (microns)	480
Coating System :	HVOF	Time to complete one pass (second):	30
Spray Distance (in) :	15	Pass length (mm):	305
Gun Speed (%):	30	Radial Speed RPM:	90

Coating Process Data

Cycle No.	No. of Spray Passes	No. of Cooling Passes	Actual No. of Spray Passes	Spray Operating Parameters						
				Oxygen Flow (cft/hr)	Fuel Rate (gal/hr)	Feeder Speed RPM	Powder Feed Rate (g/min)	Spray Temp. (C)	Cooling Temp. (C)	Thickness (microns)
1	4	10	4	1950	6.0	7.2	90	160	55	361
2	4	10	8	1950	6.0	7.2	90	180	60	401
3	4	10	12	1950	6.0	7.2	90	177	50	440
4	4	10	16	1950	6.0	7.2	90	170	47	482

BATCH No.= 03**First Layer Coating Data Sheet**

Powder Used in this layer Percentage
 SM-5812 100%

Initial Coating Layer Thickness (microns)	0	Targeted Coating Layer Thickness (microns)	160
Coating System :	HVOF	Time to complete one pass (second):	30
Spray Distance (in) :	15	Pass length (mm):	305
Gun Speed (%):	30	Radial Speed RPM:	90

Coating Process Data

Cycle No.	No. of Spray Passes	No. of Cooling Passes	Actual No. of Spray Passes	Spray Operating Parameters						
				Oxygen Flow (cft/hr)	Fuel Rate (gal/hr)	Feeder Speed RPM	Powder Feed Rate (g/min)	Spray Temp. (C)	Cooling Temp. (C)	Thickness (microns)
1	4	10	4	1950	6.0	7.2	77	162	63	34
2	4	10	8	1950	6.0	7.2	77	170	65	66
3	4	10	12	1950	6.0	7.2	77	166	45	90
4	4	10	16	1950	6.0	7.2	77	175	65	127
5	4	10	20	1950	6.0	7.2	77	167	60	162

Second Layer Coating Data Sheet

Powder Used in this layer Percentage
 SM-5812 80%
 AMDRY 9954 20%

Initial Coating Layer Thickness (microns)	162	Targeted Coating Layer Thickness (microns)	320
Coating System :	HVOF	Time to complete one pass (second):	30
Spray Distance (in) :	15	Pass length (mm):	305
Gun Speed (%):	30	Radial Speed RPM:	90

Coating Process Data										
Cycle No.	No. of Spray Passes	No. of Cooling Passes	Actual No. of Spray Passes	Spray Operating Parameters						
				Oxygen Flow (cft/hr)	Fuel Rate (gal/hr)	Feeder Speed RPM	Powder Feed Rate (g/min)	Spray Temp. (C)	Cooling Temp. (C)	Thickness (microns)
1	4	10	4	1950	6.0	7.2	77	162	60	180
2	4	10	8	1950	6.0	7.2	77	170	55	220
3	4	10	12	1950	6.0	7.2	77	175	65	280
4	4	10	16	1950	6.0	7.2	77	175	50	322

Third Layer Coating Data Sheet

Powder Used in this layer	Percentage
SM-5812	60%
AMDRY 9954	40%

Initial Coating Layer Thickness (microns)	322	Targeted Coating Layer Thickness (microns)	480
Coating System :	HVOF	Time to complete one pass (second):	30
Spray Distance (in) :	15	Pass length (mm):	305
Gun Speed (%):	30	Radial Speed RPM:	90

Coating Process Data										
Cycle No.	No. of Spray Passes	No. of Cooling Passes	Actual No. of Spray Passes	Spray Operating Parameters						
				Oxygen Flow (cft/hr)	Fuel Rate (gal/hr)	Feeder Speed RPM	Powder Feed Rate (g/min)	Spray Temp. (C)	Cooling Temp. (C)	Thickness (microns)
1	4	10	4	1950	6.0	7.0	77	160	55	350
2	4	10	8	1950	6.0	7.0	77	162	60	367
3	4	10	12	1950	6.0	7.0	77	150	55	380
4	4	10	16	1950	6.0	7.0	77	160	62	400
5	4	10	20	1950	6.0	7.0	77	170	60	418
6	4	10	24	1950	6.0	7.0	77	168	50	430
7	4	10	28	1950	6.0	7.0	77	165	40	458
8	4	10	32	1950	6.0	7.0	77	160	55	486

BATCH No.= 04**First Layer Coating Data Sheet**

Powder Used in this layer Percentage
 S-7412 100%

Initial Coating Layer Thickness (microns) 0 Targeted Coating Layer Thickness (microns) 160
 Coating System : HVOF Time to complete one pass (second): 30
 Spray Distance (in) : 15 Pass length (mm): 305
 Gun Speed (%): 30 Radial Speed RPM: 90

Coating Process Data

Cycle No.	No. of Spray Passes	No. of Cooling Passes	Actual No. of Spray Passes	Spray Operating Parameters						
				Oxygen Flow (cft/hr)	Fuel Rate (gal/hr)	Feeder Speed RPM	Powder Feed Rate (g/min)	Spray Temp. (C)	Cooling Temp. (C)	Thickness (microns)
1	4	10	4	1950	6.0	7.2	90	170	55	38
2	4	10	8	1950	6.0	7.2	90	172	60	80
3	4	10	12	1950	6.0	7.2	90	168	62	122
4	4	11	16	1950	6.0	7.2	90	175	59	158
5	2	10	18	1950	6.0	7.2	90	150	40	166

Second Layer Coating Data Sheet

Powder Used in this layer Percentage
 S-7412 80%
 AMDRY 9954 20%

Initial Coating Layer Thickness (microns) 166 Targeted Coating Layer Thickness (microns) 320
 Coating System : HVOF Time to complete one pass (second): 30
 Spray Distance (in) : 15 Pass length (mm): 305
 Gun Speed (%): 30 Radial Speed RPM: 90

Coating Process Data										
Cycle No.	No. of Spray Passes	No. of Cooling Passes	Actual No. of Spray Passes	Spray Operating Parameters						
				Oxygen Flow (cft/hr)	Fuel Rate (gal/hr)	Feeder Speed RPM	Powder Feed Rate (g/min)	Spray Temp. (C)	Cooling Temp. (C)	Thickness (microns)
1	4	10	4	1950	6.0	7.2	90	170	55	216
2	4	10	8	1950	6.0	7.2	90	168	60	277
3	2	10	10	1950	6.0	7.2	90	166	55	306
4	1	10	11	1950	6.0	7.2	90	160	45	322

Third Layer Coating Data Sheet

Powder Used in this layer	Percentage
S-7412	60%
AMDRY 9954	40%

Initial Coating Layer Thickness (microns)	322	Targeted Coating Layer Thickness (microns)	480
Coating System :	HVOF	Time to complete one pass (second):	30
Spray Distance (in) :	15	Pass length (mm):	305
Gun Speed (%):	30	Radial Speed RPM:	90

Coating Process Data										
Cycle No.	No. of Spray Passes	No. of Cooling Passes	Actual No. of Spray Passes	Spray Operating Parameters						
				Oxygen Flow (cft/hr)	Fuel Rate (gal/hr)	Feeder Speed RPM	Powder Feed Rate (g/min)	Spray Temp. (C)	Cooling Temp. (C)	Thickness (microns)
1	4	10	4	1950	6.0	7.2	90	180	60	361
2	4	10	8	1950	6.0	7.2	90	168	55	402
3	4	10	12	1950	6.0	7.2	90	169	50	440
4	4	10	16	1950	6.0	7.2	90	166	40	482

BATCH No.= 11**First Layer Coating Data Sheet**

Powder Used in this layer
SM-5812

Percentage
100%

Initial Coating Layer Thickness (microns) 0

Coating System : Plasma

Spray Distance (in) : 5

Gun Speed (%) : 30

Spray Rate (g/min): 31 @ 2.49 RPM

Gas Injector: 3083112

Targeted Coating Layer Thickness (microns) 160

Time to complete one pass (second): 17.5

Pass length "Gun Travel"(mm): 18

Radial Speed RPM: 76

Anode: 2083730

Cathode: 1083A720

Coating Process Data

Cycle No.	No. of Spray Passes	No. of Cooling Passes	Actual No. of Spray Passes	Spray Operating Parameters							
				Primary Ar (psi)	Auxiliary He (psi)	Carrier Ar (psi)	Voltage (volt)	Current (A)	Spray Temp. (C)	Cooling Temp. (C)	Thickness (microns)
1	4	4	4	50	100	55	48	744	120	60	
2	4	4	8	50	100	55	48	744	126	65	50
3	4	4	12	50	100	55	48	744	117	65	
4	4	4	16	50	100	55	48	744	122	58	100
5	4	4	20	50	100	55	46	743	122	63	
6	4	4	24	50	100	55	46	743	118	60	140
7	2	4	26	50	100	55	46	743	98	58	160

Second Layer Coating Data Sheet

Powder Used in this layer
SM-5812

Percentage
100%

Initial Coating Layer Thickness (microns) 160

Coating System : Plasma

Spray Distance (in) : 5

Gun Speed (%) : 30

Spray Rate (g/min): 31 @ 2.49 RPM

Gas Injector: 3083112

Targeted Coating Layer Thickness (microns) 320

Time to complete one pass (second): 17.5

Pass length "Gun Travel"(mm): 18

Radial Speed RPM: 76

Anode: 2083730

Cathode: 1083A720

Coating Process Data

Cycle No.	No. of Spray Passes	No. of Cooling Passes	Actual No. of Spray Passes	Spray Operating Parameters							
				Primary Ar (psi)	Auxiliary He (psi)	Carrier Ar (psi)	Voltage (volt)	Current (A)	Spray Temp. (C)	Cooling Temp. (C)	Thickness (microns)
1	4	4	4	50	100	55	46	745	117	62	
2	4	4	8	50	100	55	46	745	111	60	210
3	4	4	12	50	100	55	46	745	106	63	
4	4	4	16	50	100	55	46	745	116	38	250
5	4	4	20	50	100	55	46	745	106	50	280
6	4	4	24	50	100	55	46	745	113	49	300
7	4	4	28	50	100	55	46	745	107	38	330

Third Layer Coating Data Sheet

Powder Used in this layer SM-5812	Percentage 100%		
Initial Coating Layer Thickness (microns)	330	Targeted Coating Layer Thickness (microns)	480
Coating System :	Plasma	Time to complete one pass (second):	17.5
Spray Distance (in) :	5	Pass length "Gun Travel"(mm):	18
Gun Speed (%):	30	Radial Speed RPM:	76
Spray Rate (g/min):	31 @ 2.49 RPM	Anode:	20837 30
Gas Injector:	3083112	Cathode:	1083A 720

Coating Process Data

Cycle No.	No. of Spray Passes	No. of Cooling Passes	Actual No. of Spray Passes	Spray Operating Parameters							
				Primary Ar (psi)	Auxial ary He (psi)	Carri er Ar (psi)	Volt age (volt)	Cur rent (A)	Spray Temp (C)	Coolin g Temp. (C)	Thickn ess (micro ns)
1	4	4	4	50	100	55	46	745	106	64	
2	4	4	8	50	100	55	46	745	105	66	380
3	4	4	12	50	100	55	46	745	106	65	
4	4	4	16	50	100	55	46	745	108	64	410
5	4	4	20	50	100	55	46	745	108	64	430
6	4	4	24	50	100	55	46	745	106	64	460
7	3	4	27	50	100	55	46	745	106	52	480

BATCH No.= 12**First Layer Coating Data Sheet**

Powder Used in this layer Percentage
S-7412 100%

Initial Coating Layer Thickness (microns)	0	Targeted Coating Layer Thickness (microns)	160
Coating System :	Plasma	Time to complete one pass (second):	17.5
Spray Distance (in) :	5	Pass length "Gun Travel"(mm):	180
Gun Speed (%):	30	Radial Speed RPM:	76
Spray Rate (g/min)	33 @ 1.81 RPM	Anode	2083730
Gas Injector	3083112	Cathode	1083A720

Coating Process Data

Cycle No.	No. of Spray Passes	No. of Cooling Passes	Actual No. of Spray Passes	Spray Operating Parameters							
				Primary Ar (psi)	Auxiliary He (psi)	Carrier Ar (psi)	Voltage (volt)	Current (A)	Spray Temp. (C)	Cooling Temp. (C)	Thickness (microns)
1	2	4	2	50	100	55	45	743	80	48	
2	4	4	6	50	100	55	45	743	90	52	40
3	2	4	8	50	100	55	45	743	100	60	
4	2	4	10	50	100	55	45	743	98	66	
5	2	4	12	50	100	55	45	743	80	45	
6	4	4	16	50	100	55	45	743	93	39	90
7	4	4	20	50	100	55	45	743	114	40	110
8	4	4	24	50	100	55	45	743	105	60	170

Second Layer Coating Data Sheet

Powder Used in this layer Percentage
S-7412 100%

Initial Coating Layer Thickness (microns)	170	Targeted Coating Layer Thickness (microns)	320
Coating System :	Plasma	Time to complete one pass (second):	17.5
Spray Distance (in) :	5	Pass length "Gun Travel"(mm):	180
Gun Speed (%):	30	Radial Speed RPM:	76
Spray Rate (g/min)	33 @ 1.81 RPM	Anode	2083730
Gas Injector	3083112	Cathode	1083A

Coating Process Data											
Cycle No.	No. of Spray Passes	No. of Cooling Passes	Actual No. of Spray Passes	Spray Operating Parameters							
				Primary Ar (psi)	Auxial ary He (psi)	Carrier Ar (psi)	Voltage (volt)	Current (A)	Spray Temp . (C)	Cooling Temp. (C)	Thickn ess (micro ns)
1	4	4	4	50	100	55	44	744	89	56	
2	4	4	8	50	100	55	44	744	93	57	230
3	4	4	12	50	100	55	44	744	89	61	
4	4	4	16	50	100	55	44	744	104	61	280
5	4	4	20	50	100	55	44	744	93	52	
6	4	4	24	50	100	55	44	744	101	46	340

Third Layer Coating Data Sheet

Powder Used in this layer Percentage
 S-7412 100%

Initial Coating Layer Thickness (microns)	340	Targeted Coating Layer Thickness (microns)	480
Coating System :	Plasma	Time to complete one pass (second):	17.5
Spray Distance (in) :	5	Pass length "Gun Travel"(mm):	180
Gun Speed (%):	30	Radial Speed RPM:	76
Spray Rate (g/min)	33 @ 1.81 RPM	Anode	2083730
Gas Injector	3083112	Cathode	1083A720

Coating Process Data											
Cycle No.	No. of Spray Passes	No. of Cooling Passes	Actual No. of Spray Passes	Spray Operating Parameters							
				Primary Ar (psi)	Auxial ary He (psi)	Carrier Ar (psi)	Voltage (volt)	Current (A)	Spray Temp . (C)	Cooling Temp. (C)	Thickn ess (micro ns)
1	4	4	4	50	100	55	44	744	104	51	
2	4	4	8	50	100	55	44	744	99	43	380
3	3	4	11	50	100	55	44	744	86	40	
4	4	4	15	50	100	55	44	744	90	38	440
5	4	4	19	50	100	55	44	744	93	45	470
6	1	4	20	50	100	55	44	744	68	38	490

BATCH No.= 13**First Layer Coating Data Sheet**

Powder Used in this layer Percentage
 SM-5812 100%

Initial Coating Layer Thickness (microns)	0	Targeted Coating Layer Thickness (microns)	160
Coating System :	Plasma	Time to complete one pass (second):	17.5
Spray Distance (in) :	5	Pass length "Gun Travel"(mm):	18
Gun Speed (%):	30	Radial Speed RPM:	76
Spray Rate (g/min):	31 @ 2.49 RPM	Anode:	20837 30
Gas Injector:	3083112	Cathode:	1083A 720

Coating Process Data

Cycle No.	No. of Spray Passes	No. of Cooling Passes	Actual No. of Spray Passes	Spray Operating Parameters							
				Primary Ar (psi)	Auxiliary He (psi)	Carrier Ar (psi)	Voltage (volt)	Current (A)	Spray Temp. (C)	Cooling Temp. (C)	Thickness (microns)
1	4	4	4	50	100	55	48	744	120	60	
2	4	4	8	50	100	55	48	744	126	65	50
3	4	4	12	50	100	55	48	744	117	65	
4	4	4	16	50	100	55	48	744	122	58	100
5	4	4	20	50	100	55	46	743	122	63	
6	4	4	24	50	100	55	46	743	118	60	140
7	2	4	26	50	100	55	46	743	98	58	160

Second Layer Coating Data Sheet

Powder Used in this layer Percentage
 SM-5812 80%
 AMDRY 995M 20%

Initial Coating Layer Thickness (microns)	160	Targeted Coating Layer Thickness (microns)	320
Coating System :	Plasma	Time to complete one pass (second):	17.5
Spray Distance (in) :	5	Pass length "Gun Travel"(mm):	18
Gun Speed (%):	30	Radial Speed RPM:	76
Spray Rate (g/min):	30 @ 2.6 RPM	Anode:	20837 30
Gas Injector:	3083112	Cathode:	1083A

Coating Process Data											
Cycle No.	No. of Spray Passes	No. of Cooling Passes	Actual No. of Spray Passes	Spray Operating Parameters							
				Primary Ar (psi)	Auxiliary He (psi)	Carrier Ar (psi)	Voltage (volt)	Current (A)	Spray Temp. (C)	Cooling Temp. (C)	Thickness (microns)
1	4	4	4	49	100	55	48	744	105	66	
2	4	4	8	49	100	55	48	744	97	64	210
3	4	4	12	49	100	55	48	744	98	65	
4	4	4	16	49	100	55	48	744	106	61	280
5	4	4	20	49	100	55	48	744	105	61	300
6	3	4	23	49	100	55	48	744	86	63	320

Third Layer Coating Data Sheet

Powder Used in this layer	Percentage
SM-5812	60%
AMDRY 995M	40%

Initial Coating Layer Thickness (microns)	320	Targeted Coating Layer Thickness (microns)	480
Coating System :	Plasma	Time to complete one pass (second):	17.5
Spray Distance (in) :	5	Pass length "Gun Travel"(mm):	18
Gun Speed (%):	30	Radial Speed RPM:	76
Spray Rate (g/min):	33 @ 2.49 RPM	Anode:	20837 30
Gas Injector:	3083112	Cathode:	1083A 720

Coating Process Data											
Cycle No.	No. of Spray Passes	No. of Cooling Passes	Actual No. of Spray Passes	Spray Operating Parameters							
				Primary Ar (psi)	Auxiliary He (psi)	Carrier Ar (psi)	Voltage (volt)	Current (A)	Spray Temp. (C)	Cooling Temp. (C)	Thickness (microns)
1	4	4	4	50	100	54	44	744	107	63	390
2	4	4	8	50	100	54	44	744	106	96	420
3	4	4	12	50	100	54	44	744	105	54	450
4	4	4	16	50	100	54	44	744	102	56	480

BATCH No.= 14**First Layer Coating Data Sheet**

Powder Used in this layer	Percentage
S-7412	100%

Initial Coating Layer Thickness (microns)	0	Targeted Coating Layer Thickness (microns)	160
Coating System :	Plasma	Time to complete one pass (second):	32
Spray Distance (in) :	5	Pass length "Gun Travel"(mm):	310
Gun Speed (%):	30	Radial Speed RPM:	76
Spray Rate (g/min)	31 @ 1.90 RPM	Anode	208370
Gas Injector	3083112	Cathode	1083A720

Coating Process Data

Cycle No.	No. of Spray Passes	No. of Cooling Passes	Actual No. of Spray Passes	Spray Operating Parameters							
				Primary Ar (psi)	Auxiliary He (psi)	Carrier Ar (psi)	Voltage (volt)	Current (A)	Spray Temp. (C)	Cooling Temp. (C)	Thickness (microns)
1	4	4	4	50	100	55	46	742	122	59	
2	4	4	8	50	100	55	46	742	130	55	60
3	4	4	12	50	100	55	46	742	118	47	
4	4	4	16	50	100	55	46	742	122	52	120
5	4	4	20	50	100	55	46	742	123	57	150

Second Layer Coating Data Sheet

Powder Used in this layer	Percentage
S-7412	80%
AMDRY 995M	20%

Initial Coating Layer Thickness (microns)	150	Targeted Coating Layer Thickness (microns)	320
Coating System :	Plasma	Time to complete one pass (second):	32
Spray Distance (in) :	5	Pass length "Gun Travel"(mm):	310
Gun Speed (%):	30	Radial Speed RPM:	76
Spray Rate (g/min)	33 @ 1.89 RPM	Anode	208370
Gas Injector	3083112	Cathode	1083A720

Coating Process Data											
Cycle No.	No. of Spray Passes	No. of Cooling Passes	Actual No. of Spray Passes	Spray Operating Parameters							
				Primary Ar (psi)	Aux. He (psi)	Carrier Ar (psi)	Voltage (volt)	Current (A)	Spray Temp. (C)	Cooling Temp. (C)	Thickness (microns)
1	4	4	4	50	100	55	47	744	130	62	
2	4	4	8	50	100	55	47	744	128	64	220
3	4	4	12	50	100	55	47	744	126	33	260
4	4	4	16	50	100	55	47	744	120	35	290
5	4	4	20	50	100	55	47	744	121	59	330

Third Layer Coating Data Sheet

Powder Used in this layer	Percentage
S-7412	60%
AMDRY 995M	40%

Initial Coating Layer Thickness (microns)	330	Targeted Coating Layer Thickness (microns)	480
Coating System :	Plasma	Time to complete one pass (second):	32
Spray Distance (in) :	5	Pass length "Gun Travel"(mm):	310
Gun Speed (%):	30	Radial Speed RPM:	76
Spray Rate (g/min)	33 @ 1.79 RPM	Anode	20837
Gas Injector	3083112	Cathode	1083A
			720

Coating Process Data											
Cycle No.	No. of Spray Passes	No. of Cooling Passes	Actual No. of Spray Passes	Spray Operating Parameters							
				Primary Ar (psi)	Aux. He (psi)	Carrier Ar (psi)	Voltage (volt)	Current (A)	Spray Temp. (C)	Cooling Temp. (C)	Thickness (microns)
1	4	4	4	50	100	55	45	743	124	52	
2	4	4	8	50	100	55	45	743	123	58	420
3	4	4	12	50	100	55	45	743	120	55	460
4	4	4	16	50	100	55	45	743	101	33	490